Probing the Interactions of Intrinsically Disordered Proteins with Copper Ions and Lipid Membranes by Fluorescence

A thesis submitted for the degree of

Doctor of Philosophy

By

Xiangyu Teng

Department of Chemistry

Imperial College London

February 2021

Acknowledgements

I would like to express my gratitude to my supervisors Dr Liming Ying and Prof Keith Willison, for providing me this opportunity to pursue a PhD, and for their invaluable guidance and training. I would also like to thank my family, for their unconditional love and support. Without them I will never complete this work. Finally, I would like to thank all my friends and colleagues, whose company and encouragement enriched my daily life and helped me conquer difficulties during these memorable years. With special thanks to Paul Girvan, for his supervision on laboratory training, and to EPSRC National Service for Electron Paramagnetic Resonance Spectroscopy at The University of Manchester, for providing support on EPR measurement.

Declaration

I declare that this thesis, submitted to fulfil the requirements for the degree of Doctor of Philosophy at Imperial College London, titled “Probing the Interactions of Intrinsically Disordered Proteins with Copper Ions and Lipid Membranes by Fluorescence” represents my own work, unless otherwise stated.

Xiangyu Teng

February 2021

Copyright Declaration

The copyright of this thesis rests with the author and is made available under a Creative Commons Attribution Non-Commercial No Derivatives licence. Researchers are free to copy, distribute or transmit the thesis on the condition that they attribute it, that they do not use it for commercial purposes and that they do not alter, transform or build upon it. For any reuse or redistribution, researchers must make clear to others the licence terms of this work.

Publications from This Work

Results presented in Chapter 3 are included as part of three publications:

Girvan, P., Miyake, T., Teng, X., Branch, T. & Ying, L. Kinetics of the interactions between copper and amyloid-β with FAD mutations and phosphorylation at the N terminus. *ChemBioChem* **17**, 1732-1737 (2016).

Girvan, P., Teng, X., Brooks, N. J., Baldwin, G. S. & Ying, L. Redox kinetics of the amyloid-β-Cu complex and its biological implications. *Biochemistry* **57**, 6228-6233 (2018).

Teng, X., Stefaniak, E., Girvan, P., Kotuniak, R., Płonka, D., Bal, W. & Ying, L. Hierarchical binding of copper^{II} to N-truncated Aβ_{4-16} peptide. *Metallomics* **12**, 470-473 (2020).

Results presented in Chapter 5 are currently under preparation as:

Teng, X., Sheveleva, A., Tuna, F., Willison, K. & Ying, L. Acetylation rather than H50Q mutation impacts the kinetics of Cu(II) binding to α-synuclein. *Scientific Reports*.

Abstract

Amyloid-β (Aβ) and α-synuclein (αSyn) are intrinsically disordered proteins (IDPs) with limited knowledge of normal functions. Their properties of interacting with metal ions and lipid membranes could possess physiological significance, but they may also induce pathological effects such as aggregation and reactive oxygen species (ROS) generation, thereby leading to the development of Alzheimer's disease (AD) and Parkinson's disease (PD). This thesis aims to unveil the molecular mechanisms of the interactions of Aβ and αSyn with Cu^{2+} and neuronal membranes, thus providing new information about the physiological and pathological roles of Aβ and αSyn, as well as Cu^{2+} and synaptic vesicle in neuronal synapses.

An introduction of Aβ and αSyn, as well as their interactions with Cu^{2+} and lipid membranes is described in Chapter 1. Subsequently, in Chapter 2, the methods and materials used in this work are introduced.

The main results of this thesis are presented from Chapter 3, in which the kinetic interactions of Cu^{2+} with phosphorylated serine residue 8 Aβ (pS8-Aβ) and N-truncated $Aβ_{4-16}$ are presented. In this Chapter, the rate constants of Cu^{2+} binding to pS8-Aβ and N-truncated $Aβ_{4-16}$ were both determined to be ~10^8 M^{-1} s^{-1}, which are comparable to that of wild type (WT) $Aβ_{16}$. However, the binding affinity of Cu^{2+} to $Aβ_{4-16}$ is much tighter (~10^3 - 10^4 times) than those of pS8-Aβ and WT-$Aβ_{16}$. An interaction mechanism was proposed to describe the hierarchical binding of Cu^{2+} to $Aβ_{4-16}$.

The thesis then moves onto the study of αSyn. In Chapter 4, the production protocol of various fluorescently labelled and unlabelled αSyn samples is described first. The produced αSyn samples were then used in the work of Chapter 5 and Chapter 6 for investigating αSyn-Cu^{2+} interactions and αSyn-lipid interactions, respectively. In Chapter 5, the binding affinities and modes of Cu^{2+} to WT-αSyn and N-terminally acetylated (NAc) αSyn are presented. It was found that WT-αSyn shows around four orders of magnitude stronger binding affinity to Cu^{2+} than NAc-αSyn. Nevertheless, as described in Chapter 6, WT-αSyn shows weaker binding affinity with 50 nm synaptic-like small unilamellar vesicle (SUV) than NAc-αSyn. In addition, the binding

conformation of WT-αSyn on SUV was found to be mixed extended, curved or antiparallel helical structures when single αSyn binds to one SUV. However, if there are multiple αSyn molecules on one SUV, they tend to adopt the curved helical structure for association.

In Chapter 7, SUV is shown to be able to bind Cu^{2+} as well, with a high affinity (K_d = 0.7(1) nM) which is even stronger than those of Aβ and αSyn. Such strong interaction is due to the constituent DOPS. In addition, the SUV-Cu(II) complex was found to be reduction-inert for ascorbate, but reactive for glutathione. Finally, in Chapter 8, the interactions among αSyn, Cu^{2+} and lipid membranes were investigated. Based on these results, a systematic hypothesis describing how αSyn, Cu^{2+} and synaptic vesicle collaboratively work in neurotransmission has been proposed.

Overall, this thesis investigates how specified IDPs (Aβ and αSyn), Cu^{2+} and lipid membranes interact with each other from both kinetic and structural points of view. The results lead to a new hypothesis about the physiological functions of these elements, which may provide new reference points for underpinning the inner working of such an intertwined interacting network which potentially plays a significant role in neurotransmission and governs copper homeostasis in the synapse.

Contents

Contents ····· **7**

List of Figures ····· **13**

List of Tables ····· **19**

Acronyms ····· **21**

1 Introduction ····· **23**

1.1 Neurodegenerative Diseases ····· 23

1.1.1 Alzheimer's Disease ····· 24

1.1.2 Parkinson's Disease ····· 25

1.2 Intrinsically Disordered Proteins ····· 27

1.2.1 Amyloid-β ····· 27

1.2.2 α-Synuclein ····· 32

1.3 Interactions of Aβ and αSyn with Metal Ions ····· 38

1.4 Interactions of Aβ and αSyn with Neuronal Membrane Lipids ····· 41

1.5 Summary ····· 44

2 Methods and Materials ····· **47**

2.1 Fluorescence ····· 47

2.1.1 Fluorescence Anisotropy ····· 49

2.1.2 Förster Resonance Energy Transfer ····· 51

2.2 Experimental Methods ····· 52

2.2.1 Stopped Flow ····· 52

2.2.2 Fluorometry ····· 54

2.2.3 Custom-Built Confocal Microscope for FCS and smFRET ····· 55

2.2.4 Ultraviolet-Visible Spectroscopy ····· 57

2.2.5 Circular Dichroism Spectroscopy ····· 58

2.2.6 Electron Paramagnetic Resonance Spectroscopy ····· 59
2.2.7 SDS-PAGE ····· 61
2.2.8 Cleaning ····· 61
2.3 Analytical Methods ····· 62
2.3.1 Rate Equation of Chemical Reaction ····· 62
2.3.2 Hill-Langmuir Equation ····· 63
2.3.3 Fluorescence Correlation Spectroscopy ····· 64
2.3.4 Single-Molecule Förster Resonance Energy Transfer ····· 66
2.4 Materials ····· 67
2.4.1 Proteins and Peptides ····· 67
2.4.2 Lipids ····· 69
2.4.3 Fluorescent Dyes ····· 69
2.4.4 Copper(II) Chloride ····· 69
2.4.5 Copper(II) Chelators ····· 70
2.4.6 Reducing and Oxidising Agents ····· 70
2.4.7 Buffers ····· 70
2.4.8 Reagents for αSyn Production ····· 71
2.4.9 Reagents for SDS-PAGE ····· 71
2.4.10 Solvents ····· 72

3 Interactions of Serine 8 Phosphorylated Amyloid-β and N-Terminal Truncated Amyloid-β_{4-16} with Cu^{2+} ····· 73

3.1 Serine 8 Phosphorylated Aβ ····· 74
3.1.1 Association Kinetics of Cu^{2+} Binding to pS8-Aβ ····· 74
3.1.2 Dissociation and Interconversion Kinetics of pS8-Aβ-Cu(II) ····· 75
3.1.3 Dimerisation Kinetics of pS8-Aβ-Cu(II) with WT-Aβ ····· 80
3.2 N-Terminal Truncated $A\beta_{4-16}$ ····· 81
3.2.1 Association Kinetics of Cu^{2+} Binding to $A\beta_{4-16}$ ····· 81
3.2.2 $A\beta_{4-16}$-Cu(II) Possesses High Cu^{2+} Binding Affinity ····· 82
3.2.3 Mechanism of the Interactions between $A\beta_{4-16}$ and Cu^{2+} ····· 84
3.2.4 Switching Activation Energy of the Final $A\beta_{4-16}$-Cu(II) Complex ·· 88

3.2.5 Histidine Impact of Cu^{2+} Binding to $A\beta_{4-16}$ ····· 89
3.3 Redox Studies of $A\beta_{16}$-Cu Complex ····· 91
3.3.1 Redox Kinetics of $A\beta_{16}$-Cu Complex ····· 91
3.3.2 Interactions between $A\beta_{16}$-Cu and TDMQ ····· 95
3.4 Summary ····· 100

4 α-Synuclein Production and Labelling ····· 103
4.1 Expression and Purification ····· 105
4.2 Post-Translational Modification ····· 107
4.3 Mutagenesis ····· 110
4.4 Fluorescent Dye Labelling ····· 113
4.5 Summary ····· 116

5 Interactions of α-Synuclein with Cu^{2+} ····· 117
5.1 Quenching of Labelled αSyn by Cu^{2+} ····· 118
5.2 Cu^{2+} Binding Mode of αSyn ····· 120
5.2.1 WT-αSyn ····· 120
5.2.2 Possible Cu^{2+} Binding Mode of NAc-αSyn ····· 127
5.3 Kinetic Studies of the Interactions between αSyn and Cu^{2+} ····· 129
5.3.1 WT-αSyn ····· 129
5.3.2 NAc-αSyn ····· 130
5.4 Reduction Kinetics of WT-αSyn-Cu(II) ····· 132
5.4.1 Reduction by Ascorbate ····· 132
5.4.2 Reduction by GSH ····· 133
5.5 Cu^{2+} Interactions between αSyn and Other Proteins ····· 135
5.5.1 Dissociation of Aβ-Cu(II) ····· 135
5.5.2 Cu^{2+} Binding Competition between αSyn and HSA ····· 136
5.6 Summary ····· 136

6 Interactions of α-Synuclein with Lipid Membranes ····· 139
6.1 Interaction of αSyn with GM1 Micelle ····· 140
6.1.1 FCS of αSyn Binding to GM1 Micelle ····· 140

6.1.2 Binding Structure of αSyn on GM1 Micelle ····· 142
6.2 Interaction of αSyn with Synaptic-Like SUV ····· 144
6.2.1 FCS of αSyn Binding to SUV ····· 145
6.2.2 Binding Structure of αSyn on SUV ····· 146
6.2.3 Fluorescence Anisotropy Titration of αSyn Binding to SUV ····· 155
6.2.4 Kinetics of αSyn Binding to SUV by Fluorescence Anisotropy ··· 158
6.2.5 Binding of WT-αSyn to Cholesterol-Containing SUVs ····· 160
6.3 Summary ····· 162

7 Interactions of Lipid Membranes with Cu^{2+} ····· 165
7.1 Quenching of Labelled SUV by Cu^{2+} ····· 166
7.2 Interactions of Cu^{2+} with Different Lipid-Constituted SUVs ····· 166
7.3 FCS of SUV in the Presence of Cu^{2+} ····· 167
7.4 Kinetic Studies of the Interactions between SUV and Cu^{2+} ····· 168
7.5 Cu^{2+} Binding Mode of SUV ····· 169
7.6 Reduction Kinetics of SUV-Cu(II) ····· 170
7.6.1 Reduction by Ascorbate ····· 170
7.6.2 Reduction by GSH ····· 171
7.7 Competition of Cu^{2+} Binding between SUV and Protein ····· 172
7.7.1 Competition with Aβ ····· 172
7.7.2 Competition with HSA ····· 175
7.7.3 Competition with αSyn ····· 177
7.8 Summary ····· 177

8 Interactions among α-Synuclein, Lipid Membranes and Cu^{2+} ····· 179
8.1 Interactions of αSyn-SUV Conjugate with Cu^{2+} ····· 180
8.2 Interactions of SUV-Cu(II) Conjugate with αSyn ····· 185
8.3 Interactions of αSyn-Cu(II) Complex with SUV ····· 188
8.4 Interactions of Micelle-Bound αSyn with Cu^{2+} ····· 192
8.5 Summary ····· 193

9 Conclusion & Further Work ····· 195

Bibliography ····· **199**

List of Figures

1.1 Amyloid cascade hypothesis ····· 24

1.2 Sequence and generation of Aβ ····· 28

1.3 Proposed mechanisms of Aβ related key issues in AD pathology ····· 30

1.4 The primary sequence of αSyn ····· 33

1.5 The process of αSyn aggregation ····· 36

1.6 The major coordination modes of Aβ-Cu(II) complex ····· 39

1.7 The proposed coordination modes of αSyn-Cu(II) complex at physiological pH ····· 40

1.8 The lipid composition of synaptic vesicles ····· 41

2.1 Jablonski diagram ····· 48

2.2 Schematic of the stopped flow apparatus ····· 53

2.3 Optical layout of the spectrofluorometer ····· 54

2.4 Confocal microscopy ····· 55

2.5 Setup of the custom-built confocal microscope ····· 57

2.6 Autocorrelation curve of fluorescence signal ····· 64

3.1 Kinetics of Cu^{2+} binding to pS8-Aβ ····· 75

3.2 Kinetics of Cu^{2+} dissociation from pS8-Aβ-Cu(II) ····· 76

3.3 Raw traces of Cu^{2+} dissociation by a variable excess of EDTA ····· 77

3.4 Kinetics of interconversion between the two components of pS8-Aβ-Cu(II) ·78

3.5 Kinetics of Cu^{2+} bridged dimerisation of pS8-Aβ with WT-Aβ ····· 81

3.6 Kinetics of Cu^{2+} binding to $Aβ_{4-16}$ ····· 82

3.7 Structure of ATCUN binding motif ····· 82

3.8 Raw kinetic traces of Cu^{2+} dissociation by EDTA from $Aβ_{4-16}$-Cu(II) ····· 83

3.9 Comparison of raw Cu^{2+} binding traces between 1:20 and 1:1 $Aβ_{4-16}$, Cu^{2+} mixing ratio ····· 84

3.10 Raw traces of Cu^{2+} binding measurements with a series of 1:1 concentration

ratio of $A\beta_{4-16}$ and Cu^{2+} ····· 85

3.11 Kinetics of $A\beta_{4-16}/Cu^{2+}$ interactions measured by double mixing stopped flow ····· 86

3.12 Cu^{2+} binding mechanism of $A\beta_{4-16}$ ····· 87

3.13 Evolutions of the two intermediate species at various temperatures ····· 88

3.14 Arrhenius plot for the switching rate constant k_{+2} ····· 89

3.15 Kinetics of Cu^{2+} binding to $A\beta_{4-16}$ under various concentrations of histidine ·90

3.16 Kinetics of Cu^{2+} dissociation from $A\beta_{4-16}$-Cu(II)-His ····· 90

3.17 Reduction kinetics of A2P-Aβ-Cu(II) by ascorbate ····· 92

3.18 Initial rate of $A\beta_{16}$-Cu(I) oxidation against H_2O_2 concentration ····· 94

3.19 Oxidative stability test of HiLyte Fluor 488 fluorophore ····· 94

3.20 Structures of TDMQ 20, TDMQ 22 and TDMQ 37 ····· 95

3.21 Kinetics of Cu^{2+} dissociation by different TDMQ ligands from $A\beta_{16}$-Cu(II) ··96

3.22 UV-Vis (265 nm) kinetic traces of ascorbate oxidation ····· 97

3.23 UV-Vis absorption spectra of TDMQ and TDMQ-Cu(II) complexes ····· 99

3.24 Absorbance of different TDMQ-Cu(II) complexes under various molar equivalents of GSH ····· 100

4.1 Analyses of WT-αSyn purification ····· 107

4.2 Analyses of NAc-αSyn purification ····· 108

4.3 ESI-MS characterisation of oxidised NAc-αSyn ····· 109

4.4 G7C mutation introduction in vector ····· 110

4.5 SDS-PAGE analysis of G7C NAc-αSyn purification ····· 111

4.6 S9C, F94C mutation introduction in vector ····· 112

4.7 H50Q mutation introduction in vector ····· 112

4.8 SDS-PAGE analyses of G7C αSyn labelling with Alexa 488 ····· 114

4.9 SDS-PAGE analysis of S9C-F94C αSyn dually labelled by Alexa 594 and 488 ····· 115

5.1 Literature suggested Cu^{2+} binding sites in αSyn sequence ····· 117

5.2 Fluorescence quenching of residue 7 labelled WT-αSyn after mixing with Cu^{2+} ····· 119

5.3 Difference between Cu^{2+} binding to residue 7 labelled WT-αSyn and residue 140 labelled WT-αSyn ····· 119

5.4 Comparison of Cu^{2+} binding to WT-αSyn and H50Q αSyn under 1:1 αSyn, Cu^{2+} mixing ratio ····· 121

5.5 Comparison of Cu^{2+} binding to WT-αSyn and H50Q αSyn under a variable excess of Cu^{2+} ····· 123

5.6 Comparison of Cu^{2+} coordination mode dissociation by EDTA for WT-αSyn and H50Q αSyn ····· 125

5.7 Cu^{2+} dissociation from WT-αSyn-Cu(II) at different pH ····· 126

5.8 Difference between Cu^{2+} binding to WT-αSyn and NAc-αSyn ····· 127

5.9 Proposed Cu^{2+} coordination mode for NAc-αSyn ····· 128

5.10 Kinetics of Cu^{2+} binding to WT-αSyn ····· 129

5.11 Kinetics of Cu^{2+} dissociation from WT-αSyn-Cu(II) ····· 130

5.12 Kinetics of Cu^{2+} binding to NAc-αSyn ····· 131

5.13 Kinetics of Cu^{2+} dissociation from NAc-αSyn-Cu(II) ····· 131

5.14 Reduction kinetics of WT-αSyn-Cu(II) by ascorbate ····· 133

5.15 Reduction kinetics of WT-αSyn-Cu(II) by GSH ····· 134

5.16 $A\beta_{16}$-Cu(II) dissociation by WT-αSyn ····· 135

5.17 Competition between WT-αSyn and HSA for Cu^{2+} ····· 136

6.1 FCS curves of labelled WT-αSyn and GM1 micelle ····· 141

6.2 Comparison of the FCS curves for labelled WT-αSyn before and after the incubation with GM1 micelle ····· 141

6.3 Determination of the binding structure of WT-αSyn on GM1 micelle using FRET techniques ····· 143

6.4 Kinetic fluorescence changing of the donor fluorophore on WT-αSyn during αSyn binding to GM1 micelle ····· 144

6.5 FCS curve of 50 nm labelled synaptic-like SUV ····· 145

6.6 Comparison of the FCS curves for labelled WT-αSyn before and after the incubation with 50 nm synaptic-like SUV ····· 146

6.7 Far-UV CD spectra of WT-αSyn in the absence and presence of SUV ····· 147

6.8 Determination of the binding structure of single WT-αSyn on synaptic-like SUV using smFRET technique ····· 148

6.9 Determination of the binding structure of multiple WT-αSyn on synaptic-like SUV under different ratios of αSyn to SUV ····· 152

6.10 Ensemble FRET measurements of SUV-bound WT-αSyn under different ratios of αSyn to SUV ····· 153

6.11 Kinetic fluorescence changing of the donor fluorophore on WT-αSyn during αSyn binding to synaptic-like SUV ····· 154

6.12 Fluorescence anisotropy titrations of different αSyn binding to synaptic-like SUV ····· 155

6.13 Determination of the binding form of specific sites of WT-αSyn on synaptic-like SUV using fluorescence anisotropy ····· 157

6.14 Kinetics of αSyn (both WT and NAc forms) binding to SUV determined by fluorescence anisotropy ····· 158

6.15 Kinetics of αSyn (both WT and NAc forms) binding to SUV determined by fluorescence intensity ····· 159

6.16 Far-UV CD spectra of WT-αSyn in SUVs containing different levels of cholesterol ····· 160

6.17 Fluorescence anisotropy titrations of WT-αSyn binding to different cholesterol-containing SUVs ····· 161

6.18 Fluorescence anisotropy titrations of NAc-αSyn binding to different cholesterol-containing SUVs ····· 162

7.1 Fluorescence quenching of labelled synaptic-like SUV after mixing with Cu^{2+} ····· 166

7.2 Comparison of Cu^{2+} binding to the SUVs containing different lipid compositions ····· 167

7.3 Comparison of the FCS curves for labelled synaptic-like SUV in the absence and presence of Cu^{2+} ····· 167

7.4 Kinetics of Cu^{2+} binding to synaptic-like SUV ····· 168

7.5 Kinetics of Cu^{2+} dissociation from SUV-Cu(II) ····· 169

7.6 X-band EPR spectrum of Cu^{2+} bound on synaptic-like SUV ····· 170

7.7 Reduction of SUV-Cu(II) conjugate by ascorbate ····· 170

7.8 Reduction kinetics of SUV-Cu(II) conjugate by GSH ····· 172

7.9 Competition between Aβ and synaptic-like SUV for Cu^{2+} ····· 173

7.10 Minimal interactions between $A\beta_{40}$ and synaptic-like SUV ····· 174

7.11 Competition between HSA and synaptic-like SUV for Cu^{2+} ····· 175

7.12 Dissociation of SUV-Cu(II) conjugate by HSA ····· 176

7.13 Minimal interactions between HSA and synaptic-like SUV ····· 177

7.14 Proposed Cu^{2+} transportation via synaptic vesicle ····· 178

8.1 Kinetics of Cu^{2+} binding to αSyn-SUV (both WT and NAc forms) conjugates ····· 181

8.2 Kinetics of Cu^{2+} dissociation from αSyn-SUV-Cu(II) (both WT and NAc forms) ····· 182

8.3 Cu^{2+} binding to αSyn-SUV (both WT and NAc forms) under high concentrations of αSyn ····· 183

8.4 X-band EPR spectra of Cu^{2+} bound on αSyn-SUV (both WT and NAc forms) ····· 184

8.5 Fluorescence anisotropy kinetics of SUV-bound αSyn (both WT and NAc forms) after mixing with Cu^{2+} ····· 185

8.6 Fluorescence anisotropy titrations of αSyn (both WT and NAc forms) binding to SUV-Cu(II) ····· 186

8.7 Fluorescence anisotropy kinetics of αSyn (both WT and NAc forms) binding to SUV-Cu(II) ····· 187

8.8 Kinetic interactions between WT-αSyn-Cu(II) and SUV ····· 189

8.9 Proposed process of αSyn-Cu(II) complex binding to synaptic-like SUV ··· 191

8.10 Cu^{2+} binding to αSyn-GM1 (both WT and NAc forms) conjugates ····· 192

8.11 Cu^{2+} binding to αSyn-SDS (both WT and NAc forms) conjugates ····· 193

List of Tables

3.1 Kinetic parameters derived from the reaction of pS8-Aβ-Cu(II) complexes with EDTA ····· 79

3.2 Rate constants of Cu^{2+} binding to $A\beta_{4\text{-}16}$ at ~2 s ····· 85

3.3 Kinetic parameters of Cu^{2+} binding to $A\beta_{4\text{-}16}$ derived by fitting with proposed mechanistic scheme ····· 87

3.4 Kinetic parameters of Cu^{2+} dissociation derived from the reaction of $A\beta_{16}$-Cu(II) with different TDMQ ligands ····· 96

3.5 Ascorbate oxidation rates by $A\beta_{16}$-Cu(II) in the presence of different TDMQ ligands ····· 98

5.1 $g_{\parallel}$ factors and hyperfine coupling constants ($A_{\parallel}$) for the EPR spectra of NAc-αSyn-Cu(II) and WT-αSyn-Cu(II) ····· 128

5.2 Kinetic parameters of the interactions between αSyn and Cu^{2+} ····· 132

6.1 Dissociation constants of different αSyn binding to synaptic-like SUV ····· 156

6.2 Dissociation constants of WT-αSyn binding to different cholesterol-containing SUVs ····· 161

Acronyms

Aβ	amyloid-β
AD	Alzheimer's disease
APD	avalanche photodiode
APP	amyloid precursor protein
αSyn	α-synuclein
ATCUN	amino terminal copper and nickel binding
BSA	bovine serum albumin
CD	circular dichroism
CMC	critical micelle concentration
CNS	central nervous system
CSF	cerebrospinal fluid
EDTA	ethylenediaminetetraacetic acid
EPR	electron paramagnetic resonance
ESI-MS	electrospray ionization mass spectrometry
FAD	familial Alzheimer's disease
FCS	fluorescence correlation spectroscopy
FITC	fluorescein isothiocyanate
FPD	familial Parkinson's disease
FRET	Förster resonance energy transfer
GM1	monosialo-tetrahexosyl-ganglioside
GSH	glutathione
HSA	human serum albumin
IDP	intrinsically disordered protein

LBs	Lewy bodies
LUV	large unilamellar vesicle
NAc	N-terminal acetylation
NAC	non-Aβ component
NFT	neurofibrillary tangle
PC	phosphocholine
PD	Parkinson's disease
PE	phosphatidylethanolamine
PEM	photoelastic modulator
PG	phosphatidylglycerol
PHF	paired helical filament
PMT	photon multiplier tube
PS	phosphatidylserine
pS8	phosphorylated serine residue 8
PTM	post-translational modification
ROS	reactive oxygen species
SAD	sporadic Alzheimer's disease
SDS-PAGE	sodium dodecyl sulfate-polyacrylamide gel electrophoresis
SUV	small unilamellar vesicle
TCEP	tris(2-carboxyethyl)phosphine
TDMQ	N4-tetradentate monoquinoline
UV-Vis	ultraviolet-visible
WT	wild type

Chapter 1

Introduction

Neurodegenerative diseases are a group of chronic neurological disorders which are characterised by a progressive damage and loss of neurons in discrete regions of the central nervous system. Among them, Alzheimer's disease (AD) and Parkinson's disease (PD) are the most common neurodegenerative diseases. They affect millions of people worldwide but are still incurable at present. Although their etiologies are still far from fully known, increasing evidence suggests that the misfolding and fibrillisation of intrinsically disordered proteins (IDPs) such as amyloid-β (Aβ), tau proteins and α-synuclein (αSyn) could be the culprit. This thesis investigates the interactions between specified IDPs (Aβ and αSyn) and lipid membranes, metal ions, trying to uncover their molecular interaction mechanisms, which can assist to understand the potential pathological and physiological functions of IDPs.

1.1 Neurodegenerative Diseases

Neurodegenerative diseases are disastrous for neurons. They typically cause dementias or movement disorders, of which the most common cases are Alzheimer's disease and Parkinson's disease, respectively.

1.1.1 Alzheimer's Disease

Alzheimer's disease is the most common neurodegenerative disease, which affects over 50 million people worldwide in 2020[1]. It was first published by Alois Alzheimer in 1907 to describe a patient who had shown symptoms of severe cognitive impairment, and atrophy of the whole brain as well as plaques and tangles in the cerebral cortex after autopsy[2]. The etiology of AD is extremely complicated and not yet fully known. Many drugs are being designed to cure AD but so far none of them has passed phase III clinical trials.

AD is believed to be caused by a combination of multiple factors. Despite the elusive etiology, various hypotheses have been suggested to elucidate the development of AD. Among these, amyloid cascade hypothesis and tau hypothesis are the most prevalent pathogenic mechanisms.

The amyloid cascade hypothesis states that Aβ deposition is the causative factor of AD pathology, which directly results in neurofibrillary tangle (NFT) formation and neuronal loss. These two sequential events are essential to trigger the development of AD[3]. The concept of amyloid cascade has guided numerous of studies and also been improved by them. A more detailed cascade is illustrated in Fig. 1.1[4-5].

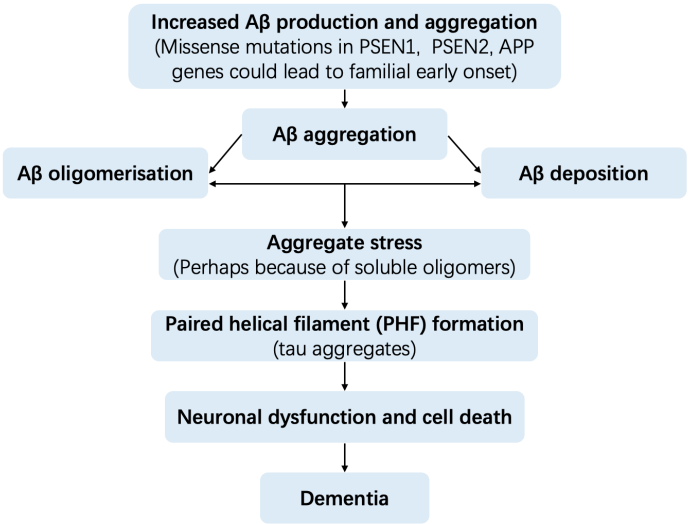


Figure 1.1 Amyloid cascade hypothesis. The deposition of Aβ is the causative agent, resulting in the following PHF formation, neuronal loss and dementia.

So far it has been suggested that soluble Aβ oligomers rather than deposited amyloid plaques are correlated with cognitive impairment. Therefore, the current focus of this hypothesis has been adjusted to small soluble oligomers[5]. The actual culprit could be in someplace on the evolutionary process between soluble oligomers and amyloid plaques, but still controversial.

The tau hypothesis states that unnaturally phosphorylated tau proteins aggregate into PHFs and NFTs[6]. Tau proteins are soluble microtubule-associated proteins, which normally stabilise microtubules in the cell cytoskeleton. Typically, the interactions of tau with microtubules are regulated by the level of tau phosphorylation that reduces affinity[7]. While in AD, tau proteins are accumulated in a hyperphosphorylated state, forming insoluble PHFs and NFTs. Similar to Aβ, current evidence indicates that tau oligomers are the toxic species[8]. Although tau proteins were considered to act downstream of Aβ in the amyloid cascade hypothesis, studies have shown that Aβ and tau play synergistic roles in the development of AD[9-10].

The metal hypothesis states that the Aβ neurotoxicity is promoted by Aβ-metal interactions in AD[11]. It was proposed based on several unnatural observations related to bio-metals, including remarkably enriched copper and zinc in amyloid plaques, aberrant metal homeostasis in AD patient brains, copper and zinc caused acceleration of Aβ aggregation as well as Aβ-Cu complex induced oxidative stress. The metal hypothesis provides a reference for AD diagnosis and therapy, which is the reagents that help regulate the distribution of bio-metal ions might be potential drugs to combat AD.

1.1.2 Parkinson's Disease

Parkinson's disease is the second most common neurodegenerative disease. Worldwide, it is estimated that more than 10 million people are suffering PD[12]. PD is currently incurable but proper treatments can help control the symptoms. It was first medically described as a nervous disorder by James Parkinson in 1817[13]. In his report, Parkinson exampled six cases and summarised the primary clinical symptoms. He supposed the proximate cause could be in the *medulla*, whereas nowadays the

substantia nigra is recognised to be the actual diseased area.

The major characteristic features of PD are the loss of dopaminergic neurons in the *substantia nigra* and intracellular deposition of Lewy bodies (LBs). Dopaminergic neuron loss leads to attenuated generation of dopamine which is a vital neurotransmitter in motor control, thereby causing parkinsonism. The mechanism of dopaminergic neuron loss is still obscure, but the deposited LBs which are composed of abnormally accumulated αSyn, is believed to be one of the crucial reasons for neuronal death.

Similar to AD, PD is a multifactorial disease as well. It has been reported that αSyn aggregation[14], mitochondrial dysfunction[15], neuroinflammation[16] and living environment[17] are related to the pathogenesis of PD. Among them, αSyn aggregation is considered to be the most important causative factor, not only because the formation of LBs is observed in most PD patients, but also the artificially overexpressing αSyn in animals can cause the formation of αSyn deposits and PD-like symptoms[18-19]. It is not entirely clear how αSyn aggregates cause PD. αSyn aggregates induced organelle disturbance and αSyn-metal complex induced oxidative stress could be the major reasons.

The dominant risk factor of PD is age. Epidemiological study has shown that the prevalence has a strong correlation with age[20]. Heredity is another major risk factor. There are approximately 5 - 10% of patients present familial PD (FPD) which is due to the missense mutations in a group of autosomal genes. So far six chromosomal regions have been identified to be responsible for monogenic PD. They are SNCA (PARK1/4) and LRRK2 (PARK8) for autosomal dominant PD; Parkin (PARK2), PINK1 (PARK6), DJ-1 (PARK7) and ATP13A2 (PARK9) for autosomal recessive PD[21]. Since αSyn in human body is encoded by SNCA gene, the FPD induced by missense mutations on SNCA gene highlights the connection between PD pathogenesis and αSyn.

As AD and PD are primarily caused by protein misfolding, sometimes they are classified into protein-misfolding diseases. In essence, the culprits of AD and PD, Aβ and αSyn, belong to the group of intrinsically disordered proteins.

1.2 Intrinsically Disordered Proteins

Proteins are essential elements and participate in a vast range of biological interactions within organisms. For a century, scientists believed that the unique functionality of a protein is defined by its specific three-dimensional structure[22]. Although some biologically functional proteins without definite ordered structure were discovered since the 1950s, the disordered domain of these proteins had mostly been ignored[23]. From the mid-1990s, a large number of studies indicated that the lack of intrinsic structure is very common in eukaryotic proteins[24-29], and the significance of intrinsic disorder has been recognised.

A previous study has estimated that the percentage of disorder in eukaryotic proteins is 35 - 51%[30]. In the disorder containing proteins, some are constituted by disordered sequences and structured domains together, while some other proteins are entirely disordered. Such entirely disordered proteins are known as intrinsically disordered proteins (IDPs), which cannot form well-defined structures spontaneously. IDPs perform a large array of biological activities, including signal regulation of cell cycle, transcription and translation[31-35], chaperone functions and modulating the assembly of bio-macromolecules[36-42]. The high structural flexibility and binding specificity enable IDPs to efficiently perform these functions through interacting with various molecules and ions. However, such interactions in some circumstances can also induce the misfolding of IDPs, and the misfolding can easily cause the dysfunction of IDPs and lead to the development of different diseases. Two well-known examples are the misfolding of amyloid-β peptide and α-synuclein, which are believed to associate with AD and PD, respectively.

1.2.1 Amyloid-β

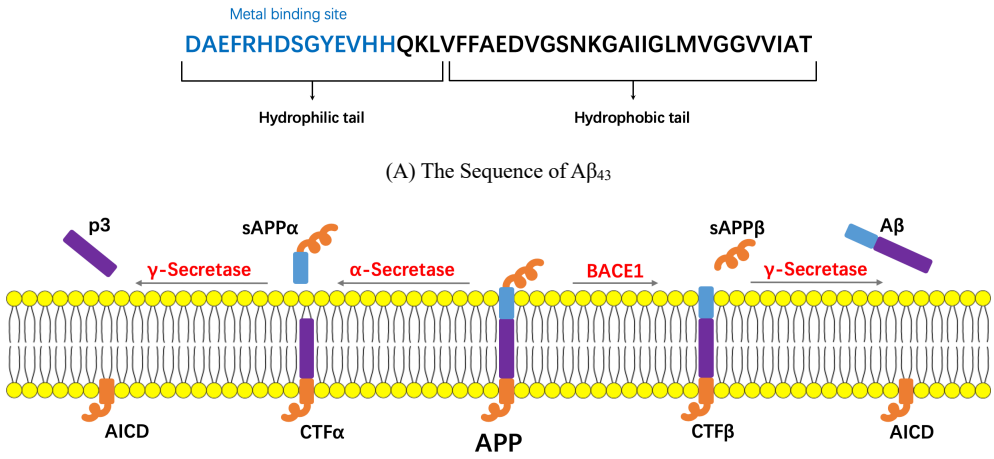
Amyloid-β is a ~4 kDa peptide composed of 36 - 43 amino acids (sequence shown in Fig. 1.2(A)), which is the main component of the amyloid plaques found in AD brains. NMR study has shown that the monomer of Aβ appears to be unstructured in aqueous solution[43]. Aβ was first isolated from the brain and cerebral vasculature of AD and

Down's syndrome patients[44-45]. Although Aβ deposits in the brain, it can be produced by a variety of cells during normal metabolism[46]. While related research has mainly discussed the association of Aβ with disease, the physiological function of Aβ is still elusive.

Physiological Aβ

Aβ is generated by the endoproteolytic cleavage of the amyloid precursor protein (APP). APP is a transmembrane glycoprotein, the native role of which is yet to be revealed. While there are some substantiated hypotheses to describe the biological function of APP, such as synaptic formation and repair[47-48], mediation of anterograde transport[49] and gene regulation[50-51].

APP can be cleaved by three endoproteases called α-, β- and γ-secretase. Aβ is generated by the sequential cleavage of β- and γ-secretases as depicted in Fig. 1.2(B).



(A) The Sequence of $A\beta_{43}$

(B) Two Processing Pathways of APP

Figure 1.2 Sequence and generation of Aβ. (A) The sequence of $A\beta_{43}$. The metal binding site is coloured with blue. **(B)** Two processing pathways of APP. The amyloidogenic pathway generates Aβ (right), while the non-amyloidogenic pathway generates p3 (left).

Generally, the first cleavage by β-secretase (BACE1) releases a soluble peptide, sAPPβ. The remaining portion of APP, CTFβ, is still bound with membrane and further cleaved by γ-secretase to produce Aβ peptides. γ-secretase can act on diverse cleavage sites to create the C-terminal of Aβ, producing different Aβ isoforms of various amino acids in

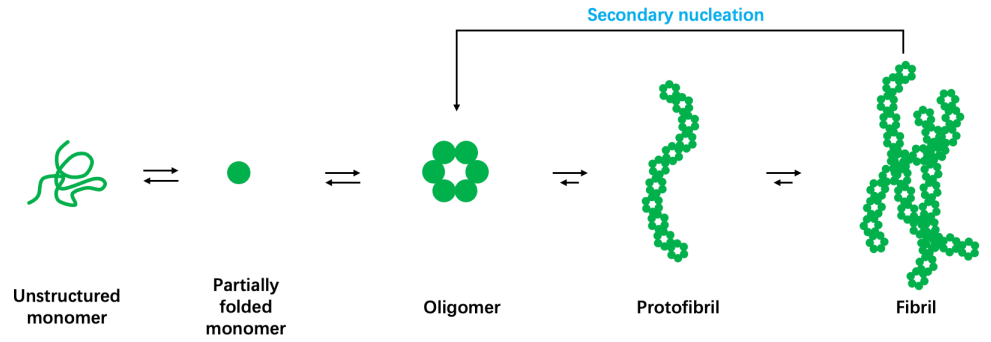
length. The most abundant isoforms are $A\beta_{40}$ and $A\beta_{42}$. This cleavage through β- and γ-secretases pathway (amyloidogenic pathway) only processes ~10% of APP. Approximately 90% of APP is cleaved successively by α- and γ-secretases, forming a non-pathogenic fragment named p3[52].

Some proposed positive effects of Aβ include the promotion of neurogenesis[53], enhancement of synaptic plasticity and memory[54-56], antimicrobial activity[57] and antioxidation[58-59]. To maintain normal conditions, the concentration of Aβ in brain extracellular fluid should be very low (~0.1 - 1 nM)[60]. If the concentration is above ~90 nM, Aβ will start to aggregate and form micelle-like oligomers[61].

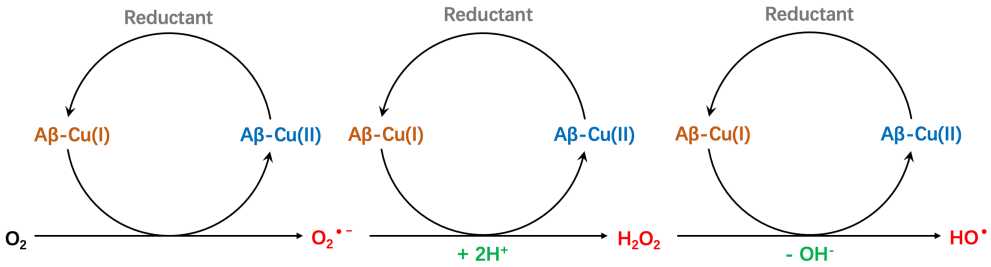
The cerebral Aβ peptides are predominantly eliminated by proteolytic degradation to maintain proteostasis[62]. Neprilysin[63-64] and insulin-degrading enzyme[65-66] are thought to be the most principal proteases. In addition to proteolytic degradation, cell mediated clearance[67-68] and transport into blood across the blood brain barrier[69-70] are other clearance pathways employed by the cells. Multiple mechanisms of Aβ removal bring on a faster clearance than generation, thus avoiding the accumulation of Aβ[71].

Pathological Aβ

The accumulation of Aβ is considered to play a crucial role in the pathogenesis of AD. Compared to $A\beta_{40}$, $A\beta_{42}$ aggregates faster because it is more hydrophobic and fibrillogenic[72]. As shown in Fig. 1.3(A), typically, during the aggregation process, the unstructured Aβ monomers first slowly transform to a partially folded form and associate with each other to yield oligomeric paranuclei. This progression can be called the primary oligomerisation pathway. The formed nuclei can then self-associate and elongate to generate short and narrow fibrils called protofibrils. This process of growth is relatively fast because of the seeding effect. The protofibrils eventually assemble into the general amyloid fibrils[73]. After a certain concentration of these amyloid fibrils has been formed, the fibrils will start to catalyse the formation of oligomer, activating a secondary oligomerisation progression. This progression will overtake the primary oligomerisation pathway to become the major source of new Aβ oligomers, leading to exponential proliferation of oligomers and fibrils[74].



(A) Aβ Aggregation



(B) Aβ-Cu Catalysed ROS Generation

Figure 1.3 Proposed mechanisms of Aβ related key issues in AD pathology. (A) Aβ aggregation. The oligomers and fibrils are initially generated via primary oligomerisation pathway. Once a critical concentration of fibrils has been formed, the fibrils will induce oligomer formation via secondary nucleation, which will become the major Aβ oligomerisation pathway. **(B)** ROS generation catalysed by Aβ-Cu complex. Aβ-Cu(II) is initially reduced to Aβ-Cu(I). Then Aβ-Cu(I) reacts with oxygen to generate various ROS.

Aβ oligomers are believed to be more toxic than monomers and fibrils. So far the mechanism of Aβ oligomer toxicity is still under debate but could be multiple. It has been reported that Aβ oligomers can bind to a number of receptors, thus disrupting their downstream pathways[75-78]. Furthermore, Aβ oligomers can create channels in membranes, causing ion dyshomeostasis[79-80]. Also, Aβ oligomers are able to sequester metal ions such as Cu^{2+} and Fe^{3+} to produce reactive oxygen species (ROS) which can oxidatively damage the cells[81]. Intracellularly, Aβ oligomers have been shown to impair proteasome activities[82]. All of these mechanisms could be the indications of Aβ oligomers pathology.

Apart from Aβ aggregation, ROS generation is another key issue in AD

pathogenesis. ROS are reactive chemicals containing oxygen. Normally they exist at low level to perform messenger function[83]. Whereas the abnormal accumulation can damage cells and tissues by increased oxidative stress. It has been proposed that mitochondrial ROS generation[84], lipid peroxidation inducement[85] and nitrosative stress[86] could be the source of pathological ROS. While the most prevailing view is bio-metal ions catalysis. Transition metal ions such as Cu^{2+} and Fe^{3+} can be reduced to Cu^{+} and Fe^{2+} by physiological reducing agents. The Cu^{+} and Fe^{2+} can then react with oxygen or hydrogen peroxide to produce oxygen radical species[87]. Aβ has been shown to promote this process[88]. As a metal-binding protein, Aβ possesses high binding affinities with these metal ions, and Aβ-Cu complex displays a highly positive formal reduction potential[89-90]. These properties can catalyse Cu^{2+} reduction to produce Cu^{+} faster, which could be the reason of the promotion of ROS generation. The Aβ-Cu catalysis mechanism of ROS generation is depicted in Fig. 1.3(B).

Post-Translational Modification

Post-translational Modified (PTM) Aβ is considered to be one of the malefactors of sporadic AD (SAD), as a variety of modified isoforms have been determined from the amyloid plaques in SAD brains, including phosphorylation[91-92], truncation[93-94], pyroglutamylation[95], oxidation[96], racemisation[97], isomerisation[98], nitric oxide-mediated modification[99] and glycosylation[100]. The majority of these studies have exhibited that PTM can promote the aggregation and boost the neurotoxicity of Aβ. Furthermore, it has been reported that PTM can reduce the proteolysis of Aβ[101]. Both factors result in the disruption of Aβ balance and lead to maladies.

Phosphorylation is a prevalent reversible PTM of protein, which is carried out through the addition of a phosphate group by a protein kinase. Phosphorylation plays an important role in the regulation of transcription, membrane transport, protein activity and signal transmission[102-103]. However, aberrant phosphorylation can cause a number of diseases. In AD, unnaturally phosphorylated tau proteins have been found to inhibit the assembly of microtubule, and such tau has been seen as another typical marker of AD[104-105]. For Aβ, serine 8 phosphorylated Aβ has been reported to accelerate the

formation of neurotoxic oligomers, and the phosphorylated oligomers could act as seeds to further increase the propensity of oligomerisation[92,106]. Thus the aberrant phosphorylation could represent a significant role in the evolution of AD, providing a potential for AD prognosis and therapy.

Truncation is another common form of PTM for Aβ. The C-terminal truncation is mostly modulated by γ-secretase because of its imprecise cleavage. While the formation of N-terminal truncation is unclear, possibly due to the proteolysis[107]. Previous studies have shown that N-terminal truncated Aβ, especially the $A\beta_{4-42}$ species, is the most abundant species in AD, thereby suggesting that $A\beta_{4-42}$ could be a therapeutic target[108-109]. Nevertheless, some other studies have indicated that $A\beta_{4-42}$ is not only abundant in AD, but also in healthy hippocampus and cortex, even exceeding the full-length $A\beta_{40}$ and $A\beta_{42}$[110-112]. In addition, although the Cu^{2+} binding affinity of $A\beta_{4-42}$ is much stronger than $A\beta_{42}$, the generated Cu^{2+} binding complex of $A\beta_{4-42}$ is redox-inert and do not produce significant ROS[113]. The evidence directs to a hypothesis that $A\beta_{4-x}$ species could act as physiological roles rather than causative factors of the disease.

Most of the origin of PTM Aβ remains unknown. So far it has been considered to be related to aging as well as genetic variants[114].

1.2.2 α-Synuclein

α-synuclein (αSyn) is a ~14 kDa protein of the synuclein family that is common to vertebrates. It was first discovered from the synaptic vesicles of *Torpedo californica*[115]. The human αSyn consists of 140 amino acids, which is encoded by the SNCA gene. αSyn is predominantly located in presynaptic terminals with an abundant concentration of ~50 μM[116], while the full extent of its physiological function is not well understood. The structure of αSyn has been proposed to be intrinsically disordered, but can undergo conformational changes to interact with lipids or form fibrils[117].

αSyn Structure

As shown in Fig. 1.4. The sequence of αSyn comprises three functionally distinct domains: N-terminal domain, non-Aβ component (NAC) domain and C-terminal

domain.



Figure 1.4 The primary sequence of αSyn. Three domains are highlighted with different colours.

The N-terminal domain (amino acids 1 - 60) is rich in amphipathic lysine and positively charged. It contains four 11-residue imperfect repeats with a highly conserved hexameric motif of KTKEGV. These periodic motifs resemble the repeat units of amphipathic α-helices in exchangeable apolipoproteins[118]. Because the amphipathic α-helix is the lipid binding motif of exchangeable apolipoproteins[119], the similar periodic motifs of αSyn was supposed to have similar lipid binding properties. This has been confirmed by a number of studies[120-122]. These studies have shown that αSyn can bind to lipid membranes via α-helical structure. Indeed this α-helical structure contains two α-helices linked by a short segment[123-125]. A recent study suggests that the lipid membrane binding structure of αSyn could be described as a multilateral model: an anchor-shaped attachment on membrane by the first α-helix with a surface attachment by the second α-helix[126].

The NAC domain, also known as the central region, is composed of amino acids 61 - 95. It is unique to αSyn among the synuclein family. As a fragment of αSyn, NAC was first found in AD amyloid deposition. It contains the most hydrophobic portion that comprises amino acids 62 - 90 of αSyn[127]. The NAC domain is believed to be responsible for αSyn aggregation because it is an indispensable constituent of αSyn fibrils and can easily form cross β-sheets[128-129]. The sequence of amino acids 66 - 74 as well as 71 - 82, both of which are in the NAC domain, have been reported to be essential for αSyn fibrillisation[130-131]. In addition, an amino acids substitution study has shown that the substitution at residues 66 - 75 can drastically diminish the formation of fibril, which provides another evidence about the role of the NAC domain in αSyn fibrillisation[132].

The remaining amino acids (amino acids 96 - 140) constitute the C-terminal domain. This domain is negatively charged and acidic due to the abundance of glutamic acid and aspartic acid residues. Interestingly, there are five proline residues in this domain, which makes the C-terminal domain become the only region containing proline residues in αSyn sequence[133]. Proline is known as a structural disruptor, which could account for the random structure of the C-terminal domain. Furthermore, the disordered property of the C-terminal domain is considered to prevent the remainder of αSyn from folding and maintain the disordered state of entire αSyn[134]. Apart from this function, the C-terminal domain has been proposed to prohibit αSyn fibrillisation through shielding the hydrophobic NAC domain[135]. This property has also been confirmed by other research using C-terminally truncated αSyn, which has exhibited a faster aggregation than full-length αSyn[136].

Physiological αSyn

Endogenous αSyn had been generally accepted as a disordered monomeric protein until two studies published in 2011 proposed a novel opinion that the native form of αSyn could be a folded tetramer[137-138]. This discovery triggered people's interest to further explore the physiological form of αSyn. However, other conclusions are identical to the previous view that the native αSyn exists as disordered monomer[139-141]. In the meantime, the proponents of the novel opinion have proposed new evidence and suggested that the form of tetramer is unstable, which could be the reason why others can only obtain monomeric αSyn[142-143]. This issue about the native form of αSyn is currently still controversial.

Although the physiological role of αSyn remains little known, its localisation at presynaptic terminals as well as the lipid binding property suggest that αSyn could have the function of modulating presynaptic membranes activities. In fact, numerous studies have shown that αSyn participates in the trafficking of synaptic vesicles[144-146]. It can promote the assembly and fusion of synaptic vesicles[147]. In addition to the direct interactions, αSyn can also regulate the activities of synaptic vesicles through interacting with synaptic proteins[148-149]. Furthermore, αSyn has been considered as a

negative neurotransmission modulator of dopamine. It inhibits not only the release of dopamine but also the synthesis[150-151]. αSyn has also been shown to protect nerve terminals[152] and affect mitochondrial functions[153] as well as DNA repair process[154]. These findings highlight the importance of αSyn in preserving synaptic health.

Recently, human αSyn in its physiological state has been identified to be predominantly N-terminally acetylated[155-156]. N-terminal acetylation (NAc) is a common co- or post-translational modification of proteins in eukaryotes. It is the addition of an acetyl group to the free amino group of N-terminus, which is catalysed by an N-terminal acetyltransferase complex. For other proteins, NAc has been found to regulate their subcellular localisations[157] and avidity[158]. While for αSyn, the significance of NAc has yet been well established. Thus far, it has been indicated that NAc can increase the lipid membranes binding affinity of αSyn and decrease the capacity of αSyn aggregation[156,159-161]. Moreover, the evidence that NAc modulates αSyn binding to protein[162], glycan[163] and copper ions[164] has been proposed. A recent study performed in neurons has shown that NAc plays a role in the regulation of αSyn neurotoxicity[165]. As a relatively new area of αSyn study, there still exists a wide range of unveiled secrets regarding to the NAc of αSyn.

αSyn clearance occurs via proteolytic degradation[166], chaperone binding[167] and autophagy[168]. Any dysfunction of these pathways can impair the balance of αSyn level and lead to the abnormal αSyn aggregation[169-170].

Pathological αSyn

Abnormally aggregated αSyn is universally acknowledged as the major constituent of Lewy bodies that are the neuropathological hallmarks of PD. The aggregation process of αSyn is similar to Aβ, which is a nucleation-dependent polymerisation[171] and is summarised in Fig. 1.5. The actual mechanisms that induce the abnormal aggregation of αSyn are yet to be fully uncovered. The current substantiated hypotheses include the dysfunction of αSyn clearance as mentioned above, and SNCA gene mutation[172-173], PTM[174], metal ions[175-177] triggered acceleration.

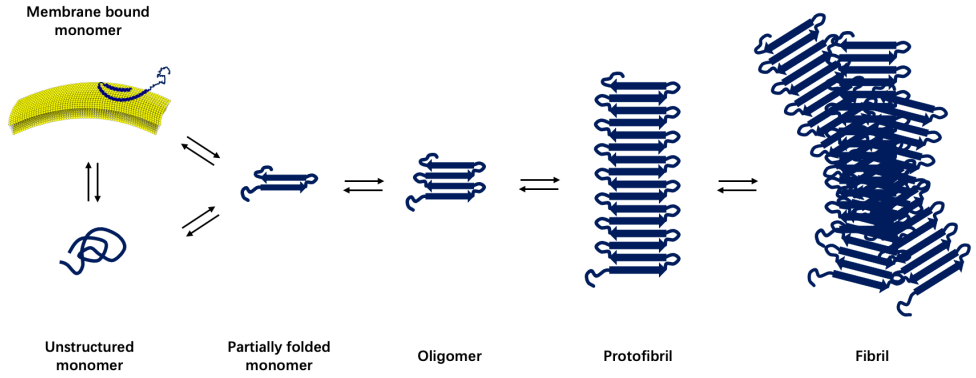


Figure 1.5 The process of αSyn aggregation. The aggregation could occur on lipid membranes or in cytosol.

αSyn fibrils have been characterised as β-sheet rich structure by ssNMR[128] and cryoEM[178]. They can promote αSyn aggregation[179] as well as intercellular transmission of pathologic αSyn[180]. Whereas αSyn oligomers are believed to be more toxic than fibrils. An *in vivo* study has demonstrated that oligomers can cause more serious dopaminergic neuron loss than fibrils[181]. αSyn oligomers probably cause neurotoxicity via multiple pathomechanisms. It occurs through inhibiting the fusion of synaptic vesicles[182], disrupting the function of organelles such as mitochondria, endoplasmic reticulum and lysosome[183-185] or inducing oxidative damage[186].

Similar to Aβ, αSyn is also a metal-binding protein, and its interaction with transition metal ions is considered to be a potential culprit of degeneration. Indeed, a series of transition metal ions has been proved to be able to accelerate the misfolding of αSyn. However, because the physiological concentrations of transition metal ions are usually in nanomolar to low micromolar regime, at such low concentration only Cu^{2+} exhibits the promotion effect[187]. In addition, αSyn can also catalyse ROS generation. It has been reported that αSyn-Cu complex possesses a high positive redox potential and can promote the formation of hydroxyl radicals[188-189]. The generated ROS can even oxidise the methionine of αSyn, which is proposed to be a plausible mechanism of αSyn aggregation[190-191].

Familial PD Mutation

Some single point mutations of αSyn have been discovered to associate with the onset of familial PD (FPD), so far including A30P, E46K, H50Q, G51D and A53T/E/V. Among them, A30P, E46K and H50Q mutants lead to the late-onset FPD, while G51D and A53T/E mutants lead to the early-onset FPD. All of these αSyn mutants are autosomal dominant, which are cause by missense mutations in the SNCA gene[192].

Interestingly, although these variants are all related to FPD development, they display different effects on the fibrillisation rate of αSyn. Generally, E46K, H50Q and A53T mutants accelerate αSyn fibrillisation, in contrast A30P, G51D and A53E mutants slow down the rate[193]. This indicates a more complicated pathomechanism. However, a study in *drosophila melanogaster* has shown that E46K, H50Q and G51D mutated αSyn can form oligomers sustainably even after fibrillisation compared to wild type αSyn. Thus the sustained formation of oligomers could be a shared pathomechanism by these αSyn variants[194].

It is notable that all known FPD mutations of αSyn are located in the N-terminal domain, which may influence the lipid membrane binding property of αSyn. The effects have been confirmed and summarised[192]. Briefly, A30P, G51D and A53E mutants attenuate the lipid binding, whereas E46K and A53T mutants exhibit increased binding ability. In addition, a comprehensive analysis has also shown reduced lipid binding by A30P, G51D and A53E mutants[195]. A recent study on the E46K mutant has detected increased lipid interactions, and suggested that the increased loss of membrane curvature selectivity of αSyn could be the critical reason of αSyn dyshomeostasis rather than enhanced membrane binding affinity[196]. Overall, the disruption of membrane normal functions by FPD mutants of αSyn could be a crucial role in synucleinopathies, thus adjusting cellular lipid avidity might be a potential therapy to compensate for the mutants induced faults.

Both Aβ and αSyn are metalloproteins. The interactions of Aβ, αSyn with metal ions may take part in many important physiological processes in brain, but they can also cause the misfolding of Aβ and αSyn, which is harmful to neurons. In addition,

both Aβ and αSyn are membrane proteins as well, misfolding of them can easily influence on the normal properties of neuronal membranes, leading to membrane dysfunction. In order to understand the connection among misfolded Aβ and αSyn, metal ions and neuronal membranes, the interactions of Aβ and αSyn with metal ions and neuronal membranes become a crucial topic to study.

1.3 Interactions of Aβ and αSyn with Metal Ions

Metal ions have crucial roles in basic life processes. Various metal ions have been shown to interact with IDPs, leading to either normal physiological regulation or abnormal pathogenesis. For example, Ca^{2+} can bind to C-terminus of αSyn, mediating the association between the random C-terminus of αSyn and synaptic vesicles. Whereas the imbalance of Ca^{2+} causes synaptic vesicle clustering[197]. Transition metal ions such as Zn^{2+}, Fe^{2+} and Cu^{2+} have been suggested to be involved in the development of neurodegenerative diseases through promoting the toxicity of IDPs[198-199]. Among these bio-metals, copper is implicated directly in multiple pathogenic mechanisms of IDPs, and thus drawing much attention from scientists.

Copper is a vital trace mineral that is necessary for many metabolic processes. In the nervous system, copper is normally involved in the maintenance of central nervous system (CNS) structure and function. It is believed that copper is stored in synaptic vesicles and able to affect synaptic vesicle trafficking, also it can modulate the activity of neurotransmitter receptors at synapses and the interactions between proteins involved in vesicle secretory pathways[200]. Copper concentration could reach 15 μM in the synaptic cleft during normal circulation[201]. However, there is numerous evidence that copper exists in AD senile plaques and PD brains at relatively higher concentrations[202-205], indicating its pathological implications in the development of AD and PD.

The interactions between Aβ and Cu^{2+} is pH dependent. At physiological pH, there are two predominant Aβ-Cu(II) modes, called Component I ($(Aβ\text{-}Cu)_I$) and Component II ($(Aβ\text{-}Cu)_{II}$), which differ in protonation state and coexist under equilibrium as

depicted in Fig. 1.6[206]. Cu^{2+} can associate to Aβ extremely fast, with an estimated rate constant of 5.0(2) × 10^8 M^{-1} s^{-1}[206]. The equilibrium dissociation constant (K_d) of Cu^{2+} binding to Aβ has been determined many times and shown various values, and a value of 1.3(2) nM for Cu^{2+} binding to $Aβ_{40}$ has been determined using kinetic technique[206]. Cu^{2+} can promote Aβ aggregation, possibly through forming a metal ion bridge between Aβ monomers[207]. In addition, as mentioned before (see Pathological Aβ in Section 1.2.1), Cu^{2+} can generate ROS, while Aβ can trap Cu^{2+} and accelerate ROS generation, leading to another major inducement of neuronal damage.

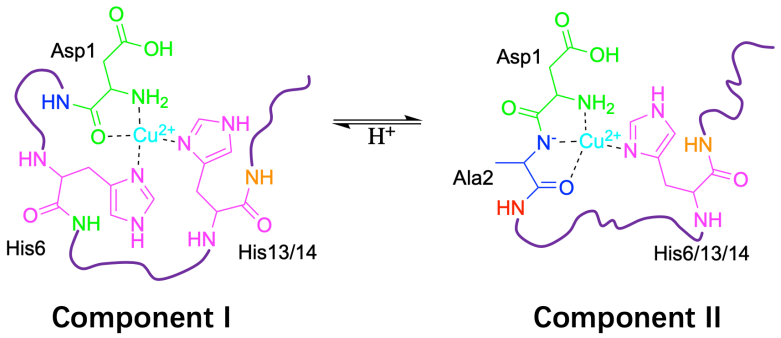


Figure 1.6 The major coordination modes of Aβ-Cu(II) complex. Component II exists at a higher pH as the amide of Ala2 is deprotonated.

For αSyn, three regions have been proposed to interact with Cu^{2+} by the electron paramagnetic resonance (EPR) study, which are centred at N-terminus, the histidine at position 50 (His50) and the aspartic acid at position 121 (Asp121), forming five Cu^{2+} coordination modes within pH 5.0 - 7.4[208-209]. Among them, three coordination modes at physiological pH are of great interest, which are referred to a two nitrogens and two oxygens mode (2N2O mode, centred at N-terminus) and a couple of three nitrogens and one oxygen modes (3N1O modes, centred at N-terminus and His50) (Fig. 1.7). However, the existence of 3N1O modes is disputed. A recent Cu^{2+} binding study has shown no evidence of the proposed 3N1O macrochelate formation, and suggested an alternative mode to explain the fact that His50 of αSyn had been discovered to interact with Cu^{2+} in EPR study, which is a ternary complex formed by Cu^{2+} bridges between N-terminus and His50 of two monomeric αSyn[210]. The measured values of Cu^{2+}

binding affinity of αSyn using different techniques are various, ranging from 0.1 nM - 60 μM[211]. Such an enormous scale could be due to the miscellaneous effects of various Cu^{2+} binding sites. In addition, Cu^{2+} has been shown to weakly bind to physiologically abundant NAc-αSyn on His50 and Asp121 sites, as the high-affinity N-terminal binding site of αSyn could be abolished by acetylation[212]. Whereas Cu^{+} can interact with NAc-αSyn more significantly, inducing α-helix formation, which may affect the properties of αSyn such as membrane binding and aggregation[213]. Similar to Aβ, Cu^{2+} can also promote αSyn accumulation and be catalysed by αSyn to generate ROS. Nevertheless, the mechanism of interactions between Cu^{2+} and αSyn could be more diverse due to the multiple binding availability. Relevant study is essential, in particular regarding the contentious Cu^{2+} binding site of His50, as His50 also plays an important role in FPD pathogenesis. Elucidating this issue would not only build up the understanding of Cu^{2+} interactions with αSyn, but also possibly provide insights into the pathology of H50Q variant induced FPD.

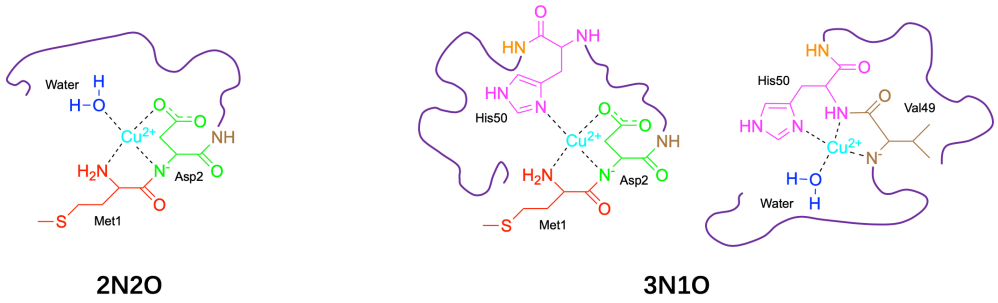


Figure 1.7 The proposed coordination modes of αSyn-Cu(II) complex at physiological pH. The N-terminal methionine involved in modes display high-affinity Cu^{2+} binding.

In addition to IDPs, Cu^{2+} has also been shown to interact with lipids of synaptic vesicles. Phosphatidylserine (PS) exhibits a reversible high-affinity association, with a binding ratio of 2:1 to Cu^{2+}[214-215]. Also, phosphatidylethanolamine (PE) is able to bind to Cu^{2+} with a relatively lower affinity compared with PS, and phosphatidylcholine (PC) bilayers containing PE displays faster oxidation by Cu^{2+} than pure PC bilayers in the presence of hydrogen peroxide[216]. These results are beneficial to understand and

explain the biological functions of membranes as well as the mechanisms of Cu^{2+} induced lipid peroxidation.

1.4 Interactions of Aβ and αSyn with Neuronal Membrane Lipids

As mentioned above, misfolded Aβ and αSyn are related to biological membrane dysfunction. Biological membranes are fluid phospholipid bilayers consisting of various lipids associated with membrane proteins. They separate two different fluid media and maintain the normal function of cells and organelles by controlling the ingress and egress of substances. Lipid membranes participate in numerous pivotal physiological interactions, one of which is the process of neurotransmission in nerve cells. In neurotransmission, there are small liposomes (~40 nm diameter[217]) clustered at presynaptic terminals called synaptic vesicles that are indispensable for the packing and transport of neurotransmitters. The lipid composition of synaptic vesicles is illustrated in Fig. 1.8. Given the essential role of lipid membranes in neurons, any disruption of them could damage the cells, leading to neurological disorders such as AD and PD.

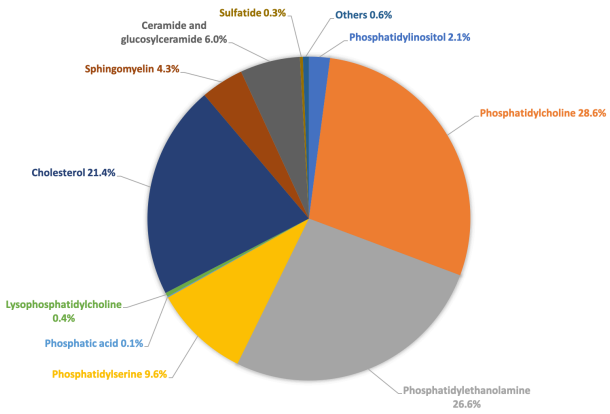


Figure 1.8 The lipid composition of synaptic vesicles. The pie chart depicts the relative percentages of different lipid classes found in synaptic vesicles. Adapted from Ref. 218.

The biological behaviour of Aβ is implicitly linked with lipid membranes as Aβ is generated from the transmembrane domain of APP. Indeed, $Aβ_{42}$ has been shown to bind and disrupt membranes using its hydrophobic N-terminus[219]. The more toxic Aβ

oligomers are probably affect membranes by multiple mechanisms as described above (see Pathological Aβ in Section 1.2.1), which can be briefly summarised as interacting with membrane proteins, inducing ion channel formation in membrane and accelerating oxidative damage of membrane. Lipid membranes can also affect Aβ activity. In membranes, the contents of cholesterol and ganglioside GM1 exhibit strong correlation with Aβ-membrane interactions.

Cholesterol and GM1 are abundant in lipid rafts which could be crucial in signal transduction and membrane fluidity regulation[220]. Cholesterol exhibits the property of fluidity regulation, as well as membrane structure stabilisation. The latter property has been suggested to prevent the interactions of membranes with Aβ[221]. However, another study has reported a reverse result that cholesterol accelerates the interactions between lipid bilayer and Aβ[222]. In addition, cholesterol has been shown to promote $A\beta_{42}$ aggregation in the presence of lipid membranes[223]. By contrast, GM1 has been shown to catalyse $A\beta_{40}$ aggregation[224], which is possibly due to seeding effect of the GM1-bound Aβ[225]. Evidence that $A\beta_{40}$ can selectively binds to GM1 further depicts $A\beta_{40}$-GM1 interactions[226-227]. Apart from these two micelle-formed lipids, vesicles composed of DOPC has also been reported to promote Aβ aggregation through accelerating secondary fibrillisation of the existed Aβ fibrils[228].

αSyn is commonly accepted as a membrane protein since its capability of interacting with synaptic vesicles. Structural investigation of association modes is essential to understand the nature of the interactions between αSyn and membranes. The general membrane binding structure of αSyn is considered as a double α-helices linked by a short segment, as described above (see αSyn Structure in Section 1.2.2). However, there is still a lack of consensus in details. For example, several studies have shown that αSyn binds to small unilamellar vesicles (SUV) with extended helix structure[124,229-230], while others suggested a bent helix structure[231-232]. The length of membrane-bound helix of αSyn is controversial, ranging from residues 1 - 25 to residues 1 - 97[233-235]. By contrast, an agreement is reached that the N-terminus of αSyn is partially inserted in the membrane, which could be a way of αSyn remodelling membranes[126,236-237].

The property of vesicles has significant impact on the interactions of αSyn with lipid membranes. Curvature is one of the factors, as the bent helix structure of αSyn is only found in the interactions with SUV[231-232], while for the interactions with large unilamellar vesicles (LUV), αSyn displays the extended helix structure[125]. Furthermore, it has been reported that bilayers with larger curvature exhibit higher αSyn binding affinity[238]. Interestingly, αSyn not only tends to associate with highly curved membranes, but has also been proposed to induce membrane curvature[239]. Apart from curvature, charge and lipid composition of vesicles also matter significantly. Monomeric αSyn has been shown to preferentially bind to vesicles containing anionic phospholipids such as phosphatidylserine (PS), phosphatidic acid (PA) and phosphatidylglycerol (PG), but it does not interact with neutral vesicles of phosphatidylcholine (PC)[240]. This could be attributed to the electrostatic attraction between negatively charged membranes and multiple positively charged lysine residues of αSyn[241]. In addition, despite its binding with anionic phospholipids, αSyn reveals different affinity with different lipids, which has been suggested as PA > PS ≈ PG[238]. Moreover, vesicles composed of different lipids show diverse stability against αSyn. It has been reported that DOPG vesicles can be disrupted by monomeric αSyn more easily than DOPS[242]. Negatively charged lipid membranes are considered to promote αSyn aggregation. However, so far it is extensively accepted that αSyn aggregation is modulated by the ratio of lipid to αSyn rather than only lipid. Higher ratio leads to the inhibition of αSyn aggregation, which could be due to scattered αSyn binding with lipid vesicles, resulting in the absence of monomeric αSyn for oligomer elongation[243-245]. Also, cholesterol has been proposed to reduce the binding of αSyn to synaptic-like vesicles[246]. While GM1 exhibits different effects on αSyn aggregation: accelerating aggregation at mildly acidic condition[247], whereas inhibiting aggregation at neutral pH[248].

Lipid membranes remarkably affect the biological behaviours of αSyn, and vice versa, αSyn regulates membrane bio-activities in both physiological and pathological processes (see Physiological αSyn and Pathological αSyn in Section 1.2.2). The interactions between lipid membranes and αSyn are intricate, enigmatic and largely

undetermined. Efforts toward unravelling this complication can give more concrete insights into the physiological functions of αSyn as well as novel therapeutic strategies for synucleinopathies.

1.5 Summary

AD and PD are the most common neurodegenerative diseases and they are currently incurable. Aβ and αSyn, which are essentially both members of the group of IDPs with unknown function, are well-accepted to be involved in AD and PD. It has been found that Aβ and αSyn can easily undergo aggregation to generate oligomers, fibrils and deposits. Although the exact pathology of AD and PD is still elusive, the toxic Aβ and αSyn oligomers, as well as the aggregates induced ROS generation are believed to be the key events of AD and PD pathogenesis. Transition metal ions such as Cu^{2+}/Cu^{+} and Fe^{3+}/Fe^{2+} are found to play crucial roles in Aβ and αSyn aggregation as well as ROS generation. In addition, it has been reported that lipid membranes can also regulate Aβ and αSyn aggregation, and the resultant Aβ and αSyn aggregates can reversely affect the properties of lipid membranes, sometimes leading to membrane damage and cell death. Hence, it is necessary to study the interactions of Aβ and αSyn with metal ions and lipid membranes to know the potential Aβ and αSyn related pathogenesis of AD and PD better.

This thesis investigates such interactions using multiple fluorescence techniques, aiming to understand the molecular mechanisms of these interactions as well as the physiological and pathological roles of Aβ, αSyn, Cu^{2+} and synaptic vesicles.

The methods employed and the materials used in this thesis are described in Chapter 2. As fluorescence technique is the major applied method, the relevant principles are introduced as well.

In Chapter 3, the kinetic interactions of Cu^{2+} with phosphorylated serine residue 8 Aβ and N-truncated $Aβ_{4-16}$ are investigated. The kinetic parameters and the mechanism schemes of these interactions are proposed. In addition, some important kinetic parameters of the redox reaction of wild type (WT) $Aβ_{16}$-Cu complex are determined.

A preliminary study about the TDMQ impact of $A\beta_{16}$-Cu induced ROS generation is also described.

In Chapter 4, the expression and purification as well as the fluorescent dye-labelling of various αSyn are described. The produced αSyn samples are used throughout in this thesis.

In Chapter 5, the interactions of Cu^{2+} with WT-αSyn, H50Q mutated αSyn and N-terminally acetylated (NAc) αSyn are investigated. The corresponding kinetic parameters and Cu^{2+} coordination mode structures are proposed. Furthermore, the reduction kinetics of WT-αSyn-Cu(II) complex is studied as well.

In Chapter 6, αSyn is shown to bind to lipid membranes such as GM1 micelle and synaptic-like small unilamellar vesicle (SUV). The binding forms of WT-αSyn on GM1 micelle and SUV are proposed. In addition, the binding affinities and rate constants of WT-αSyn and NAc-αSyn binding to SUV are determined.

In Chapter 7, SUV is shown to be able to bind Cu^{2+}, and the constituent DOPS is confirmed to be in charge of this binding. The kinetic parameters of the interactions between SUV and Cu^{2+} are determined. Also, the reduction kinetics of SUV-Cu(II) complex is investigated. The important role of synaptic vesicles in neuronal Cu^{2+} transmission is suggested based on the results.

In Chapter 8, the interactions among αSyn, SUV and Cu^{2+} are studied through investigating the interactions of αSyn-SUV complex with Cu^{2+}, SUV-Cu(II) complex with αSyn and αSyn-Cu(II) complex with SUV. The potential roles of these three elements in neurotransmission are described.

Finally, Chapter 9 concludes the work in this thesis and proposes several hypotheses about the physiological and pathological roles of Aβ, αSyn, Cu^{2+} and synaptic vesicles based on the results obtained in this work.

Chapter 2

Methods and Materials

In this Chapter, the commonly utilised methods and materials for this project are summarised. Fluorescence technique is the basic approach in this study.

2.1 Fluorescence[249]

Fluorescence technique is widely applied in biological sciences as it is extremely sensitive and specific. Fluorescence is a type of light emission by certain molecules that have absorbed electromagnetic radiation. Its generation can be depicted by a Jablonski diagram, as shown in Fig. 2.1.

Typically, the electrons of molecule are in the lowest possible energy levels, presenting in the ground state (S_0). In fluorescence, an electron can absorb a photon of energy, exciting itself to a higher electronic state (in this case, S_1 or S_2), but this only occurs when the energy of the photon matches the difference of energy values between the two states, which reflects the specificity. The process of absorption is very fast, on the order of 10^{-15} s.

Following excitation, the electron at higher electronic state will dissipate the extra energy and return to the lowest energy level. There are several ways to release energy in the transition. The first is vibrational relaxation, through which the electron transmits

the extra energy to redistribute other vibrational modes in the same molecule or to the surrounding molecules, and then move into lower vibrational levels. An alternative pathway is internal conversion, through which the electron can give up energy and directly move from a higher electronic state to a lower electronic state. This could happen when vibrational levels strongly overlap electronic levels. However, internal conversion is difficult to occur between the first excited state (S_1) and the ground state (S_0), as the difference of energy is too large to overlap. The processes of these two pathways are relatively fast, which take place in a range from 10^{-14} s to 10^{-11} s.

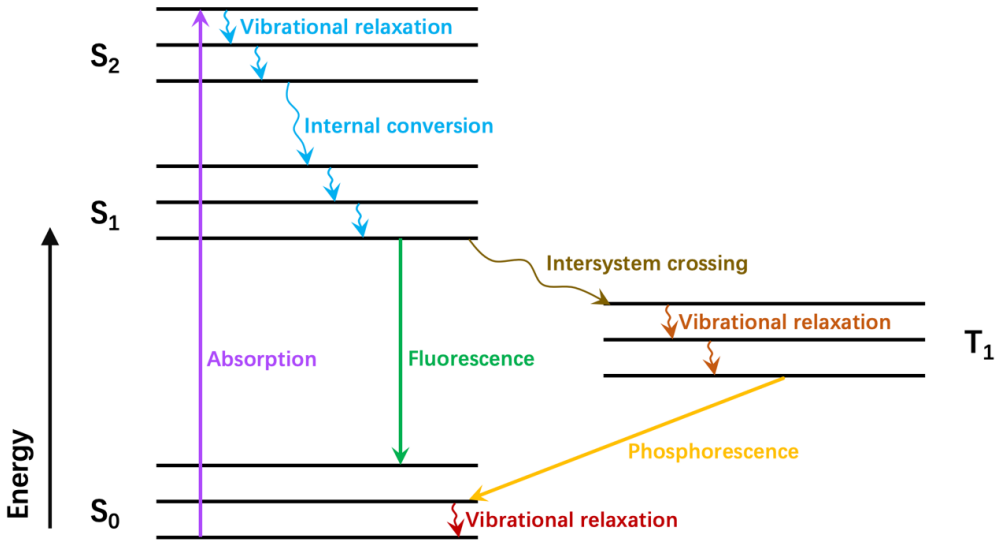


Figure 2.1 Jablonski diagram. The diagram illustrates the electronic transitions in molecules.

Fluorescence is another form of energy transfer, which is through photon emission. Normally, fluorescence occurs during the transition from the lowest vibrational level of S_1 to S_0, which is stated by the Kasha's rule, following vibrational relaxation or internal conversion. After fluorescence emission, the electron falls back to S_0 at any of vibrational levels that obeys the Franck-Condon principle. The energy of emitted photon in fluorescence is always lower than absorbed photon because of the energy dissipation in preceding vibrational relaxation or internal conversion. This difference is known as the Stokes shift, which is applied in fluorescence spectroscopy to separate excitation and emission light. Fluorescence emission is a relatively slow process,

usually occurring in 10^{-9} - 10^{-7} s.

In addition to the formation of excited singlet states (S_n) of electrons after excitation, excited triplet states (T_n) are also formed, which is through a relaxation pathway named intersystem crossing. This transition changes the spin state of electron, thus being classified as a forbidden transition since it is not allowed by selection rules. The transition occurs preferably when the vibrational levels of the two excited states overlap and is slower than vibrational relaxation or internal conversion, typically occurring in 10^{-11} - 10^{-6} s.

When the electron is in an excited triplet state, its return to S_0 may still cause photon emission. The most common radiation is phosphorescence, of which the process is also a forbidden transition and very slow, on the order of 10^{-3} s to 100 s or even longer.

In fluorescence studies, photobleaching is always a significant problem, which is probably caused by molecular oxygen induced permanent damage of fluorophores. Since the ground state of O_2 is a triplet state, which makes O_2 able to react with the fluorophore that is in an excited triplet state, and quench it irreversibly. The application of oxygen scavenging systems is beneficial to improve the problem of photobleaching[250]. For some fluorophores, the addition of oxygen scavengers can effectively enhance their lifetimes 10 - 100 fold longer than normal.

2.1.1 Fluorescence Anisotropy[249]

Fluorescence anisotropy is a phenomenon that the fluorescence emitted by a polarised light excited fluorophore has unequal intensities along different polarisation axes. It can be defined as the ratio of the polarised component intensity to the total intensity:

$$r = \frac{I_{\parallel} - I_{\perp}}{I_{\parallel} + 2I_{\perp}} \tag{2.1}$$

where $I_{\parallel}$ is the detected fluorescence intensity when the excitation and emission polarisation is parallel, and $I_{\perp}$ is the detected fluorescence intensity when the excitation and emission polarisation is perpendicular. In measurements, as the sample is always excited by vertically polarised light, Eq. 2.1 can be then denoted as:

$$r = \frac{I_{VV} - I_{VH}}{I_{VV} + 2I_{VH}} \tag{2.2}$$

where I_{VV} is the detected fluorescence intensity when both the excitation and emission polarisers are situated vertically, and I_{VH} is the detected fluorescence intensity when the excitation polariser is situated vertically while the emission polariser is situated horizontally.

For optical equipment, there are always instrumental artifacts that vary the light transmission in the two orthogonal orientations. To overcome the artifacts, a correction factor known as G-factor is introduced as:

$$G = \frac{I_{HV}}{I_{HH}} \tag{2.3}$$

where I_{HV} is the detected fluorescence intensity when the excitation polariser is situated horizontally while the emission polariser is situated vertically, and I_{HH} is the detected fluorescence intensity when both the excitation and emission polarisers are situated horizontally. Defining G-factor in this way is because the horizontal and vertical intensities of emission light are equal if the fluorophore is excited by horizontally polarised light. The modified equation for anisotropy determination will be:

$$r = \frac{I_{VV} - GI_{VH}}{I_{VV} + 2GI_{VH}} \tag{2.4}$$

Fluorescence anisotropy is correlated with the rotational correlation time (τ_c) of fluorescent molecule by the Perrin equation:

$$r = \frac{r_0}{1 + \tau/\tau_c} \tag{2.5}$$

where r_0 is the upper limit for anisotropy and τ is the fluorescence lifetime of the fluorophore. If the shape of the molecule is approximated to a sphere, the rotational correlation time (τ_c) can be denoted as:

$$\tau_c = \frac{\eta MV}{RT} \tag{2.6}$$

where η is the solution viscosity, M is the molecular weight of the molecule, V is the specific hydrodynamic volume, R is the gas constant and T is the absolute temperature.

Combined with Eq. 2.5 with Eq. 2.6, we can infer that increasing the molecular mass of fluorescent molecule can give rise to the value of anisotropy. This consequence provides an important approach to study intermolecular binding interactions, especially for the determination of binding affinity.

2.1.2 Förster Resonance Energy Transfer[251]

Förster resonance energy transfer (FRET, sometimes called fluorescence resonance energy transfer) is a non-radiative energy transition between two different fluorophores. It occurs when the two fluorophores are close enough (1 - 10 nm) and the emission spectrum of one of the fluorophores (donor) overlaps the absorption spectrum of the other (acceptor). In the transition, the excited donor fluorophore transfers energy to the acceptor through a dipole-dipole coupling, then the acceptor emits fluorescence. The energy transfer efficiency (E) can be denoted as:

$$E = \frac{1}{1 + (r/R_0)^6} \tag{2.7}$$

where r is the distance between donor and acceptor fluorophores and R_0 is the Förster radius of the two fluorophores. The Förster radius is the distance at which the energy transfer efficiency is 50%, typically in the range of 20 - 90 Å. It relates to the spectroscopic properties of donor and acceptor fluorophores, which can be calculated by:

$$R_0^6 = \frac{9000(\ln 10)\kappa^2 \Phi_D}{128\pi^5 N_A n^4} J(\lambda) = 8.79 \times 10^{-5}\, \kappa^2 \Phi_D n^{-4} J(\lambda) \tag{2.8}$$

where κ^2 is the dipole orientation factor (typically assumed to be 2/3 for randomly rotating dipoles), Φ_D is the quantum yield of donor fluorescence in the absence of the acceptor, N_A is the Avogadro constant, n is the refractive index of the medium and J is the overlap integral describing the degree of spectral overlap between the donor emission spectrum and the acceptor absorption spectrum, which can be given by:

$$J(\lambda) = \int_0^\infty F_D(\lambda)\varepsilon_A(\lambda)\lambda^4 d\lambda \tag{2.9}$$

where λ is the wavelength, $F_D(\lambda)$ is the normalised donor emission spectrum and $\varepsilon_A(\lambda)$ is the acceptor molar extinction coefficient.

So far, FRET technique is extensively employed in many biophysical areas. Since FRET is a distance-dependent physical process, it can be used to determine the distance between different regions in a biomolecule as well as monitoring the dynamic changes of that distance, providing deep insight into conformational transition of biomolecules.

2.2 Experimental Methods

2.2.1 Stopped Flow

Stopped flow technique is ideal for the fast kinetic studies. It allows the measurement of fast chemical reaction process in time, which is achieved by rapidly mixing solutions from different syringes in the observation chamber and then monitoring immediately. Multiple spectroscopic signals can be used to monitor reaction process including absorbance, anisotropy, FRET and fluorescence. In this project, fluorescence of the sample was predominantly employed as the monitored signal and detected by a stopped flow machine (KinetAsyst SF-61DX2, Hi-Tech Scientific). The circuit of the machine is shown in Fig. 2.2.

The machine has two available modes to detect the reaction processes in different mixing steps, which are named single mixing mode and double mixing mode.

Single mixing mode allows the detection of reaction process in a one-step mixing. Typically, two samples are placed into syringes C & D, while syringes A & B are disconnected. Syringes C & D are pushed up simultaneously by the pneumatic drive 2, shoving samples through the flow circuit, mixing them just before entering the optical cell and immediately flowing the mixture into the cell. Shortly after that (~1 ms), the flowing will be stopped once the terminal stop syringe has been filled with ~90 μL of solution and hits the stop stop, and at that time the data recording begins.

Double mixing mode allows the detection of two reaction processes in a continuous two-step mixing, of which the second process is monitored more commonly. Typically, samples for the first mixing are placed into syringes A & B, sample for the

second mixing is placed into syringe C, and buffer is placed into syringe D. Before mixing, the front stop is adjusted above drive 1 to allow a certain amount of solution (in this case, ~150 μL) can be pushed into the age loop. Whereas the back stop is adjusted below drive 2 to prevent any solution being pushed into syringes C & D. After the stop mounting, drive 1 will be pneumatically pushed up first, mixing the samples from syringes A & B, flowing the mixture into the age loop, and then hitting the front stop. At that time, a timer is triggered to clock. Once the set delay time has elapsed, drive 2 will be pushed up, using the buffer in syringe D to shove the aged mixture out from the age loop, and mixing it with the sample which is simultaneously shoved out from syringe C in the second mixer, further flowing the final mixture into the optical cell. After a short while (~1 ms), the terminal stop syringe hits the stop stop (filled with ~240 μL of solution), the flowing will be stopped and the data recording begins.

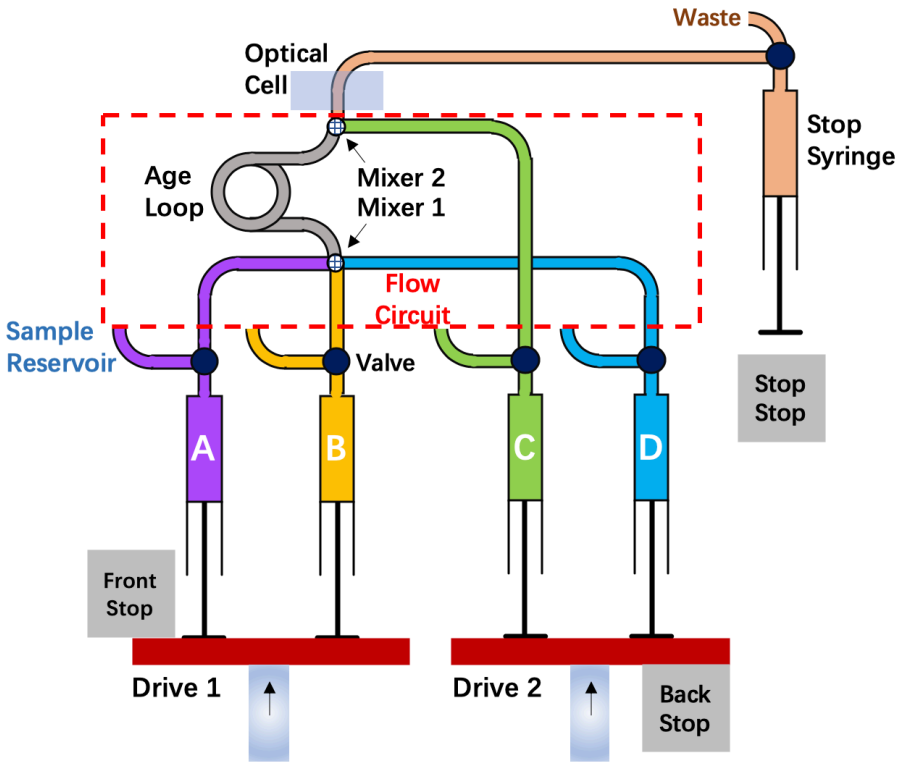


Figure 2.2 Schematic of the stopped flow apparatus.

In measurements, samples were excited by laser from a fibre coupled laser diode

(MCLS1-473-20, Thorlabs) at 473 nm. Fluorescence emission was filtered using a 515 nm long pass filter (515GY, Comar) to remove the excitation light before being monitored by a photon multiplier tube (PMT). The data points were recorded using the log time-scale scheme. Since the dead time of the instrument is ~1 ms, the data points below 2 ms were excluded in data analysis. The collected data points depict the trace of reaction process, of which a minimum of 9 repeats were averaged to obtain the final trace for analysis. In some analyses, raw reaction traces were normalised for shape comparison, which was carried out by multiplying factors to make the amplitudes identical.

2.2.2 Fluorometry

A spectrofluorometer (FluoroMax-4, Horiba) was used in this project to measure the fluorescence spectra and anisotropy of samples, as well as the kinetics of slow chemical reactions. A brief illustration of the optical paths through the machine is shown in Fig. 2.3.

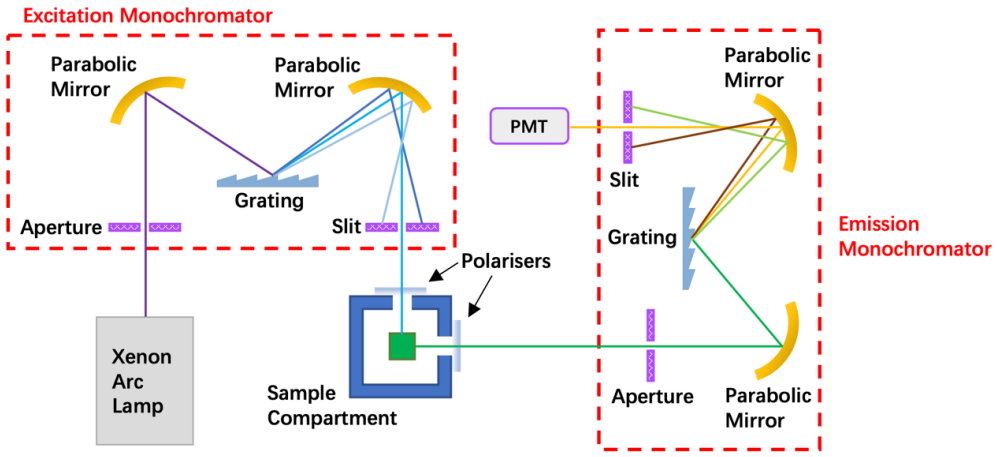


Figure 2.3 Optical layout of the spectrofluorometer.

The light source of the spectrofluorometer is UV and visible light produced by a xenon arc lamp. When passing through a monochromator, the light is separated into different wavelengths. The wavelength of excitation light and the bandwidth of

wavelength can be selected by setting the position and width of the slit on monochromator. On the emission side, there is a similar monochromator to select the wavelength of emission light. The selected fluorescence is detected by a PMT, which is used to count the number of photons over a set integration time (0.1 - 0.3 s). In measurements, samples were placed into a quartz fluorescence cuvette (105.250-QS, Hellma Analytics) which has a minimum capacity of ~120 µL. The cuvette was inserted into a cell holder in the sample compartment for detection. When measuring fluorescence anisotropy, two polarisers that are installed on the optical entrance and exit of the sample compartment will be activated to select the specific polarised light. Anisotropy values are calculated automatically using the detected parameters of intensity.

2.2.3 Custom-Built Confocal Microscope for FCS and smFRET

Confocal microscopy is an optical microscopy technique with relatively high resolution for detection in a small volume (typically on the order of femtolitres). It uses a spatial pinhole (aperture) to block out-of-focus light, eliminating background signal dramatically and thus increasing the resolution. The general principle is illustrated in Fig. 2.4. Because the observation volume, which is called confocal volume, is extremely small and only allows very few molecules to be detected, confocal microscopy is ideal for single-molecule detection. In this project, a custom-built

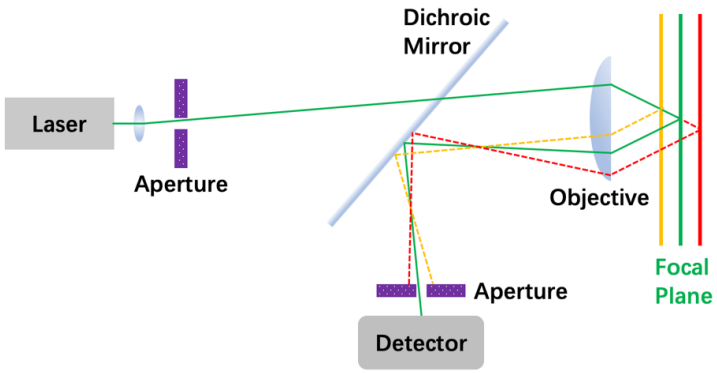


Figure 2.4 Confocal microscopy. An aperture in front of the detector blocks out-of-focus light from out-of-focus planes. Only the in-focus light (green line) can pass through the aperture and reach the detector.

confocal microscope was employed to perform the measurements of fluorescence correlation spectroscopy (FCS) and single-molecule FRET (smFRET).

The configuration of the confocal microscope used in this project is shown in Fig. 2.5. The argon ion laser (35LAP321-230, Melles Griot) is used as the excitation light source. The laser beam is redirected by a mirror, subsequently passes through a neutral density filter wheel that is used to adjust the laser intensity. Then the beam is totally reflected by a Dove prism, which removes the plasma lines of laser. After that, the beam is focused by the beam expander to a point where is centred on a spatial filter, so that the optical aberrations can be removed. Then a collimating lens is used to recollimates the beam. The beam is redirected again by mirrors and passes through an aperture which is used to reduce and optimise the beam size[252]. Before the entry of the beam into microscope, a measurement of laser power is always performed by an optical power meter (S122, Thorlabs). The inverted microscope (Eclipse TE2000-U, Nikon) used here contains a dichroic mirror, a high numerical aperture objective (CFI Apochromat TIRF 60×C Oil, NA 1.49, Nikon) and a lens. The incident beam is reflected by the dichroic mirror to the objective whose surface is covered by fluorescence-free immersion oil (Type FF, Cargille Labs). A chambered coverslip containing sample solution is placed on the objective and the beam is focused by the objective into solution 6 μm away from the bottom surface of coverslip. The fluorescence beam emitted from the sample is allowed to pass through the dichroic mirror, and focused by the lens to the centre of a confocal pinhole. Then the emission beam is separated by a beam splitter / dichroic mirror. The avalanche photodiode (APD) detectors used in this optical system have a dead time of 50 ns, which means that after detection of a photon, the following photons cannot be detected in this 50 ns. To improve this in FCS measurements, a 50/50 beam splitter is used to halve the beam. Two split beams will be detected independently and the signals will be cross-correlated to remove the effect of dead time, thus improving the temporal resolution. While in smFRET measurements, the dichroic mirror is used to separate the fluorescence of donor and acceptor for detection. The beams are cleaned by emission filters to remove misdirected excitation light and background fluorescence before they reach APDs (SPCM-AQR-14 single photon counting module, PerkinElmer).

The APDs are connected to a digital hardware correlator (Flex02-01D/C, Correlator.com) with a sampling time of 1.5625 ns for FCS measurements, and also connected to a multichannel scaler (MCS-pci, ORTEC) with a maximum input counting rate of 150 MHz for smFRET measurements.

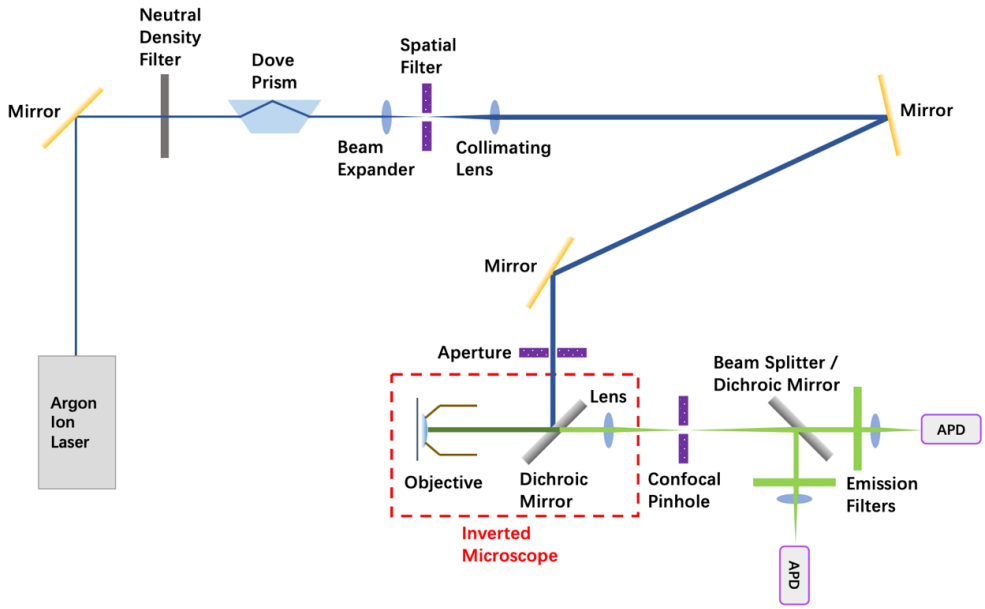


Figure 2.5 Setup of the custom-built confocal microscope.

2.2.4 Ultraviolet-Visible Spectroscopy

Ultraviolet-visible (UV-Vis) spectroscopy is a technique that measures the UV-visible light absorption of samples. In this project, an UV-Vis spectrophotometer (Lambda 25, PerkinElmer) was used to perform measurements. The machine has two lamps, one is a deuterium lamp which provides UV light, and the other is a halogen lamp which provides visible light. The light is dispersed by a monochromator to produce a spectrum and then passes through slits that have fixed width of 1 nm. After that, the light is reflected into the sample compartment and then detected by a photodiode detector. In measurements, a quartz absorption cuvette (104.002-QS, Hellma Analytics) with a path length of 10 mm was filled with ~700 µL of sample solution and inserted into the cell holder in the sample compartment for detection. The

absorbance (A) of a sample is defined as:

$$A = -\log_{10} T \tag{2.10}$$

where T is the transmittance of the sample.

Absorption measurements are extensively applied to determine the concentration of a sample (c) via the Beer-Lambert law:

$$A = \varepsilon c l \tag{2.11}$$

where ε is the molar extinction coefficient of the sample at a specific wavelength and l is the optical path length in centimetres. For normal proteins, if they contain aromatic amino acids, especially tryptophan or tyrosine, the absorbance at 280 nm and corresponding molar extinction coefficient can be used to determine the concentration. While for single-dye labelled samples, the peak absorbance along with the manufacturer provided extinction coefficient of the dye is always used to determine the concentration.

2.2.5 Circular Dichroism Spectroscopy

Circular dichroism (CD) spectroscopy is a chiro-optical spectroscopic technique that is widely used in the secondary structure analysis of biomolecules, particularly proteins. The detection is based on the CD property of chiral molecules which is, generally, the differential absorption of left- and right-handed circularly polarised light at some wavelengths. The difference between the two absorbance is the presented CD signal in measurements. While for historical reasons, most of studies present the CD signal as the degrees of ellipticity (θ), which is calculated by:

$$\tan\,\theta = \frac{E_R - E_L}{E_R + E_L} \tag{2.12}$$

where E_R and E_L are the magnitudes of the electric fields of the detected right- and left-circularly polarised light, respectively. Since the square of the magnitude of the electric field is proportional to the light intensity, Eq. 2.12 can be then transformed to the following equation which links CD signal with the intensity of detected light (I):

$$\tan\ \theta = \frac{\sqrt{I_R} - \sqrt{I_L}}{\sqrt{I_R} + \sqrt{I_L}} \tag{2.13}$$

θ is dependent on sample concentration and optical path length, the dependence can be removed by defining molar ellipticity ($[\theta]$) as:

$$[\theta] = \frac{100\theta}{cl} \tag{2.14}$$

where c is the sample concentration in molar, l is the optical path length in centimetres and the factor of 100 converts path length from centimetres in metres. This equation will give the final unit of deg cm^2 $dmol^{-1}$ on CD signal.

Some common motifs in the secondary structure of biomolecules such as helices and β-sheets have representative CD spectral signatures in the UV range of wavelengths. Thus CD measurements can provide conformational information of the detected biomolecules. In this project, a CD spectrometer (Chirascan V100, Applied Photophysics) was used to carry out measurements. A xenon arc lamp is installed in the spectrometer to produce UV and visible light. The light is dispersed into linearly polarised monochromatic light by a dual polarising prism system and then passes through slits. Subsequently, the linearly polarised light is converted into left and right circularly polarised light alternately by a photoelastic modulator (PEM). After that, the light passes into the sample handling unit and is detected by a PMT. In measurements, a quartz absorption cuvette (110-QS, Hellma Analytics) with a relatively short path length (1 mm) was used, as long optical path in solution could cause high absorption of light, which may result in weak signal for detection. For the same reason, the concentration of sample as well as the selected buffer should be considered to optimise measurements. In this study, ~70 μM of αSyn prepared in 10 mM phosphate buffer was applied in measurements after multiple tests.

2.2.6 Electron Paramagnetic Resonance Spectroscopy

Electron paramagnetic resonance (EPR) spectroscopy is a technique for the study of chemical species with unpaired electrons. As the electron has the spin quantum

number m_s = -1/2 or +1/2, in an external magnetic field, the magnetic moment of an unpaired electron will be either antiparallel or parallel to the field, which corresponds to two energy states due to the Zeeman effect. The state energy difference (ΔE) between these two states is:

$$\Delta E = h\upsilon = g_e \mu B_0 \tag{2.15}$$

where h is the Planck constant, υ is the microwave frequency, g_e is the g factor of electron, μ is the Bohr magneton and B_0 is the strength of the external magnetic field. By absorbing or emitting the energy of ΔE, the unpaired electron can move between these two states. Typically, for a system in thermodynamic equilibrium, there are more electrons at the lower energy state due to the Maxwell-Boltzmann distribution. Thus a net absorption of energy will be presented, and this is the origin of EPR signal. In EPR measurements, the samples will be exposed to a fixed-frequency microwave and an increasing-strength magnetic field. The microwave energy absorption at different magnetic field strength will be monitored and then converted to its first derivative, which is showed as the typical EPR spectrum.

In practice, in addition to the external magnetic field, any local magnetic fields produced by atoms or molecules can influence the unpaired electron. In this circumstance, Eq. 2.15 becomes:

$$\Delta E = h\upsilon = g_e \mu B_0 (1 - \sigma) = g \mu B_0 \tag{2.16}$$

where σ represents the effect of local magnetic fields and g is the g factor. The determined g factor can provide chemical information about the electronic structure of the unpaired electron-bound molecules.

The magnetic interaction between unpaired electrons and nuclear spins in atoms can cause hyperfine coupling, which will introduce additional energy states, resulting in splitting of the fine structure of spectral lines into several hyperfine lines. For a number of (n) equivalent nuclei which have the nuclear spin of I, a single spectral line will be split into $2nI + 1$ hyperfine lines. The magnetic field spacing between two neighbouring hyperfine lines caused by the same nucleus is called the hyperfine

coupling constant (*A*) of the nucleus. Hyperfine coupling can provide information about the number and identity of atoms in a compound, as well as the distance between the unpaired electron and the nuclei.

In this project, EPR technique was used to detect Cu^{2+} in compounds. The facilities were supported by EPSRC National Service for Electron Paramagnetic Resonance Spectroscopy at The University of Manchester. Facilities operations and spectral simulations were supported by Dr Alena Sheveleva and Dr Floriana Tuna of The University of Manchester.

2.2.7 SDS-PAGE

Sodium dodecyl sulfate-polyacrylamide gel electrophoresis (SDS-PAGE) was employed in this project to analyse expressed protein samples, as the use of SDS allows to analyse proteins solely by mass. In experiments, the Tris-glycine polyacrylamide gels were cast using a tetra handcast system (Mini-PROTEAN, Bio-Rad), and assembled into a tetra vertical electrophoresis cell (Mini-PROTEAN, Bio-Rad) for electrophoresis. During electrophoresis, a molecular weight marker (Precision Plus Protein Dual Xtra prestained protein standard, Bio-Rad) was used to identify the mass of proteins. After electrophoresis, the gels were stained using Coomassie protein stain (InstantBlue, Expedeon) for visualisation. In imaging, the gels were normally imaged using a digital imager (ImageQuant LAS 4000, GE Healthcare). While for fluorescent gels, a laser scanner (Typhoon FLA 9500, GE Healthcare) was used to capture the fluorescent images.

2.2.8 Cleaning

The residual samples adsorbed on the surface of equipment can cause corrosion as well as contamination for the next experiment. Thus the equipment must be cleaned after use, especially the reusable quartz cuvettes and stopped flow machine. In this project, the equipment was initially rinsed with MQ water. Then ~4 mM EDTA was used to remove adsorbed transition metal ions. After that, the equipment was rinsed with MQ water again to flush out excess EDTA, and finally left in 1% surface

disinfectant (Decon 90, Thermo Fisher Scientific) overnight to remove adsorbed proteins and lipids. The equipment was flushed with MQ water and buffer to wash out disinfectant prior to performing experiments.

2.3 Analytical Methods

2.3.1 Rate Equation of Chemical Reaction

The rate equation is the fundament of kinetic mechanism studies. It links the reaction rate with the concentration of reactants through a rate constant, which is an essential factor for the understanding of reaction mechanisms. For a typical second-order reaction with two reactants, the rate equation is expressed as:

$$r = k[\mathrm{A}][\mathrm{B}] \tag{2.17}$$

where *r* is the reaction rate, *k* is the rate constant, [A] and [B] are the concentrations of reactants A and B, respectively. If one of the reactants (e.g., reactant B) is applied in great excess, the reaction will be under pseudo first-order conditions, and Eq. 2.17 can be simplified into:

$$r = k'[\mathrm{A}] \tag{2.18}$$

where *k'* is the pseudo first-order rate constant and equals to *k*[B]. The differential form of Eq. 2.18 is:

$$-\frac{d[\mathrm{A}]}{dt} = k'[\mathrm{A}] \tag{2.19}$$

After integration and rearrangement:

$$[\mathrm{A}]_t = [\mathrm{A}]_0 e^{-k't} \tag{2.20}$$

where *t* is the reaction time, $[\mathrm{A}]_t$ is the concentration of reactant A at time *t* and $[\mathrm{A}]_0$ is the initial concentration. In this project, most of second-order chemical reactions in kinetic studies are under pseudo first-order conditions. The reaction traces obtained from stopped flow experiments were fitted using multiple exponentials to analyse the different steps in reaction process:

$$[\mathrm{A}]_t = A_1 e^{-k_1' t} + A_2 e^{-k_2' t} + A_3 e^{-k_3' t} + C \tag{2.21}$$

where A is the amplitude of different steps in traces and C is the background fluorescence. The pseudo first-order rate constant (k') can be derived from Eq. 2.21. In some cases, the mean rate constant (k'_{mean}) was required and derived from:

$$k'_{\mathrm{mean}} = \frac{A_1 k_1' + A_2 k_2' + A_3 k_3'}{A_1 + A_2 + A_3} \tag{2.22}$$

whose standard error was calculated by:

$$\sigma_F^2 = \left(\frac{\partial F}{\partial A_1}\right)^2 \cdot \sigma_{A_1}^2 + \left(\frac{\partial F}{\partial k_1}\right)^2 \cdot \sigma_{k_1}^2 + \left(\frac{\partial F}{\partial A_2}\right)^2 \cdot \sigma_{A_2}^2 + \left(\frac{\partial F}{\partial k_2}\right)^2 \cdot \sigma_{k_2}^2 + \left(\frac{\partial F}{\partial A_3}\right)^2 \cdot \sigma_{A_3}^2 + \left(\frac{\partial F}{\partial k_3}\right)^2 \cdot \sigma_{k_3}^2 \tag{2.23}$$

After k' determination at different excess B concentrations, because:

$$k' = k[\mathrm{B}] \tag{2.24}$$

the rate constant (k) can be finally determined from the slope of this linear function.

2.3.2 Hill-Langmuir Equation

The Hill-Langmuir equation is frequently used to describe the binding of a ligand L to a receptor molecule. It presents as a rearrangement of the ratio of ligand-bound receptors to total receptors (θ), which is a function of the ligand concentration ([L]):

$$\theta = \frac{1}{1 + (K_{\mathrm{A}}/[\mathrm{L}])^n} = \frac{1}{1 + K_{\mathrm{d}}/[\mathrm{L}]^n} \tag{2.25}$$

where K_{A} is the microscopic dissociation constant, K_{d} is the dissociation constant and n is the Hill coefficient. The Hill coefficient (n) refers to the cooperativity of ligand binding. If $n > 1$, the binding is positively cooperative, which means that the bound ligands can increase the affinity of receptors for other ligands. If $n = 1$, the binding is noncooperative, and in this situation, the affinity between receptors and ligands is independent on the bound ligands. If $n < 1$, the binding is negatively cooperative, then the bound ligands on receptors will prevent other ligands to bind.

In this project, the data points of fluorescence anisotropy were fitted using the Hill-Langmuir equation to determine binding affinity (K_d), because anisotropy can be used to assess the intermolecular binding as discussed above. The data points were obtained from anisotropy titrations. The equation used here was modified as:

$$\theta = \frac{A}{1 + K_d/[\mathrm{L}]^n} + C \tag{2.26}$$

where A is the amplitude of curves and C is the value of the start point. In analysis, the binding reactions were assumed to be noncooperative, i.e., $n = 1$, which presented well-fitted sigmoidal curves.

2.3.3 Fluorescence Correlation Spectroscopy

Fluorescence correlation spectroscopy (FCS) is a method used to analyse the fluorescence intensity fluctuations which is caused by Brownian motion of fluorescent particles. The data are extracted by performing an autocorrelation on fluorescence intensity, which essentially evaluates the similarity between the same fluorescence signal observed at different time points t and $t+\tau$. The normalised autocorrelation function ($G(\tau)$) is:

$$G(\tau) = \frac{\langle \delta I(t) \delta I(t+\tau) \rangle}{\langle I(t) \rangle^2} + 1 = \frac{\langle I(t) I(t+\tau) \rangle}{\langle I(t) \rangle^2} \tag{2.27}$$

where pointed brackets represent averaging over all values of time, $\delta I(t) = I(t) - \langle I(t) \rangle$ is the deviation from the mean intensity. $I(t)$ and $I(t+\tau)$ are the fluorescence intensities at

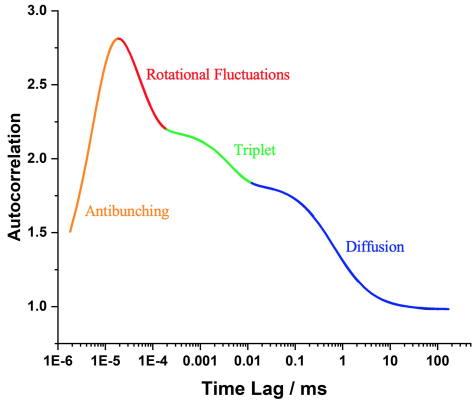


Figure 2.6 Autocorrelation curve of fluorescence signal. The curve shows the timescales of different processes[253].

time t and $t+\tau$, respectively. The function transforms the signal to a trace as shown in Fig. 2.6. In this project, only longer time scale behaviour such as "diffusion" and "triplet" can be detected due to the dead time of APD detectors. The signals detected by two identical APD detectors were pseudo-autocorrelated, i.e., two identical signals from each APD were cross-correlated, rather than real autocorrelated. Such method can remove the influence from the dead time of APDs, thus producing better-quality traces.

By fitting FCS traces, much information about the monitored fluorescent molecules can be determined. In this project, most of the information was derived from the diffusion part of traces, including the average diffusion time, the average concentration and the average hydrodynamic radius of samples. The diffusion part of traces can be fitted by:

$$G(\tau) = \frac{G(0)}{[1 + (\tau/\tau_D)]\sqrt{1 + \omega^{-2}(\tau/\tau_D)}} + G(\infty) \tag{2.28}$$

where $G(0)$ is the amplitude of the correlation curve, ω is the ratio of axial to radial radius of the observation volume and τ_D is the average time for a molecule to diffuse through the observation volume. If a confocal microscope with a large pinhole size (~100 μm diameter) is used for observation, the axial radius of the confocal volume will be much larger than the radial radius. Thus the signal of fluctuations due to diffusion in axial direction will be negligible. Also, the value of ω will be very large and Eq. 2.28 can be simplified to:

$$G(\tau) = \frac{G(0)}{1 + (\tau/\tau_D)} + C \tag{2.29}$$

The diffusion part of FCS traces obtained by confocal microscopy in this project was fitted using this function, to determine the average diffusion time (τ_D) and $G(0)$.

As $G(0)$ is inversely proportional to the average number of diffusing molecules in the confocal volume, the average concentration of the sample (c) can be estimated by:

$$c = \frac{1}{G(0)N_A V} \tag{2.30}$$

where N_A is the Avogadro constant and V is the volume of the confocal spot.

The average diffusion time (τ_D) is related to the diffusion coefficient (D):

$$\tau_D = \frac{\omega_0^2}{4D} \tag{2.31}$$

where ω_0 is the radius of the confocal spot. If the diffusing molecules are spherical, the average hydrodynamic radius of the sample (R) can be determined by the Stokes-Einstein equation:

$$D = \frac{k_B T}{6\pi\eta R} \tag{2.32}$$

where k_B is the Boltzmann constant, T is the absolute temperature and η is the solution viscosity.

In addition to the diffusion part, the triplet part is always shown if the excitation laser power is high. In this case, the following modified equation can be used to fit the correlation function:

$$G(\tau) = \frac{G(0)}{1 + (\tau/\tau_D)}(1 - F + Fe^{-\tau/\tau_m}) + C \tag{2.33}$$

where F is the fraction of fluorescent particles in the triplet state and τ_m is the mean triplet lifetime. If there are multiple fluorescent species with different τ_D (e.g., τ_1 & τ_2), the diffusion part of traces can be fitted by the further modified equation:

$$G(\tau) = [\frac{G_1(0)}{1 + (\tau/\tau_1)} + \frac{G_2(0)}{1 + (\tau/\tau_2)}](1 - F + Fe^{-\tau/\tau_m}) + C \tag{2.34}$$

As $G_1(0)$ and $G_2(0)$ can be derived by fitting, the relative fractions of these fluorescent species can be then determined by:

$$F_1 = \frac{G_1(0)}{G_1(0) + G_2(0)} \quad \text{and} \quad F_2 = \frac{G_2(0)}{G_1(0) + G_2(0)} \tag{2.35}$$

The mean diffusion time of the whole system can be determined as well if it is required.

2.3.4 Single-Molecule Förster Resonance Energy Transfer

For the radiometric FRET measurements, the apparent energy transfer efficiency (E) is determined by:

$$E = \frac{I_A/\eta_A}{I_A/\eta_A + I_D/\eta_D} \tag{2.36}$$

where I_A and I_D are the measured photon counts from the acceptor channel and donor channel respectively, η_A and η_D are the photon detection efficiencies of the two channels. Typically, the collected data are corrected by a factor to eliminate the effect of crosstalk which is caused by the leakage of donor emission into acceptor channel. Also a threshold value is required to remove background noise. The corrected data are then exported as the sum of E events and plotted in the form of a histogram for analysis. In this project, the histograms were fitted by a Gaussian distribution function to extract useful parameters:

$$f(E) = \frac{A}{w\sqrt{\pi/2}} e^{-2(\frac{E-E_c}{w})^2} \tag{2.37}$$

where A is the amplitude of the peak, w is twice the value of standard deviation and E_c is the centre position of the peak. These parameters provide the information about the population of different FRET efficiency states.

2.4 Materials

2.4.1 Proteins and Peptides

Amyloid-β

All amyloid-β (Aβ) peptides (except for A2P-$A\beta_{16}$) were purchased from Anaspec via Cambridge Bioscience, while the A2P-$A\beta_{16}$ was purchased from Synpeptide. The Aβ sequences are shown at the end of this section. In this project, the Aβ peptides which are composed of the first 16 amino acids were commonly used as model peptides. This is because these short Aβ peptides contain the proposed metal binding sites and meanwhile they are less possible to aggregate than full-length Aβ. All of these model Aβ peptides were dissolved in 50 mM HEPES buffer containing 100 mM NaCl (pH 7.5) and stored at -20 ℃. While for the $A\beta_{40}$ peptide, 1% ammonium hydroxide was used as solvent to prevent the aggregation, and the prepared stock solution was also stored at -

20 °C.

All fluorescent Aβ peptides (except for A2P-$Aβ_{16}$) were labelled with HiLyte 488 dye (HiLyte Fluor, Anaspec), while the A2P-$Aβ_{16}$ was labelled with fluorescein isothiocyanate (FITC). When preparing Aβ solutions, the concentration of labelled Aβ solution was determined using the extinction coefficient for the peak absorbance of the dye (ε = 70000 M^{-1} cm^{-1} for HiLyte 488 and ε = 73000 M^{-1} cm^{-1} for FITC). Whereas for unlabelled Aβ, the molar extinction coefficient at 280 nm (ε = 1490 M^{-1} cm^{-1}) was used.

Aβ Sequences

Labelled Aβ:

$Aβ_{16}$ DAEFR HDSGY EVHHQ K

pS8-$Aβ_{16}$ DAEFR HDSGY EVHHQ K

$Aβ_{4-16}$ FRHDS GYEVH HQK

A2P-$Aβ_{16}$ DPEFR HDSGY EVHHQ K

Unlabelled Aβ:

$Aβ_{16}$ DAEFR HDSGY EVHHQ K

$Aβ_{40}$ DAEFR HDSGY EVHHQ KLVFF AEDVG SNKGA IIGLM VGGVV

where the labelling sites are coloured green, phosphorylation site is coloured blue and mutation site is coloured red.

α-Synuclein

In this project, all α-synuclein (αSyn) samples were self-produced (see Chapter 4). The full-length αSyn sequence is:

MDVFMKGLSK AKEGVVAAAE KTKQGVAEAA GKTKEGVLYV
GSKTKEGVVH GVATVAEKTK EQVTNVGGAV VTGVTAVAQK
TVEGAGSIAA ATGFVKKDQL GKNEEGAPQE GILEDMPVDP
DNEAYEMPSE EGYQDYEPEA

Serum Albumins

Human serum albumin (HSA) and bovine serum albumin (BSA) were purchased

from Sigma-Aldrich. HSA solution was prepared to perform some competition experiments, while BSA solution was prepared as surface blocking agents to prevent the instrumental surface adsorption of detected proteins.

2.4.2 Lipids

Multiple lipids were used in this project including monosialo-tetrahexosyl-ganglioside (GM1), cholesterol, 1,2-dioleoyl-sn-glycero-3-phosphoethanolamine (DOPE), 1,2-dioleoyl-sn-glycero-3-phospho-L-serine (DOPS), 1,2-dioleoyl-sn-glycero-3-phosphocholine (DOPC), 1-palmitoyl-2-oleoyl-sn-glycero-3-phospho-(1'-rac-glycerol) (POPG), 1,2-dioleoyl-sn-glycero-3-phosphoethanolamine-N-(7-nitro-2-1,3-benzoxadiazol-4-yl) (NBD-DOPE, head group labelled) and Coagulation Reagent I (DOPE:DOPS:DOPC (5:3:2 w/w)). All lipids (except for GM1) were purchased from Avanti Polar Lipids, while GM1 was purchased from Sigma-Aldrich. All lipids were purchased as lyophilised powders. In experiments they were dissolved in chloroform and mixed as required, then aliquoted and dried under a nitrogen stream to obtain lipid films. The lipid films were left under nitrogen flow overnight to remove any remained solvent and then stored at -20 ℃. For preparing small unilamellar vesicles (SUVs), the lipid films were first hydrated in buffer with agitation for 1 h. Then the obtained lipid suspension was extruded through a polycarbonate membrane with 50 nm pores (Nuclepore, Whatman) 15 times using an extruder (Mini-Extruder, Avanti Polar Lipids). The SUV suspension can be stored at 4 ℃ for at least 2 days.

2.4.3 Fluorescent Dyes

Alexa Fluor 488 C_5 maleimide dye and Alexa Fluor 594 C_5 maleimide dye were used predominantly in this project. They were purchased as powders from Thermo Fisher Scientific and used to label αSyn. The dyes were dissolved in dimethyl sulfoxide (DMSO), aliquoted and stored at -20 ℃.

2.4.4 Copper(II) Chloride

$CuCl_2$ was purchased from Thermo Fisher Scientific. In experiments, it was

dissolved in ultrapure water to prepare a 20 mM stock solution and stored at 4 ℃.

2.4.5 Copper(II) Chelators

N4-tetradentate monoquinoline (TDMQ) ligands were provided as powders by Dr Anne Robert (Coordination Chemistry Laboratory, French National Centre for Scientific Research), dissolved in 50 mM HEPES buffer containing 100 mM NaCl (pH 7.5) and stored at -20 ℃. Ethylenediaminetetraacetic acid (EDTA) solution was purchased from PanReac AppliChem and diluted in different concentrations as required.

2.4.6 Reducing and Oxidising Agents

All reagents were purchased from Sigma-Aldrich. In redox experiments, the solutions of the reducing agents ((+)-sodium L-ascorbate and L-glutathione (GSH)) were always freshly prepared to minimise autoxidation. Hydrogen peroxide solutions used in the experiments were diluted from a 35 wt. % hydrogen peroxide solution and stored at 4 ℃. In fluorescent dye labelling experiments, the reducing agent Tris(2-carboxyethyl)phosphine hydrochloride (TCEP-HCl) was dissolved in water and stored at -20 ℃.

2.4.7 Buffers

Most of the experiments in this project were performed using 4-(2-hydroxyethyl)-1-piperazineethanesulfonic acid (HEPES) buffers containing 100 mM NaCl, as HEPES only has little impact on the existence of Cu^{2+}. Whereas in αSyn production and CD measurements, 2-amino-2-(hydroxymethyl)-1,3-propanediol (Tris) buffers and phosphate buffers were used respectively. HEPES buffer solutions were purchased from PanReac AppliChem and diluted in different concentrations as required. While Tris-HCl and phosphate buffered saline (PBS) were purchased as powders from Sigma-Aldrich. Sodium chloride, which was purchased from Sigma-Aldrich, was dissolved in buffers as required to maintain the ionic strength at near physiological conditions. The pH of buffers was adjusted by hydrochloric acid purchased from Sigma-Aldrich.

2.4.8 Reagents for αSyn Production

Competent Cells

DH5α and BL21(DE3) competent cells were purchased from Thermo Fisher Scientific and stored at -80 ℃.

Plasmids and Primers

Plasmids were purchased as transformed bacteria from Addgene and stored at -80 ℃. All primers were self-designed and custom synthesised by Integrated DNA Technologies and stored at -20 ℃.

Other Reagents

All reagents (except for protease inhibitor) were purchased as powders from Sigma-Aldrich, while protease inhibitor was purchased as tablets from Roche. In experiments, lysogeny broth (LB) was dissolved in water and autoclaved prior to use. Antibiotics such as ampicillin was dissolved in water to prepare a 100 mg/mL stock solution and stored at -20 ℃, while chloramphenicol was dissolved in ethanol to prepare a 25 mg/mL stock solution and stored at -20 ℃. Isopropyl β-d-1-thiogalactopyranoside (IPTG) was dissolved in water to prepare a 1 M stock solution and stored at -20 ℃. Streptomycin sulfate and ammonium sulfate were dissolved in water as well prior to use in purification.

2.4.9 Reagents for SDS-PAGE

Gels

The gels contain Tris-HCl, 30% acrylamide mix-19:1 (5% crosslinker), sodium dodecyl sulfate (SDS), ammonium persulfate (APS) and N,N,N',N'-tetramethylethane-1,2-diamine (TEMED). All reagents (except for Tris-HCl and SDS) were purchased from Bio-Rad, while SDS was purchased from Sigma-Aldrich. SDS was dissolved in water to prepare 10% solution prior to use. APS was dissolved in water to prepare 10% solution as well. 30% acrylamide mix solution, APS solution and TEMED were stored

at 4 ℃.

Buffers

The running buffer contains Tris-HCl, glycine and SDS, while the loading buffer contains Tris-HCl, glycerol, SDS, dithiothreitol (DTT) and bromophenol blue. Glycine, glycerol, DTT and bromophenol blue were all purchased from Sigma-Aldrich.

2.4.10 Solvents

Multiple solvents were used to dissolve different reagents. Ultrapure water with a resistivity of 18.2 MΩ cm, which was produced by a water purification system (Milli-Q, Merck Millipore), was used to prepare buffers, dilute solutions and dissolve most of the reagents. Other solvents including ammonium hydroxide, methanol, ethanol, chloroform and DMSO were all purchased from Sigma-Aldrich.

Chapter 3

Interactions of Serine 8 Phosphorylated Amyloid-β and N-Terminal Truncated Amyloid-β_{4-16} with Cu^{2+}

Amyloid-β (Aβ) is believed to play an important role in the development of Alzheimer's disease (AD). However, the molecular identity of Aβ which causes synapse loss and impaired synaptic transmission is still largely undetermined. Currently, various post-translationally modified Aβ species have been identified in the brains of AD patients[107,254-255]. Among them, N-terminal truncated $A\beta_{4-42}$ is the most dominant isoform in the hippocampus and the cortex[110]. In addition, another abundant modified Aβ, phosphorylated serine residue 8 Aβ (pS8-Aβ) has been found to accelerate the formation of toxic Aβ aggregates[256]. Thus, studying these two Aβ isoforms is crucial and may provide guidance to the preventative and therapeutic approaches of AD.

Cu^{2+} is essential in neurotransmission regulation, however, it is also considered to play a key role in Aβ aggregation and reactive oxygen species (ROS) generation, as the concentration of Cu^{2+} in amyloid plaques is much higher than normal brain extracellular space[201]. The study of the interactions between Aβ and Cu^{2+} may give insight into the pathophysiology of AD. However, the existence of labile Cu^{2+} released in the synaptic cleft during neuronal excitation is transient, leading to the interaction process becoming

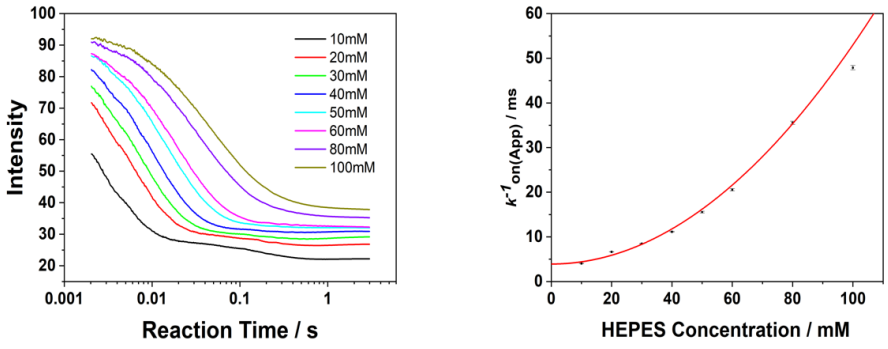
too rapid to be captured by thermodynamic methods alone. Taking advantage of the capability of rapid detection, kinetic methods are required for these studies. Previously, Branch *et al.* has already completed the study of the interactions between wild type Aβ ($A\beta_{16}$, $A\beta_{40}$) and Cu^{2+}, using an independently developed kinetic method[206]. They determined the equilibrium dissociation constant (K_d) values of Cu^{2+} binding to $A\beta_{16}$ and $A\beta_{40}$ (1.1(1) nM and 1.3(2) nM, respectively), and found the binding rate is fast enough to bind with Cu^{2+} in synaptic cleft. Also, a mechanistic model of the interactions has been proposed. Here, a similar kinetic method was employed to investigate the interactions between pS8-Aβ, N-truncated $A\beta_{4\text{-}16}$ and Cu^{2+}, respectively.

In this Chapter, the experiments are mainly performed using stopped flow kinetic technique. The quenching of a covalently attached fluorophore on Aβ by paramagnetic Cu^{2+} is utilised to record reaction progress. Using this method, the mechanistic schemes and essential kinetic parameters of the interactions between pS8-Aβ, N-truncated $A\beta_{4\text{-}16}$ and Cu^{2+} are determined. Furthermore, some essential redox kinetic parameters of $A\beta_{16}$-Cu complex are determined, and a preliminary investigation about the TDMQ impact of $A\beta_{16}$-Cu induced ROS generation was carried out.

3.1 Serine 8 Phosphorylated Aβ

3.1.1 Association Kinetics of Cu^{2+} Binding to pS8-Aβ

The kinetic studies of interactions between Cu^{2+} and pS8-Aβ was first performed. Determination of the association rate constant (k_{on}) is important for the understanding of Cu^{2+} binding with Aβ during neurotransmission. To measure k_{on} of Cu^{2+} binding with pS8-Aβ, 20 nM HiLyte Fluor 488 labelled pS8-Aβ was mixed with 400 nM $CuCl_2$ in HEPES-NaCl buffer. The traces were recorded as a function of time. However, HEPES has weak binding affinity with Cu^{2+}. Due to this, the amount of "free" Cu^{2+} that is able to bind to Aβ is lower than what is actually added during the Cu^{2+} binding reaction. Thus the HEPES effect should be taken into account. This effect can be eliminated by performing experiment under varying HEPES concentration condition. The results are shown in Fig. 3.1(A).



(A) Raw Traces (B) HEPES Dependence of $k_{on(App)}$

Figure 3.1 Kinetics of Cu^{2+} binding to pS8-Aβ. (A) Raw traces of pS8-Aβ binding with Cu^{2+} under various concentrations of HEPES. The experiments were performed in HEPES and 100 mM NaCl buffer solution at 298 K (pH 7.5). **(B)** HEPES dependence of $k_{on(App)}$. The HEPES independent k_{on} value is 6.4(4) × 10^8 M^{-1} s^{-1}. Error bars represent the uncertainty in the values determined from fits.

After measurement, the raw traces were fitted with multi-exponentials, and the fastest rate values of these traces were taken to be the apparent association rate ($k_{on(App)}$). To determine the HEPES independent reaction rate, the inverse apparent association rates ($k_{on(App)}^{-1}$) against HEPES concentration were empirically fitted with a parabola centred at zero:

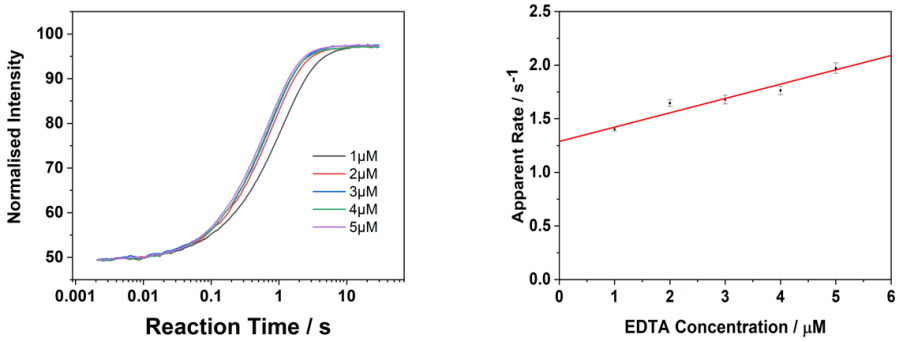
$$k^{-1}_{on(App)} = A[\text{HEPES}]^2 + C \qquad (3.1)$$

where A indicates the shape of parabola, and C is the intercept. The fitted curve is shown in Fig. 3.1(B). Extrapolating the inverse rates down to the intercept, the HEPES independent k_{on} could be determined to be 6.4(4) × 10^8 M^{-1} s^{-1}. This value is close to the value of 5.0(2) × 10^8 M^{-1} s^{-1} determined for the $A\beta_{16}$ peptide[206], suggesting that Ser8 phosphorylation has little effect on the Cu^{2+} binding rate of Aβ peptide.

3.1.2 Dissociation and Interconversion Kinetics of pS8-Aβ-Cu(II)

To determine the binding affinity of Cu^{2+} and pS8-Aβ by kinetic experiments, not only the association but also the dissociation rate constant (k_{off}) is required. In this measurement, 50 nM labelled pS8-Aβ was mixed in 1:1 stoichiometry with 50 nM $CuCl_2$ in HEPES buffer (50 mM HEPES, 100mM NaCl). Then this equilibrium mixture

of Aβ, Cu^{2+} and Aβ-Cu(II) complexes was treated with various low-micromolar concentrations of EDTA to remove unbound Cu^{2+} and Cu(II) from Aβ-Cu(II) complexes. The results are shown in Fig. 3.2(A). The traces were fitted with double-exponentials to obtain the apparent rates of different phases, and the mean rate was calculated as the apparent dissociation rate ($k_{off(App)}$). Extrapolating to zero EDTA concentration determined the value of $k_{off(App)}$ to be 1.29(5) s^{-1} (Fig. 3.2(B)). Thus K_d value of Cu^{2+} binding to pS8-Aβ was calculated to be 2.0(2) nM. In addition, the second-order rate constant for the dissociation with EDTA was determined from the slope to be 1.3(2) × 10^5 M^{-1} s^{-1}. This value is more than twice the value of 0.55(3) × 10^5 M^{-1} s^{-1} for the $Aβ_{16}$ peptide[206], suggesting that the Cu^{2+} bound on pS8-Aβ could be more easily attacked by a second ligand compared with the natural peptide. This could potentially result in more facile copper-bridged dimer formation.



(A) Normalised Traces (B) Apparent Dissociation Rates

Figure 3.2 Kinetics of Cu^{2+} dissociation from pS8-Aβ-Cu(II). (A) Normalised traces of Cu^{2+} dissociation from pS8-Aβ-Cu(II) under various concentrations of EDTA. The experiments were performed in 50 mM HEPES and 100 mM NaCl buffer solution at 298 K (pH 7.5). **(B)** Apparent dissociation rates of Cu^{2+} by EDTA from pS8-Aβ-Cu(II). The EDTA independent k_{off} value is 1.29(5) s^{-1}. Error bars represent the uncertainty in the values determined from fits.

Next, the interconversion kinetics of the two pS8-Aβ-Cu(II) coordination modes at physiological pH were investigated. As discussed in Chapter 1, previous research of Cu^{2+} binding to WT-Aβ suggests that there exist two interconverting coordination modes of Aβ-Cu(II) which differ in their protonation state at physiological pH under equilibrium, which are referred to as Component I (for the protonated species) and

Component II (for the deprotonated species)[206,257]. To determine the interconversion kinetics of pS8-Aβ-Cu(II), 50 nM labelled pS8-Aβ was mixed with 50 nM $CuCl_2$ to form 1:1 stoichiometry complex. Then this mixture was treated with a variable excess of EDTA. Such an experiment can separate different coordination modes of Aβ-Cu(II) on reaction traces based on their different reaction rates with EDTA. The raw traces are shown in Fig. 3.3. Two phases are clearly visible at higher EDTA concentrations where the reactions with EDTA are much faster than the interconversion, indicating that there are also two coordination modes for pS8-Aβ-Cu(II), which is quite similar to WT-Aβ-Cu(II). These traces can be well-fitted by the same model for the interactions between WT-Aβ and Cu^{2+} (Fig. 3.4(A))[206], suggesting that the interconversion mechanism of pS8-Aβ-Cu(II) is similar to that of WT-Aβ-Cu(II). Relative amplitudes and apparent rates derived from the fit, as well as fitted curves and error boundaries, are shown in Fig. 3.4(B) and Fig. 3.4(C). The derived kinetic parameters are summarised in Table 3.1, with values of WT-Aβ shown for comparison.

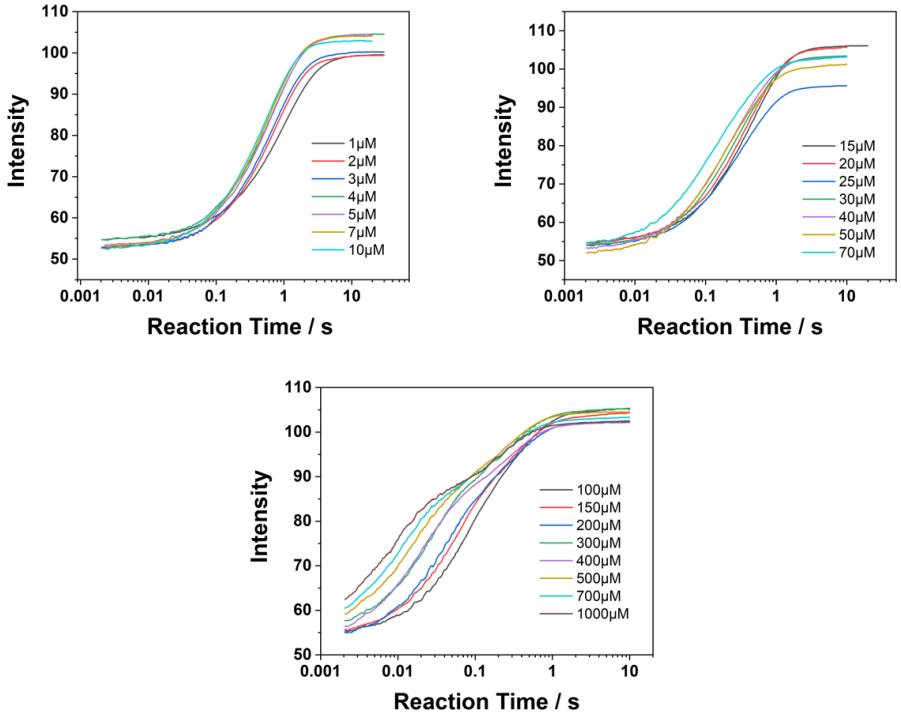
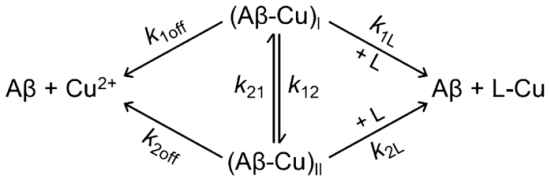
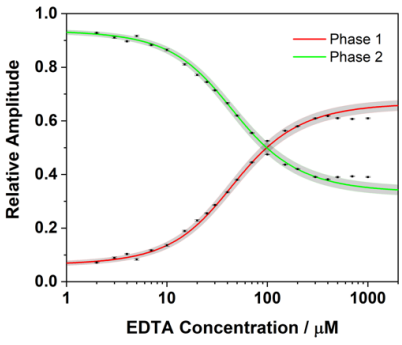


Figure 3.3 Raw traces of Cu^{2+} dissociation by a variable excess of EDTA. Two phases are clearly visible at higher EDTA concentrations. The experiments were performed in 50 mM HEPES and 100 mM NaCl buffer solution at 298 K (pH 7.5).

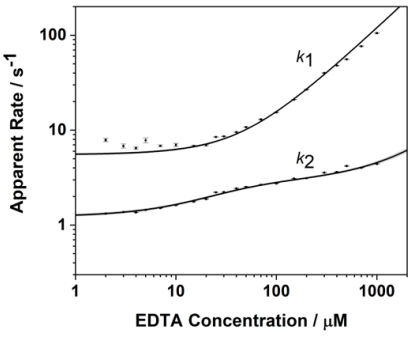
Compared with WT-Aβ$_{16}$, Ser8 phosphorylation does not appear to have much impact on the rate of Cu^{2+} binding. The little faster rate than WT-Aβ$_{16}$ could be attributed to the extra negative charge from the phosphate group enhancing the electrostatic attraction between the approaching Cu^{2+} and the peptide. By contrast, the rate of Cu^{2+} dissociation from Component I (k_{1off}) of pS8-Aβ is over two times faster than that of wild type Aβ peptide. This effect suggests that the Cu^{2+} binding to pS8-Aβ is weaker than that to WT-Aβ. Furthermore, the faster Cu^{2+} dissociation of pS8-Aβ indicates that the extra negative charge from phosphorylation is not a determinant for Cu^{2+} binding. For the interconversion between the two coordination modes, Ser8 phosphorylation could have an impact because the rate constants (k_{12} and k_{21}) occur ~50% faster than that of WT-Aβ$_{16}$. Apart from these, the rate constant of Component I and Cu^{2+} ligand reaction (k_{1L}) is almost the same with that of WT-Aβ, as well as H6R and D7N mutated Aβ$_{16}$[258]. In fact, the reaction of EDTA with Component I is of more interest as it is two orders of magnitude faster than that with Component II, and so the formation of copper-bridged ternary complex likely proceeds through Component I.



(A) Reaction Model



(B) Relative Amplitudes



(C) Apparent Rates

Figure 3.4 Kinetics of interconversion between the two components of pS8-Aβ-Cu(II). (A) Reaction model for data fitting. **(B)** Relative amplitudes and **(C)** Apparent rates for the two phases of pS8-Aβ-Cu(II) dissociation under various concentrations of EDTA.

Table 3.1 Kinetic parameters derived from the reaction of pS8-Aβ-Cu(II) complexes with EDTA. Data obtained from fits in Figure 3.4.

	pS8-Aβ	WT-Aβ$_{16}$[206]
k_{1off} / s^{-1}	2.25(6)	0.8(1)
k_{1L} / 10^5 M^{-1} s^{-1}	1.16(2)	1.3(1)
k_{12} / s^{-1}	1.48(9)	0.9(2)
k_{2off} / s^{-1}	-	-
k_{2L} / 10^3 M^{-1} s^{-1}	1.6(1)	1.48(6)
k_{21} / s^{-1}	3.01(6)	2.22(3)

At high EDTA concentrations, the bi-molecular reactions are much faster than the interconversion between the two forms of Aβ-Cu(II) complex. Under this condition, the curve of relative amplitudes in Fig. 3.4(B) indicates that the Component I is the dominant species under equilibrium (assuming that the dyes in the two coordination modes have the same brightness). The interconversion of two Aβ-Cu(II) coordination modes involves the switch of a proton as shown in Scheme 3.1.

$$(\text{A}\beta\text{-Cu})_{\text{I}} \underset{k_{21}}{\overset{k_{12}}{\rightleftharpoons}} (\text{A}\beta\text{-Cu})_{\text{II}} + \text{H}^+$$

Scheme 3.1 The switch of a proton between the two components

Thus, using the rate constants k_{12} and k_{21} derived from the fit, the pK_a value of pS8-Aβ-Cu(II) complexes could be determined by the Henderson–Hasselbalch equation:

$$\text{p}K_a = \text{pH} + \log_{10}(k_{21}/k_{12}) \tag{3.2}$$

and the pK_a value was determined to be 7.81(3).

In addition, as the dissociation rate constant of Component II is much slower than that of Component I and interconversion rate constants, it can be ignored. Thus the final mechanism scheme of Cu^{2+} binding to pS8-Aβ could be proposed in Scheme 3.2.

$$\text{A}\beta + \text{Cu}^{2+} \underset{k_{off}}{\overset{k_{on}}{\rightleftharpoons}} (\text{A}\beta\text{-Cu})_{\text{I}} \underset{k_{21}}{\overset{k_{12}}{\rightleftharpoons}} (\text{A}\beta\text{-Cu})_{\text{II}}$$

Scheme 3.2 Cu^{2+} binding mechanism of pS8-Aβ

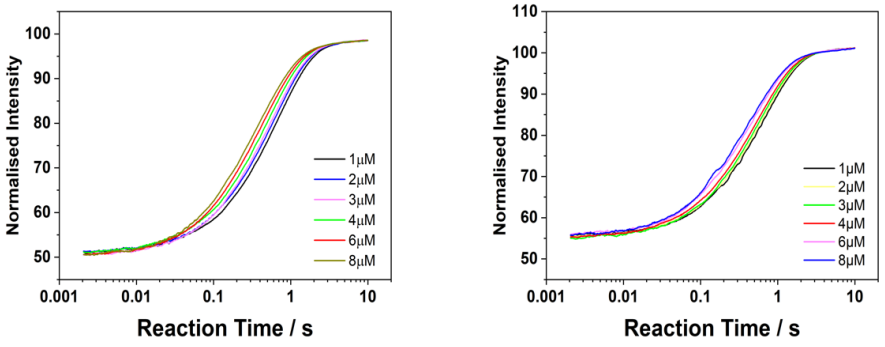
Based on the scheme, the apparent equilibrium association constant (K_a) of pS8-Aβ-Cu(II) could be determined by:

$$K_a = \frac{[(A\beta\text{-}Cu)_I] + [(A\beta\text{-}Cu)_{II}]}{[A\beta][Cu^{2+}]} = \frac{k_{on}}{k_{off}}\left(1 + \frac{k_{12}}{k_{21}}\right) \quad (3.3)$$

and as the inverse of K_a, the apparent equilibrium dissociation constant (K_d) was calculated to be 2.4(2) nM under this scheme.

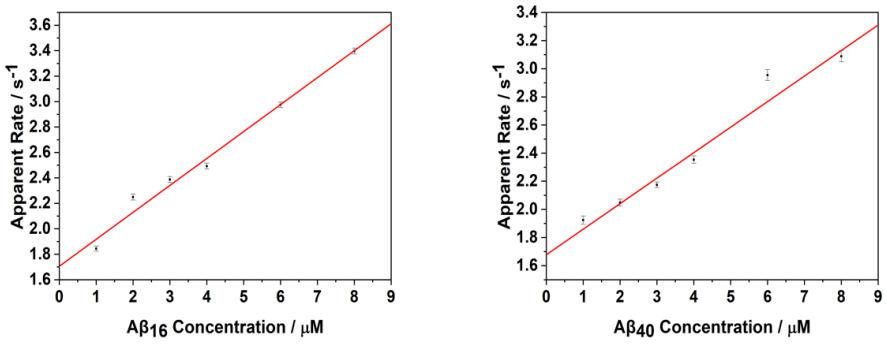
3.1.3 Dimerisation Kinetics of pS8-Aβ-Cu(II) with WT-Aβ

It is well acknowledged that Cu^{2+} could participate in Aβ aggregation. The previous studies have shown that Cu^{2+} could increase the dimerisation rate of Aβ more than two orders of magnitude higher than normal[206,259]. In addition, an atomic force spectroscopy study suggested that copper could act as a bridge between the two Aβ peptides, thus enhancing the stability of the peptide-peptide complex[260]. To assess the impact of Ser8 phosphorylation on the copper bridged dimerisation of Aβ, the formation rate constant of pS8-Aβ-Cu(II)-Aβ ternary complex was determined. 50 nM labelled pS8-Aβ was mixed with 50 nM $CuCl_2$ to pre-form pS8-Aβ-Cu(II) complex, then the mixture was treated with various concentrations of unlabelled $Aβ_{16}$ and unlabelled $Aβ_{40}$. Fluorescence recovery can be observed as the fluorophore in ternary complex is less quenched than that in binary complex. The normalised traces are shown in Fig. 3.5(A). The slopes of fitted data (Fig. 3.5(B)) were used to determine the rate constants, which were 2.1(1) × 10^5 M^{-1} s^{-1} and 1.8(2) × 10^5 M^{-1} s^{-1} for pS8-Aβ-Cu(II)-$Aβ_{16}$ and pS8-Aβ-Cu(II)-$Aβ_{40}$, respectively. Compared with the value of 1.22(8) × 10^5 M^{-1} s^{-1} for $Aβ_{16}$-Cu(II)-$Aβ_{40}$ formation[206], the value of pS8-Aβ-Cu(II)-Aβ complex is approximately 50% larger. The faster dimerisation rate observed for pS8-Aβ may account for the increased level of Aβ phosphorylation and aggregation found in AD brains.



Dimerisation with $A\beta_{16}$ Dimerisation with $A\beta_{40}$

(A) Normalised Traces



Dimerisation with $A\beta_{16}$ Dimerisation with $A\beta_{40}$

(B) Apparent Dimerisation Rates

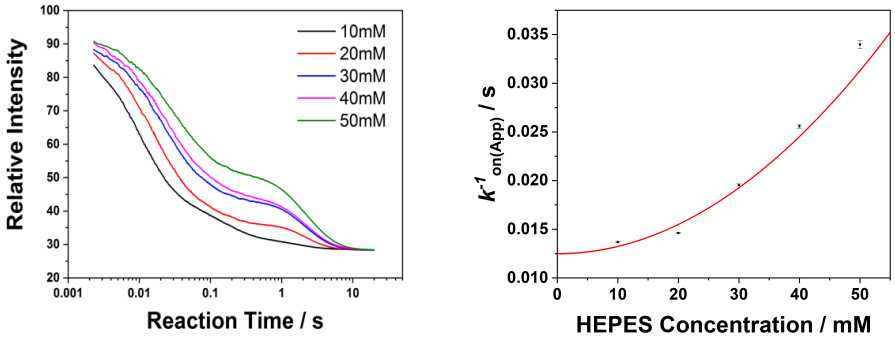
Figure 3.5 Kinetics of Cu^{2+} bridged dimerisation of pS8-Aβ with WT-Aβ. (A) Normalised traces of Cu^{2+} bridged dimerisation between pS8-Aβ and various concentrations of WT-Aβ. The experiments were performed in 50 mM HEPES and 100 mM NaCl buffer solution at 298 K (pH 7.5). **(B)** Apparent dimerisation rates of pS8-Aβ-Cu(II) with WT-Aβ. Error bars represent the uncertainty in the values determined from fits.

3.2 N-Terminal Truncated $A\beta_{4\text{-}16}$

3.2.1 Association Kinetics of Cu^{2+} Binding to $A\beta_{4\text{-}16}$

Having studied the kinetics of interactions between Cu^{2+} and pS8-Aβ, I next moved onto investigating Cu^{2+} interactions with the physiologically abundant N-truncated $A\beta_{4\text{-}16}$. The determination of the association rate constant (k_{on}) for Cu^{2+} binding to $A\beta_{4\text{-}16}$ is similar to that for pS8-Aβ. 20 nM labelled $A\beta_{4\text{-}16}$ was mixed with 400 nM $CuCl_2$ under various HEPES concentrations. The reaction traces are shown in

Fig. 3.6(A). The intercept of fitted data (Fig. 3.6(B)) was used to determine k_{on}, which is 2.0(1) × 10^8 M^{-1} s^{-1}, 2.5 times slower than the value of $A\beta_{16}$ peptide [206]. This could be attributed to $A\beta_{4-16}$ losing two negative charges, which makes the peptide more positive, thereby weakening the electrostatic attraction for Cu^{2+}.



(A) Raw Traces (B) HEPES Dependence of $k_{on(App)}$

Figure 3.6 Kinetics of Cu^{2+} binding to $A\beta_{4-16}$. (A) Raw traces of $A\beta_{4-16}$ binding with Cu^{2+} under various concentrations of HEPES. The experiments were performed in HEPES and 100 mM NaCl buffer solution at 298 K (pH 7.5). **(B)** HEPES dependence of $k_{on(App)}$. The HEPES independent k_{on} value is 2.0(1) × 10^8 M^{-1} s^{-1}. Error bars represent the uncertainty in the values determined from fits.

3.2.2 $A\beta_{4-16}$-Cu(II) Possesses High Cu^{2+} Binding Affinity

It is known that $A\beta_{4-x}$ contains the amino terminal copper and nickel (ATCUN) binding motif (structure is shown in Fig. 3.7), which enables a very tight binding with Cu^{2+}[261]. A previous study suggested that Cu^{2+} binding affinity of $A\beta_{4-x}$ is more than three orders of magnitude stronger than that of WT-Aβ, and Cu^{2+} transfer from $A\beta_{16}$-Cu(II) to $A\beta_{4-16}$ has been detected[113]. To prove and determine the high Cu^{2+} binding

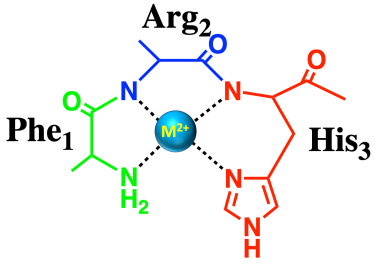
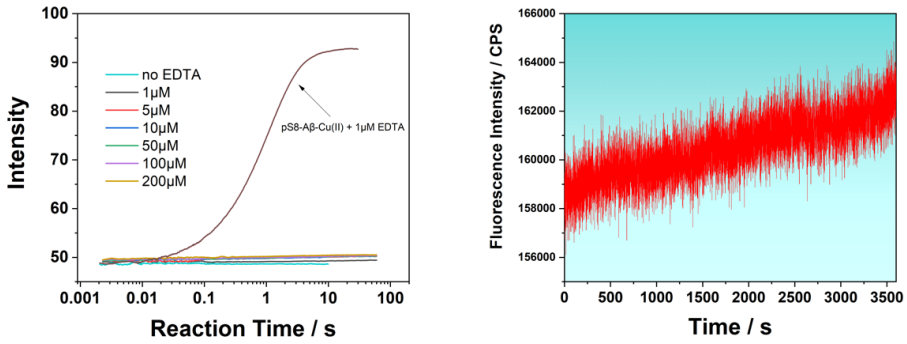


Figure 3.7 Structure of ATCUN binding motif. M represents Cu or Ni.

affinity of Aβ$_{4-16}$, 50 nM labelled Aβ$_{4-16}$ was mixed with 50 nM $CuCl_2$ to form Aβ$_{4-16}$-Cu(II) complex. Then this mixture was treated with a variable excess of EDTA (1 - 200 μM) in the stopped flow machine. The results are shown in Fig. 3.8(A). Fluorescence recoveries are quite small during this 1 minute run time, suggesting that the Cu^{2+} dissociation of Aβ$_{4-16}$-Cu(II) is too slow to be measured in this time range. Therefore, a long time recording experiment was performed using a fluorometer. The experiment was measured 1 h after mixing 50 nM Aβ$_{4-16}$-Cu(II) complex with 200 μM EDTA in fluorescence cuvette. The result is shown in Fig. 3.8(B). The fluorescence recovery is visible but still too small to be fitted. This could be because the concentration of EDTA was not high enough. However, compared with the Cu^{2+} dissociation experiments of pS8-Aβ-Cu(II) and WT-Aβ-Cu(II), the high Cu^{2+} binding affinity of Aβ$_{4-16}$ can be identified.



(A) Dissociation in Stopped Flow (B) Dissociation in Fluorometer

Figure 3.8 Raw kinetic traces of Cu^{2+} dissociation by EDTA from Aβ$_{4-16}$-Cu(II). (A) Measurement by stopped flow, with a comparison of Cu^{2+} dissociation from pS8-Aβ-Cu(II). **(B)** Measurement by fluorometer. Both fluorescence recoveries are too small to be fitted, suggesting that Cu^{2+} is hard to remove by EDTA from Aβ$_{4-16}$-Cu(II). The experiments were performed in 50 mM HEPES and 100 mM NaCl buffer solution at 298 K (pH 7.5).

The Cu^{2+} dissociation rate constant (k_{off}) of Aβ$_{4-16}$-Cu(II) was finally estimated by my collaborator Ewelina Stefaniak, which is ~5 × 10^{-5} s^{-1}. Using this value to do division with k_{on} proposed before, gives K_d of ~250 fM. This value is ~2 × 10^{-4} times for K_d of WT-Aβ, indicating that the Cu^{2+} binding affinity of Aβ$_{4-16}$ is ~5 × 10^3 times stronger than that of WT-Aβ, which is in agreement with the previous conclusion.

3.2.3 Mechanism of the Interactions between $A\beta_{4\text{-}16}$ and Cu^{2+}

As $A\beta_{4\text{-}16}$ binds to Cu^{2+} via its ATCUN motif, the Cu^{2+} binding mechanism could be different from that of pS8-Aβ and WT-Aβ. The difference of Cu^{2+} binding traces and K_d values between these Aβ isoforms can also provide some evidence. On Cu^{2+} binding traces of $A\beta_{4\text{-}16}$, I observed two obvious steps of fluorescence quenching, which is different from pS8-Aβ and WT-Aβ. I assumed that the quenching could be attributed to two Cu^{2+} binding steps caused by the excess Cu^{2+}, i.e., two Cu^{2+} ions are involved in the binding reaction and each Cu^{2+} binding corresponds to a quenching step. To explore this, 1 μM labelled $A\beta_{4\text{-}16}$ was mixed with 1 μM $CuCl_2$, the 1:1 mixing ratio should avoid the second Cu^{2+} binding. Compared with the previous binding trace under excess Cu^{2+}, two steps of fluorescence quenching can still be clearly observed (Fig. 3.9). This result suggests that the two-step quenching of Cu^{2+} binding to $A\beta_{4\text{-}16}$ cannot be described as the involvement of two Cu^{2+} ions.

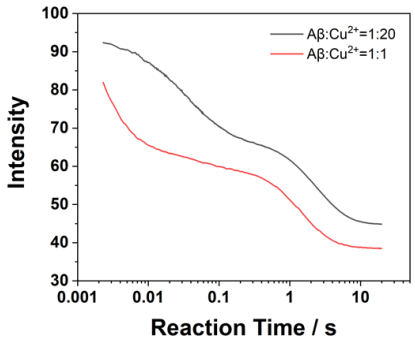


Figure 3.9 Comparison of raw Cu^{2+} binding traces between 1:20 and 1:1 $A\beta_{4\text{-}16}$, Cu^{2+} mixing ratio. Two steps of fluorescence quenching can still be clearly observed at 1:1 $A\beta_{4\text{-}16}$, Cu^{2+} mixing ratio, suggesting that the two-step quenching is not due to the excess Cu^{2+}. The experiments were performed in 50 mM HEPES and 100 mM NaCl buffer solution at 298 K (pH 7.5).

To gain a glimpse of the possible reaction mechanism of Cu^{2+} binding to $A\beta_{4\text{-}16}$, the binding experiments at 1:1 mixing ratio of labelled $A\beta_{4\text{-}16}$ to Cu^{2+} at increasing concentrations (0.5 - 2.5 μM) were performed. The raw traces are shown in Fig. 3.10. At higher concentrations (≥ 2 μM), the reaction process is displayed in more detail due to the relatively fast reaction rate, and three steps can be observed, rather than two steps mentioned above. By determining the rate constants *k*' of the second decrease at ~2 s,

I noticed that the reaction process is becoming concentration independent after ~2 s (results from the fit are summarised in Table 3.2). Thus I infer that there exists an intramolecular process following the initial Cu^{2+} binding.

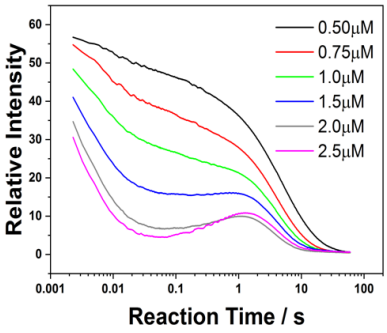


Figure 3.10 Raw traces of Cu^{2+} binding measurements with a series of 1:1 concentration ratio of $A\beta_{4-16}$ and Cu^{2+}. Raw traces showing the evidence of intermediate species formation. The experiments were performed in 50 mM HEPES and 100 mM NaCl buffer solution at 298 K (pH 7.5).

Table 3.2 Rate constants of Cu^{2+} binding to $A\beta_{4-16}$ at ~2 s. Data obtained from fits in Figure 3.10.

[Aβ], [Cu^{2+}] / μM	0.50	0.75	1.0	1.5	2.0	2.5
k' / 10^{-1} s^{-1}	3.23(1)	2.38(2)	2.08(2)	2.63(1)	2.82(2)	2.96(1)

Next, a double mixing stopped flow technique was employed to further explore the potential intermediate complexes formation after initial Cu^{2+} binding. In such experiments, 2 μM labelled $A\beta_{4-16}$ and 2 μM $CuCl_2$ were mixed in an age loop and after various delay times, an excess of EDTA was added to "freeze" the reaction, i.e., to stop the processing interconversion immediately and chelate Cu^{2+} from intermediates (Fig. 3.11). Taking advantage of the disparities in reactivity of different $A\beta_{4-16}$-Cu(II) species with EDTA, the time evolution of individual species population could be resolved and analysed, enabling us to depict details of the binding process. As shown in Fig. 3.11, the amplitude of fluorescence recovery strongly depends on the delay time. The recovery starts to become very small after 1.98 s, indicating that a much more inert (less reactive towards EDTA) complex is formed after ~2 s of initial Cu^{2+} binding. I equate

this complex, $(A\beta\text{-}Cu)_D$, to the final stable ATCUN-type $A\beta_{4\text{-}16}$-Cu(II) complex. Furthermore, because the reaction rate is concentration independent after ~2 s as mentioned above, I infer that a peptide conformational rearrangement process leading to this final complex must occur at ~2 s.

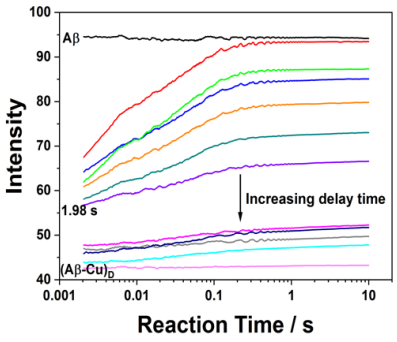
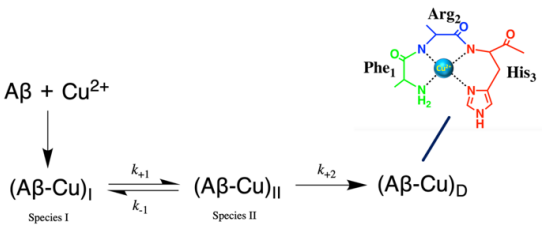
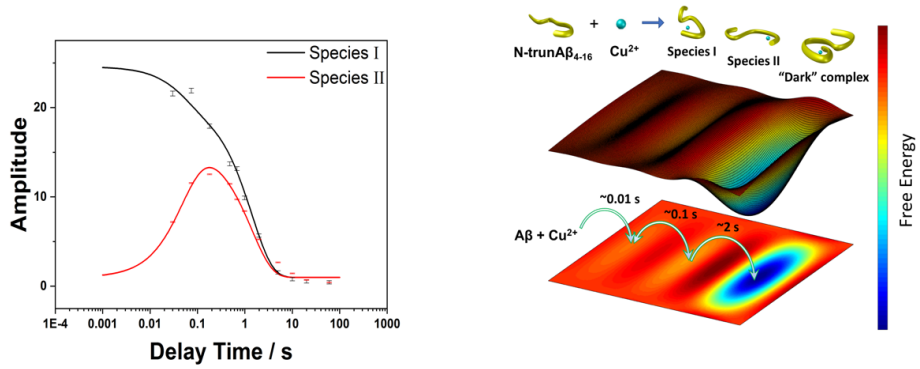


Figure 3.11 Kinetics of $A\beta_{4\text{-}16}/Cu^{2+}$ interactions measured by double mixing stopped flow. Raw traces showing the change in amplitude as the delay time between the mixing of an equal concentration of Cu^{2+} and $A\beta_{4\text{-}16}$ (2 mM) and the addition of EDTA is increased from 50 ms to 1 min. The experiments were performed in 50 mM HEPES and 100 mM NaCl buffer solution at 298 K (pH 7.5).

In order to describe the whole reaction process of Cu^{2+} binding to $A\beta_{4\text{-}16}$, I proposed a mechanistic scheme as shown in Fig. 3.12(A). To validate it, the individual amplitudes of two phases in Fig. 3.11 were determined by double-exponentials global fitting with sharing the rates, and then further fitted by the scheme using KinTek software (Fig. 3.12(B)). The amplitudes indicate the amounts of the two intermediates, Species I and Species II, at different reaction process stages, and could be fitted well by the proposed mechanistic scheme, with the fitted rate constants as listed in Table 3.3. Finally, to represent the mechanism graphicly, a corresponding free energy landscape illustration of Cu^{2+} binding to $A\beta_{4\text{-}16}$ is shown in Fig. 3.12(C).



(A) Mechanistic Scheme



(B) Individual Amplitudes Fitting (C) Free Energy Landscape

Figure 3.12 Cu^{2+} binding mechanism of $A\beta_{4\text{-}16}$. (A) Reaction mechanism of Cu^{2+} binding to $A\beta_{4\text{-}16}$ and formation of the high affinity $A\beta_{4\text{-}16}$-Cu(II) complex, $(A\beta\text{-}Cu)_D$ (Cu^{2+} binding site shown above). **(B)** Fitting of the individual amplitudes at different Cu^{2+} binding process stages of the two phases by the proposed reaction mechanism. **(C)** Proposed free energy landscape of Cu^{2+} binding to $A\beta_{4\text{-}16}$. ‘‘Dark’’ complex refers to the very stable ATCUN-type $A\beta_{4\text{-}16}$-Cu(II) complex.

Table 3.3 Kinetic parameters of Cu^{2+} binding to $A\beta_{4\text{-}16}$ derived by fitting with proposed mechanistic scheme. Data obtained from fits in Figure 3.12.

	k_{+1}	k_{-1}	k_{+2}
k value / s^{-1}	4.10(1)	10.34(2)	3.31(4)

The abundance of $A\beta_{4\text{-}x}$ in healthy human brain[110], the redox-inert property of $A\beta_{4\text{-}x}$-Cu(II) complex[113], and the high Cu^{2+} binding affinity give rise to an opinion that $A\beta_{4\text{-}x}$ may have a physiological role, such as a Cu^{2+} scavenger in synapses, rather than just a culprit of AD. However, it is not clear how this final stable complex relays copper to maintain the copper cycling. Here it has been found that the lifetimes of Species I and Species II complexes are comparable to the intervals between pulses of neurotransmitter release in glutamatergic neuronal pathways[262]. This suggests that Species I and in particular the longer-lived Species II complex which enable to release copper, could be the actual roles to move copper around during neurotransmission.

3.2.4 Switching Activation Energy of the Final Aβ$_{4\text{-}16}$-Cu(II) Complex

The switching activation energy of (Aβ-Cu)$_D$ was subsequently determined. To measure this, the double mixing experiment performed above was conducted at various temperatures. The switching rate constant (k_{+2}) of (Aβ-Cu)$_D$ can be then determined by fitting the individual amplitudes of two intermediates.

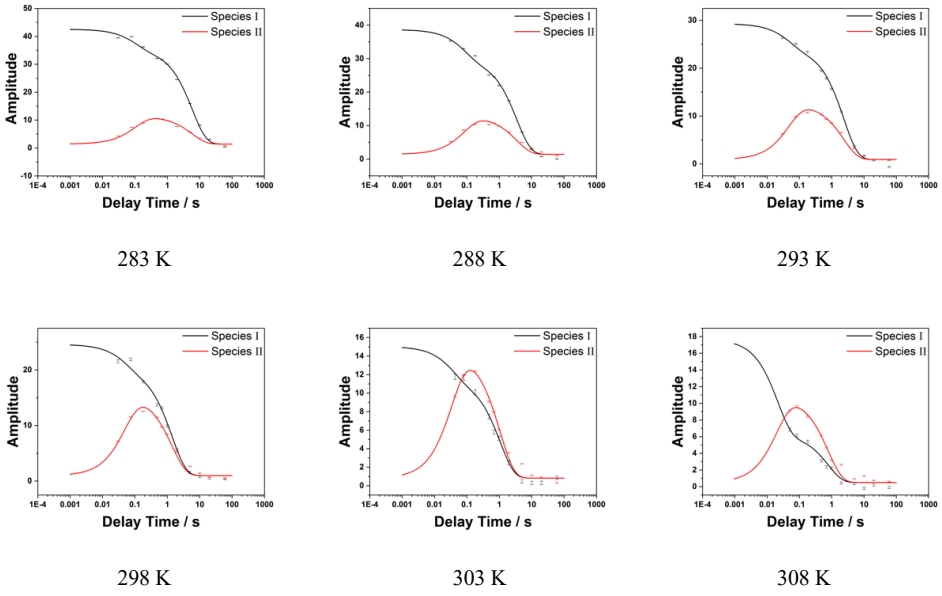


Figure 3.13 Evolutions of the two intermediate species at various temperatures. Fitted curves showing temperature dependence of the evolutions. Error bars represent the uncertainty in the values determined from fits.

By measuring k_{+2} at various temperatures (Fig. 3.13), the switching activation energy of (Aβ-Cu)$_D$, E_a, can be calculated by the Arrhenius equation:

$$k_{+2} = Ae^{-E_a/(RT)} \tag{3.4}$$

this equation can be rearranged to give a linear fit for E_a as:

$$\ln k_{+2} = \ln A - E_a/(RT) \tag{3.5}$$

where k_{+2} is the switching rate constant, R is the universal gas constant, T is the absolute temperature (in kelvins) and A is the pre-exponential factor. The switching activation energy of (Aβ-Cu)$_D$ was calculated to be 64(3) kJ mol^{-1} (Fig. 3.14).

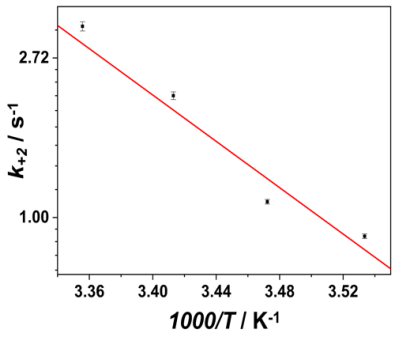


Figure 3.14 Arrhenius plot for the switching rate constant k_{+2}. The determined switching activation energy is 64(3) kJ mol^{-1}. Error bars represent the uncertainty in the values determined from fits.

3.2.5 Histidine Impact of Cu^{2+} Binding to $A\beta_{4-16}$

Histidine is one of the essential amino acids in human body. The imidazole moiety of histidine commonly serves as a ligand, no matter in metalloproteins or in free CSF. Previous research indicated that histidine can form a Cu^{2+} bridged ternary complex with HSA which also contains ATCUN motif[263]. Thus I supposed that histidine may also have effect on Cu^{2+} binding to $A\beta_{4-16}$. A preliminary study was carried out to explore this.

Histidine Delays the Cu^{2+} Binding Reaction

A Cu^{2+} binding experiment was performed firstly. 20 nM labelled $A\beta_{4-16}$ was pre-mixed with various concentrations of histidine, then the mixture was treated with 400 nM $CuCl_2$. The traces are shown in Fig. 3.15. I noticed that the reaction time is prolonged, and is dependent on histidine concentration. This indicates that histidine can affect Cu^{2+} binding to $A\beta_{4-16}$. In addition, fluorescence recovery at ~0.1 s was observed, indicating that there exists an intermediate which could be $A\beta_{4-16}$-Cu(II)-His ternary complex, as the fluorophore in ternary complex is less quenched. However, it is hard to see this recovery process when the histidine concentration is 5 μM, which is possibly due to the negligible initial Cu^{2+} binding by $A\beta_{4-16}$.

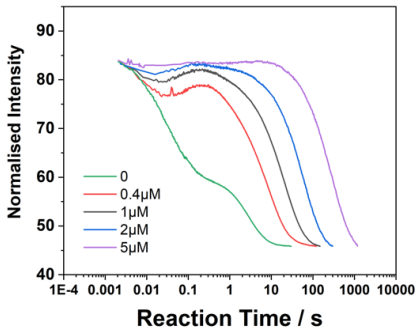
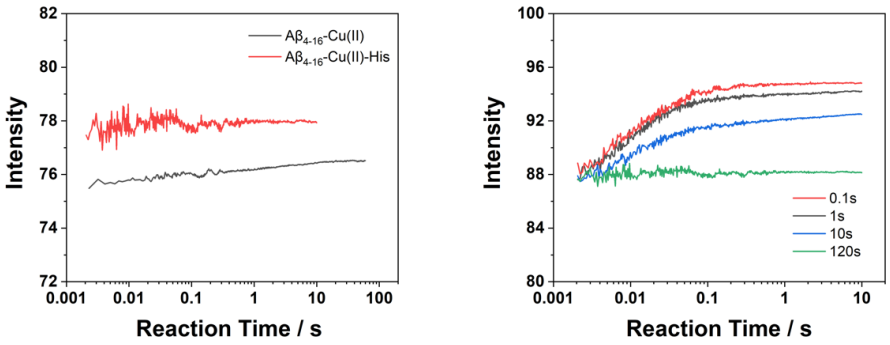


Figure 3.15 Kinetics of Cu^{2+} binding to $A\beta_{4-16}$ under various concentrations of histidine. Raw traces showing the delay of Cu^{2+} binding process by histidine, and the evidence of intermediates formation. The experiments were performed in HEPES and 100 mM NaCl buffer solution at 298 K (pH 7.5).

Final Complex Possesses High Cu^{2+} Binding Affinity

Next, a Cu^{2+} dissociation experiment was performed to assess Cu^{2+} binding affinity of the final coordination complex. 20 nM labelled $A\beta_{4-16}$ was pre-mixed with 1 μM histidine, and then mixed with 400 nM $CuCl_2$. After 2 min for completing reaction, this mixture was treated with an excess of EDTA (200 μM). The fluorescence recovery is as small as that of Cu^{2+} dissociation of pure $A\beta_{4-16}$ (Fig. 3.16(A)), suggesting that the



(A) Dissociation by EDTA (B) Dissociation at Different Binding Stages

Figure 3.16 Kinetics of Cu^{2+} dissociation from $A\beta_{4-16}$-Cu(II)-His. (A) Fluorescence recovery of Cu^{2+} dissociation. The recovery is as small as that of $A\beta_{4-16}$-Cu(II), suggesting that the Cu^{2+} binding affinity of the ternary complex is high. **(B)** Double mixing traces showing the change in amplitude under various delay times between the mixing of $A\beta_{4-16}$, histidine with Cu^{2+} and the addition of excess EDTA. The experiments were performed in 50 mM HEPES and 100 mM NaCl buffer solution at 298 K (pH 7.5).

Cu^{2+} binding affinity of the final complex is still high. To explore more details about the complex formation process, another double mixing experiment was performed. 20 nM labelled $A\beta_{4-16}$ was pre-mixed with 1 μM histidine, then treated with 400 nM $CuCl_2$, and after various delay times, excess EDTA was added to quench the reaction. Fig. 3.16(B) shows such double mixing traces. The fluorescence recovery is dependent on the delay time as well, indicating that Cu^{2+} affinity of the intermediate is strengthened gradually, and the intermediate eventually transforms to a stable complex. This Cu^{2+} binding process is similar to that of $A\beta_{4-16}$ alone but relatively slow.

Finally, I give a concluding hypothesis on the histidine effect on Cu^{2+} binding to $A\beta_{4-16}$. When $A\beta_{4-16}$ co-exists with histidine, it would still be able to bind to Cu^{2+}. Histidine is also involved in and binds to $A\beta_{4-16}$-Cu(II) to form $A\beta_{4-16}$-Cu(II)-His ternary complex. Then this complex could undergo rearrangement, which is relatively slow due to histidine involvement. At the end of the process, the final stable complex is formed. It is necessary to perform more experiments to further validate this hypothesis. Considering the possible role of physiological copper transporter for $A\beta_{4-16}$, histidine could be an important modulator in copper transit. This work is significant and could help to boost our understanding of $A\beta_{4-16}$ physiological function.

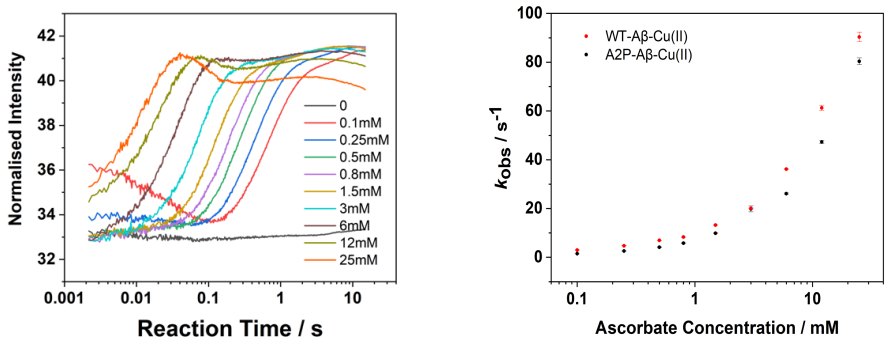
3.3 Redox Studies of $A\beta_{16}$-Cu Complex

3.3.1 Redox Kinetics of $A\beta_{16}$-Cu Complex

The generation of reactive oxygen species (ROS) is regarded as one of the key events of the pathogenesis of AD. The ROS generation ability of Aβ binding to redox active metal, such as copper, has been well accepted as contributing to the progression of AD. It has been suggested that ROS is generated during the redox cycling of Aβ-metal complex[201]. For such a short-lived process, kinetic analysis would be the ideal approach to gain insight into the mechanism.

A study about redox kinetics of $A\beta_{16}$-Cu complex has been reported by our group[264]. What I did in this study was the control experiment of Component I reduction, and the oxidation rate constant determination of $A\beta_{16}$-Cu(I). Before I conducted my

part of the experiment, we had found that the reduction of $A\beta_{16}$-Cu(II) complex by ascorbate has two phases. We assumed that the fast phase corresponds to Component I and the slow one corresponds to Component II, as Components I and II of $A\beta_{16}$ co-exist at the experimental pH of 7.5. To validate our assumption, control experiments, when either Component I or Component II predominated, were required. For the slow phase, murine Aβ had been applied as the control. While an A2P mutated $A\beta_{16}$ was introduced for the fast phase. The reason why we chose A2P-Aβ is because the pK_a of the interconversion between Components I and II for A2P-Aβ is 8.8[265], indicating that the equilibrium between Components I and II for A2P-Aβ will be almost exclusively Component I at experimental pH of 7.5. In such a control experiment, 50 nM FITC labelled A2P-Aβ was mixed with 50 nM $CuCl_2$ to pre-form A2P-Aβ-Cu(II) complex, and then the complex was treated with various concentrations of sodium ascorbate. As the reduced Cu(I) gains an electron and becomes diamagnetic, fluorescence quenched by Cu(II) would be recovered. The results are shown in Fig. 3.17(A). The quenching at higher concentrations of ascorbate could be due to the collisional quenching effect, and has negligible impact on the transient reducing process. The raw curves were fitted by double-exponentials to obtain the apparent rate values. As expected, the rate of A2P-Aβ-Cu(II) matches the fast phase of $A\beta_{16}$-Cu(II) (Fig. 3.17(B)). Further combined with the result from the slow phase, we confirmed that the reduction step of redox cycling and final ROS generation of $A\beta_{16}$-Cu(II) complex proceed via Component I[264].



(A) Normalised Traces (B) Apparent Reduction Rates

Figure 3.17 Reduction kinetics of A2P-Aβ-Cu(II) by ascorbate. (A) Normalised traces of A2P-Aβ-Cu(II) complex reduction under various concentrations of ascorbate. The experiments were

performed in 50 mM HEPES and 100 mM NaCl buffer solution at 298 K (pH 7.5). **(B)** Comparison of the apparent reduction rates between the fast phase of WT-Aβ-Cu(II) and A2P-Aβ-Cu(II) showing similarity. Error bars represent the uncertainty in the values determined from fits.

Oxidation process is as important as reduction for the understanding of the redox cycling of $A\beta_{16}$-Cu(II) complex. However, the experiments could be much less tractable due to the instability of Cu(I) salts. To circumvent this, a double mixing approach was employed. Taking advantage of the short delay time between mixings, the reduced $A\beta_{16}$-Cu(I) would remain before mixing with oxidising agent. 50 nM HiLyte Fluor 488 labelled $A\beta_{16}$ was pre-mixed with 50 nM $CuCl_2$ to form $A\beta_{16}$-Cu(II) complex, then the complex was reduced by adding 50 μM sodium ascorbate. After a short delay, the mixture was oxidised back by adding various concentrations of hydrogen peroxide. There is a problem with this approach, which is that after the final mixing step, ascorbate and hydrogen peroxide will both be present. This causes the occurrence of both oxidation and reduction of $A\beta_{16}$-Cu during the reaction process. However, at the very start of oxidation, there should be no $A\beta_{16}$-Cu(II) and so reduction would not occur. Thus, the rate of absolute oxidation can be approximately extracted by taking the slope of a line tangent to the initial portion of reaction curves. To confirm whether ascorbate could affect the initial oxidation process, such experiment was conducted again with 100 μM sodium ascorbate for comparison. Fig. 3.18 shows how the initial oxidation rate of $A\beta_{16}$-Cu(I) changes with H_2O_2 concentration. The linear relationship between the rate of oxidation and H_2O_2 concentrations indicates that the oxidation is a bi-molecular association process. The oxidation rate constants of two experiments were determined from slopes, which were $4.4(2) \times 10^2$ M^{-1} s^{-1} for 50 μM ascorbate and $4.3(2) \times 10^2$ M^{-1} s^{-1} for 100 μM ascorbate, respectively. Such close values of two very different ascorbate concentrations suggests that the initial rate of oxidation is independent of ascorbate concentration, which confirms that ascorbate does not participate in the oxidation process initially and the extracted initial rate is the absolute oxidation rate.

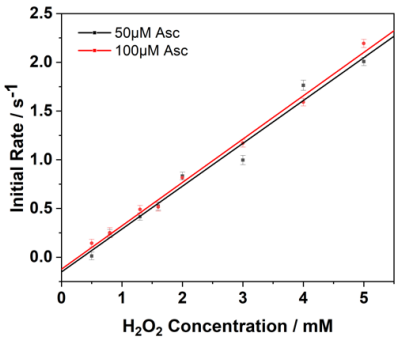


Figure 3.18 Initial rate of Aβ16-Cu(I) oxidation against H_2O_2 concentration. The linear fits suggest that the initial oxidation rate of Aβ16-Cu(I) is concentration independent of the ascorbate used to prepare the Aβ16-Cu(I). Error bars represent the uncertainty in the values determined from fits.

Finally, an oxidative stability test of the fluorophore was carried out. In order to ensure the fluorescence quenching was not due to oxidative damage of the HiLyte Fluor 488 by hydrogen peroxide, 50 nM HiLyte Fluor 488 labelled Aβ16 was mixed with various concentrations (≥ what were used in this study) of hydrogen peroxide. The results are shown in Fig. 3.19. It can be seen that even under vastly excess H_2O_2 concentrations and recording times, fluorescence decrease due to oxidation of the fluorophore is negligible, suggesting that the effect of H_2O_2 on HiLyte Fluor 488 is insignificant.

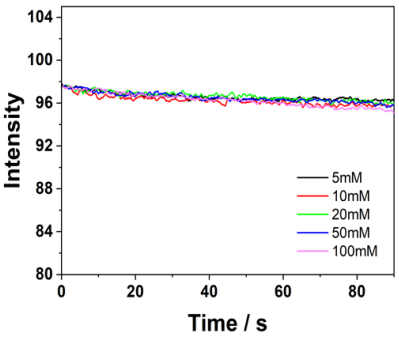


Figure 3.19 Oxidative stability test of HiLyte Fluor 488 fluorophore. Raw traces showing the negligible fluorescence change after mixing labelled Aβ16 with various concentrations of H_2O_2. The experiments were performed in 50 mM HEPES and 100 mM NaCl buffer solution at 298 K (pH 7.5).

3.3.2 Interactions between Aβ16-Cu and TDMQ

This part of research was performed collaboratively by Iok Ian Kong and me.

N4-tetradentate monoquinoline (TDMQ) is a designed neutral copper ligands series which acts as copper chelators to inhibit copper induced oxidative stress. The advantages of more specific chelation with copper and no effect on catalytic activities of the enzymes in redox regulation such as Cu-Zn superoxide dismutase and tyrosinase make TDMQ an ideal drug candidate for AD[266-267]. In this preliminary study, TDMQ 20, TDMQ 22 and TDMQ 37 were selected to study (structures shown in Fig. 3.20). The properties of inhibiting Aβ16-Cu induced oxidation and copper transfer of these three ligands were assessed.

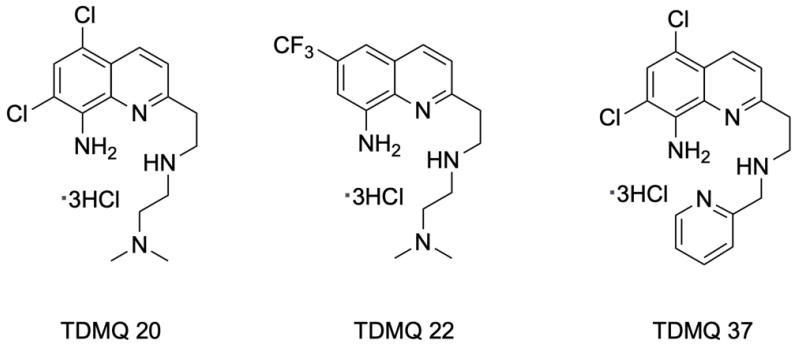
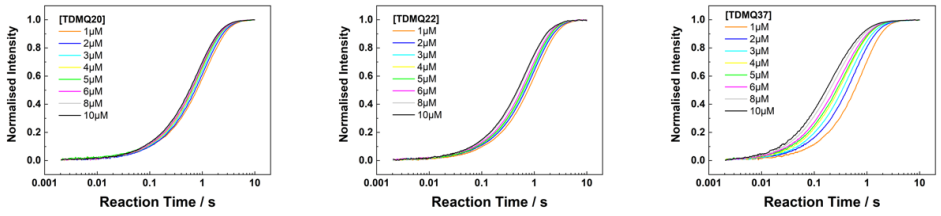


Figure 3.20 Structures of TDMQ 20, TDMQ 22 and TDMQ 37.

Dissociation Kinetics of Aβ16-Cu(II) by TDMQ

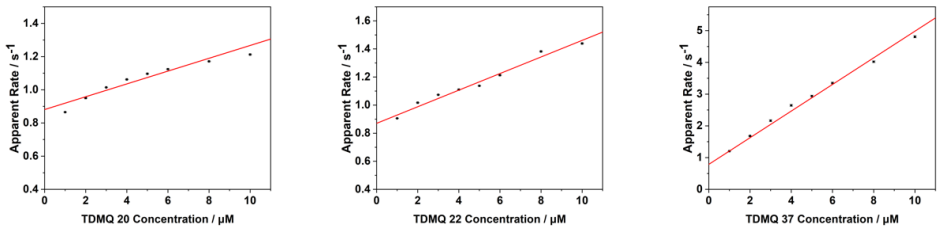
We first investigated the dissociation kinetics of Aβ16-Cu(II) by TDMQ. 50 nM labelled Aβ16 was mixed with 50 nM $CuCl_2$, then the mixture was treated with various concentrations of TDMQ 20, TDMQ 22 or TDMQ 37. The traces are shown in Fig. 3.21(A). By fitting the curves with double-exponentials, the apparent dissociation rates can be determined. These values were used to determine the second-order dissociation rate constants for Aβ16-Cu(II) with TDMQ (Fig. 3.21(B)). The determined dissociation kinetic parameters are listed in Table 3.4, with values of dissociation by EDTA shown for comparison. We noticed that the second-order rate constants for Aβ16-Cu(II) dissociation by TDMQ 20 and TDMQ 22 are close to the values of dissociation with

EDTA, while the rate constant for TDMQ 37 is much higher, suggesting that the copper chelating ability of TDMQ is similar to or even higher than that of EDTA.



TDMQ 20 TDMQ 22 TDMQ 37

(A) Normalised Traces



TDMQ 20 TDMQ 22 TDMQ 37

(B) Apparent Dissociation Rates

Figure 3.21 Kinetics of Cu^{2+} dissociation by different TDMQ ligands from $A\beta_{16}$-Cu(II). (A) Normalised traces of Cu^{2+} dissociation from $A\beta_{16}$-Cu(II) under various concentrations of different TDMQ ligands. The experiments were performed in 50 mM HEPES and 100 mM NaCl buffer solution at 298 K (pH 7.5). **(B)** Apparent dissociation rates of Cu^{2+} by different TDMQ ligands from $A\beta_{16}$-Cu(II). Error bars represent the uncertainty in the values determined from fits.

Table 3.4 Kinetic parameters of Cu^{2+} dissociation derived from the reaction of $A\beta_{16}$-Cu(II) with different TDMQ ligands. Data obtained from fits in Figure 3.21.

	$k_{off(App)}$ / s^{-1}	Second-order k / 10^5 M^{-1} s^{-1}
TDMQ 20	0.88(2)	0.39(5)
TDMQ 22	0.87(2)	0.59(4)
TDMQ 37	0.79(1)	4.2(1)
EDTA[206]	0.8(1)	0.55(3)

TDMQ Inhibits the Oxidation Activity Induced by $A\beta_{16}$-Cu

As reported, TDMQ 20 exhibits an enhanced reducing ability to the oxidative stress induced by $A\beta_{16}$-Cu[266]. In order to understand this ability of other TDMQ ligands, the oxidation activity of $A\beta_{16}$-Cu in the presence of various TDMQ was measured. The measurements were performed using an indirect method that is monitoring the ascorbate oxidation level under $A\beta_{16}$-Cu with various TDMQ. An UV-Vis technique was employed to measure this level, as the absorbance of ascorbate will be changed by oxidation, reflecting the oxidation activity induced by $A\beta_{16}$-Cu under different conditions. In this experiment, 11 μM unlabelled $A\beta_{16}$ was mixed with 10 μM $CuCl_2$, a little excess of Aβ can ensure that there is no free Cu^{2+} to affect ascorbate. After incubating 15 min at room temperature, 11 μM TDMQ was added and mixed. Then the mixture was incubated for another 15 min. Afterwards, this mixture was added in a quartz cuvette containing excess sodium ascorbate solution (100 μM). The maximum absorbance of ascorbate at 265 nm was recorded immediately and continuously for 30 min. The measurements without ascorbate were also carried out under the same conditions as controls, and the results were subtracted from those of measurements with ascorbate. From the final results as shown in Fig. 3.22, it can be seen that ascorbate was fully oxidised by $CuCl_2$ in ~14 min. The oxidation activity of $A\beta_{16}$-Cu(II) is a little lower than free Cu^{2+} but still strong. While in the presence of

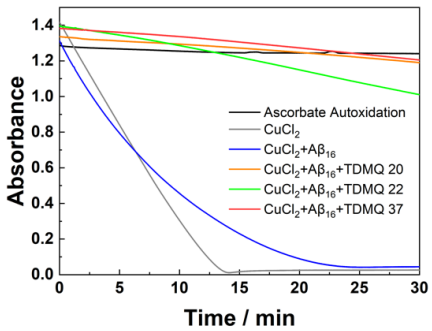


Figure 3.22 UV-Vis (265 nm) kinetic traces of ascorbate oxidation. Raw traces showing much small changes under addition of TDMQ, suggesting that TDMQ can inhibit the oxidation activity. The experiments were performed in 50 mM HEPES and 100 mM NaCl buffer solution at 298 K (pH 7.5).

Table 3.5 Ascorbate oxidation rates by $A\beta_{16}$-Cu(II) in the presence of different TDMQ ligands. Data obtained from fits in Figure 3.22.

	Ascorbate oxidation rate / 10^3 min^{-1}
Ascorbate Autoxidation	1.223(4)
$CuCl_2$	112.99(2)
$CuCl_2$ + $A\beta_{16}$	84.0(1)
$CuCl_2$ + $A\beta_{16}$ + TDMQ 20	4.664(3)
$CuCl_2$ + $A\beta_{16}$ + TDMQ 22	13.185(5)
$CuCl_2$ + $A\beta_{16}$ + TDMQ 37	6.024(4)

TDMQ and $A\beta_{16}$-Cu, copper can hardly oxidise ascorbate, as only 10.9%, 27.7% and 12.8% of ascorbate were oxidised in 30 min for TDMQ 20, TDMQ 22 and TDMQ 37, respectively. TDMQ 20 seems to possess the best inhibition. In addition, the ascorbate oxidation rates under various conditions can be determined by linear fit of the raw data. The values are summarised in Table 3.5 and also indicate that TDMQ can efficiently inhibit $A\beta_{16}$-Cu caused oxidation for ascorbate. This could be attributed to the structural feature of TDMQ, which can stabilise Cu(II) over Cu(I).

Efficiency Comparison of Copper Transfer from Various TDMQ to GSH

Glutathione (GSH) is one of the master antioxidants in the human body. It has been reported that GSH plays an essential role for the detoxification of ROS in brain cells[268]. In addition, GSH has a high affinity with Cu(I). The reduced Cu(I) can be captured and bound by GSH to form GSH-Cu(I) complex, and this GSH-Cu(I) complex is known as a physiological copper supplier to copper-proteins[269-271]. Consequently, GSH is pivotal in copper metabolism and could act as both Cu(II) reducing agent and copper transporter to mediate the physiological copper homeostasis[272].

To assess the capability of copper transfer from TDMQ-Cu(II) to GSH, another UV-Vis experiment was designed and performed. We first determined the maximum absorbance wavelengths of TDMQ and TDMQ-Cu(II) complexes. Fig. 3.23 shows the results. Both TDMQ 20 and TDMQ 37 show the maximum absorbance at 258 nm,

while TDMQ 22 shows at 252 nm. For TDMQ-Cu(II) complexes, the wavelengths were 243 nm, 236 nm and 242 nm for TDMQ 20-Cu(II), TDMQ 22-Cu(II) and TDMQ 37-Cu(II), respectively. All absorbance peaks of TDMQ-Cu(II) complexes are well-separated from those of corresponding TDMQ ligands. Thus by monitoring the generation of TDMQ ligands at their maximum absorbance wavelengths, the capability

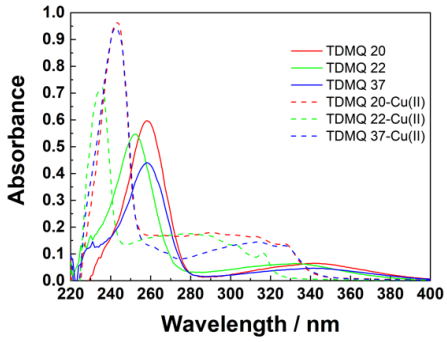


Figure 3.23 UV-Vis absorption spectra of TDMQ and TDMQ-Cu(II) complexes. All absorbance peaks of TDMQ-Cu(II) complexes are well-separated from those of corresponding TDMQ ligands. The experiments were performed in 50 mM HEPES and 100 mM NaCl buffer solution at 298 K (pH 7.5).

of copper transfer to GSH could be evaluated. To determine this, 20 μM TDMQ was mixed with 20 μM $CuCl_2$ in an UV cuvette and incubated for 5 min at room temperature. Then the absorbance was measured as a blank. After this, 20 - 260 molar equivalents of GSH were added in, and blank subtracted absorbance was recorded. The absorbance changes of three TDMQ ligands are shown in Fig. 3.24. All absorbance exhibits dependence on GSH equivalents, suggesting that copper from TDMQ-Cu(II) complexes can be transferred to GSH. We also noticed that only 100 molar equivalent GSH was required to fully transfer copper from TDMQ 20-Cu(II), whereas 200 and 240 molar equivalents GSH were required for TDMQ 22-Cu(II) and TDMQ 37-Cu(II). This indicates that copper from TDMQ 20-Cu(II) could be extracted by GSH more easily, which highlights the higher copper transfer efficiency of TDMQ 20 through GSH pathways, bringing TDMQ 20 to the position of the best drug candidate among these three TDMQ ligands.

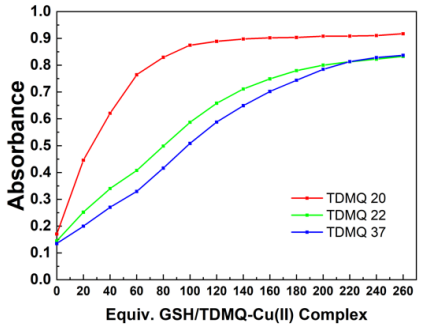


Figure 3.24 Absorbance of different TDMQ-Cu(II) complexes under various molar equivalents of GSH. Curves showing fully recovered absorbance at higher concentrations of GSH, suggesting that copper can be transferred to GSH from TDMQ. The experiments were performed in 50 mM HEPES and 100 mM NaCl buffer solution at 298 K (pH 7.5).

3.4 Summary

In this Chapter, a series of kinetic studies about the interactions between Aβ and Cu^{2+} has been investigated, including Cu^{2+} binding and dissociation and intermediate interconversion of serine 8 phosphorylated Aβ and N-truncated $A\beta_{4\text{-}16}$, as well as redox kinetics of WT-$A\beta_{16}$-Cu complex.

It has been shown from the derived kinetic parameters that serine 8 phosphorylation appears to have little effect on Cu^{2+} binding to Aβ. However, both dissociation and dimerisation are accelerated by phosphorylation. Although there are some differences, pS8-Aβ still shares the similar Cu^{2+} binding mechanism to WT-Aβ and FAD mutated Aβ, and may contribute to the aggregation of Aβ in the brain of sporadic AD patients.

Compared with pS8-Aβ, the Cu^{2+} binding to $A\beta_{4\text{-}16}$ seems to be more complicated. It has been shown that $A\beta_{4\text{-}16}$ exhibits a strong binding affinity of Cu^{2+}. The binding process is hierarchical and relatively prolonged. After initial Cu^{2+} binding, two intermediate species can be observed, of which Species I forms in millisecond scale, while Species II forms at ~2 s interconverting from Species I and finally transforms to a stable complex, $(A\beta\text{-}Cu)_D$. A mechanistic scheme has been proposed and validated to describe the Cu^{2+} binding mechanism. It has also been shown that the presence of

histidine can prolong the Cu^{2+} binding process of $A\beta_{4-16}$, which may lead to a hypothesis that histidine acts as a copper transit modulator of $A\beta_{4-16}$.

The determination of hydrogen peroxide oxidation rate constant of the unstable $A\beta_{16}$-Cu(I) complex has been shown using a designed double mixing stopped flow technique. In addition, a preliminary exploration of an AD drug candidate series named TDMQ, has been reported here. It has been found that TDMQ can inhibit $A\beta_{16}$-Cu induced ROS generation. Also, TDMQ can transfer copper to GSH, of which the best transfer efficiency was presented by TDMQ 20. Such results give a positive assessment to TDMQ for drug discovery.

Chapter 4

α-Synuclein Production and Labelling

Having studied the interactions between Aβ and copper, I next moved onto studying another IDP, α-synuclein (αSyn). As introduced in Chapter 1, αSyn is a small intrinsically disordered protein expressed at high levels in presynaptic nerve terminal[115]. Although the physiological role of αSyn is still debated, several studies have suggested that αSyn could interact with phospholipid membranes[273-275]. In contrast, the aggregation of αSyn is believed to strongly associate with the pathogenesis of Parkinson's disease (PD)[180,276-278], as the pathological hallmarks of PD, Lewy bodies, are predominantly constituted by αSyn[279-281]. In the misfolding progress, Cu^{2+} has been proposed to promote the aggregation and oxidative oligomerisation of αSyn[282-284]. Therefore, studying the interactions of αSyn with membranes and Cu^{2+} is essential to uncover the biological function of αSyn as well as the pathological mechanisms of PD.

In order to investigate αSyn, producing high-quality αSyn samples is the fundamental mission. There are several demonstrated strategies to produce αSyn, including extraction from brain tissue[280], expression in mammalian cell lines[285] and in *Escherichia coli* (*E. coli*)[286]. Among these, extraction from brain tissue is inefficient due to its low yield. In addition, it would be difficult to obtain pure αSyn samples with various mutations or modifications using this method. Furthermore, since the αSyn

isoforms in physiological conditions are mostly N-terminally acetylated, thereby obtaining wild type samples in some way is impossible. The same problem is also present when applying expression in mammalian cell lines[287]. However, expression in *E. coli* could obviate all these questions, thus could be the most suitable approach.

The first report of bacterial expression of αSyn was in 1994[286]. A recombinant technique was created and achieved the expression in *E. coli*. Since then, many methods for αSyn purification have been developed and improved. Although methods are various, the start of purification always begin with cell lysis. Two strategies are widely applied, osmotic shock protocol[288] and ultrasound sonication protocol[289]. It has been suggested previously that osmotic shock is the best choice to release αSyn from *E. coli* because the expressed αSyn is located in the periplasm rather than in the cytoplasm[290]. However, in current research, it has been found that the use of $MgCl_2$ in the osmotic shock protocol could induce conformational change of αSyn[291], and the αSyn yield of lysis by the ultrasound sonication protocol is no different from the osmotic shock protocol[292]. Collectively, ultrasound sonication could be the more reliable cell lysis strategy.

As αSyn is an intrinsically disordered protein, the protein structure is insensitive under denaturing conditions such as heating and acidification. Thus it can be treated with denaturing methods to isolate from other proteins[293-295]. There are some non-denaturing protocols as well, for example, the "later fusion stratagems"[296] and commercial "IMPACT system (New England Biolabs)"[297], which basically can fuse αSyn to another protein or peptide, and then isolate the fusion proteins using specific chromatography columns and subsequent cleavage to obtain the pure αSyn sample. However, it has been reported that the yield and purity of αSyn produced using these protocols are low[288]. Also, specific equipment and reagents are essential for these non-denaturing methods, which could lead to the problems of overcost and low reliability.

The denaturing methods, with their advantages of simple operation, cheap budget, high efficiency and quality, have become the primary technique for αSyn purification. The heating protocol is the most extensively used method, as heating can thermally denature and precipitate natively cytoplasmic proteins without damaging unstructured

αSyn, and is simple to operate. An acidification protocol is an alternative method. However, the αSyn yield is much lower than heating protocol[292]. Therefore, the heating protocol is preferable to purify αSyn.

In this Chapter, I present the detailed procedures for expression and purification, as well as mutagenesis, fluorescent labelling and post-translational modification of the protagonist for the following research, αSyn.

4.1 Expression and Purification

Expression

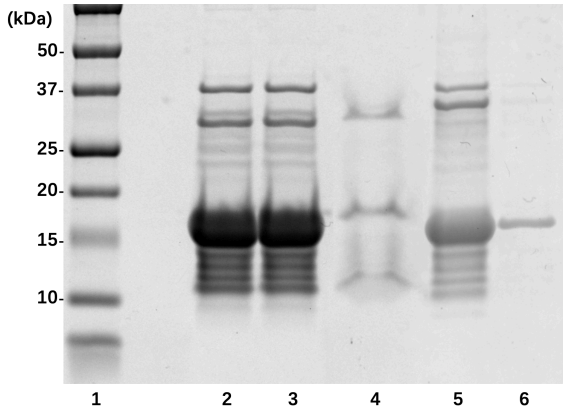
A recombinant bacterial expression technique was applied for αSyn expression. The pT7-7 asyn WT plasmid for wild type αSyn (WT-αSyn) expression was obtained as a gift from Hilal Lashuel (Addgene plasmid # 36046). The plasmid was cloned in DH5α *E. coli* and extracted using a plasmid miniprep kit (Monarch, New England Biolabs), and then transformed in BL21(DE3) *E. coli* via heat shock. The transformed BL21(DE3) *E. coli* cells were grown on lysogeny broth (LB) agar plates containing 100 μg mL^{-1} ampicillin at 37 ℃ for 15 h. After that, a single colony was selected and cultured overnight in 10 mL of LB containing 100 μg mL^{-1} ampicillin at 37 ℃. 500 μL of this cultured LB was mixed with 500 μL of 50% autoclaved glycerol to make a bacteria stock and stored at -80 ℃. This stock was used to prepare other overnight cultures in the future.

Apart from this 500 μL, 8 mL of the overnight cultured LB was used to inoculate 800 mL of LB containing 100 μg mL^{-1} ampicillin. The cells were incubated at 37 ℃ with 220 rpm shaking until the OD_{600} reached 0.7. Subsequently, IPTG was added to a final concentration of 1mM to induce αSyn expression. The cells were further incubated 3 h at 37 ℃ with 220 rpm shaking, and then harvested by centrifugation at 8000 g for 30 min at 4 ℃. The cell pellet was stored at -80 ℃.

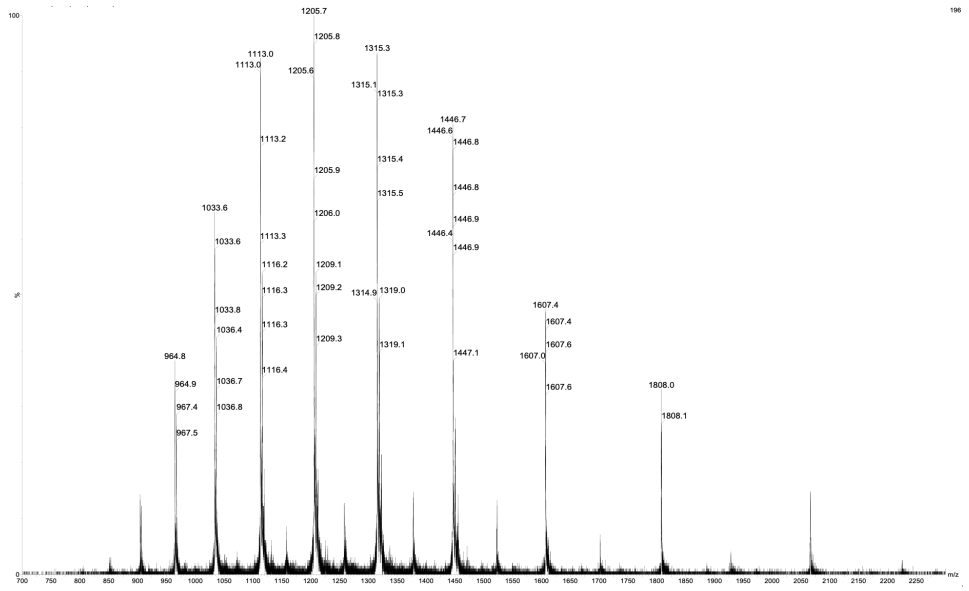
Purification

A heating protocol was employed for αSyn purification. The frozen cell pellet was

thawed on ice and resuspended in Tris-HCl buffer (20 mM Tris-HCl, 50 mM NaCl, 5 mM EDTA, pH 7.4). A protease inhibitor tablet (cOmplete, Roche) was dissolved in the suspension to protect protein from degradation before performing cell lysis. After 2 min cell lysis by ultrasound sonication, the suspension was boiled at 90 ℃ for 20 min and then centrifuged at 16000 g for 20 min. The supernatant was collected and filtered by 0.2 μm syringe filter to remove all cell debris. Subsequently, streptomycin sulfate was added to the supernatant to a final concentration of 10 mg mL^{-1}, and the mixture was stirred for 15 min at 4 ℃ to precipitate nucleic acids. After centrifugation at 16000 g for 20 min, the supernatant was collected and ammonium sulfate was added to 50% saturation. The mixture was stirred for 30 min at 4 ℃ and centrifuged again at 16000 g. Then the pellet was collected and resuspended in Tris-HCl buffer (20 mM Tris-HCl, 50 mM NaCl, pH 7.4) and dialysed overnight with 2 L of the same buffer. The purified αSyn was aliquoted, flash frozen in liquid nitrogen and stored at -80 ℃. Samples of each purification step were analysed by SDS-PAGE to verify results before pursuing next step (Fig. 4.1(A)). The band at ~17 kDa corresponds to αSyn, a little higher molecular weight could be due to the binding of N-terminal acidic tail with SDS molecules[292]. The bands at ~35 - 37 kDa could be due to some aggregated αSyn or impurities, but they finally disappeared after purification. The final αSyn sample was characterised by ESI-MS and the result is as expected (Fig. 4.1(B)). Protein concentration was determined from the absorbance at 280 nm with an extinction coefficient of 5960 M^{-1} cm^{-1} using an UV-Vis spectrometer.



(A) SDS-PAGE



(B) ESI-MS

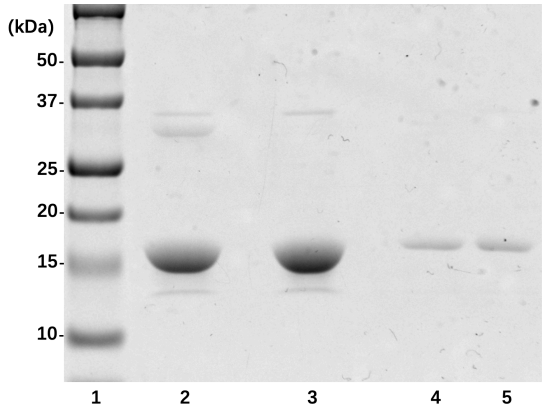
Figure 4.1 Analyses of WT-αSyn purification. (A) SDS-PAGE analysis of samples in each purification step. Lane 1 – molecular weight ladder; Lane 2 – supernatant obtained from centrifugation of boiled sample; Lane 3 – supernatant obtained from centrifugation of streptomycin sulfate treated sample; Lane 4 – supernatant obtained from centrifugation of ammonium sulfate treated sample; Lane 5 – resuspension of the pellet precipitated by ammonium sulfate; Lane 6 – final purified sample. **(B)** ESI-MS characterisation of purified WT-αSyn. Molecular masses were calculated as: $m/z = [M + nH^+] / n^+$, $M = (m/z \times n) - n$. The molecular mass is 14456 Da.

4.2 Post-Translational Modification

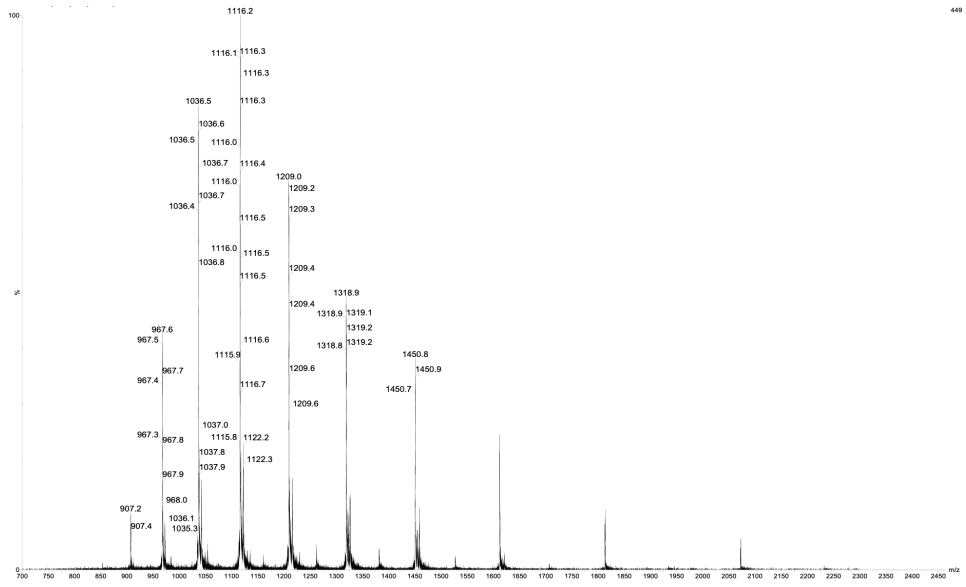
N-Terminal Acetylation

Currently, growing evidence has indicated that the predominant isoform of αSyn *in vivo* undergoes N-terminal acetylation[156,213], which highlights the importance of the study for N-terminally acetylated αSyn (NAc-αSyn). Recombinant NAc-αSyn was produced for the study in this work. The pT7-7 plasmid was transformed together with a pNatB (pACYCduet-naa20-naa25) plasmid encoding the components of yeast NatB acetylase complex into BL21(DE3) *E. coli*. The pNatB plasmid was a gift from Dan Mulvihill (Addgene plasmid # 53613). The transformed BL21(DE3) *E. coli* cells were grown on LB agar plates containing 100 μg mL^{-1} ampicillin and 25 μg mL^{-1} chloramphenicol at 37 °C for 15 h. After that, a single colony was selected to inoculate

10 mL of LB containing 100 μg mL^{-1} ampicillin and 25 μg mL^{-1} chloramphenicol, which was then cultured overnight at 37 °C. This pre-cultured LB was used to make a bacteria stock and inoculate 800 mL of LB containing 100 μg mL^{-1} ampicillin and 25 μg mL^{-1} chloramphenicol for NAc-αSyn expression. The expression and purification were carried out as described in Section 4.1. The SDS-PAGE analysis of the samples in each purification step and ESI-MS characterisation of the final sample are shown in Fig. 4.2. A 43 Da increase of molecular mass indicates the formation of an acetyl group on αSyn molecule.



(A) SDS-PAGE



(B) ESI-MS

Figure 4.2 Analyses of NAc-αSyn purification. (A) SDS-PAGE analysis of samples in each purification step. Lane 1 – molecular weight ladder; Lane 2 – supernatant obtained from

centrifugation of boiled sample; Lane 3 – supernatant obtained from centrifugation of streptomycin sulfate treated sample; Lane 4 – resuspension of the pellet precipitated by ammonium sulfate; Lane 5 – final purified sample. **(B)** ESI-MS characterisation of purified NAc-αSyn. Molecular masses were calculated as: $m/z = [M + nH^+] / n^+$, $M = (m/z \times n) - n$. The molecular mass is 14499 Da.

Oxidation

It has been reported that methionine oxidation can inhibit the fibrilisation of αSyn[298-299]. In order to study the oxidation effect on NAc-αSyn, methionine oxidised NAc-αSyn was produced. NAc-αSyn was thawed on ice to prepare 300 μM solution in Tris-HCl buffer (20 mM Tris-HCl, 50 mM NaCl, pH 7.4). Then the solution was treated with 300 mM hydrogen peroxide and stirred 15 min at room temperature. Oxidation was stopped by adding molar equivalent of sodium thiosulfate. The protein solution was desalted using a desalting column (PD-10, GE Healthcare) following the provided protocol. The oxidised NAc-αSyn was aliquoted and stored at -80 ℃. The ESI-MS characterisation is shown in Fig. 4.3. Compared with NAc-αSyn, the result shows an increase of 64 Da in molecular mass, which indicates that four oxygen atoms were latched onto NAc-αSyn molecule. As there are four methionine residues but no cysteine in NAc-αSyn molecule, such result can indicate that all four methionine residues of NAc-αSyn were successfully oxidised.

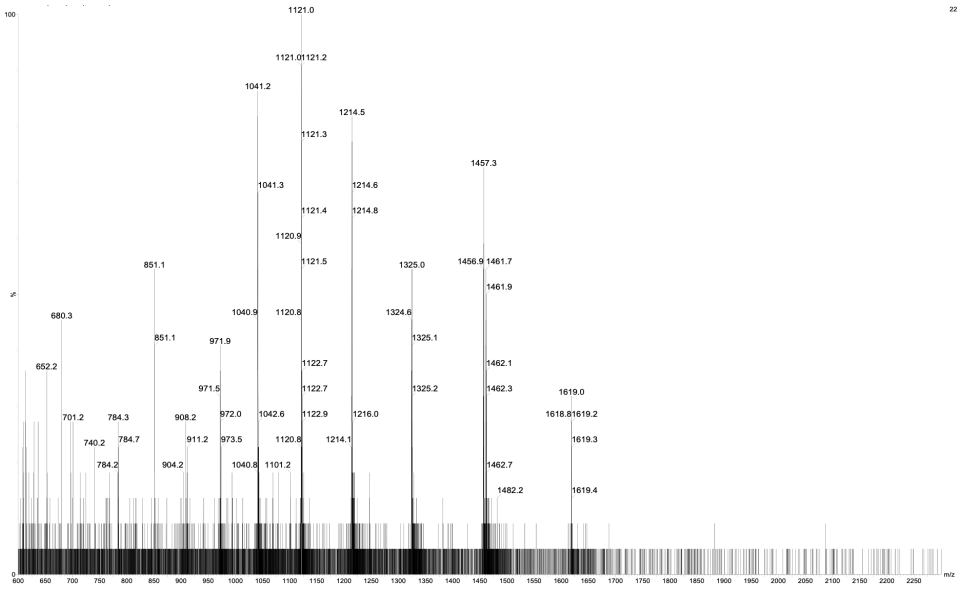


Figure 4.3 ESI-MS characterisation of oxidised NAc-αSyn. Molecular masses were calculated as: $m/z = [M + nH^+] / n^+$, $M = (m/z \times n) - n$. The molecular mass is 14563 Da.

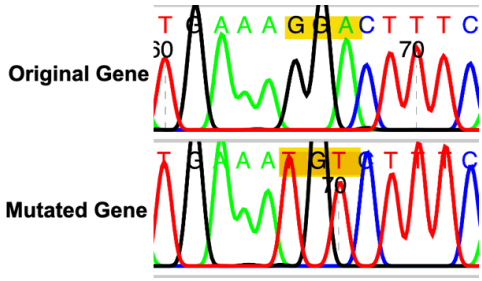
4.3 Mutagenesis

Cysteine Mutation for Fluorescent Dye Labelling

To investigate αSyn by fluorescence, the glycine at position 7 was selected to mutate and label with a fluorescent dye. This position is close to copper binding site of αSyn, thus the labelled dye can sensitively probe the interactions between copper and αSyn. A cysteine codon (TGT) was introduced in the pT7-7 plasmid to substitute the codon of glycine 7 using a site-directed mutagenesis kit (Phusion, Thermo Fisher Scientific) following the manufacturer's protocol. The designed primers and mutation analysis result are shown in Fig. 4.4. After mutation introduction, the G7C WT-αSyn and G7C NAc-αSyn were expressed and purified as described in Section 4.1 and 4.2.

Fwd.	5'-CCAAGGAGGGAGTTGTGGC	19
Rev.	5'-CCTTTGAAAGACATTTCATGAATACATC	28

(A) Primers



(B) Mutation Analysis

Figure 4.4 G7C mutation introduction in vector. (A) Designed primers. **(B)** Mutation analysis by Sanger sequencing showing a successful codon substitution of glycine 7 (GGA) to cysteine (TGT).

The SDS-PAGE analysis is shown in Fig. 4.5. The dense band at ~35 kDa could be due to the formation of αSyn dimer as the thiol group of cysteine can easily react with each other to form disulfide bond. Since the mutated position 7 is the only cysteine residue in the αSyn mutant, the specific fluorescent labelling at this position can be achieved using a maleimide-based fluorophore via the thiol-maleimide conjugation.

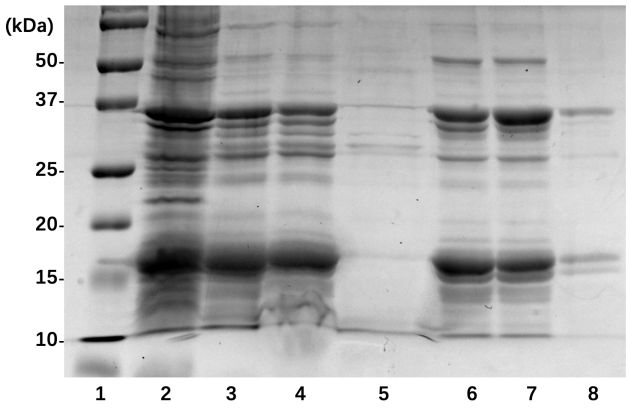
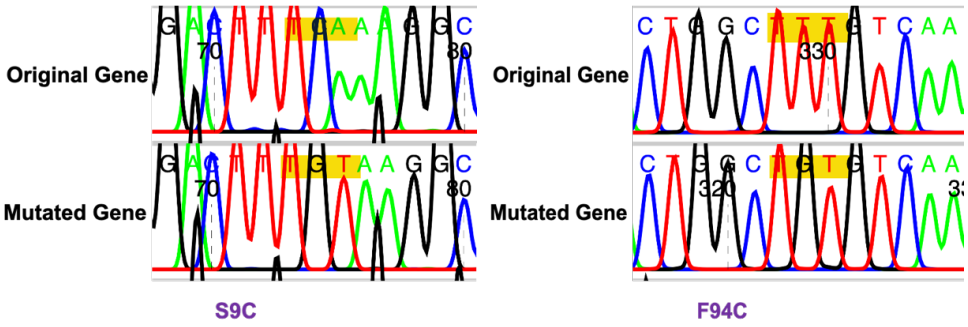


Figure 4.5 SDS-PAGE analysis of G7C NAc-αSyn purification. Lane 1 – molecular weight ladder; Lane 2 – boiled sample; Lane 3 – supernatant obtained from centrifugation of boiled sample; Lane 4 – supernatant obtained from centrifugation of streptomycin sulfate treated sample; Lane 5 – supernatant obtained from centrifugation of ammonium sulfate treated sample; Lane 6 – resuspension of the pellet precipitated by ammonium sulfate; Lane 7 – dialysed sample; Lane 8 – final purified sample. Dimer band can be observed due to the formation of disulfide bond.

In addition to the G7C αSyn mutant, a sample of serine 9 to cysteine-phenylalanine 94 to cysteine (S9C-F94C) dually mutated αSyn was produced using the similar genetic modification approach. These two cysteine mutations are located in N-terminal region and NAC region of αSyn respectively, and both of the regions can form amphipathic α-helices to easily associate with negatively charged lipid membranes[300-301]. If the cysteine mutations were labelled with two different maleimide-based fluorophores as donor and acceptor chromophores, this αSyn variant will be ideal for the study of the interactions between lipid membranes and αSyn using FRET techniques. The designed primers and mutation analysis result are shown in Fig. 4.6, and the protein was expressed and purified using analogous methods as described above.

S9C	Fwd.	5'-GCCAAGGAGGGAGTTGTGG	19
	Rev.	5'-CTTACAAAGTCCTTTCATGAATACATCCA	29
F94C	Fwd.	5'-AGCCACTGGCTGTGTCAAAAAG	22
	Rev.	5'-GCTGCAATGCTCCCTGCT	18

(A) Primers



(B) Mutation Analysis

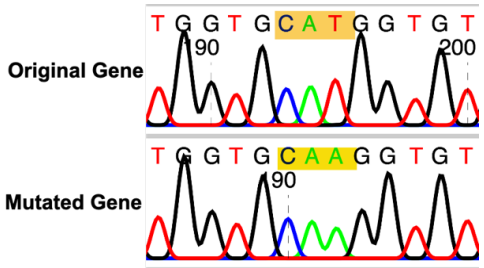
Figure 4.6 S9C, F94C mutation introduction in vector. (A) Designed primers. **(B)** Mutation analysis by Sanger sequencing showing successful codon substitutions of serine 9 (TCA) to cysteine (TGT), phenylalanine 94 (TTT) to cysteine (TGT).

FPD Mutation (H50Q)

The histidine 50 to glutamine (H50Q) substitution of αSyn has been reported as one of the familial Parkinson's disease (FPD) mutations[302-303], and can enhance the aggregation of αSyn[304]. In addition, the histidine at position 50 has been suggested as an important copper binding site of αSyn[209]. To investigate the role of histidine 50 in αSyn, a H50Q mutated αSyn was produced using the similar genetic modification

Fwd.	5'-GAGTGGTGCAAGGTGTGGC	19
Rev.	5'-CCTCCTTGGTTTTGGAGCCTAC	22

(A) Primers



(B) Mutation Analysis

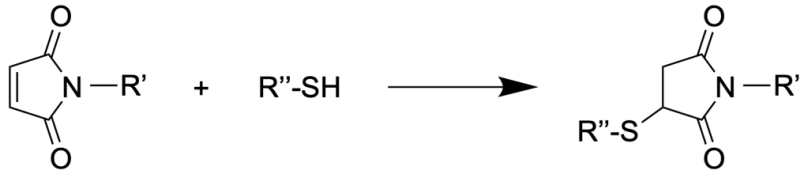
Figure 4.7 H50Q mutation introduction in vector. (A) Designed primers. **(B)** Mutation analysis by Sanger sequencing showing a successful codon substitution of histidine 50 (CAT) to glutamine (CAA).

approach. The designed primers and mutation analysis result are shown in Fig. 4.7, and the protein was expressed and purified using analogous methods as described above.

4.4 Fluorescent Dye Labelling

Single Labelling

Labelling of G7C αSyn was achieved via a selective thiol-maleimide conjugation. Alexa 488 C_5 maleimide dye (Alexa Fluor, Thermo Fisher Scientific) was selected as the fluorescent dye due to its high quantum yield and stability against photobleaching[305]. The labelling proceeds through a Michael addition pathway, forming a thioether as the final product, as shown in Scheme. 4.1.



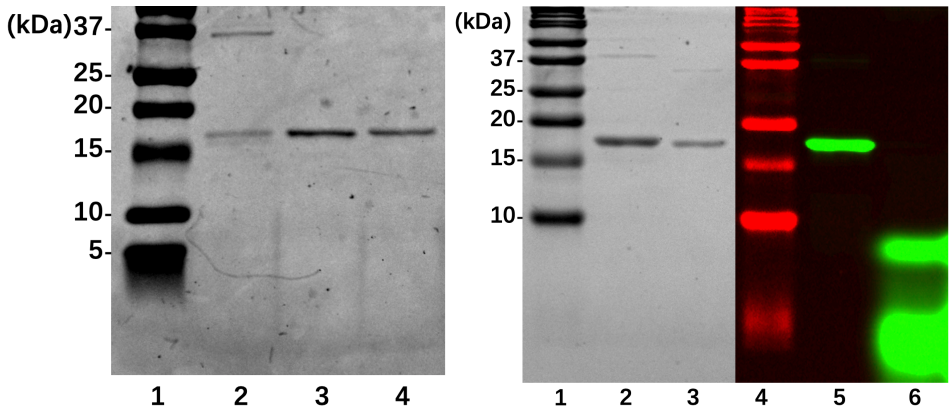
Scheme 4.1 The mechanism of labelling reaction. R' represents the remaining portion of Alexa maleimide dye molecules; R'' represents the remaining portion of G7C αSyn.

The labelling was performed generally according to the manufacturer's instruction with optimisation. Alexa dye was dissolved in DMSO to prepare 10 mM stock solution. Tris-HCl buffer (20 mM Tris-HCl, 50 mM NaCl, pH 7.4) was deoxygenated by bubbling with nitrogen for 1 h. G7C αSyn aliquots were thawed on ice, and a 10-fold molar excess of TCEP was added in αSyn solution to reduce disulfide bonds. After 30 min stirring, the solution was eluted with the bubbled buffer through a desalting column (PD-10, GE Healthcare) to remove TCEP. The concentration of eluted αSyn solution was determined by the absorbance at 280 nm, using an extinction coefficient of 5960 M^{-1} cm^{-1}. Subsequently, the Alexa dye stock was added to the eluted αSyn solution in a molar ratio of 3: 1 (dye: αSyn). The mixture was stirred in dark for 3 h before quenched by DTT. After that, the labelled αSyn was desalted using another desalting column, and concentrated at 15000 g for 5 min through a 10K MWCO protein concentrator (Pierce,

Thermo Fisher Scientific) to remove all free dye. The labelled αSyn was flash frozen and stored at -80 ℃. Fig. 4.8 shows the SDS-PAGE analyses of the labelling. The final concentration was determined from the absorbance at 495 nm with an extinction coefficient of 72000 M^{-1} cm^{-1}. The labelling efficiency (η) was calculated by:

$$\eta = \frac{\varepsilon_1 A_{\text{dye}}}{\varepsilon_2 (A_{280\,\text{nm}} - \gamma A_{\text{dye}})} \tag{4.1}$$

where A is the absorbance, ε_1 is the extinction coefficient of αSyn at 280 nm, ε_2 is the extinction coefficient for the peak absorbance of the fluorophore, γ is a correction factor for fluorophore's contribution to the absorbance at 280 nm (0.11 for Alexa 488). The labelling efficiency was calculated to be ~95%.



(A) Disulfide Bonds Reduction (B) Labelled Samples

Figure 4.8 SDS-PAGE analyses of G7C αSyn labelling with Alexa 488. (A) Analysis of samples in disulfide bonds reduction. Lane 1 – molecular weight ladder; Lane 2 – diluted G7C αSyn sample; Lane 3 – G7C αSyn under excess TCEP; Lane 4 – TCEP removed G7C αSyn before labelling. The results indicate that the reduced disulfide bonds can stay opening for a while after TCEP removal, giving chance for dye labelling. **(B)** Analysis of labelled samples. The same gel is displayed in staining and fluorescent scanning. Lane 1, 4 – molecular weight ladder; Lane 2, 5 – G7C αSyn labelled under TCEP removal; Lane 3, 6 – G7C αSyn labelled under the presence of TCEP.

According to the fluorescently scanned gel analysis in Fig. 4.8(B), it can be seen that the G7C αSyn sample without TCEP removal was difficult to be labelled by the Alexa maleimide dye, while the TCEP removed sample was labelled efficiently. This

interesting result indicates that TCEP could interfere with the thiol-maleimide labelling reaction, which is consistent with a previous report by Tyagarajan K, *et al*[306]. However, it is still generally accepted that TCEP is not necessary to be removed during the labelling with maleimide dye. This is also believed by the dye manufacturer and thus the labelling protocol provided by them may mislead plenty of researchers. The result presented here could give a suggestion to optimise the protocol of protein labelling with maleimide dye.

Dual Labelling

Dual labelled S9C-F94C αSyn was produced for FRET measurements. Alexa 488 C_5 maleimide dye (Alexa Fluor, Thermo Fisher Scientific) was selected as the donor chromophore, and Alexa 594 C_5 maleimide dye (Alexa Fluor, Thermo Fisher Scientific) was used as the acceptor. The labelling was performed in an analogous way to single labelling, except that a dye-protein mixing molar ratio of 6: 2: 1 (Alexa 594: Alexa 488: αSyn) was used. The SDS-PAGE analysis is shown in Fig. 4.9.

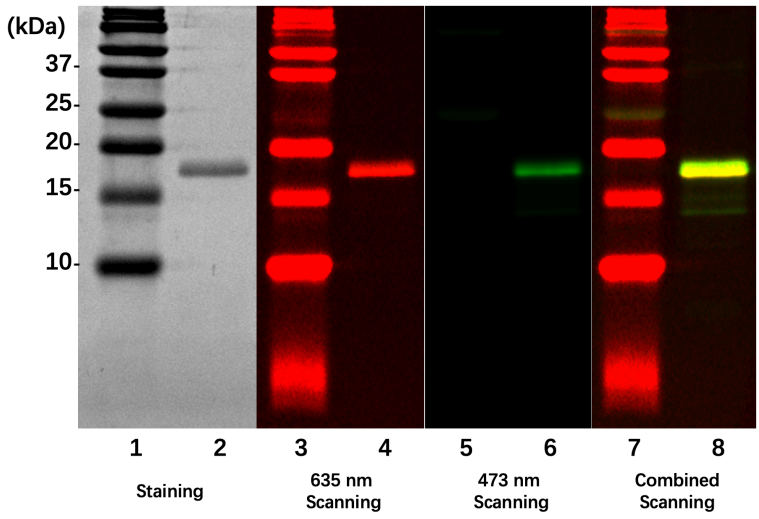


Figure 4.9 SDS-PAGE analysis of S9C-F94C αSyn dually labelled by Alexa 594 and 488. The same gel is displayed in staining and fluorescent scanning at different wavelengths of light (635 nm scanning to visualise Alexa 594 and 473 nm scanning to visualise Alexa 488). Lane 1, 3, 5, 7 – molecular weight ladder under different conditions; Lane 2, 4, 6, 8 – labelled αSyn under different conditions.

4.5 Summary

In this Chapter, the expression, purification and labelling of multiple αSyn samples have been described. Heating protocol was employed for purification because temperature only has insignificant effect on the structure of αSyn. Post-translational modified αSyn samples such as N-terminally acetylated αSyn and oxidised αSyn were produced. To produce fluorescently labelled αSyn, cysteine mutation was introduced in αSyn via genetic modification approach for specific labelling of maleimide fluorophore, as there is no cysteine in normal αSyn. Through optimisation, the final labelling efficiency can reach ~95%, which is ideal for my further study.

It is interesting to find that TCEP can disrupt the labelling reaction that is substantially a thiol-maleimide conjugation. As a widely used reducing agent, TCEP is believed to be inert to thiol-reactive reagents. Thus most of scientists believe that the desalting step before labelling can be deleted to simplify the labelling protocol. However, my results give an opposite opinion and show a significant disturbance by TCEP. This could be helpful to optimise the protein labelling protocol using maleimide dye as well as other thiol-maleimide reaction experiments.

Overall, a reliable source of αSyn sample for research has finally been established. The produced samples were used throughout in further study of αSyn.

Chapter 5

Interactions of α-Synuclein with Cu^{2+}

The interactions between Cu^{2+} and α-synuclein (αSyn) is always of great interest to many scientists, as there is evidence that Cu^{2+} could change the properties of normal αSyn, which could be important in the pathogenesis of Parkinson's disease (PD)[190,282]. Compared to amyloid-β, αSyn has a longer protein sequence and more proposed copper binding sites. To date, three potential Cu^{2+} binding sites have been reported as illustrated in Fig. 5.1. Five Cu^{2+} binding modes centred at these sites have been suggested and three of them are proposed to exist under physiological conditions[208-209]. However, previous studies have shown disagreement in the description of these coordination modes. The main controversy is focused on whether the residue histidine 50 (His50) of αSyn is involved in Cu^{2+} binding. More research is needed to address this question.

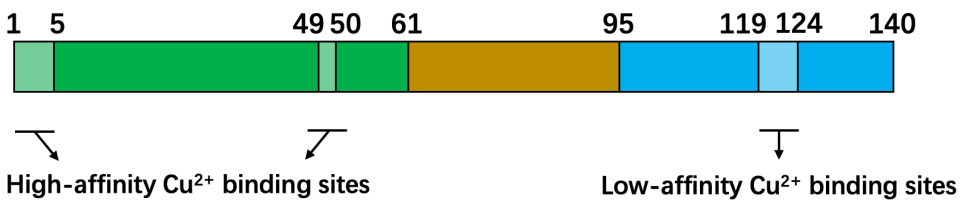


Figure 5.1 Literature suggested Cu^{2+} binding sites in αSyn sequence.

So far, most of the αSyn *in vivo* is believed to be N-terminally acetylated (NAc). Nevertheless, NAc-αSyn only shows weak binding affinity with Cu^{2+}. Because there are few sources to consult the absolute value of the weak affinity, it is consequently worthy of investigation.

αSyn is able to catalyse the copper induced reactive oxygen species (ROS) generation, which could play a key role in the development of PD. The kinetic mechanism is essential for the judgement of whether the ROS generation is occurring on a timescale that is relevant to PD. Whereas it currently has only received little attention.

In this Chapter, kinetic techniques are mainly utilised to elucidate the following key questions about the interactions between αSyn and Cu^{2+}: the existing form of αSyn-Cu(II) complex at low αSyn concentration, the binding affinity of αSyn (WT and NAc forms) with Cu^{2+} as well as the reduction kinetics of αSyn-Cu(II) complex.

5.1 Quenching of Labelled αSyn by Cu^{2+}

When investigating the interactions between Cu^{2+} and proteins, one of the major approaches is measuring the paramagnetic Cu^{2+} induced fluorescence quenching of the fluorescent-labelled proteins. In Chapter 3, I have already used this method to study the interactions between Cu^{2+} and Aβ. While for αSyn, as the sample is self-produced and attached with a different fluorescent dye from Aβ, it is necessary to first measure the fluorescence quenching level of the sample to estimate the observation sensitivity.

The measurement was performed under excitation at 488 nm using a fluorometer. The fluorescence of 100 nM residue 7 labelled wild type αSyn (G7C-l αSyn) was measured with and without 100 μM $CuCl_2$ in HEPES buffer (50 mM HEPES, 100 mM NaCl). The averaged spectra of 5 repeats are shown in Fig. 5.2. It can be seen that the Cu^{2+} induced quenching level is significant. Indeed, the level was calculated to be ~91%. Such a big amplitude change indicates that the change of the fluorescence signal in the interaction process between Cu^{2+} and labelled αSyn can be recorded and distinguished clearly, which builds a solid basis for the following experiments.

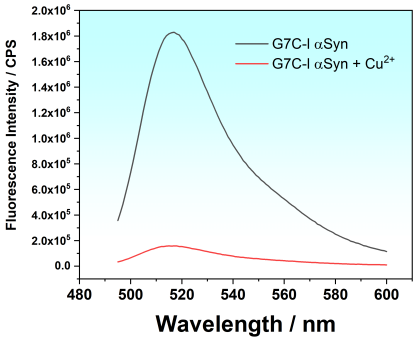


Figure 5.2 Fluorescence quenching of residue 7 labelled WT-αSyn after mixing with Cu^{2+}. Huge quenching can be observed from the emission spectra when the labelled αSyn was treated with Cu^{2+}. The measurements were performed in 50 mM HEPES and 100 mM NaCl buffer solution at 298 K (pH 7.5).

The labelling position could also affect the quenching. To validate this, the residue 140 labelled αSyn (A140C-l αSyn) was produced to make a comparison with G7C-l αSyn. The reactions of both labelled αSyn with Cu^{2+} were carried out in a stopped flow machine. 25 nM αSyn was mixed with 500 nM $CuCl_2$ in buffer and the reaction traces were recorded as function of time (Fig. 5.3). As shown in Fig. 5.3, the quenching level of A140C-l αSyn is much smaller than that of G7C-l αSyn. The reason for such remarkable difference is that the residue 140 is farther away from the N-terminal high-affinity Cu^{2+} binding site than residue 7. The Cu^{2+} bound on N-terminus can easily

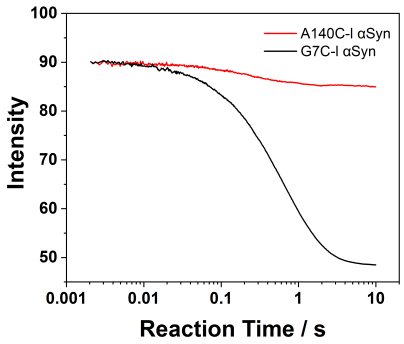


Figure 5.3 Difference between Cu^{2+} binding to residue 7 labelled WT-αSyn and residue 140 labelled WT-αSyn. The Cu^{2+} binding induced quenching of residue 7 labelled WT-αSyn is much larger than that of residue 140 labelled WT-αSyn, suggesting that such quenching is relevant to the distance between the bound Cu^{2+} and fluorophore. The measurements were performed in 50 mM HEPES and 100 mM NaCl buffer solution at 298 K (pH 7.5).

quench the fluorophore at residue 7 but can hardly interact with the fluorophore at residue 140. The traces suggest that such quenching is distance-dependent and the labelling on residue 7 has no effect on the N-terminal Cu^{2+} binding of WT-αSyn. Based on above results, the high Cu^{2+} quenching amplitude of G7C-l αSyn can be confirmed. Thus G7C-l αSyn was selected and used throughout most of this project.

5.2 Cu^{2+} Binding Mode of αSyn

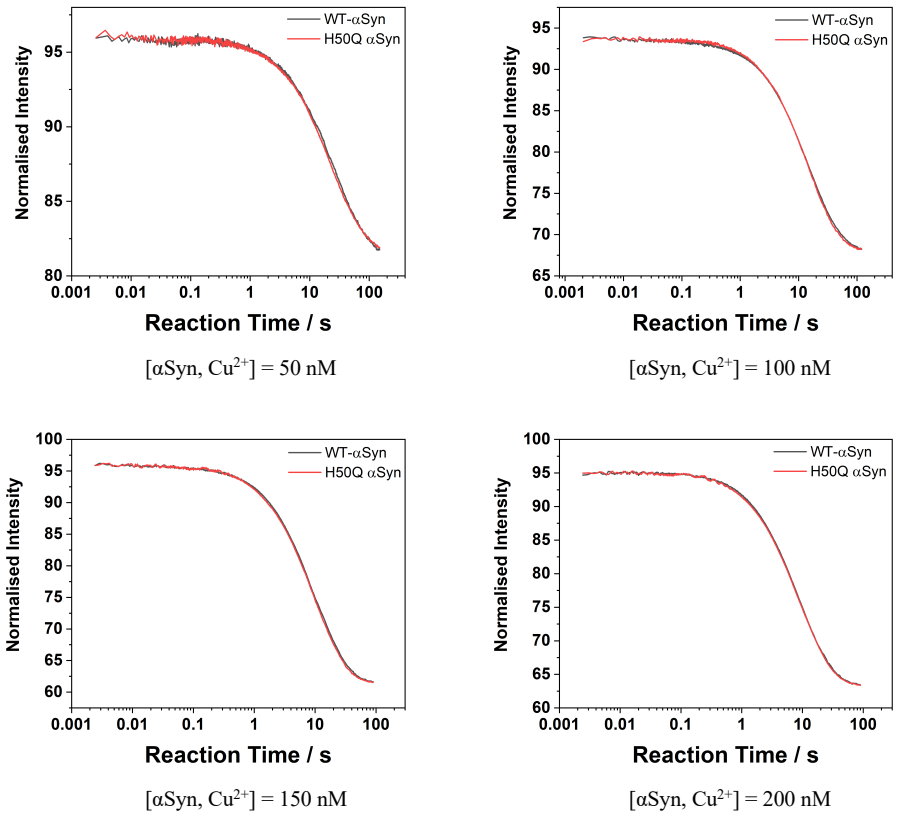
5.2.1 WT-αSyn

The complication of how Cu^{2+} binds to normal αSyn draws much of scientists' attention. As described in Chapter 1, there are three proposed coordination modes of WT-αSyn-Cu(II) at physiological pH, whereas the description of two "3N1O" modes where His50 is involved in Cu^{2+} binding is currently controversial (mode structures are shown in Section 1.4). The studies that support the description of these modes were mostly performed at relatively high αSyn concentration (in the millimolar regime). While at low αSyn concentration the situation may change, and little is known whether His50 is still involved in Cu^{2+} binding when αSyn concentration is reduced to as low as micromolar or nanomolar.

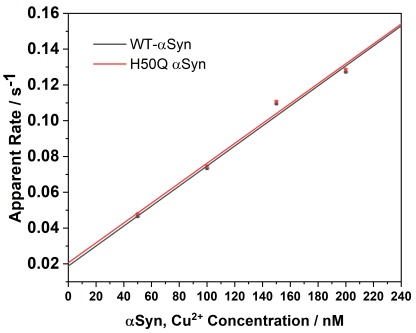
To study whether the His50 of αSyn can affect Cu^{2+} binding to αSyn, kinetic techniques were applied. A His50 mutated αSyn, H50Q αSyn, was selected as a control sample of WT-αSyn. The Cu^{2+} binding experiments of both αSyn were performed and the Cu^{2+} association rate constants (k_{on}) were derived to distinguish the difference. The binding experiments were first performed using 1:1 mixing ratio of labelled αSyn to Cu^{2+} with increasing concentrations (50 - 200 nM). The comparison of normalised raw traces is shown in Fig. 5.4(A). As the reaction follows second-order reaction mechanism, the apparent Cu^{2+} association rates ($k_{on(App)}$) were determined by fitting the reaction traces using the following equation derived from second-order reaction rate equation:

$$[\mathrm{A}]_t = \frac{A}{Ak_{on(App)}t + 1} + C \tag{5.1}$$

where t is the reaction time, $[A]_t$ is the concentration of αSyn at time t, A is the amplitude of trace and C is the background fluorescence. The derived $k_{on(App)}$ were linearly fitted



(A) Normalised Traces

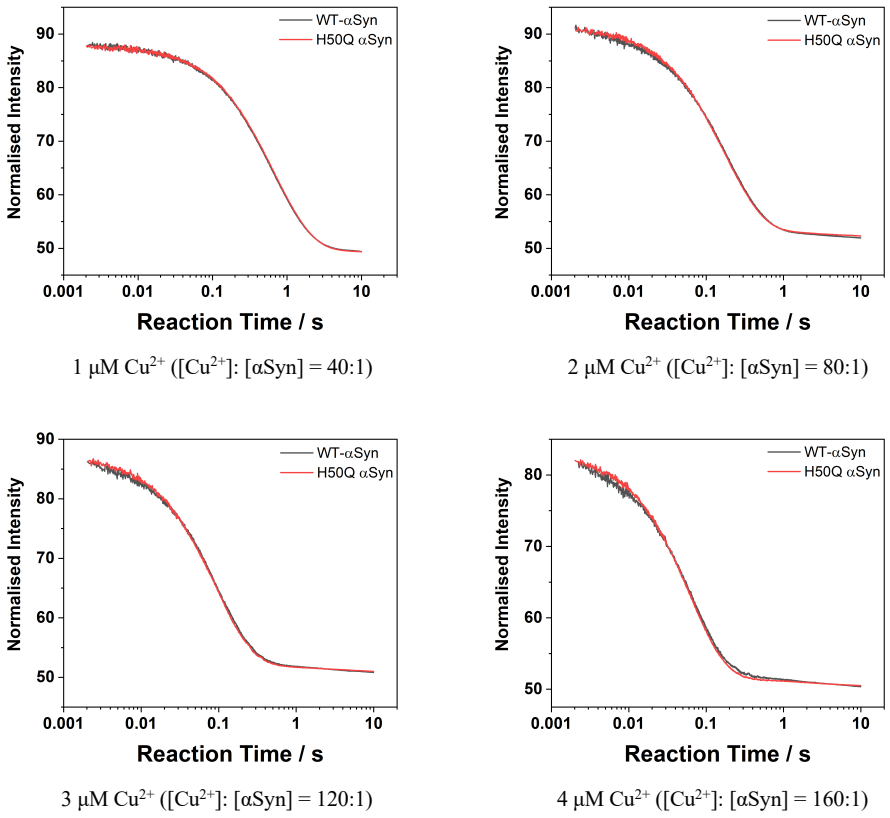


(B) Apparent Cu^{2+} Association Rates

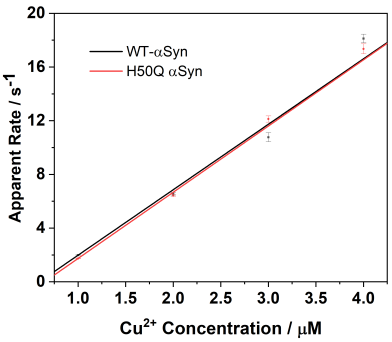
Figure 5.4 Comparison of Cu^{2+} binding to WT-αSyn and H50Q αSyn under 1:1 αSyn, Cu^{2+} mixing ratio. (A) Comparison of normalised Cu^{2+} binding traces between WT-αSyn and H50Q αSyn under various conditions. The experiments were performed in 50 mM HEPES and 100 mM NaCl buffer solution at 298 K (pH 7.5). **(B)** Comparison of apparent Cu^{2+} association rates between WT-αSyn and H50Q αSyn. Error bars represent the uncertainty in the values determined from fits.

against the concentration of Cu^{2+} to obtain k_{on} from slopes (Fig. 5.4(B)). k_{on} of Cu^{2+} binding to WT-αSyn and H50Q αSyn were determined to be 5.6(5) × 10^5 M^{-1} s^{-1} and 5.5(3) × 10^5 M^{-1} s^{-1} respectively. Such close values of k_{on} and identical reaction traces indicate that the 1:1 Cu^{2+} binding interactions of WT-αSyn and H50Q αSyn share the same mechanism at low αSyn concentration, i.e., His50 of WT-αSyn is not involved in Cu^{2+} binding under this condition.

Next, I performed the Cu^{2+} binding experiments of both αSyn under a variable excess of Cu^{2+} to explore the effect of Cu^{2+} molar ratios. In the experiments, 25 nM labelled WT-αSyn and labelled H50Q αSyn samples were both treated with various concentrations of excess $CuCl_2$. Fig. 5.5(A) shows the comparison of normalised raw traces. The traces were fitted with multi-exponentials to determine reaction rates, and the fastest values were taken to be $k_{on(App)}$. Fig. 5.5(B) shows how $k_{on(App)}$ varies with Cu^{2+} concentration. It can be seen that at excess molar ratio of Cu^{2+} to αSyn,



(A) Normalised Traces

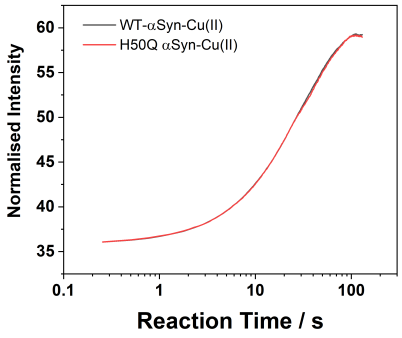


(B) Apparent Cu^{2+} Association Rates

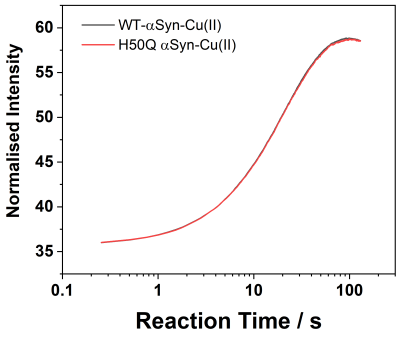
Figure 5.5 Comparison of Cu^{2+} binding to WT-αSyn and H50Q αSyn under a variable excess of Cu^{2+}. (A) Comparison of normalised Cu^{2+} binding traces between WT-αSyn and H50Q αSyn under various concentrations of Cu^{2+}. The experiments were performed in 50 mM HEPES and 100 mM NaCl buffer solution at 298 K (pH 7.5). **(B)** Comparison of apparent Cu^{2+} association rates between WT-αSyn and H50Q αSyn. Error bars represent the uncertainty in the values determined from fits.

$k_{on(App)}$ of Cu^{2+} binding to WT-αSyn and H50Q αSyn are still close. k_{on} of Cu^{2+} binding to WT-αSyn and H50Q αSyn were determined to be 4.8(3) × 10^6 M^{-1} s^{-1} and 4.9(2) × 10^6 M^{-1} s^{-1} respectively. These results further indicate that the His50 of WT-αSyn does not participate in Cu^{2+} binding to WT-αSyn.

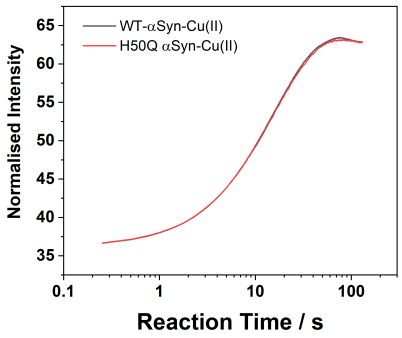
After this, I performed Cu^{2+} dissociation experiments to further confirm whether the His50 involved in Cu^{2+} coordination modes of αSyn exist under 1:1 stoichiometric ratio of αSyn to Cu^{2+}. In such experiments, 50 nM labelled WT-αSyn and labelled H50Q αSyn samples were both pre-mixed with 50 nM $CuCl_2$. Then both mixtures were treated with various concentrations of EDTA. The comparison of normalised raw traces (Fig. 5.6(A)) shows identical shape between the dissociation of two αSyn-Cu(II) complexes. In addition, the very similar Cu^{2+} dissociation rate constants for αSyn-Cu(II) of these two αSyn (0.017(4) s^{-1} for WT-αSyn-Cu(II) and 0.015(5) s^{-1} for H50Q αSyn-Cu(II), respectively), which were determined from the intercepts of linearly fitted apparent rates (Fig. 5.6(B)), can provide the evidence that the αSyn-Cu(II) coordination modes of WT-αSyn and H50Q αSyn are essentially identical. Thereby the existence of the His50 involved in 3N1O modes for WT-αSyn can be excluded.



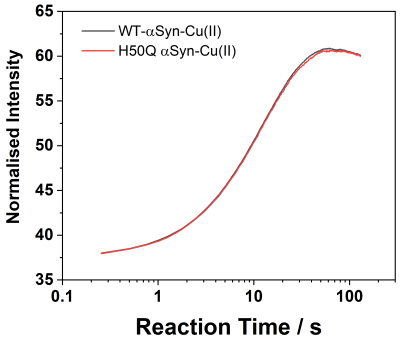
10 μM EDTA



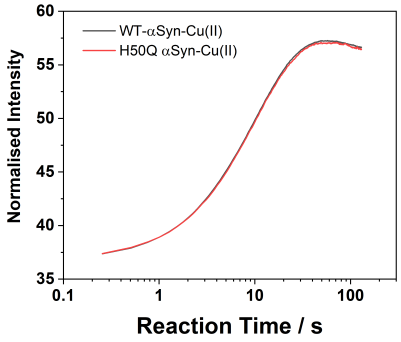
20 μM EDTA



30 μM EDTA

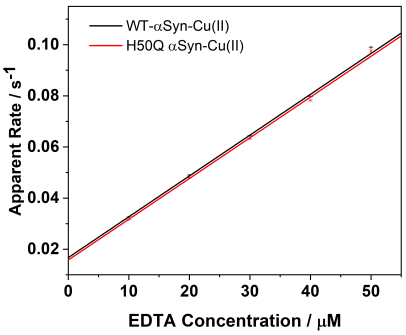


40 μM EDTA



50 μM EDTA

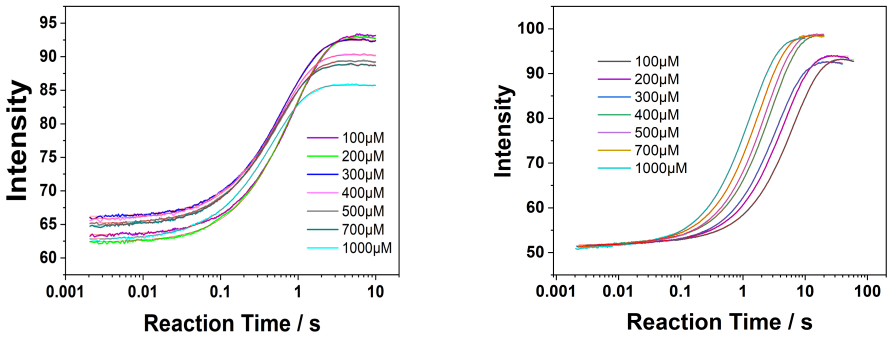
(A) Normalised Traces



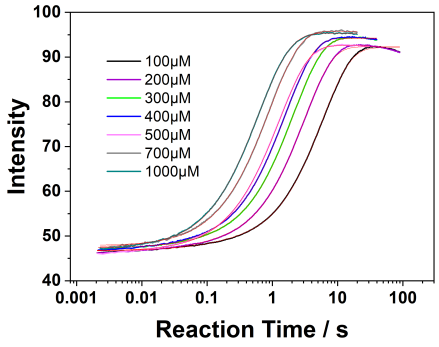
(B) Apparent Dissociation Rates

Figure 5.6 Comparison of Cu^{2+} coordination mode dissociation by EDTA for WT-αSyn and H50Q αSyn. (A) Comparison of normalised Cu^{2+} dissociation traces between WT-αSyn-Cu(II) and H50Q αSyn-Cu(II) under various concentrations of EDTA. The experiments were performed in 50 mM HEPES and 100 mM NaCl buffer solution at 298 K (pH 7.5). **(B)** Comparison of the apparent dissociation rates of Cu^{2+} by EDTA between WT-αSyn-Cu(II) and H50Q αSyn-Cu(II). Error bars represent the uncertainty in the values determined from fits.

I also conducted the Cu^{2+} dissociation experiments of WT-αSyn-Cu(II) at three different pH (pH 5.5, pH 6.5 and pH 7.5) to determine pH effect on the stability of WT-αSyn-Cu(II) complex. The experiments were conducted using 50 nM labelled WT-αSyn which was pre-mixed with 50 nM $CuCl_2$ in buffer to form αSyn-Cu(II) complex, and the mixture was subsequently treated with various concentrations of EDTA. The raw traces and fitted curves are shown in Fig. 5.7(A). The apparent dissociation rates ($k_{off(App)}$) of WT-αSyn-Cu(II) complex at different pH can be derived from the dissociation traces by the single exponential fit. The rates were linearly fitted to obtain the EDTA independent k_{off} (Fig. 5.7(B)). The determined k_{off} values were 0.826(5) s^{-1}, 0.092(1) s^{-1} and 0.018(2) s^{-1} for the αSyn-Cu(II) complex at pH 5.5, pH 6.5 and pH 7.5, respectively. The k_{off} at lower pH is around one order of magnitude larger than that at higher pH, which roughly equals the extent of protonation. In addition, the second-order rate constants for the dissociation with EDTA were determined from the slopes to be 1.70(2) × 10^3 M^{-1} s^{-1}, 6.6(3) × 10^2 M^{-1} s^{-1} and 1.55(7) × 10^3 M^{-1} s^{-1} for the αSyn-Cu(II) complex at pH 5.5, pH 6.5 and pH 7.5, respectively. The second-order rate constant determined at pH 6.5 is very different from others, which suggests that there may exist unknown interactions between WT-αSyn-Cu(II) and EDTA at pH 6.5.

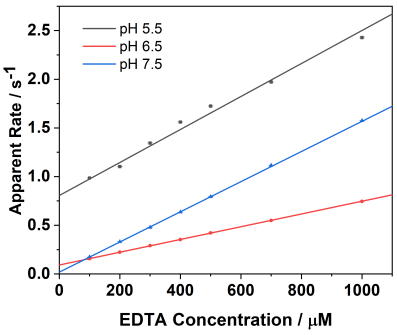


pH 5.5 pH 6.5



pH 7.5

(A) Raw Traces and Fits



(B) Apparent Dissociation Rates

Figure 5.7 Cu^{2+} dissociation from WT-αSyn-Cu(II) at different pH. (A) Raw Cu^{2+} dissociation traces and fitted curves (shown as red solid curves) for WT-αSyn-Cu(II) under various concentrations of EDTA at different pH. All of the traces can be fitted perfectly by single exponential fit. The experiments were performed in 50 mM HEPES and 100 mM NaCl buffer solution at 298 K. **(B)** Apparent dissociation rates of Cu^{2+} by EDTA at different pH values. Error bars represent the uncertainty in the values determined from fits.

5.2.2 Possible Cu^{2+} Binding Mode of NAc-αSyn

NAc-αSyn has been identified to be the most abundant isoform in the human physiological state. Hence, the study around NAc-αSyn becomes very crucial to understand the nature of human αSyn. The interactions between Cu^{2+} and NAc-αSyn could be interesting and relevant, although current research suggests that such interactions are weaker than that of WT-αSyn.

To validate the difference of Cu^{2+} binding between NAc-αSyn and WT-αSyn, 25 nM of different labelled αSyn samples (both NAc and WT forms) were reacted with 500 nM $CuCl_2$, and the traces are shown in Fig. 5.8. It can be seen that Cu^{2+} binding of WT-αSyn can reach the bottom plateau in 10 s. Whereas for NAc-αSyn, the reaction proceeds much more slowly. The results provide the evidence that Cu^{2+} binding to NAc-αSyn is harder than that to WT-αSyn, and thus the binding mechanisms of these two forms of αSyn should be different. This difference can be explained logically in that N-terminal acetylation destroys the high-affinity Cu^{2+} binding site at the N-terminus of αSyn.

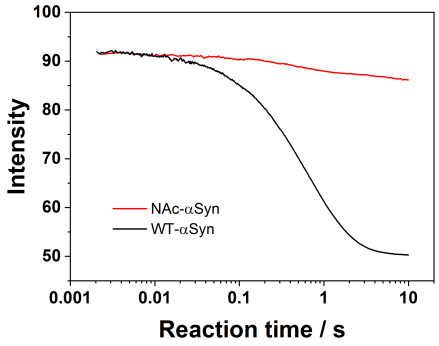
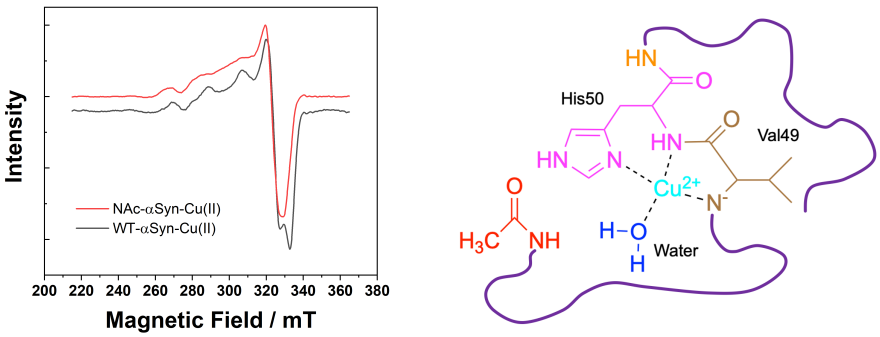


Figure 5.8 Difference between Cu^{2+} binding to WT-αSyn and NAc-αSyn. Cu^{2+} binding to WT-αSyn is completed much faster than that to NAc-αSyn, suggesting different binding mechanisms. The measurements were performed in 50 mM HEPES and 100 mM NaCl buffer solution at 298 K (pH 7.5).

If the Cu^{2+} binding site at N-terminus is abolished, the two remaining low-affinity binding sites which are centred at His50 and Asp121 respectively, could be responsible for Cu^{2+} binding. To catch a glimpse of the possible Cu^{2+} binding mode of NAc-αSyn, an X-band EPR measurement was conducted. In order to make the measurement at the

physiological concentration of αSyn, 50 μM NAc-αSyn was used and mixed with 50 μM $CuCl_2$ as the EPR sample. After waiting for the binding completion, the sample was flash-frozen with liquid helium. For the purpose of comparison, the sample of WT-αSyn-Cu(II) was also measured. Fig. 5.9(A) shows the spectra. The typical Cu^{2+} hyperfine couplings for nitrogen/oxygen rich equatorial coordination (270 - 310 mT) were observed. The $g_{\parallel}$ factors and hyperfine coupling constants ($A_{\parallel}$) were derived by spectral simulation and summarised in Table 5.1. These values were analysed by the Peisach-Blumberg plot to deduce the possible structural mode[307]. For WT-αSyn-Cu(II), the parameters were found to be in agreement with the 2N2O mode, which provides further evidence to strengthen the previous conclusion. While the parameters



(A) EPR Spectra (B) Cu^{2+} Coordination Mode

Figure 5.9 Proposed Cu^{2+} coordination mode for NAc-αSyn. (A) X-band EPR spectra of Cu^{2+} bound on NAc-αSyn and WT-αSyn. Clear difference can be observed between these two spectra. The spectra were measured at 20 K, 9.4 GHz. **(B)** Suggested Cu^{2+} coordination mode for NAc-αSyn.

Table 5.1 $g_{\parallel}$ factors and hyperfine coupling constants ($A_{\parallel}$) for the EPR spectra of NAc-αSyn-Cu(II) and WT-αSyn-Cu(II). Data obtained from simulation in Figure 5.9(A).

	$g_{\parallel}$ factor	$A_{\parallel}$ / G
NAc-αSyn-Cu(II)	2.29	195
WT-αSyn-Cu(II)	2.245	208

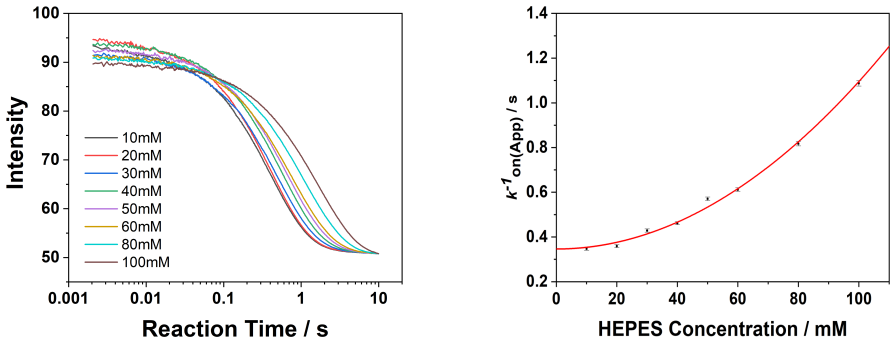
of NAc-αSyn-Cu(II) were found to correspond with the 3N1O mode more closely. This mode could be a His50 centred form, as the Asp121 centred form is proposed to be 4O

and prefers to exist at acidic environment. The proposed Cu^{2+} binding structure of NAc-αSyn is illustrated in Fig. 5.9(B).

5.3 Kinetic Studies of the Interactions between αSyn and Cu^{2+}

5.3.1 WT-αSyn

To fully understand the Cu^{2+} binding mechanism of αSyn, the kinetic parameters are required. The association rate constant (k_{on}) of Cu^{2+} binding to WT-αSyn was first determined using stopped flow. In this measurement, 25 nM labelled WT-αSyn was mixed with 500 nM $CuCl_2$ in HEPES-NaCl buffer. The concentration of HEPES in buffer was varied to perform HEPES dependent measurement. The raw traces are shown in Fig. 5.10(A). The data were fitted with a parabola centred at zero (Fig. 5.10(B)) as described in Chapter 3 to determine HEPES independent k_{on}, which is 5.7(1) × 10^6 M^{-1} s^{-1}, two orders of magnitude slower than that of $A\beta_{16}$ peptide[206].

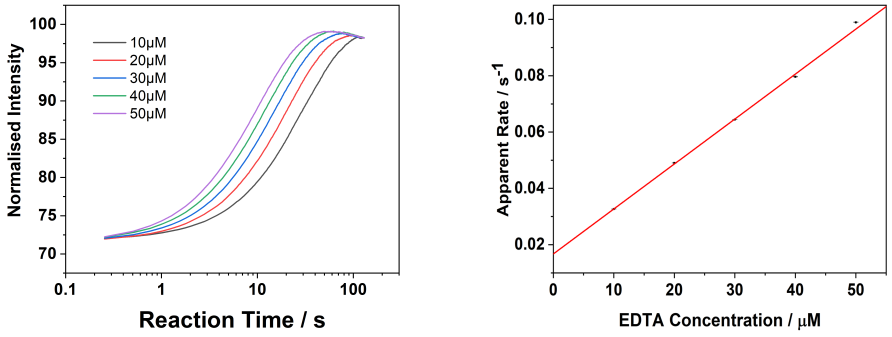


(A) Raw Traces (B) HEPES Dependence of $k_{on(App)}$

Figure 5.10 Kinetics of Cu^{2+} binding to WT-αSyn. (A) Raw traces of WT-αSyn binding with Cu^{2+} under various concentrations of HEPES. The experiments were performed in HEPES and 100 mM NaCl buffer solution at 298 K (pH 7.5). **(B)** HEPES dependence of $k_{on(App)}$. The HEPES independent k_{on} value is 5.7(1) × 10^6 M^{-1} s^{-1}. Error bars represent the uncertainty in the values determined from fits.

Subsequently, the Cu^{2+} dissociation rate constant (k_{off}) was determined. The labelled WT-αSyn and $CuCl_2$ were pre-mixed at 50 nM. Then the mixture was treated with various concentrations of EDTA. The results are shown in Fig. 5.11(A). The dissociation rate constant was determined from the intercept of linearly fitted apparent

rates, which is 0.017(4) s^{-1} (Fig. 5.11(B)). This value together with k_{on} determined above, gave the dissociation constant (K_d) to be 3.0(7) nM. Compared with the Cu^{2+} binding affinity of WT-Aβ determined by the same method[206], the affinity of WT-αSyn is around three times weaker.



(A) Normalised Traces (B) Apparent Dissociation Rates

Figure 5.11 Kinetics of Cu^{2+} dissociation from WT-αSyn-Cu(II). (A) Normalised traces of Cu^{2+} dissociation from WT-αSyn-Cu(II) under various concentrations of EDTA. The experiments were performed in 50 mM HEPES and 100 mM NaCl buffer solution at 298 K (pH 7.5). **(B)** Apparent dissociation rates of Cu^{2+} by EDTA from WT-αSyn-Cu(II). The EDTA independent k_{off} value is 0.017(4) s^{-1}. Error bars represent the uncertainty in the values determined from fits.

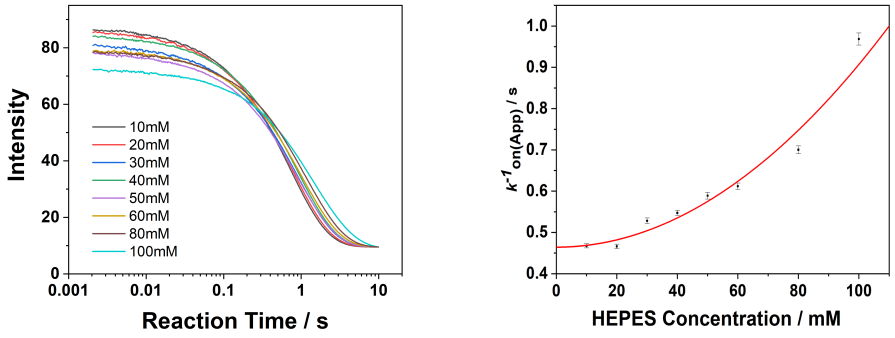
In addition, the second-order rate constant for the reaction of WT-αSyn-Cu(II) with EDTA (k_L) can be determined from the slope of the linear fitting in Fig. 5.11(B), which is 1.60(2) × 10^3 M^{-1} s^{-1}. This value is much lower than that of WT-Aβ-Cu(II), suggesting that it is more difficult for EDTA to extract Cu^{2+} from WT-αSyn-Cu(II) than WT-Aβ-Cu(II), even though the latter has higher affinity with Cu^{2+} than the former.

5.3.2 NAc-αSyn

As mentioned above, literature has suggested that NAc-αSyn displays weak binding to Cu^{2+}. However, there is currently no experimental data to assess how weak it is. Thus, it is essential to determine the Cu^{2+} binding affinity of NAc-αSyn.

Similar to WT-αSyn, HEPES independent k_{on} of Cu^{2+} binding to NAc-αSyn was first determined. In this measurement, to accelerate the reaction process, 500 μM $CuCl_2$ was mixed with 25 nM labelled NAc-αSyn under various HEPES concentrations. The

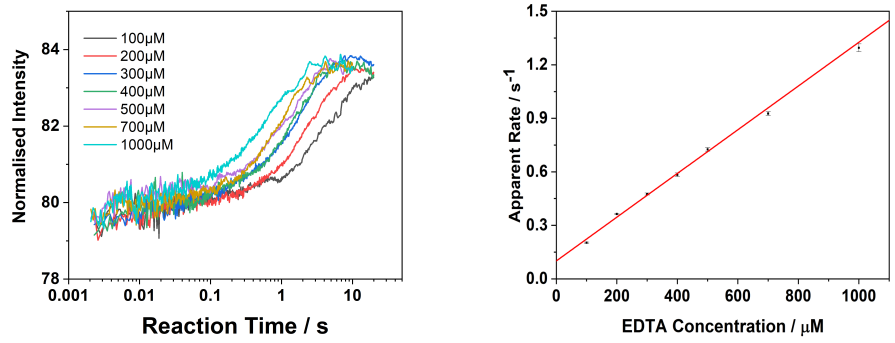
results are shown in Fig. 5.12(A). k_{on} value was determined to be 4.3(2) × 10^3 M^{-1} s^{-1} (Fig. 5.12(B)), approximately three orders of magnitude slower than that of WT-αSyn.



(A) Raw Traces (B) HEPES Dependence of $k_{on(App)}$

Figure 5.12 Kinetics of Cu^{2+} binding to NAc-αSyn. (A) Raw traces of NAc-αSyn binding with Cu^{2+} under various concentrations of HEPES. The experiments were performed in HEPES and 100 mM NaCl buffer solution at 298 K (pH 7.5). **(B)** HEPES dependence of $k_{on(App)}$. The HEPES independent k_{on} value is 4.3(2) × 10^3 M^{-1} s^{-1}. Error bars represent the uncertainty in the values determined from fits.

The subsequent measurement is k_{off} determination. 50 nM labelled NAc-αSyn was pre-mixed with unlabelled NAc-αSyn to a total protein concentration of 10 μM. Then the protein solution was mixed with 10 μM $CuCl_2$. After waiting for binding, the mixture was reacted with various concentrations of EDTA. The results are shown in Fig. 5.13(A). k_{off} value was determined to be 0.10(1) s^{-1} (Fig. 5.13(B)). The determined



(A) Normalised Traces (B) Apparent Dissociation Rates

Figure 5.13 Kinetics of Cu^{2+} dissociation from NAc-αSyn-Cu(II). (A) Normalised traces of Cu^{2+} dissociation from NAc-αSyn-Cu(II) under various concentrations of EDTA. The experiments were performed in 50 mM HEPES and 100 mM NaCl buffer solution at 298 K (pH 7.5). **(B)**

Apparent dissociation rates of Cu^{2+} by EDTA from NAc-αSyn-Cu(II). The EDTA independent k_{off} value is 0.10(1) s^{-1}. Error bars represent the uncertainty in the values determined from fits.

k_{on} and k_{off} gave the value of K_d to be 23(3) μM. Thereby the Cu^{2+} binding affinity of NAc-αSyn is around four orders of magnitude weaker than that of WT-αSyn. A summary of these parameters is shown in Table 5.2.

Table 5.2 Kinetic parameters of the interactions between αSyn and Cu^{2+}. Data summarised from above fits.

	WT-αSyn	NAc-αSyn
k_{on} / M^{-1} s^{-1}	5.7(1) × 10^6	4.3(2) × 10^3
k_{off} / s^{-1}	0.017(4)	0.10(1)
k_L / M^{-1} s^{-1}	1.60(2) × 10^3	1.23(5) × 10^3

5.4 Reduction Kinetics of WT-αSyn-Cu(II)

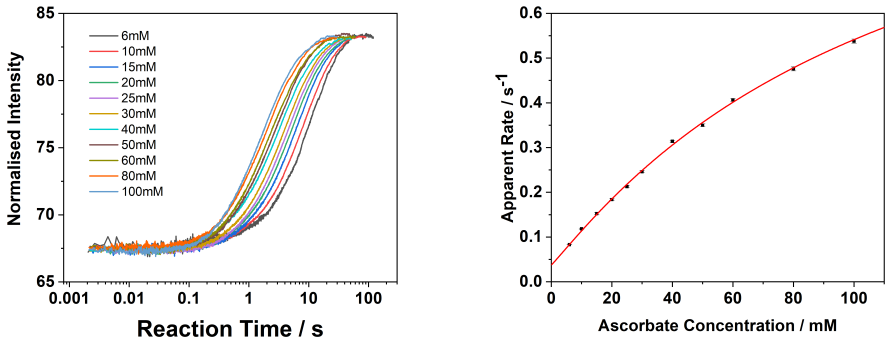
Similar to Aβ-Cu(II), αSyn-Cu(II) can also take part in the redox cycling to generate reactive oxygen species (ROS), inducing oxidative damage to cells. Because the involvement of αSyn-Cu(II) in the redox cycling typically starts from the reduction by physiological reducing agents such as ascorbate and glutathione (GSH), in this work I put my primary focus on the reduction of αSyn-Cu(II), and kinetic method is the ideal strategy for investigating these transient interactions.

5.4.1 Reduction by Ascorbate

Ascorbate is a common antioxidant in the whole human body. It is present at a relatively high concentration of 160 μM in CSF[308] and takes part in numerous synaptic activities[309], showing undeniable importance in synaptic modulation. Previously we studied the reduction of Aβ-Cu(II) by ascorbate (see Section 3.3.1). Here I have applied the analogous method to study the reduction kinetics of WT-αSyn-Cu(II).

As Cu^{2+} is a paramagnetic ion with a single unpaired electron, it can readily interact with a fluorophore's first excited state which also possesses a single unpaired electron and make the fluorescence of the fluorophore quenched. However, once Cu^{2+}

is reduced to Cu^{+}, the copper ion will no longer possess single unpaired electron and thus the fluorescence will be recovered. The measurements were designed and performed based on this principle. 50 nM labelled WT-αSyn was pre-mixed with 50 nM $CuCl_2$ to form WT-αSyn-Cu(II) complex, then the solution was treated with various concentrations of sodium ascorbate. The normalised traces are shown in Fig. 5.14(A). The traces demonstrate the dependence of reaction rate on ascorbate concentration. However as shown in the data summarised in Fig. 5.14(B), the reduction rates are extremely slow even at 10 - 100 mM ascorbate, which are not comparable with those of Aβ-Cu(II) (see Section 3.3.1). Such inactive reduction may indicate that the metabolism of αSyn-Cu(II) is not via ascorbate pathway, and αSyn-Cu(II) cannot participate in the redox cycling via the reduction by ascorbate.



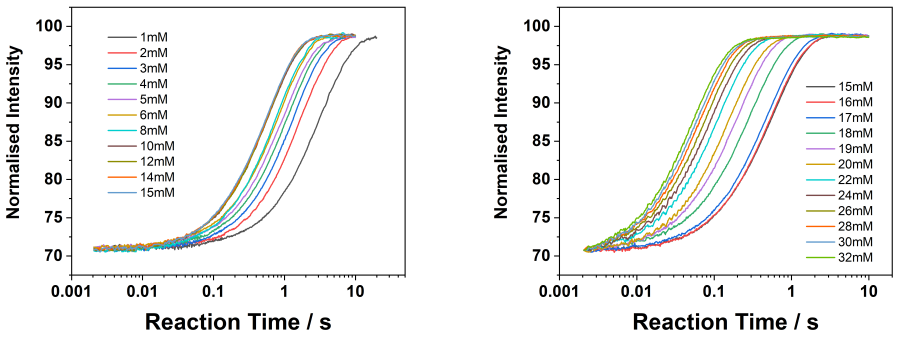
(A) Normalised Traces (B) Apparent Reduction Rates

Figure 5.14 Reduction kinetics of WT-αSyn-Cu(II) by ascorbate. (A) Normalised traces of WT-αSyn-Cu(II) complex reduction under various concentrations of ascorbate. The experiments were performed in 50 mM HEPES and 100 mM NaCl buffer solution at 298 K (pH 7.5). **(B)** Apparent reduction rates of WT-αSyn-Cu(II) under various concentrations of ascorbate. Error bars represent the uncertainty in the values determined from fits.

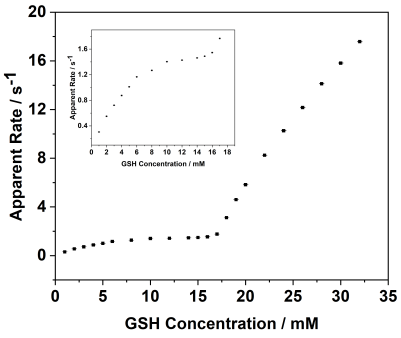
5.4.2 Reduction by GSH

Subsequently, I performed another reduction experiment using GSH which is a more abundant antioxidant in cells (intracellular concentration ranges from 0.1 to 15 mM but in most cells is between 1 - 2 mM[310-311]). In this experiment, αSyn-Cu(II) was pre-formed by mixing 50 nM labelled WT-αSyn with 50 nM $CuCl_2$, and then reduced by various concentrations of GSH. The experimental traces are shown in Fig. 5.15(A).

The reduction rates were obtained by single exponential fitting of the traces, and then plotted against the concentration of GSH as shown in Fig. 5.15(B). Intriguingly, the reduction rate exhibits a hierarchical increase with increasing GSH concentration. 16 mM GSH is a hinge point. If GSH concentration is lower than this, the increase of the reduction rate is slow and seems to be "controlled". Whereas if GSH concentration is higher than 16 mM, the speed of reduction will be dramatically raised and become "out of control". Considering this value is very close to the highest intracellular concentration of GSH, this unexpected discovery may be able to explain why physiological GSH is maintained under 15 mM. It is worth further investigation to uncover the exact mechanism.



(A) Normalised Traces



(B) Apparent Reduction Rates

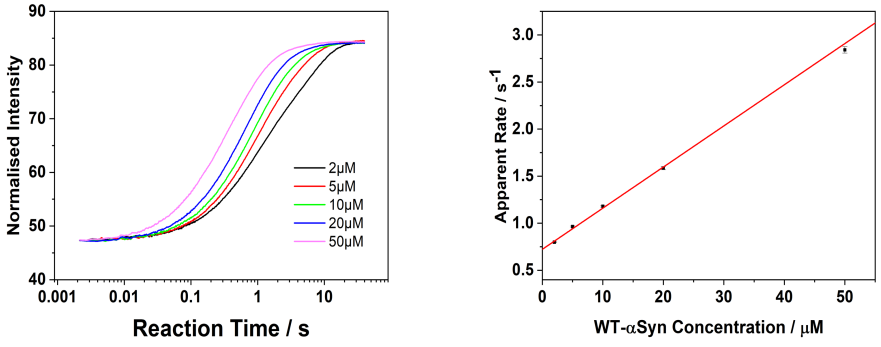
Figure 5.15 Reduction kinetics of WT-αSyn-Cu(II) by GSH. (A) Normalised traces of WT-αSyn-Cu(II) complex reduction under various concentrations of GSH. The experiments were performed in 50 mM HEPES and 100 mM NaCl buffer solution at 298 K (pH 7.5). **(B)** Apparent reduction rates of WT-αSyn-Cu(II) under various concentrations of GSH. The rates derived under relatively low concentrations of GSH are re-plotted in the inset for clarity. Error bars represent the uncertainty in the values determined from fits.

5.5 Cu^{2+} Interactions between αSyn and Other Proteins

In addition to αSyn, many proteins in the brain can interact with Cu^{2+} such as Aβ and HSA. Aβ has been investigated by our group and we have shown that it presents with slightly stronger Cu^{2+} affinity than αSyn. Whereas the concentration of Aβ in the brain is much lower than αSyn, in contrast, HSA exists at ~3 μM in the brain[312], which is relatively closer to the physiological concentration of αSyn. Furthermore, HSA contains the ATCUN motif and thus presents high affinity of Cu^{2+} (0.90(9) pM[313]). Therefore, HSA may be able to affect the Cu^{2+} interactions with αSyn. This could be interesting and meaningful to study.

5.5.1 Dissociation of Aβ-Cu(II)

To explore whether the addition of αSyn could influence Aβ-Cu(II) complex, 50 nM labelled $A\beta_{16}$ was pre-mixed with 50 nM $CuCl_2$, and the solution was treated with various concentrations of WT-αSyn. All traces in Fig. 5.16(A) show obvious recovery. Although the Cu^{2+} binding affinity of Aβ is stronger than that of WT-αSyn, considering that the difference is slight, a large excess of WT-αSyn would still be able to push the chemical equilibrium to dissociation. This could be the reason for the observed fluorescence recovery. By fitting the derived data from the traces, the second-order



(A) Normalised Traces (B) Apparent Dissociation Rates

Figure 5.16 $A\beta_{16}$-Cu(II) dissociation by WT-αSyn. (A) Normalised traces of Cu^{2+} dissociation from $A\beta_{16}$-Cu(II) under various concentrations of WT-αSyn. The experiments were performed in 50 mM HEPES and 100 mM NaCl buffer solution at 298 K (pH 7.5). **(B)** Apparent dissociation rates of $A\beta_{16}$-Cu(II) under various concentrations of WT-αSyn. Error bars represent the uncertainty in the values determined from fits.

reaction rate constant for $A\beta_{16}$-Cu(II) with WT-αSyn can be determined, which is 4.4(2) × 10^4 M^{-1} s^{-1} (Fig. 5.16(B)). Also, the spontaneous dissociation rate constant of $A\beta_{16}$-Cu(II) was determined to be 0.72(1) s^{-1}, similar to the value determined from the reaction with EDTA.

5.5.2 Cu^{2+} Binding Competition between αSyn and HSA

Since HSA possesses high Cu^{2+} affinity, the question arises how it will affect Cu^{2+} binding to αSyn when it co-exists with αSyn? To investigate this, 50 nM labelled WT-αSyn was first pre-mixed with 5 μM HSA, then the mixture was mixed with various concentrations of $CuCl_2$. The results are shown in Fig. 5.17. Compared with the results of previous Cu^{2+} binding experiment of WT-αSyn, the quenching amplitude of αSyn becomes very small, indicating that Cu^{2+} binding to αSyn is severely inhibited by HSA. However, αSyn may still be able to compete against HSA in the binding of Cu^{2+} on short timescales, as the quenching is always visible. On longer timescales, αSyn cannot compete with HSA anymore. The bound Cu^{2+} on αSyn will be displaced by HSA, resulting in the marginal fluorescence recovery.

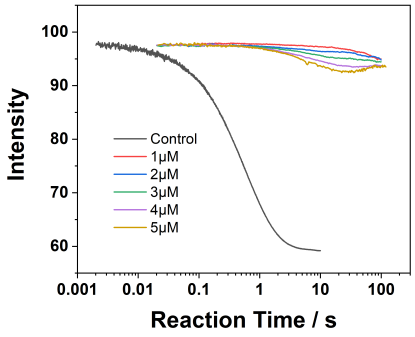


Figure 5.17 Competition between WT-αSyn and HSA for Cu^{2+}. The control trace represents 1 μM Cu^{2+} binding to 50 nM WT-αSyn without HSA. Raw traces show that only small amount of Cu^{2+} is bound to HSA-mixed WT-αSyn under various concentrations of Cu^{2+}, suggesting that HSA can inhibit Cu^{2+} binding to WT-αSyn. The experiments were performed in 50 mM HEPES and 100 mM NaCl buffer solution at 298 K (pH 7.5).

5.6 Summary

This Chapter has discussed the interactions between Cu^{2+} and αSyn. Using kinetic methods, I have shown that WT-αSyn binds to Cu^{2+} via its N-terminal binding site. I

have also demonstrated that the disputed His50 site is not involved in the high-affinity Cu^{2+} binding. Moreover, through EPR measurements, I have proposed the structures of WT-αSyn-Cu(II) complex (centred at N-terminus) and NAc-αSyn-Cu(II) complex (centred at His50).

I have determined that the Cu^{2+} binding affinity of WT-αSyn is around three times weaker than that of WT-Aβ. Whereas the affinity of NAc-αSyn is much lower, which is around four orders of magnitude weaker than that of WT-αSyn. Such large difference is due to the abolishment of the N-terminal high-affinity Cu^{2+} binding site by acetylation.

αSyn-Cu complex is considered to participate in the redox cycling to catalyse ROS production via its reduced αSyn-Cu(I) complex which is typically generated from the reductive metabolism of αSyn-Cu(II). There are multiple reductive pathways in human body. Here I have shown that ascorbate may not be in charge of the physiological reduction of αSyn-Cu(II) as the reduction is extremely inactive. By contrast, GSH presents relatively high reduction rate and could play a key role in the metabolism of αSyn-Cu(II) *in vivo*. However, the reduction mechanism could be complicated and further exploration is needed.

Finally I have shown that excess WT-αSyn can extract Cu^{2+} from Aβ-Cu(II). Considering the physiological concentration of αSyn is always higher than Aβ, this discovery could lead to a hypothesis that αSyn may act as a modulator of Aβ-Cu(II). In addition, I have shown that if WT-αSyn co-exists with HSA, the Cu^{2+} binding to αSyn will be prevented, suggesting that Cu^{2+} binding to αSyn is weaker than that to HSA.

Chapter 6

Interactions of α-Synuclein with Lipid Membranes

In Chapter 5, I have discussed the interactions between α-synuclein (αSyn) and an important synaptic metal – copper. In this Chapter, I move onto investigating how αSyn interacts with synaptic lipid membranes. So far, αSyn is extensively accepted as a membrane protein due to its localisation on synaptic vesicles, presence of similar structural repeats to apolipoproteins and multiple reported functional interactions with lipid membranes. Numerous studies have shown that αSyn can bind to lipid membranes via a double α-helical structure. However, many details about the binding structure such as the arrangement of these two helices and the interaction sites with lipid membranes are still under debate and obscure. Addressing these questions could be essential to comprehending the nature of αSyn-lipid interactions.

One of the major reported functions of αSyn is regulating the trafficking of synaptic vesicles. Synaptic vesicles are pivotal in neurotransmission. The bound αSyn on synaptic vesicles could reduce the mobility of them, and thus reducing the release of neurotransmitters. To understand and evaluate this functional regulation, the kinetic mechanism of the interactions between αSyn and synaptic vesicle needs to be elucidated,

and the determination of the binding affinity and binding rate constant of the interactions would be required.

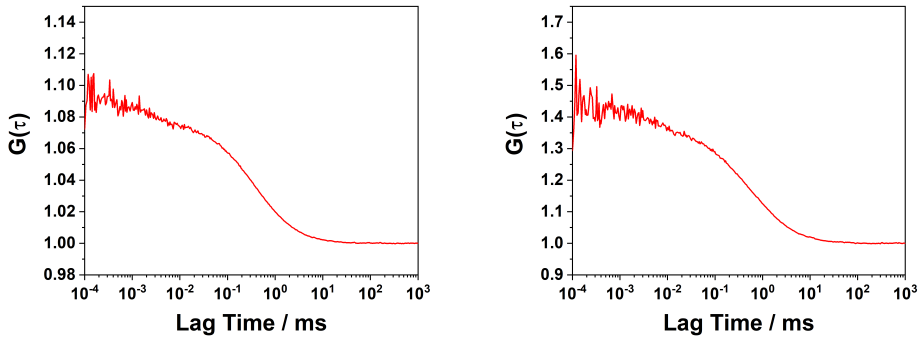
In this Chapter, a synthetic small unilamellar vesicle (SUV) system (size and lipid composition are similar to synaptic vesicles) is used as a model to mimic synaptic vesicles. FCS and FRET techniques are applied to investigate the lipid binding capability and binding structure of αSyn. The binding rate constant and affinity of αSyn with the synaptic-like SUV are determined using the fluorescence anisotropy method.

6.1 Interaction of αSyn with GM1 Micelle

Ganglioside GM1 is a negatively charged glycosphingolipid abundant in lipid rafts on membranes. In solution, GM1 forms micelles spontaneously when its concentration is above the critical micelle concentration (CMC) of 20 nM[314]. The micelle consists of 168(4) GM1 molecules and have a hydrodynamic radius of 5.67(6) nm based on a previous FCS measurement[315]. GM1 is reported to interact with αSyn and prevent the fibrillisation of αSyn[248]. However, the molecular understanding of how αSyn interacts with GM1 micelle has yet to be determined.

6.1.1 FCS of αSyn Binding to GM1 Micelle

To investigate how αSyn interacts with GM1 micelle, the first mission is to confirm whether αSyn could bind to GM1 micelle. This can be worked out by measuring the change of the diffusion time (τ_D) of labelled αSyn before and after interacting with GM1 micelle. FCS would be ideal for this purpose. Fig. 6.1 shows the FCS curves of Alexa 488 labelled WT-αSyn and BODIPY FL (BODIPY, Thermo Fisher Scientific) labelled GM1 micelle in free solution, and the values of τ_D were measured to be 0.34(3) ms for αSyn and 0.53(1) ms for GM1 micelle, respectively. It can be seen that αSyn diffuses faster than GM1 micelle. Thus, if αSyn binds to GM1 micelle, an increase in τ_D of αSyn would be observed.



(A) WT-αSyn (B) GM1 Micelle

Figure 6.1 FCS curves of labelled WT-αSyn and GM1 micelle. (A) WT-αSyn. **(B)** GM1 micelle. Approximately 5 nM labelled WT-αSyn or GM1 micelle was added in 50 mM HEPES and 100 mM NaCl buffer solution (pH 7.5) at 298 K for measurement. Data were obtained over 120 s acquisition time. For the measurement of WT-αSyn, 0.3 mg mL^{-1} BSA was pre-mixed in the buffer to coat the chamber surface.

Fig. 6.2 shows the FCS curve for labelled WT-αSyn which was incubated with GM1 micelle for 10 min, as well as the curves for freely diffusing WT-αSyn and GM1 micelle. Binding has occurred as indicated by the increase in diffusion time. The τ_D of αSyn-GM1 was determined to be 0.54(3) ms, larger than the value of freely diffusing αSyn and close to that of GM1 micelle. Thus, it is clear that αSyn is able to bind GM1 micelle.

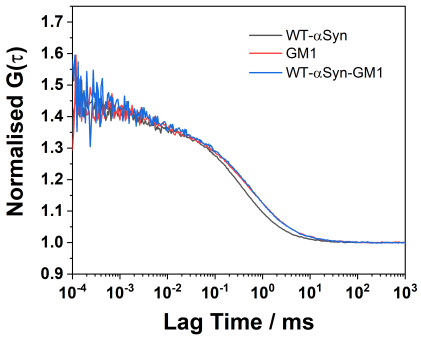
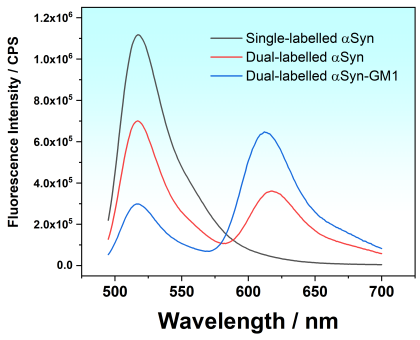


Figure 6.2 Comparison of the FCS curves for labelled WT-αSyn before and after the incubation with GM1 micelle. The curves show that WT-αSyn is able to bind GM1 micelle. The measurements were performed in 50 mM HEPES and 100 mM NaCl buffer solution at 298 K (pH 7.5). Data were obtained over 120 s acquisition time.

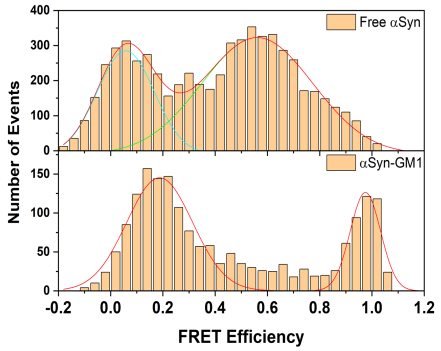
6.1.2 Binding Structure of αSyn on GM1 Micelle

Having confirmed the binding capability of αSyn to GM1 micelle, I next determined the binding structure of αSyn on GM1 micelle. The FRET technique was applied for this purpose. As introduced in Chapter 2, FRET is capable of measuring the distance between two interacting chromophores. Thereby it is powerful and particularly useful for investigating the structural arrangement of biomolecules, e.g., the arrangement of double α-helices of lipid-bound αSyn. In this work, αSyn is dual-labelled on the residue 9 and 94 which are mutated to cysteine and located separately in two α-helix regions as described in Chapter 4.

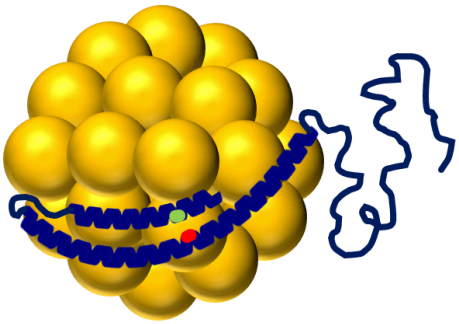
I first performed an ensemble FRET measurement to preliminarily explore the structural arrangement of αSyn on GM1 micelle. In the measurement, 50 nM dual-labelled WT-αSyn was mixed with 10 μM GM1 (~60 nM micelle). After 10 min incubation, the donor fluorophore was excited at 488 nm. The emission spectrum of αSyn-GM1 is shown in Fig. 6.3(A), with the emission spectrum of 50 nM dual-labelled αSyn in free solution for comparison. The higher acceptor emission peak and lower donor peak observed on the spectrum of αSyn-GM1 suggest that the fluorophores on GM1-bound αSyn manifest stronger FRET interactions than the same fluorophores on free αSyn. Thus, it can be inferred that the two α-helices of GM1-bound αSyn are arranged closer than those of free αSyn. Such arrangement may suggest an antiparallel helical structure for GM1-bound αSyn as shown in Fig. 6.3(C). In addition, the FRET efficiency histogram obtained from single-molecule FRET (smFRET) measurement of



(A) Ensemble FRET



(B) smFRET



(C) Binding Structure of WT-αSyn on GM1 Micelle

Figure 6.3 Determination of the binding structure of WT-αSyn on GM1 micelle using FRET techniques. (A) Ensemble FRET spectra. **(B)** smFRET histograms. **(C)** Diagram representation for the proposed binding structure of WT-αSyn on GM1 micelle. Both measurements give the evidence that the structure of GM1-bound WT-αSyn should be an antiparallel helix as shown. Two labelling positions are coloured with green and red. The measurements were performed in 50 mM HEPES and 100 mM NaCl buffer solution at 298 K (pH 7.5).

GM1-bound αSyn (Fig. 6.3(B)) shows abundant population with high FRET efficiency, further supporting the proposed antiparallel helical structure of αSyn on GM1 micelle.

After this, I performed a kinetic FRET study to explore the dynamic process of αSyn structural transformation during αSyn binding to GM1 micelle. The stopped flow technique was applied for this purpose. The measurement was conducted through monitoring the FRET induced fluorescence quenching of the donor, which was achieved by mounting a 510 – 560 nm emission bandpass filter (ET535/50m, Chroma Technology Corp) in front of the detector, as this filter only allows the donor emission to pass through. In the measurement, 50 nM dual-labelled WT-αSyn was mixed with various concentrations of GM1 lipid, and the donor quenching traces were recorded as a function of time (Fig. 6.4). The continuous quenching can be observed from the traces, indicating increasing FRET efficiency in the binding process. This may suggest that when αSyn binds to GM1 micelle, the two α-helices of αSyn will be bent, making donor and acceptor fluorophores approach each other and finally form an antiparallel helical structure.

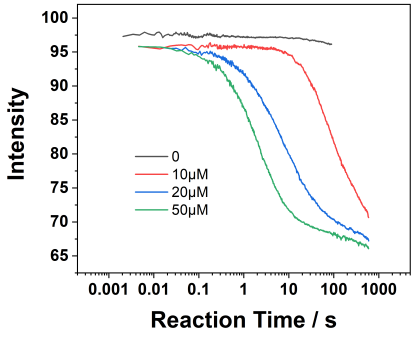


Figure 6.4 Kinetic fluorescence changing of the donor fluorophore on WT-αSyn during αSyn binding to GM1 micelle. The quenching under different lipid concentrations indicates increasing energy transfer from donor, suggesting that the donor and acceptor on WT-αSyn are approaching during the binding, which is due to the bending process of the bound αSyn. The experiments were performed in 50 mM HEPES and 100 mM NaCl buffer solution at 298 K (pH 7.5).

6.2 Interaction of αSyn with Synaptic-Like SUV

αSyn has been reported to functionally interact with synaptic vesicles. Such interactions could be essential for the regulation of synaptic transmission. However, the molecular interaction mechanism is not well-documented, especially regarding the structural arrangement of αSyn on synaptic vesicles and the interaction kinetics, which are key events that need to be addressed.

To study these, a sample of synaptic vesicle is required. Typically, researchers use unilamellar vesicles to mimic synaptic vesicles, as samples of natural synaptic vesicles are difficult to obtain. Thus far researchers have employed multiple unilamellar vesicle systems, among which a 50 nm diameter small unilamellar vesicle (SUV) system containing DOPE:DOPS:DOPC (5:3:2 w/w) is considered as a good mimic for synaptic vesicle due to its similar size and lipid composition. This SUV system is used throughout this work.

For a unilamellar vesicle, the number of constituting lipids (n) can be estimated by:

$$n = \frac{4\pi r^2 + 4\pi(r-l)^2}{a} \tag{6.1}$$

where r is the radius of vesicle, l is the bilayer thickness and a is the surface area per lipid molecule. The values of l and a for the employed SUV in this work have been reported to be ~5.2 nm and ~0.5 nm^2, respectively[236]. Thus, the number of constituting lipids (n) in one SUV can be calculated to be ~2.56×10^4.

6.2.1 FCS of αSyn Binding to SUV

To confirm whether αSyn could bind to SUV, the FCS technique was applied. The FCS curve of 50 nm NBD-DOPE labelled SUV is shown in Fig. 6.5. Since the actual sizes of 50 nm SUV are a distribution of sizes around 50 nm, rather than a unique size of 50 nm, the diffusion time (τ_D) of different SUVs could have variation. This can be analysed by an autocorrelation function accounting for multiple fluorescent species as introduced in Section 2.3.3, and here I applied a two species equation to describe fast and slowly diffusing species. The fitting indicated that ~96% of the species diffuses slowly, with τ_D of 5.90(5) ms, and the remaining ~4% diffuses fast with τ_D of 0.41(3) ms. These values gave the mean diffusion time of 5.68(5) ms for SUV, which is much larger than the τ_D of αSyn. Thus, when αSyn diffuses in the presence of SUV, it should be able to observe an obvious increase in τ_D of αSyn if αSyn could bind to SUV.

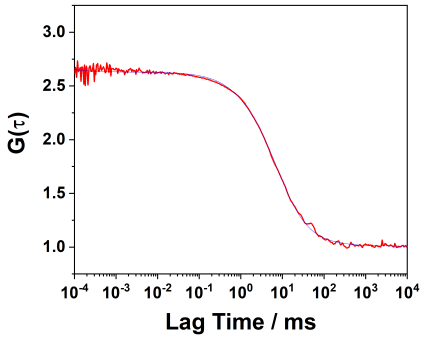


Figure 6.5 FCS curve of 50 nm labelled synaptic-like SUV. The fitted curve is shown as the blue curve. Approximately 1 mM total mixed lipid was added in 50 mM HEPES and 100 mM NaCl buffer solution (pH 7.5) at 298 K to measure. Data were obtained over 120 s acquisition time.

The FCS curve for labelled WT-αSyn which was incubated with SUV for 10 min is shown in Fig. 6.6, and the FCS curves for freely diffusing WT-αSyn and SUV are shown together for comparison. It can be seen that binding has occurred. The fitting

gave the mean τ_D of 5.61(3) ms, much larger than the value of freely diffusing αSyn and close to that of SUV, indicating that αSyn is able to bind to SUV.

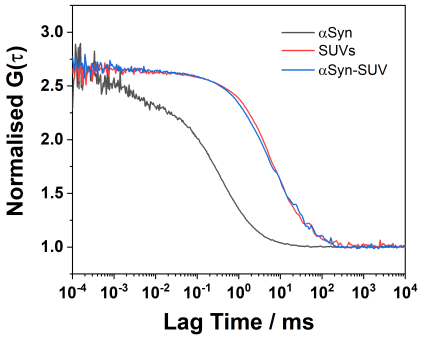


Figure 6.6 Comparison of the FCS curves for labelled WT-αSyn before and after the incubation with 50 nm synaptic-like SUV. The curves show that WT-αSyn is able to bind to SUV. The measurements were performed in 50 mM HEPES and 100 mM NaCl buffer solution at 298 K (pH 7.5). Data were obtained over 120 s acquisition time.

6.2.2 Binding Structure of αSyn on SUV

The structural arrangement of αSyn on unilamellar vesicle depends on many factors including lipid composition, membrane curvature and fluidity as well as the net charge of vesicle. In case of negatively charged SUVs, researchers have suggested that αSyn prefers to bind them via an antiparallel helical structure[231-232]. While for the synaptic-like SUV in this work, how αSyn molecules are arranged on the vesicle has yet to be studied.

Fig. 6.7 shows the far-UV CD spectra for free WT-αSyn and WT-αSyn in the presence of SUV. It is clear that α-helical structure is generated when WT-αSyn binds to SUV, as the $[\theta]_{220}$ of αSyn in the presence of SUV is much lower than that of free αSyn.

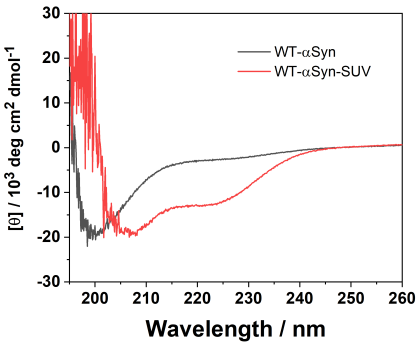
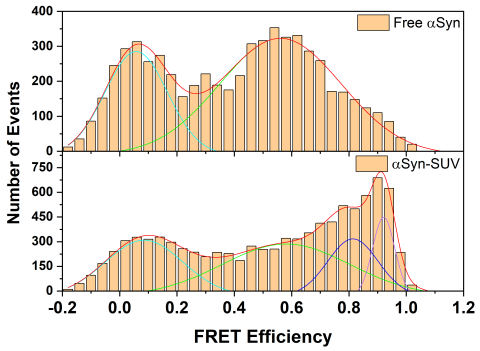
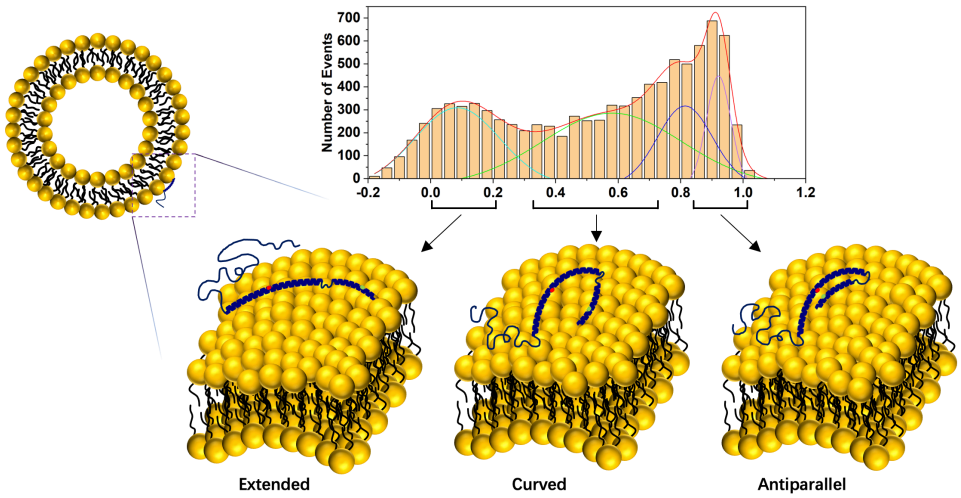


Figure 6.7 Far-UV CD spectra of WT-αSyn in the absence and presence of SUV. 15 μM αSyn was added in 1 mm cuvette to measure. The measurements were performed in 1× PBS buffer solution at 298 K (pH 7.5). Each spectrum is the average of 5 repeats.

To gain deeper insight into the binding structure of αSyn to SUV, the FRET technique was applied. I first used smFRET method to investigate the binding structure of one individual αSyn molecule on a single SUV. In the experiment, 5 nM dual-labelled WT-αSyn was mixed with 1 mM total lipid (~40 nM SUV). The excess SUV used here ensured that one SUV would only bind one αSyn and there would be negligible free αSyn. The mixture was incubated 10 min and diluted by a factor of 10 before measurement. Fig. 6.8(A) shows the FRET efficiency histogram. Compared with the histogram of αSyn in free solution, the histogram of individual αSyn bound to SUV displays multiple peaks at low, medium and high FRET efficiency. This indicates that single αSyn could bind to one SUV via mixed extended, curved or antiparallel helical structures as illustrated in Fig. 6.8(B).



(A) smFRET Histograms

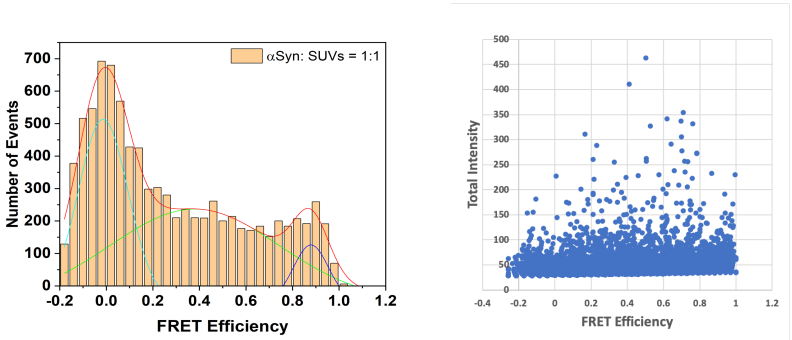


(B) Different Binding Structures of Single WT-αSyn Molecule on Synaptic-Like SUV

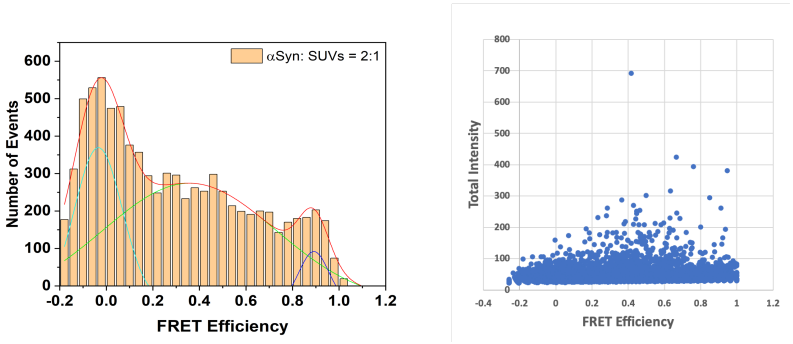
Figure 6.8 Determination of the binding structure of single WT-αSyn on synaptic-like SUV using smFRET technique. (A) smFRET histograms. A threshold of 40 counts was used to remove background. The lines represent Gaussian fits to data. Multiple peaks represent multiple binding structures of WT-αSyn. The measurements were performed in 50 mM HEPES and 100 mM NaCl buffer solution at 298 K (pH 7.5). **(B)** Diagram representation for the different suggested binding structures of WT-αSyn on SUV. Two labelling positions are coloured with green and red. Extended, curved and antiparallel helical structures of SUV-bound αSyn correspond to the histogram peaks at low, medium and high FRET efficiency, respectively.

As one synaptic vesicle can usually bind multiple αSyn monomers, the study of multiple αSyn binding to a single SUV could be more physiologically relevant, and the binding structure of αSyn would also need to be elucidated. For this purpose, I performed a series of smFRET measurements for SUV-bound αSyn under various αSyn to SUV ratios ranging from 1:1 to 100:1. In the experiments, 8 nM SUV (~205 μM total lipid) was mixed with various concentrations of dual-labelled WT-αSyn to form different ratios of αSyn-SUV conjugate. After 10 min incubation, all samples were diluted 16 times for the smFRET measurements. The laser power and threshold value were adjusted to avoid the bias in positive events selection when the number of labelled αSyn molecules per SUV increases. Approximately 8000 FRET events were collected for each sample. It should be mentioned that the measurements are more like "single-particle FRET" rather than smFRET, as there should be around one SUV particle with several labelled αSyn molecules in the field when the ratio of αSyn to SUV is higher

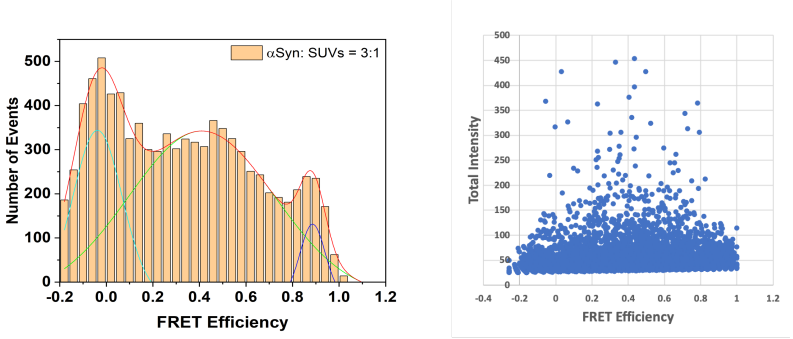
than 1:1. Thus, the collected FRET events are essentially the average FRET of labelled αSyn molecules detected in the field. Fig. 6.9 shows the FRET efficiency histograms, as well as the scatter graphs representing the correlation between FRET efficiency and total fluorescence intensity (sum of donor and acceptor signals). I noticed that the population exhibiting medium FRET efficiency gradually increases with the rise of the ratio of αSyn to SUV, and becomes the predominant population at high ratios. Whereas the high FRET efficiency population always decreases. This could be because when multiple αSyn monomers start to bind to one SUV, they prefer to use a curved helical structure to associate. Such conformation could be more natural than others for αSyn binding to SUV surface. After the initial binding, if αSyn concentration is not very high, the space of SUV surface will be enough for the bound αSyn to change structure to an antiparallel helical structure that is a more stable conformation for the binding of a small amount of αSyn on SUV. However, if αSyn concentration is very high, a large amount of αSyn will bind to SUV, and thus the space of SUV surface will be limited for αSyn conformational changing. Once the surface of SUV has been fully occupied, the structure of SUV-bound αSyn will no longer be able to change and only show the initial binding structure, i.e., the curved helical structure. In this experiment, such case is occurred when the ratio of αSyn to SUV reaches 45:1, as the shape of FRET histograms no longer changes after the ratio of 45:1. Therefore, this observation may indicate that the limitation for the number of αSyn on one SUV is around 45. In addition, as the population exhibiting medium FRET efficiency is predominant at high ratios of αSyn to SUV, rather than the population with high FRET efficiency, it is unlikely that the αSyn molecules detected under this condition can undergo oligomerisation on SUV.



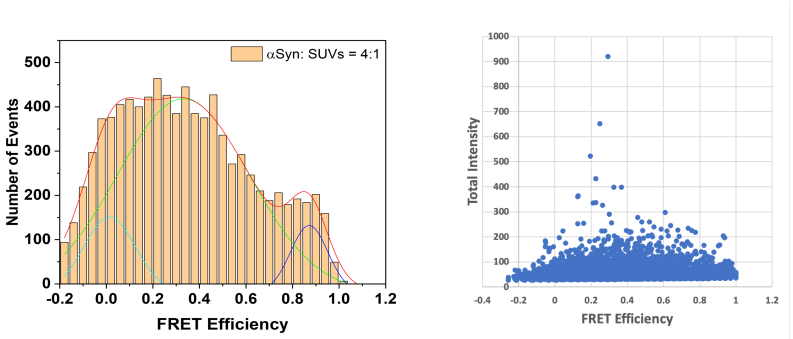
WT-αSyn: SUV = 1:1



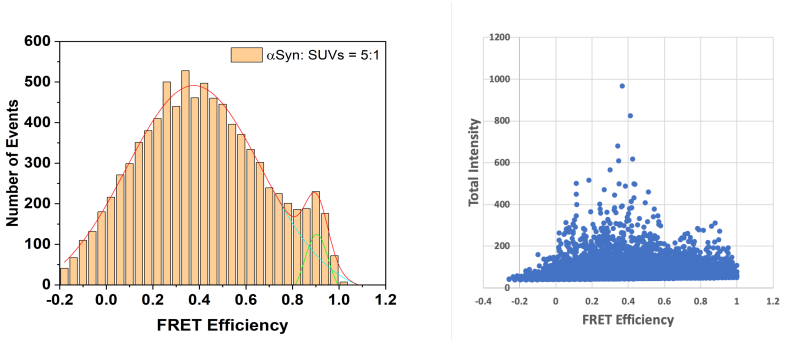
WT-αSyn: SUV = 2:1



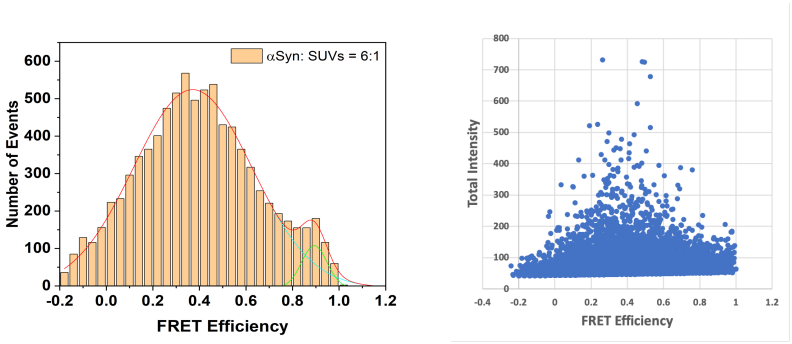
WT-αSyn: SUV = 3:1



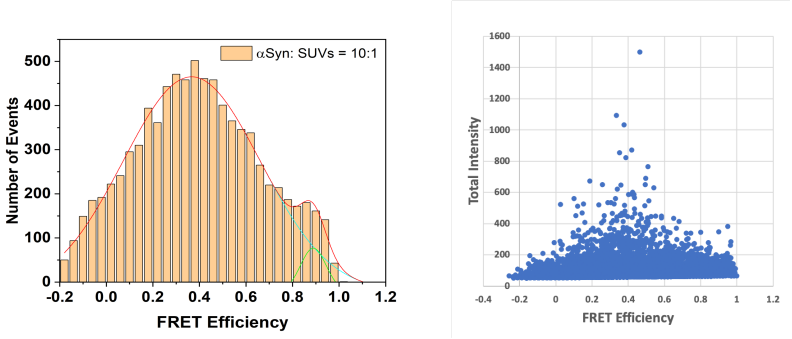
WT-αSyn: SUV = 4:1



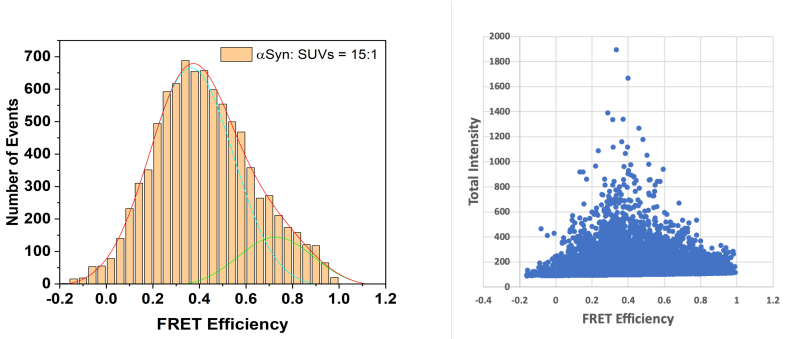
WT-αSyn: SUV = 5:1



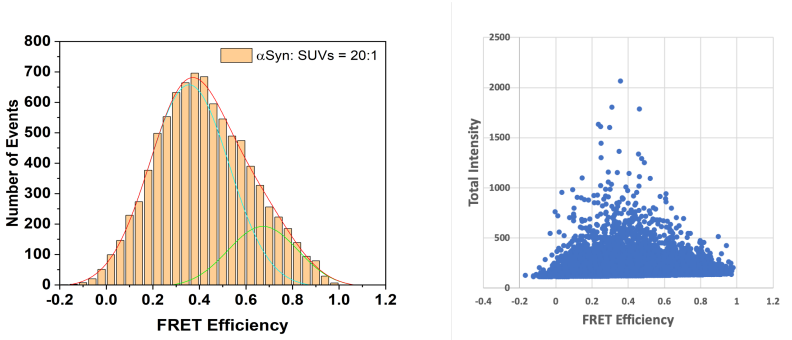
WT-αSyn: SUV = 6:1



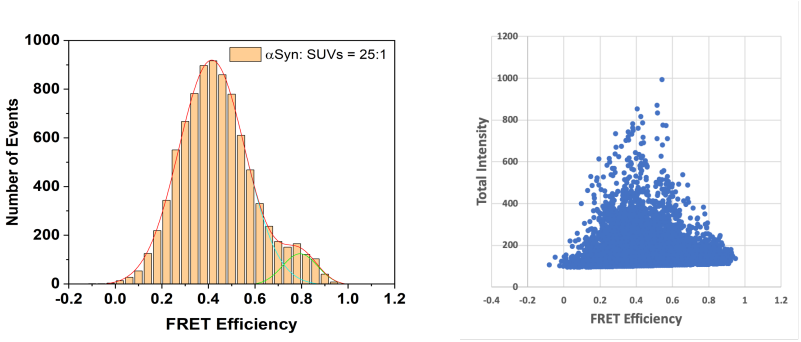
WT-αSyn: SUV = 10:1



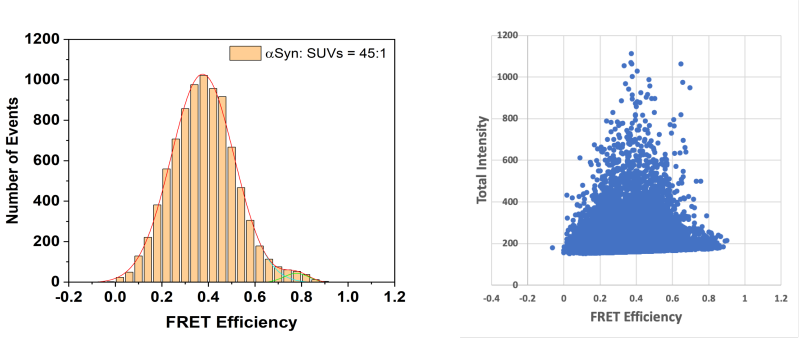
WT-αSyn: SUV = 15:1



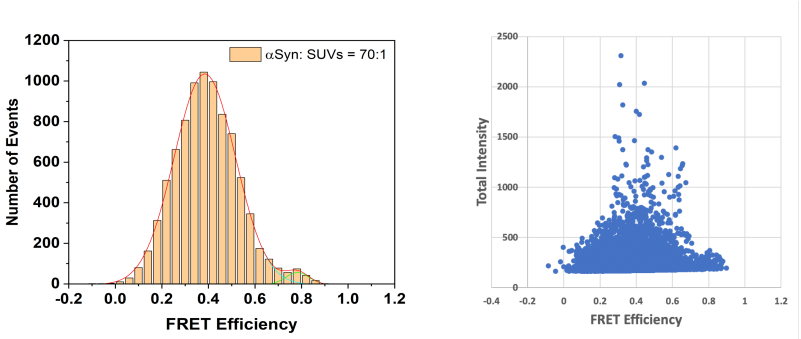
WT-αSyn: SUV = 20:1



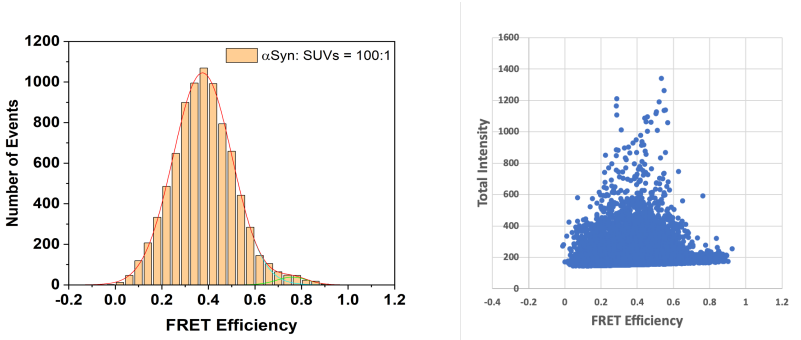
WT-αSyn: SUV = 25:1



WT-αSyn: SUV = 45:1



WT-αSyn: SUV = 70:1

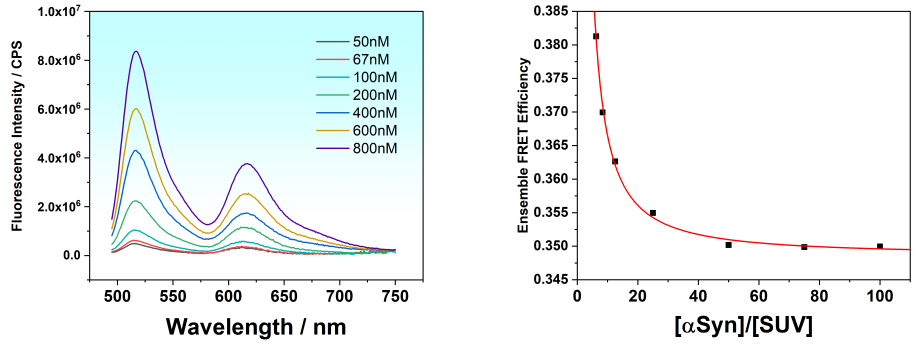


WT-αSyn: SUV = 100:1

Figure 6.9 Determination of the binding structure of multiple WT-αSyn on synaptic-like SUV under different ratios of αSyn to SUV. The lines on smFRET histograms represent Gaussian

fits to data. The peak at medium efficiency becomes predominant when αSyn concentration is high, which corresponds to a curved helical structure of SUV-bound αSyn. Whereas the peak at high efficiency which corresponds to an antiparallel helical structure of SUV-bound αSyn is diminishing upon increasing αSyn. Scatter diagrams illustrate the signal intensity distribution for the detected FRET events. The measurements were performed in 50 mM HEPES and 100 mM NaCl buffer solution at 298 K (pH 7.5).

Such inferences can also be validated by the ensemble FRET measurement. 8 nM SUV (~205 μM total lipid) was mixed with various concentrations of dual-labelled WT-αSyn. After 10 min incubation, the samples were excited using 488 nm light and the emission spectra were recorded (Fig. 6.10(A)). The peak area of acceptor emission was divided by the sum of the peak area of donor and acceptor emission to obtain the total FRET efficiency, and the determined FRET efficiency was plotted against the ratio of αSyn to SUV as shown in Fig. 6.10(B). It can be seen that the total FRET efficiency decreases upon increasing ratio of αSyn to SUV until the ratio reaches ~50:1, where the total FRET efficiency starts to remain steady. Such results are in agreement with the results of smFRET, as it can be observed from smFRET histograms that the peak at high FRET efficiency gradually shrinks upon increasing ratio of αSyn to SUV until the ratio reaches 45:1.



(A) Ensemble FRET Spectra

(B) Ensemble FRET Efficiency

Figure 6.10 Ensemble FRET measurements of SUV-bound WT-αSyn under different ratios of αSyn to SUV. (A) Ensemble FRET spectra under various concentrations of labelled WT-αSyn. The measurements were performed in 50 mM HEPES and 100 mM NaCl buffer solution at 298 K (pH 7.5). **(B)** Ensemble FRET efficiency. The decreasing trend suggests that the SUV-bound WT-αSyn presenting high FRET efficiency, i.e., the antiparallelly structured αSyn, is diminishing upon increasing αSyn concentration. When αSyn concentration is raised to an [αSyn]: [SUV] value of 50, the structure of SUV-bound WT-αSyn will no longer change.

In smFRET histograms, it is worth noting that at very high ratios of αSyn to SUV (≥ 45:1), a small population with high FRET efficiency is always present. The signal intensity distribution diagrams in Fig. 6.9 show that these high FRET events are distributed at low total fluorescence intensity, implying fewer detected αSyn molecules on the SUV than expected. Since all SUVs should be saturated with αSyn at such high ratios of αSyn to SUV, the events with lower number of detected αSyn could come from the small sized SUVs as these SUVs can only accommodate a small number of αSyn. Therefore, I infer that the high FRET events at high ratios of αSyn to SUV should come from the αSyn that is bound on the super small vesicles. While the αSyn on normal sized vesicles (50 nm diameter) presents medium FRET efficiency.

Finally, I studied the dynamic structural transformation of αSyn during the binding to SUV. An analogous kinetic FRET measurement as described in Section 6.1.2 was performed to determine this. 50 nM dual-labelled WT-αSyn was mixed with 205 μM and 410 μM total lipid (approximately 8 nM and 16 nM SUV), and the traces were recorded as function of time (Fig. 6.11). The traces show an increase and then a decline

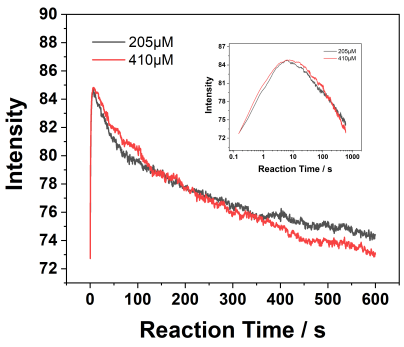


Figure 6.11 Kinetic fluorescence changing of the donor fluorophore on WT-αSyn during αSyn binding to synaptic-like SUV. The traces under different lipid concentrations indicate that the FRET interaction between donor and acceptor is initially reduced and then increased during the binding, suggesting that the two fluorophores on WT-αSyn are initially moved away and then pulled close to each other, which is because the bound αSyn is initially extended and then bent during the binding. The traces plotted in log scale are shown in the inset to visualise the change at initial short timescales. The experiments were performed in 50 mM HEPES and 100 mM NaCl buffer solution at 298 K (pH 7.5).

in intensity, indicating that the energy transfer from donor to acceptor fluorophores decreases first and then increases. This could be because the two α-helices of αSyn are initially rather extended when they bind to SUV, and subsequently these two helices bend, making the two α-helices closer to each other. It is notable that the donor intensity at the end and at the beginning of the traces are very similar. This indicates that the FRET efficiency of the stabilised αSyn on SUV should be comparable to that of free αSyn, i.e., presenting medium FRET efficiency. Thus, the predominant conformation of the SUV-bound αSyn is likely to possess a curved helical structure, which is consistent with the result obtained from smFRET measurement described above.

6.2.3 Fluorescence Anisotropy Titration of αSyn Binding to SUV

Having determined the binding structure of αSyn on SUV, I next performed fluorescence anisotropy titrations to determine the binding affinity of αSyn with SUV. In the measurements, 100 nM G7C labelled αSyn was titrated against various concentrations of the mixed lipid, and fluorescence anisotropy values were recorded by a fluorometer. Fig. 6.12 shows the anisotropy titration curves for different αSyn samples, which are fitted by the Hill-Langmuir equation, and the derived dissociation constants (K_d) are summarised in Table 6.1. K_d values indicate that the membrane affinity of H50Q αSyn is ~25% stronger than that of WT-αSyn, and the affinity of NAc-αSyn is over three times stronger than that of WT-αSyn.

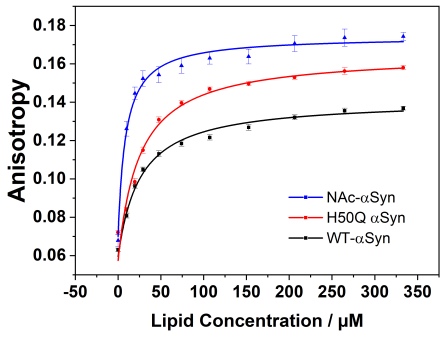


Figure 6.12 Fluorescence anisotropy titrations of different αSyn binding to synaptic-like SUV. Each data point was obtained by the average of 10 repeats. The measurements were performed in 50 mM HEPES and 100 mM NaCl buffer solution at 298 K (pH 7.5). Error bars represent standard deviation of 10 measurements.

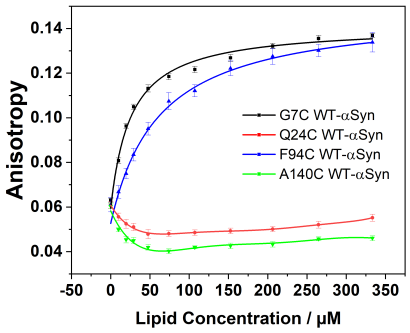
Table 6.1 Dissociation constants of different αSyn binding to synaptic-like SUV. Data obtained from fits in Figure 6.12.

	WT-αSyn	H50Q αSyn	NAc-αSyn
K_d / μM	26(5)	19(4)	8(2)

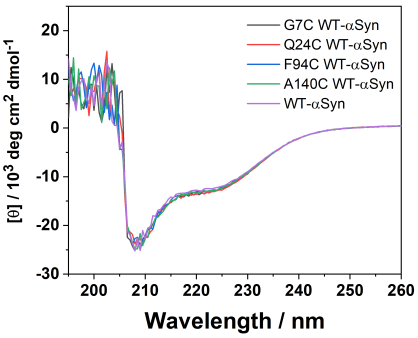
It should be emphasised that the chemical environment of the fluorophores can impact fluorescence anisotropy significantly, which could be the reason why these three αSyn samples present different fluorescence anisotropy values under the same conditions. Indeed, a recent study has reported that the first 14 amino acids of NAc-αSyn can insert into the membrane ~2 Å deeper than that of WT-αSyn[126]. H50Q αSyn may also undergo this situation but to a lesser extent when it associates with SUV, causing variations of the environment surrounding the fluorophores and raising the value of fluorescence anisotropy.

Such correlation between chemical environment and fluorescence anisotropy of the fluorophore can also be utilised to study the membrane binding of specific sites of αSyn. Multiple cysteine variants of WT-αSyn (G7C, Q24C, F94C and A140C) were produced and the cysteine sites were labelled with Alexa 488 maleimide dye. Analogous titration measurements were then conducted. The anisotropy titration curves for these specific site-labelled αSyn are shown in Fig. 6.13(A). Control experiments were carried out using CD spectroscopy to confirm that cysteine mutation has no effect on the membrane binding structure of αSyn (Fig. 6.13(B)). As expected, different site-labelled αSyn samples exhibit different fluorescence anisotropy, indicating different environments surrounding these labelled sites. A140C labelled αSyn displays the lowest and random fluorescence anisotropy values, which is in agreement with the accepted view that the C-terminus of αSyn does not bind to SUV so that lipid membrane has negligible effect on the rotation of dye label in solution. In addition, compared with G7C labelled αSyn, F94C labelled αSyn displays lower fluorescence anisotropy and affinity (K_d = 59(3) μM), which could be because the region around residue 94 of αSyn is just loosely attached on the membrane. The most surprising finding comes from the result of Q24C labelled αSyn, of which the fluorescence anisotropy values were

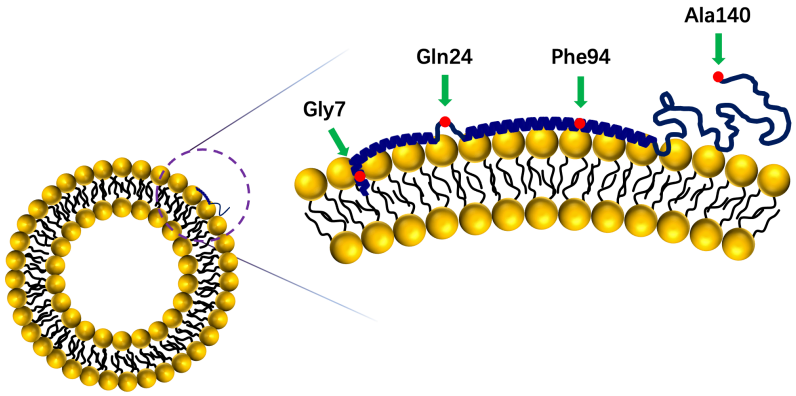
anticipated to be similar with the values of G7C labelled αSyn, as the residue 24 was believed to bind with membranes as well. However, the observed random values may suggest that the region around residue 24 of αSyn acts more like the C-terminus of αSyn, i.e., it does not bind to SUV. Whereas its fluorescence anisotropy values seem still larger than those of C-terminus labelled αSyn, which could be because the membrane bindings of adjacent regions restrict its free rotation. A summary for the proposed membrane binding forms of these specific sites of αSyn are illustrated in Fig. 6.13(C).



(A) Fluorescence Anisotropy Titrations



(B) CD Spectra

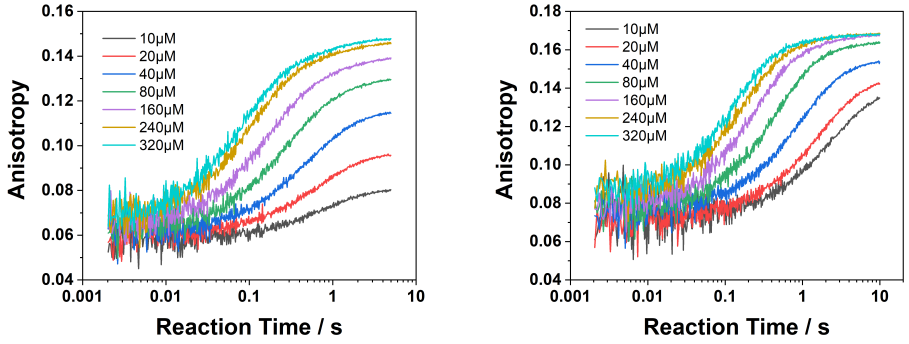


(C) Binding Forms of Specific Sites of WT-αSyn on Synaptic-Like SUV

Figure 6.13 Determination of the binding form of specific sites of WT-αSyn on synaptic-like SUV using fluorescence anisotropy. (A) Fluorescence anisotropy titration curves of different site-labelled WT-αSyn binding to SUV. The random anisotropy values of Q24C and A140C labelled αSyn may indicate that the residue 24 and 140 of SUV-bound WT-αSyn are not attached on SUV. The measurements were performed in 50 mM HEPES and 100 mM NaCl buffer solution at 298 K (pH 7.5). **(B)** CD spectra of different cysteine variants of SUV-bound WT-αSyn. The spectra show that the listed cysteine mutations have no effect on the membrane binding structure of WT-αSyn. The measurements were performed in 1× PBS buffer solution at 298 K (pH 7.5). **(C)** Diagram representation for the proposed membrane binding forms of the listed sites of WT-αSyn.

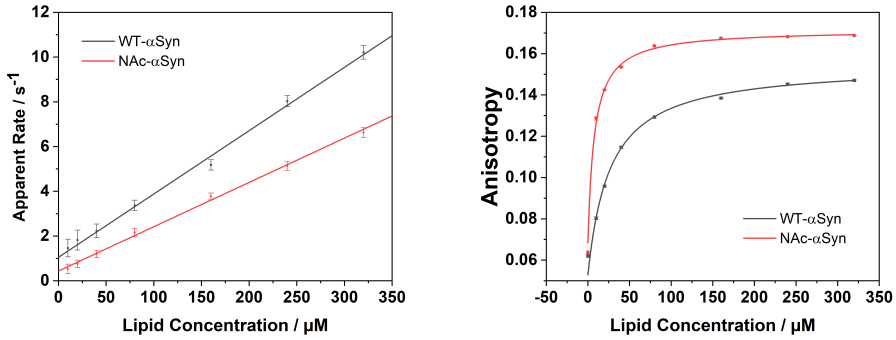
6.2.4 Kinetics of αSyn Binding to SUV by Fluorescence Anisotropy

The time-dependent increase of fluorescence anisotropy in the binding process of αSyn to SUV could be utilised to determine the lipid binding rate constant of αSyn. The stopped flow technique was employed for this purpose. 50 nM labelled αSyn was mixed with various concentrations of lipid, and the fluorescence anisotropy increase was recorded as a function of time. Fig. 6.14(A) shows such raw traces for WT-αSyn and NAc-αSyn. The slopes of fitted data (Fig. 6.14(B)) were used to determine the lipid binding rate constants, which are 2.91(6) × 10^4 M^{-1} s^{-1} and 1.98(4) × 10^4 M^{-1} s^{-1} for WT-αSyn and NAc-αSyn, respectively.



WT-αSyn NAc-αSyn

(A) Raw Kinetic Anisotropy Traces



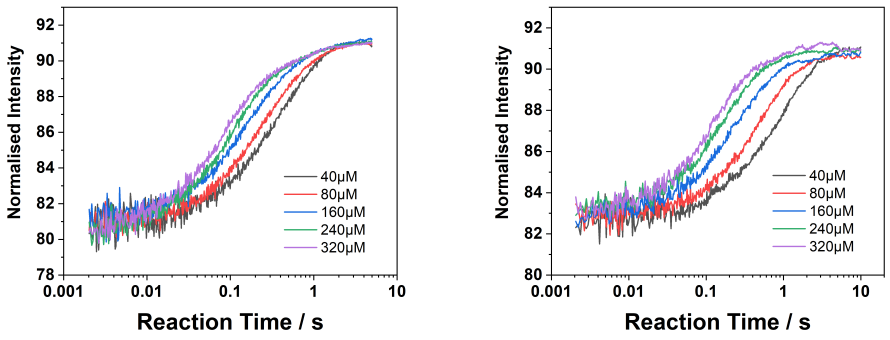
(B) Apparent Binding Rates (C) Final Anisotropy at Plateau

Figure 6.14 Kinetics of αSyn (both WT and NAc forms) binding to SUV determined by fluorescence anisotropy. (A) Raw kinetic anisotropy traces of αSyn binding to various concentrations of SUV (shown in the concentrations of lipid). The experiments were performed in 50 mM HEPES and 100 mM NaCl buffer solution at 298 K (pH 7.5). **(B)** Apparent binding rates of αSyn to SUV. **(C)** Final anisotropy from the fits as a function of SUV concentration (shown in the

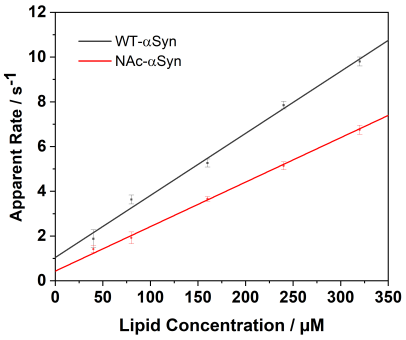
concentrations of lipid). The plots were fitted to derive the binding affinity values of αSyn to SUV, giving similar results to the values determined by anisotropy titration experiments. Error bars represent the uncertainty in the values determined from fits.

In addition, the plateau values derived from the traces were used as the final values of fluorescence anisotropy to build a theoretical "titration" curve to obtain the binding affinity of αSyn with SUV (Fig. 6.14(C)). The K_d values for membrane binding of WT-αSyn and NAc-αSyn were determined to be 26(3) μM and 8(3) μM, respectively, which are consistent with the K_d values derived from the fluorescence anisotropy titration experiments.

It is worth mentioning that the fluorescence intensity of the labelled αSyn also increases during αSyn binding to SUV, as shown in Fig. 6.15(A). The increase in rate is dependent on the concentration of SUV. Fig. 6.15(B) shows the linear fit for the rate



(A) Normalised Fluorescence Traces



(B) Apparent Binding Rates

Figure 6.15 Kinetics of αSyn (both WT and NAc forms) binding to SUV determined by fluorescence intensity. (A) Normalised fluorescence traces of αSyn binding to various

concentrations of SUV (shown in the concentrations of lipid). The experiments were performed in 50 mM HEPES and 100 mM NaCl buffer solution at 298 K (pH 7.5). **(B)** Apparent binding rates of αSyn to SUV. The derived binding rate constants of αSyn to SUV are almost the same as the values determined by the kinetic anisotropy experiments. Error bars represent the uncertainty in the values determined from fits.

against the concentration of lipid. The slopes give the rate constants of 2.89(5) × 10^4 M^{-1} s^{-1} for WT-αSyn and 1.99(2) × 10^4 M^{-1} s^{-1} for NAc-αSyn, which are almost the same as the lipid binding rate constants determined by the kinetic measurements of anisotropy as described above. Such results may suggest that the Alexa 488 dye could be used as a probe for lipid binding, showing how protein interacts with lipid membrane by the change of fluorescence intensity.

6.2.5 Binding of WT-αSyn to Cholesterol-Containing SUVs

Cholesterol is a vital component of synaptic vesicles, contributing ~21.4% of the total lipid contents. To study whether cholesterol has an impact on the binding of WT-αSyn to SUV, CD measurements of WT-αSyn binding to various cholesterol-containing SUVs were performed (Fig. 6.16). As can be observed, the cholesterol in SUVs does not seem to affect the binding so much, except that its percentage reaches 50%. This indicates that the normal level of cholesterol in SUV may not impact the α-helical structure formation of WT-αSyn during αSyn binding to SUV.

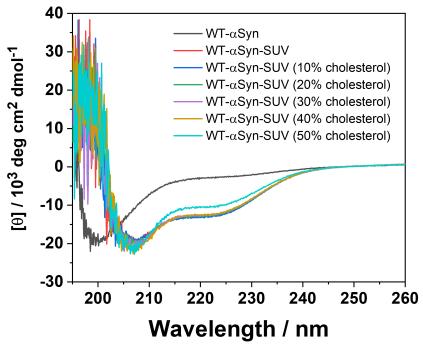


Figure 6.16 Far-UV CD spectra of WT-αSyn in SUVs containing different levels of cholesterol. 15 μM αSyn was mixed with various cholesterol-containing SUVs (1 mM total lipid) in 1 mm cuvette to measure. The measurements were performed in 1× PBS buffer solution at 298 K (pH 7.5). Each spectrum is the average of 5 repeats.

I next conducted fluorescence anisotropy titration experiments to investigate such effect on membrane binding affinity of WT-αSyn. Fig. 6.17 shows the fitted anisotropy curves, and the determined K_d values are summarised in Table 6.2. Compared with the K_d of αSyn binding to cholesterol-free SUV, the values of αSyn binding to cholesterol-containing SUVs are smaller, indicating stronger affinity. In addition, although the differences are slight, the K_d values of αSyn binding to different cholesterol-containing SUVs still show a decrease upon increasing cholesterol level, suggesting that cholesterol could strengthen αSyn binding to SUV. Such result has not been observed

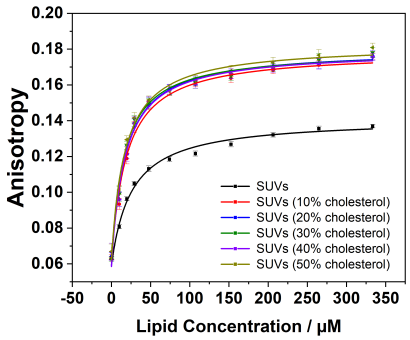


Figure 6.17 Fluorescence anisotropy titrations of WT-αSyn binding to different cholesterol-containing SUVs. Each data point was obtained by the average of 10 repeats. The measurements were performed in 50 mM HEPES and 100 mM NaCl buffer solution at 298 K (pH 7.5).

Table 6.2 Dissociation constants of WT-αSyn binding to different cholesterol-containing SUVs. Data obtained from fits in Figure 6.17.

Cholesterol content / %	0	10	20	30	40	50
K_d / μM	26(5)	19(8)	17(6)	16(6)	15(5)	14(6)

from the CD measurements above, which may indicate that the binding affinity of WT-αSyn to SUV is independent on the α-helical structure formation of WT-αSyn.

I also performed a preliminary test about cholesterol effect on NAc-αSyn binding to SUV using fluorescence anisotropy titration. Interestingly, the affinity seems to be reduced by cholesterol, which is different from WT-αSyn (Fig. 6.18, the K_d of NAc-αSyn binding to 10% cholesterol-containing SUV and 40% cholesterol-containing SUV

are 24(9) μM and 13(6) μM, respectively, which are greater than the K_d of NAc-αSyn binding to normal SUV). It is worth performing more experiments to investigate this effect in detail in future.

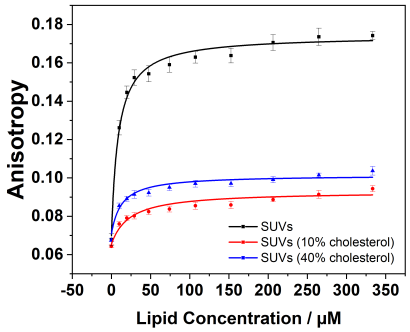


Figure 6.18 Fluorescence anisotropy titrations of NAc-αSyn binding to different cholesterol-containing SUVs. Each data point was obtained by the average of 10 repeats. The measurements were performed in 50 mM HEPES and 100 mM NaCl buffer solution at 298 K (pH 7.5).

6.3 Summary

In this Chapter, I have shown that WT-αSyn can bind to GM1 micelle via an antiparallel helical structure. However, when binding to synaptic-like SUV, single WT-αSyn displays a mixture of extended, curved and antiparallel helical structures. Furthermore, in case of multiple αSyn molecules binding to one SUV, αSyn predominantly displays a curved helical structure.

Using fluorescence anisotropy methods, I have found that NAc-αSyn and H50Q WT-αSyn both show higher SUV membrane binding affinity than WT-αSyn, of which NAc-αSyn has the highest affinity. This indicates that both N-terminal acetylation and H50Q mutation of αSyn could affect its binding to synaptic-like SUV. Furthermore, I have determined the SUV membrane binding rate constants of WT-αSyn and NAc-αSyn by conducting kinetic measurements via fluorescence anisotropy. Considering the potential role of αSyn in regulating the mobility of synaptic vesicles, these parameters could be crucial references for the understanding of regulation mechanism.

Fluorescence anisotropy is related to the molecular environments surrounding fluorophores. Based on this, I have predicted the potential SUV membrane attaching

forms for some specific sites of WT-αSyn, including the residue 7, 24, 94 and 140. This provides new details about the membrane binding structure of αSyn.

I have also shown that cholesterol can enhance the binding affinity of WT-αSyn to SUV. However, the physiological cholesterol level in SUV seems not an important factor for the binding. Conversely, for NAc-αSyn binding to SUV, cholesterol shows the opposite effect, reducing the binding affinity. More investigations would need to be carried out to establish the modulation mechanisms of cholesterol on αSyn binding to SUV.

Overall, this Chapter has delved into the binding of αSyn to lipid membranes from the direction of αSyn binding structure and affinity. The study provides insights into the interaction mechanisms of αSyn with lipid membranes and could be useful for clarifying the physiological and pathological roles of αSyn.

Chapter 7

Interactions of Lipid Membranes with Cu^{2+}

Lipid membranes and copper are both crucial in neurotransmission. Nonetheless, the interactions between them have been poorly investigated. Thus far researchers put their focus mainly on the proteins on membranes to explore the interactions of synaptic membranes with copper. However, the role of lipid membrane itself has been largely ignored.

In the brain, copper is believed to be predominantly protein-bound, and transferred by synaptic vesicle in the secretory pathway. However, a previous study has suggested that phosphatidylserine (PS), which is a major lipid component of synaptic vesicle, possesses extremely high affinity with Cu^{2+} (K_d in the picomolar regime)[215]. This leads to a hypothesis that the synaptic vesicle may be able to bind and transfer Cu^{2+} by itself without the implication of proteins. More details are needed to understand the mechanisms.

In this Chapter, the Cu^{2+} affinity of synaptic-like SUV as well as the reduction of SUV-Cu(II) conjugate are investigated using stopped flow. The potential role of synaptic vesicle in copper transportation is illuminated.

7.1 Quenching of Labelled SUV by Cu^{2+}

The fluorescent SUV samples were prepared by mixing NBD-DOPE with the DOPE:DOPS:DOPC (5:3:2 w/w) lipid mixture at a molar ratio of ~1:1000. The procedures are described in Chapter 2. Similar to other fluorescently labelled Cu^{2+}-binding proteins/peptides, prior to conducting the study, the Cu^{2+} induced fluorescence quenching level of the labelled SUV needs to be examined. Fig. 7.1 shows the emission spectra of the labelled SUV (1 mM total lipid) with and without adding 100 μM $CuCl_2$ under excitation at 473 nm. A clear fluorescence quenching can be observed upon the addition of Cu^{2+}, indicating that Cu^{2+} can bind to the synaptic-like SUV. The quenching level was calculated to be ~52%. Such level is large enough for the detection of the interaction process between Cu^{2+} and the labelled SUV.

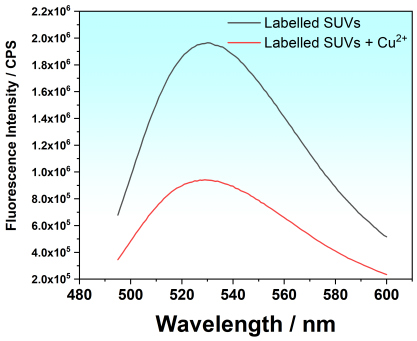


Figure 7.1 Fluorescence quenching of labelled synaptic-like SUV after mixing with Cu^{2+}. Obvious quenching can be observed from the emission spectra when the labelled SUV was treated with Cu^{2+}. The measurements were performed in 50 mM HEPES and 100 mM NaCl buffer solution at 298 K (pH 7.5).

7.2 Interactions of Cu^{2+} with Different Lipid-Constituted SUVs

To study the interactions between SUV and Cu^{2+}, it is necessary to complete a controlled experiment to identify which lipid constituent in SUV can interact with Cu^{2+}. For this purpose, labelled SUV samples containing various lipid compositions were prepared. The labelled SUV samples (100 μM total lipid) were mixed with 500 nM $CuCl_2$, and the binding reaction traces were recorded as function of time (Fig. 7.2). The figure shows that only SUVs containing DOPS display significant fluorescence

quenching, suggesting that DOPS is the sole Cu^{2+}-reactive lipid constituent in the synaptic-like SUV.

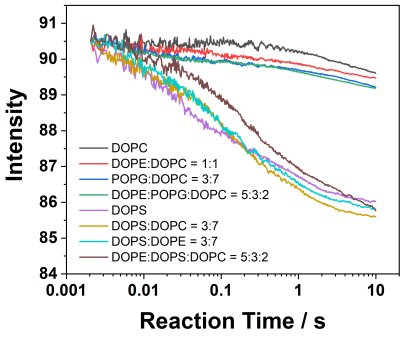


Figure 7.2 Comparison of Cu^{2+} binding to the SUVs containing different lipid compositions. Only DOPS-containing SUVs show significant interactions with Cu^{2+}. The measurements were performed in 50 mM HEPES and 100 mM NaCl buffer solution at 298 K (pH 7.5).

7.3 FCS of SUV in the Presence of Cu^{2+}

Metal ions could have effect on the curvature of lipid vesicles. To confirm whether Cu^{2+} could impact the size of synaptic-like SUV, FCS technique was applied to monitor the change of the diffusion time (τ_D) of labelled SUV before and after mixing with Cu^{2+}. Such FCS curves are shown in Fig. 7.3. It can be seen that the FCS curves display

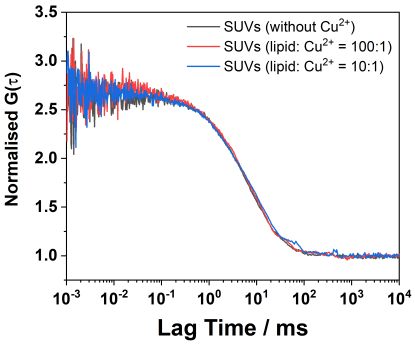


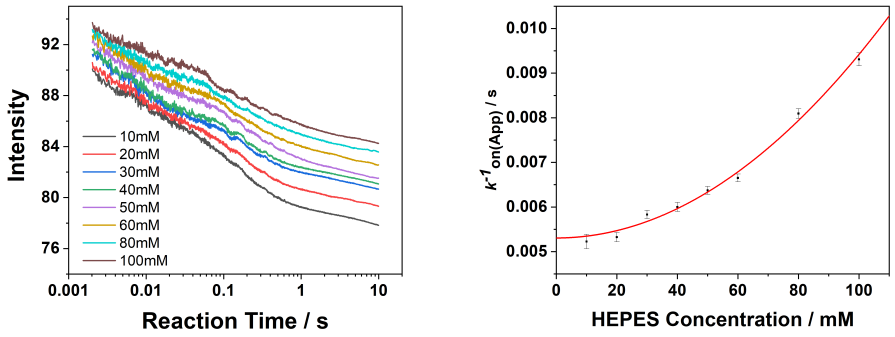
Figure 7.3 Comparison of the FCS curves for labelled synaptic-like SUV in the absence and presence of Cu^{2+}. The curves show that Cu^{2+} binding does not affect the size of SUV. The measurements were performed in 50 mM HEPES and 100 mM NaCl buffer solution at 298 K (pH 7.5). Data were obtained over 120 s acquisition time.

identical shape. In fact, the τ_D for labelled SUV in the presence of Cu^{2+} were determined to be 5.69(2) ms under 100:1 molar ratio of SUV lipid to Cu^{2+} and 5.70(4) ms under

10:1 molar ratio of SUV lipid to Cu^{2+}, which are very similar to the τ_D of 5.68(5) ms for labelled SUV in the absence of Cu^{2+}. This suggests that Cu^{2+} binding to SUV will not change the size of SUV.

7.4 Kinetic Studies of the Interactions between SUV and Cu^{2+}

The kinetic parameters would be essential and helpful for our comprehension of the interaction mechanisms. To determine these parameters, stopped flow was employed. I first determined the association rate constant (k_{on}) of Cu^{2+} binding to SUV. The labelled SUV (100 μM total lipid containing 30 μM DOPS) was mixed with 1 μM $CuCl_2$ under various HEPES concentrations to derive HEPES independent k_{on}. The raw traces shown in Fig. 7.4(A) were fitted with multi-exponentials as described in Chapter 3 to obtain association rates. k_{on} was obtained from the fitted data, which is 6.3(3) × 10^6 M^{-1} s^{-1} (Fig. 7.4(B)).



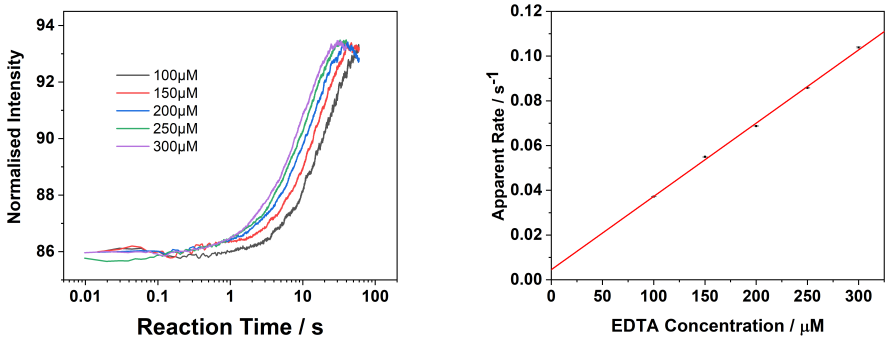
(A) Raw Traces

(B) HEPES Dependence of $k_{on(App)}$

Figure 7.4 Kinetics of Cu^{2+} binding to synaptic-like SUV. (A) Raw traces of SUV binding with Cu^{2+} under various concentrations of HEPES. The experiments were performed in HEPES and 100 mM NaCl buffer solution at 298 K (pH 7.5). **(B)** HEPES dependence of $k_{on(App)}$. The HEPES independent k_{on} value is 6.3(3) × 10^6 M^{-1} s^{-1}.

Subsequently, I determined the Cu^{2+} dissociation rate constant (k_{off}) of SUV-Cu(II) conjugate. In the measurement, the labelled SUV (100 μM total lipid) was pre-mixed with 1 μM $CuCl_2$ to form SUV-Cu(II) conjugate. Then the solution was treated with various concentrations of EDTA. Such traces are shown in Fig. 7.5(A). The intercept of linearly fitted data gave the value of k_{off} to be 4.6(5) × 10^{-3} s^{-1} (Fig. 7.5(B)).

Combined with the determined k_{on}, the dissociation constant (K_d) of Cu^{2+} binding to SUV can be calculated to be 0.7(1) nM. Such value is lower than those of WT-Aβ and αSyn. A strong Cu^{2+} binding affinity of synaptic-like SUV is consequently verified.



(A) Normalised Traces (B) Apparent Dissociation Rates

Figure 7.5 Kinetics of Cu^{2+} dissociation from SUV-Cu(II). (A) Normalised traces of Cu^{2+} dissociation from SUV-Cu(II) under various concentrations of EDTA. The experiments were performed in 50 mM HEPES and 100 mM NaCl buffer solution at 298 K (pH 7.5). **(B)** Apparent dissociation rates of Cu^{2+} by EDTA from SUV-Cu(II). The EDTA independent k_{off} value is 4.6(5) $\times 10^{-3}$ s^{-1}.

The linear fitting shown in Fig. 7.5(B) can also give the second-order rate constant for SUV-Cu(II) dissociation by EDTA from the slope. The value was determined to be 313(5) M^{-1} s^{-1}, which is over five times lower than that of αSyn-Cu(II) complex. Thus the Cu^{2+} bound on SUV-Cu(II) is much more difficult to be dissociated by a second ligand than the Cu^{2+} on αSyn-Cu(II) as well as WT-Aβ-Cu(II) complex.

7.5 Cu^{2+} Binding Mode of SUV

To determine how Cu^{2+} binds to SUV, an X-band EPR measurement was carried out. SUV sample (15 mM total lipid) was mixed with 50 μM $CuCl_2$, and then the sample was flash-frozen with liquid helium for measurement. The spectrum is shown in Fig. 7.6. The $g_{\parallel}$ factor and hyperfine coupling constant ($A_{\parallel}$) obtained by spectral simulation were 2.262, 203 G respectively. Using Peisach-Blumberg plot to analyse the result, I found that these parameters can correspond to a 2N2O binding mode, which is in agreement with the previous report[214].

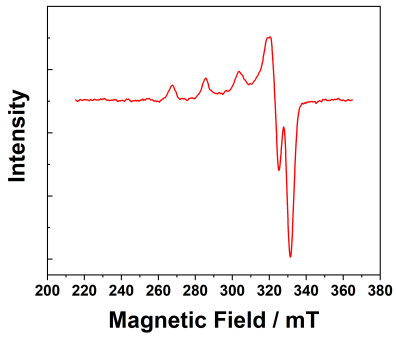


Figure 7.6 X-band EPR spectrum of Cu^{2+} bound on synaptic-like SUV. The derived parameters suggest a 2N2O Cu^{2+} binding mode as reported[214]. The spectrum was measured at 20 K, 9.4 GHz.

7.6 Reduction Kinetics of SUV-Cu(II)

Considering the observed high Cu^{2+} binding affinity of synaptic-like SUV, I suspected that synaptic vesicle could play a more important role than current thinking in copper transportation and regulation, and the exploration for the potential metabolic mechanisms of SUV-Cu(II) conjugate such as the reductive pathways would be crucial for the further understanding.

7.6.1 Reduction by Ascorbate

Similar to the previous proposal (see Section 5.4), I first studied the reduction kinetics of SUV-Cu(II) conjugate with ascorbate. The labelled SUV sample (100 μM

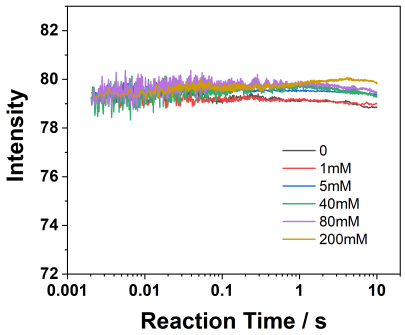


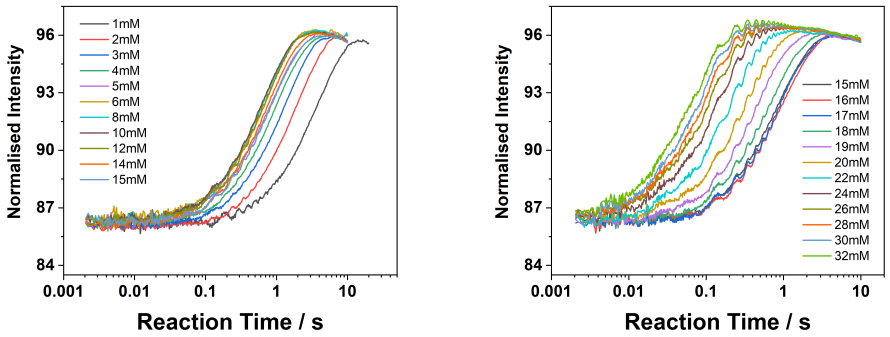
Figure 7.7 Reduction of SUV-Cu(II) conjugate by ascorbate. Raw traces show no fluorescence recovery under various concentrations of ascorbate, suggesting that ascorbate cannot reduce SUV-

Cu(II) conjugate. The experiments were performed in 50 mM HEPES and 100 mM NaCl buffer solution at 298 K (pH 7.5).

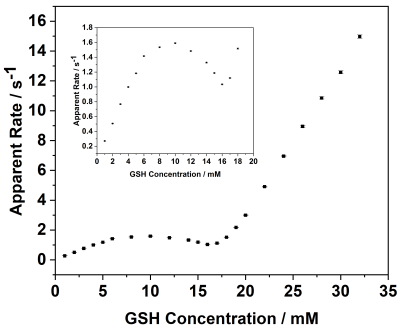
total lipid) was pre-mixed with 1 μM $CuCl_2$ to form SUV-Cu(II) conjugate, then the solution was treated with various concentrations of sodium ascorbate (Fig. 7.7). Interestingly, the traces do not show any fluorescence recovery, indicating that the SUV-Cu(II) conjugate is very reduction-inert for ascorbate.

7.6.2 Reduction by GSH

The reduction experiment under GSH treatment was subsequently conducted. In the measurement, SUV-Cu(II) was pre-formed by mixing the labelled SUV (100 μM total lipid) with 1 μM $CuCl_2$, and then reduced by various concentrations of GSH. GSH can efficiently reduce SUV-Cu(II) conjugate, suggesting that the reductive metabolism of Cu^{2+} on synaptic vesicle may undergo GSH pathway. The reduction traces are shown in Fig. 7.8(A), and the derived reduction rates from single exponential fitting are plotted in Fig. 7.8(B). Intriguingly, the reduction rates of SUV-Cu(II) display the similar trend to the reduction rates of αSyn-Cu(II) by GSH, exhibiting a hierarchical increase upon increasing GSH concentration and becoming "out of control" when GSH concentration is higher than 16 mM. Thus, I propose that this extraordinary reduction mechanism could be the distinctive character of GSH reduction, which might be the reason why the upper limit of physiological GSH concentration is approximately 15 mM.



(A) Normalised Traces



(B) Apparent Reduction Rates

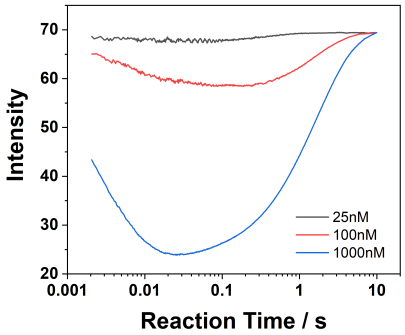
Figure 7.8 Reduction kinetics of SUV-Cu(II) conjugate by GSH. (A) Normalised traces of SUV-Cu(II) conjugate reduction under various concentrations of GSH. The experiments were performed in 50 mM HEPES and 100 mM NaCl buffer solution at 298 K (pH 7.5). **(B)** Apparent reduction rates of SUV-Cu(II) under various concentrations of GSH. The rates derived under relatively low concentrations of GSH are re-plotted in the inset for clarity.

7.7 Competition of Cu^{2+} Binding between SUV and Protein

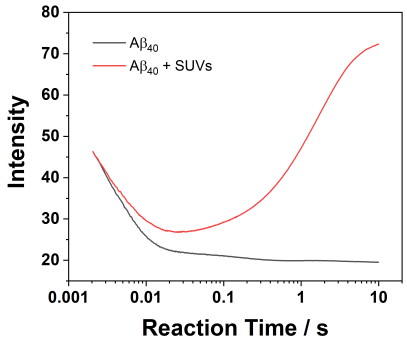
7.7.1 Competition with Aβ

Previously I have already shown that Aβ possesses high affinity with Cu^{2+}, and it can bind with Cu^{2+} approximately 100 times faster than synaptic-like SUV. Thus in synapse, Aβ may be able to exhibit competition for Cu^{2+} with synaptic vesicle. To study this, 25 nM labelled $A\beta_{40}$ was pre-mixed with SUV (100 μM total lipid), then the mixture was treated with various concentrations of $CuCl_2$. Fig. 7.9(A) shows that $A\beta_{40}$ is initially bound to Cu^{2+}. However, Cu^{2+} will then be dissociated by SUV at longer timescales as fluorescence of $A\beta_{40}$ is recovered. Similar competition traces can be presented by other Aβ species (Fig. 7.9(B)). As the magnitude of fluorescence quenching of Aβ in the presence of SUV is smaller than that of Aβ in free solution, the factual competition process can be described as Aβ and SUV are initially bound to Cu^{2+} independently, and when Cu^{2+} is all bound, SUV will start to dissociate Cu^{2+} from Aβ-Cu(II). In terms of competition with $A\beta_{4\text{-}16}$, this Cu^{2+} dissociation seems to occur on $A\beta_{4\text{-}16}$-Cu(II) intermediates rather than the final $A\beta_{4\text{-}16}$-Cu(II) complex, as the final $A\beta_{4\text{-}16}$-Cu(II) complex has been shown to be formed after ~2 s of initial Cu^{2+} binding (see

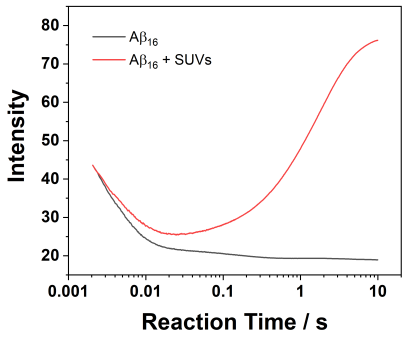
Section 3.2.3), but here we can see Cu^{2+} dissociation by SUV starts at ~0.01 s after initial binding.



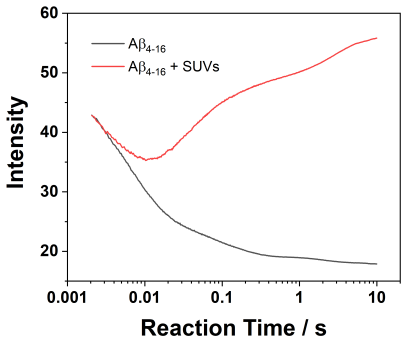
(A) Cu^{2+} Competition between $A\beta_{40}$ and SUV



$A\beta_{40}$



$A\beta_{16}$

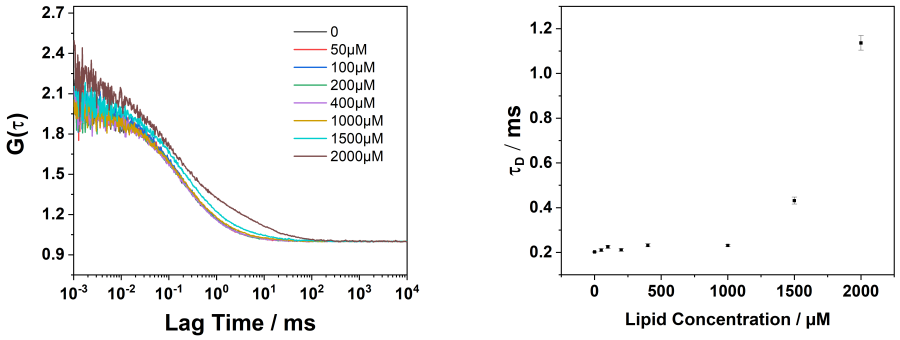


$A\beta_{4-16}$

(B) Comparison of Cu^{2+} Binding to Aβ and Aβ-SUV Mixture

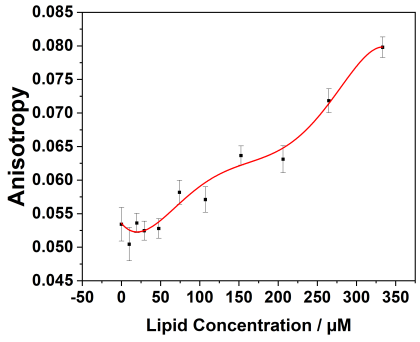
Figure 7.9 Competition between Aβ and synaptic-like SUV for Cu^{2+}. (A) Cu^{2+} competition between $A\beta_{40}$ and SUV. Raw traces under various concentrations of Cu^{2+} show that Cu^{2+} is initially bound to SUV-mixed $A\beta_{40}$ but then dissociated by SUV. **(B)** Comparison of Cu^{2+} binding to different Aβ and Aβ-SUV mixture. The experiments were performed in 50 mM HEPES and 100 mM NaCl buffer solution at 298 K (pH 7.5).

There is a caveat to the experiment as we do not know whether Aβ could also interact with SUV. To determine this, FCS measurements were performed. The labelled $A\beta_{40}$ was mixed with various concentrations of SUV (shown in the concentrations of lipid) and incubated for 15 min before measuring. The diffusion times (τ_D) of $A\beta_{40}$ under different conditions were recorded. Fig. 7.10(A) shows the FCS curves and the change of τ_D. It can be seen that $A\beta_{40}$ does not show binding to SUV until the concentration of SUV lipid rises higher than 1 mM, where $A\beta_{40}$ is just partially bound on SUV as the mean τ_D is still much smaller than the τ_D of SUV (5.68(5) ms as shown in Section 6.2.1). In addition, the anisotropy titration experiment also indicates that $A\beta_{40}$ does not bind to SUV (Fig. 7.10(B)). Thus, I have confirmed that $A\beta_{40}$ does not interact with SUV under the conditions of competition experiments.



FCS Curves　　Change of τ_D

(A) FCS Measurements



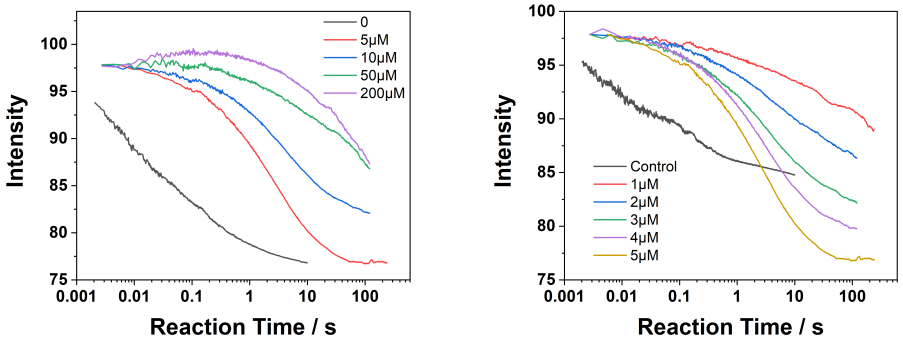
(B) Fluorescence Anisotropy Titrations

Figure 7.10　Minimal interactions between $A\beta_{40}$ and synaptic-like SUV. (A) FCS measurements for labelled $A\beta_{40}$ in the presence of various concentrations of SUV lipid. **(B)**

Fluorescence anisotropy titration curves of $A\beta_{40}$ binding to SUV. Both experiments show that $A\beta_{40}$ only has minimal interactions with SUV. The experiments were performed in 50 mM HEPES and 100 mM NaCl buffer solution at 298 K (pH 7.5).

7.7.2 Competition with HSA

As a major Cu^{2+} carrier and a common protein in the brain, HSA may also be able to affect the Cu^{2+} binding to synaptic vesicle. To study this, the labelled SUV (100 μM total lipid) was pre-mixed with various concentrations of HSA, then the mixture was mixed with 5 μM $CuCl_2$. Fig. 7.11(A) shows that the presence of HSA can slow down Cu^{2+} binding to SUV, but cannot stop the binding. This suggests that initially HSA can compete against SUV in the binding of Cu^{2+}. However, at longer timescales, Cu^{2+} will be transferred to SUV as fluorescence of SUV is decreased. Considering that the Cu^{2+} binding affinity of HSA (0.90(9) pM[313]) is actually higher than that of SUV (0.7(1) nM), this Cu^{2+} transfer may occur on HSA-Cu(II) intermediates rather than the final HSA-Cu(II) complex, which is similar to the competition process of Cu^{2+} binding between $A\beta_{4\text{-}16}$ and SUV as described above. If the experiment was performed under physiological HSA concentration (5 μM) with various concentrations of $CuCl_2$, such competition can also be observed (Fig. 7.11(B)).



(A) Cu^{2+} Competition under Various [HSA]

(B) Cu^{2+} Competition under Various [Cu^{2+}]

Figure 7.11 Competition between HSA and synaptic-like SUV for Cu^{2+}. (A) Cu^{2+} competition between HSA and SUV under various concentrations of HSA. Raw traces show that HSA can slow down Cu^{2+} binding to SUV. **(B)** Cu^{2+} competition between HSA and SUV under various concentrations of Cu^{2+}. The control trace represents 1 μM Cu^{2+} binding to SUV (100 μM total lipid) without HSA. The experiments were performed in 50 mM HEPES and 100 mM NaCl buffer solution at 298 K (pH 7.5).

To confirm whether HSA can drag Cu^{2+} out from SUV-Cu(II) conjugate, I performed the experiment of SUV-Cu(II) dissociation by HSA. In the experiment, the labelled SUV (100 μM total lipid) was pre-mixed with 1 μM $CuCl_2$ to form SUV-Cu(II) conjugate, and then the mixture was treated with various concentrations of HSA. The experimental traces are shown in Fig. 7.12. It can be noticed that no matter how high the concentration of HSA is, the fluorescence level of SUV-Cu(II) is maintained the same and no fluorescence recovery can be observed, which indicates that HSA cannot dissociate Cu^{2+} from SUV-Cu(II). Although HSA was reported to possess the higher Cu^{2+} binding affinity than SUV, this observation may suggest that the initial HSA-Cu(II) intermediate is much weaker than SUV-Cu(II) conjugate, thus making HSA unable to dissociate SUV-Cu(II).

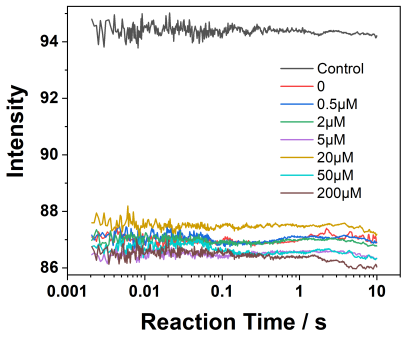
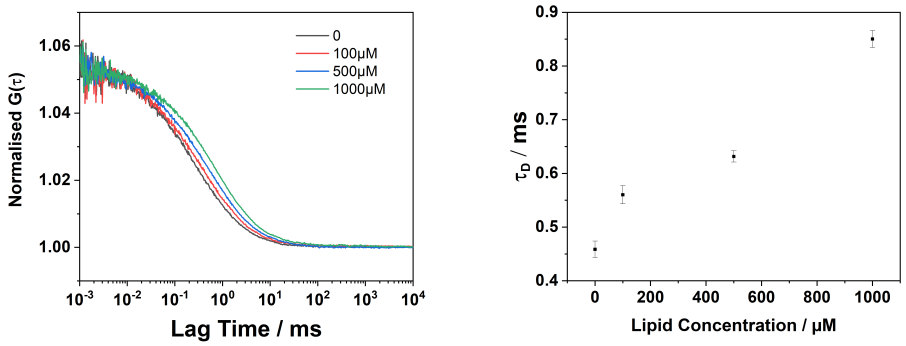


Figure 7.12 Dissociation of SUV-Cu(II) conjugate by HSA. Raw traces show no fluorescence recovery under various concentrations of HSA, suggesting that HSA cannot dissociate SUV-Cu(II) conjugate. The control trace represents the signal of labelled SUV (100 μM total lipid) after mixing with 5 μM HSA. The experiments were performed in 50 mM HEPES and 100 mM NaCl buffer solution at 298 K (pH 7.5).

In addition, the binding of SUV with HSA was determined to eliminate its effect on the Cu^{2+} interactions using FCS techniques. Fig. 7.13 shows the FCS curves of labelled HSA in the presence of various concentrations of SUV (shown in the concentrations of lipid) and the change of the τ_D for HSA. Although the τ_D seems to be increased upon increasing concentration of SUV, compared with the value of 5.68(5) ms for SUV, the τ_D values shown in this measurement are much smaller, which

indicates that HSA only manifests limited interaction with SUV, and such interaction could be negligible for the Cu^{2+} interactions between SUV and HSA.



FCS Curves　　Change of τ_D

Figure 7.13　Minimal interactions between HSA and synaptic-like SUV. FCS measurements for labelled HSA in the presence of various concentrations of SUV lipid show small change in τ_D, suggesting that HSA only has minimal interactions with SUV. The measurements were performed in 50 mM HEPES and 100 mM NaCl buffer solution at 298 K (pH 7.5).

7.7.3 Competition with αSyn

As mentioned before, αSyn can easily bind to SUV, which is different from Aβ and HSA. In the trinity of αSyn, SUV and Cu^{2+}, all elements can interact with each other. Hence the interactions among them could be quite complicated. This work will be discussed in detail in Chapter 8.

7.8 Summary

In this Chapter, it has been shown that the DOPS-containing synaptic-like SUV can strongly bind Cu^{2+} in a 2N2O binding mode (K_d = 0.7(1) nM). The formed SUV-Cu(II) conjugate is too redox-inert to be reduced by ascorbate. Whereas it can be efficiently reduced under physiological concentrations of GSH. In addition, it has been shown that the co-existed Aβ and HSA can initially compete the binding of Cu^{2+} against SUV. However, the bound Cu^{2+} on them will be eventually transferred to SUV.

Taken the results together, the crucial role of synaptic vesicle in copper transportation can be predicted as described below. Under physiological condition,

synaptic vesicles display high affinity with Cu^{2+}, making them capture Cu^{2+} easily and protect the bound Cu^{2+} from being taken by ubiquitous and abundant copper binding proteins such as HSA. This ensures that Cu^{2+} can be transported safely. On the other hand, the vesicle-bound Cu^{2+} displays reductive inactivity to ascorbate but superior activity to GSH. In the brain, the GSH pathway could be more protective to neurons than the ascorbate pathway because GSH can chelate and take away the reduced Cu^{+} that is known to be a catalyst of ROS generation, thereby preventing synaptic ROS production. Therefore, my experimental evidence seems to suggest that synaptic vesicle binding can lead Cu^{2+} to the correct reductive metabolic pathway. Overall, due to these special properties that synaptic vesicle possesses, I would like to infer that synaptic vesicles themselves could act as a major Cu^{2+} carrier and transporter in the brain. The general Cu^{2+} transportation process is illustrated in Fig. 7.14 and described below. Synaptic vesicle binds Cu^{2+} in synapse which may contain common copper binding proteins such as HSA, and transports Cu^{2+} to GSH. The bound Cu^{2+} will be reduced to Cu^{+} form and chelated by GSH, proceeding to the next transportation or cycling step.

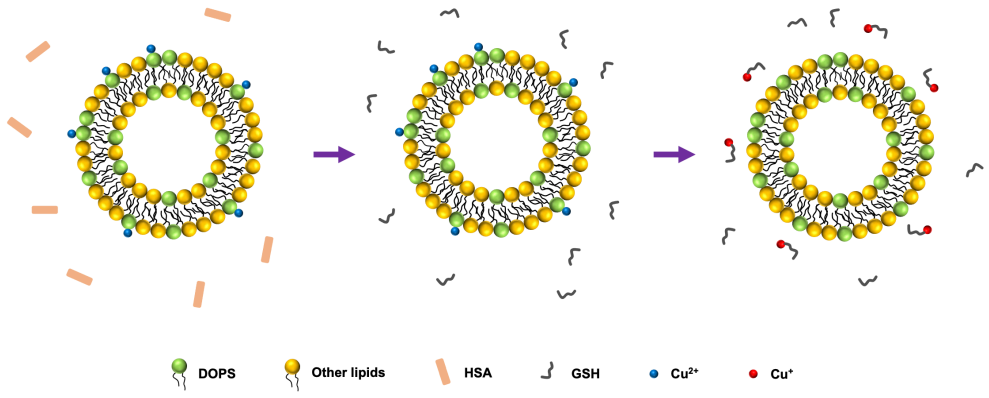


Figure 7.14 Proposed Cu^{2+} transportation via synaptic vesicle. DOPS in synaptic vesicle is in charge of high-affinity Cu^{2+} binding. The bound Cu^{2+} is then transferred to GSH in reduced Cu^{+} form.

Chapter 8

Interactions among α-Synuclein, Lipid Membranes and Cu^{2+}

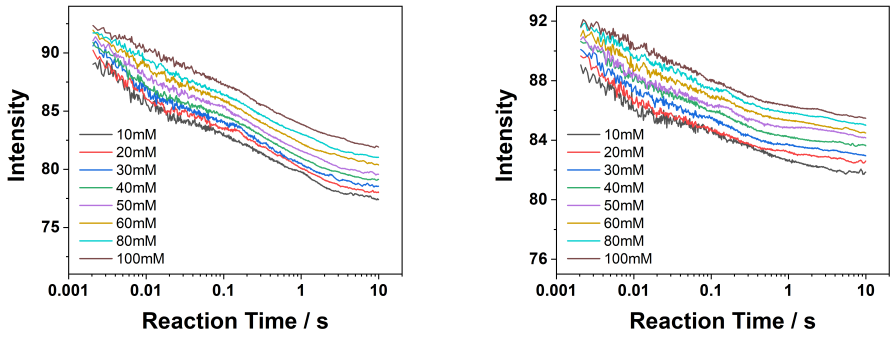
In synapse, there are multiple copper proteins co-existing with synaptic vesicles. They collaborate with each other to maintain copper homeostasis. At the end of the Chapter 7, I have discussed the Cu^{2+} competition between Aβ, HSA and synaptic-like SUV. These two proteins only show limited or no interaction with SUV. However, as α-synuclein (αSyn) is known to efficiently bind to SUV, the trio of αSyn, SUV and Cu^{2+} could show different and more complicated interaction mechanisms.

The study of the interactions among αSyn, lipid membrane and Cu^{2+} is currently limited. Researchers typically used PS-free SUVs to bind with αSyn and investigated how such SUV-bound αSyn interacts with Cu^{2+}[316]. Such studies evade Cu^{2+} binding to SUV which would occur under physiological condition and investigate Cu^{2+} binding simply to SUV-bound αSyn, which are less physiologically relevant. In order to understand the physiological roles of αSyn and synaptic vesicle in copper homeostasis, the interactions among αSyn, Cu^{2+} and PS-containing synaptic-like SUV must be investigated. This Chapter describes such work using multiple spectroscopic techniques.

8.1 Interactions of αSyn-SUV Conjugate with Cu^{2+}

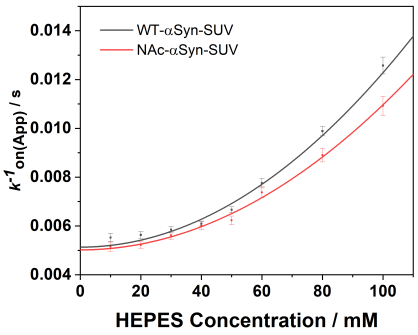
As αSyn, synaptic-like SUV and Cu^{2+} can interact with each other, when they co-exist in solution, multiple different interactions could be occurred simultaneously, namely the interactions of αSyn-SUV conjugate with Cu^{2+}, SUV-Cu(II) conjugate with αSyn and αSyn-Cu(II) complex with SUV.

The exploration starts with the investigation of the interactions between αSyn-SUV conjugate and Cu^{2+}. In previous Chapters, I have shown that both WT-αSyn and synaptic-like SUV can bind to Cu^{2+}, whereas WT-αSyn exhibits weaker binding affinity. If WT-αSyn is associated with SUV, is it still able to bind to Cu^{2+}? To address this question, stopped flow technique was applied. 25 nM labelled WT-αSyn was pre-mixed with 100 μM lipid (approximately 4 nM SUV). After 10 min incubation, 1 μM $CuCl_2$ was blended in the mixture under various concentrations of HEPES in buffer, and the reaction traces were recorded as function of time. Same measurement for NAc-αSyn-SUV with Cu^{2+} was performed as well. Fig. 8.1(A) shows the raw traces. Not only the shapes of the Cu^{2+} binding traces for both αSyn-SUV conjugates are very similar, but also they are similar to the shape of the traces for Cu^{2+} binding to SUV (see traces in Section 7.4). In contrast, the shape of all these traces is quite different from that for Cu^{2+} binding to αSyn (see traces in Section 5.3). Indeed, the derived HEPES independent association rate constants (k_{on}) of Cu^{2+} binding to WT-αSyn-SUV and NAc-αSyn-SUV are 6.4(7) × 10^6 M^{-1} s^{-1} and 6.6(5) × 10^6 M^{-1} s^{-1} respectively (Fig.



WT-αSyn-SUV NAc-αSyn-SUV

(A) Raw Traces



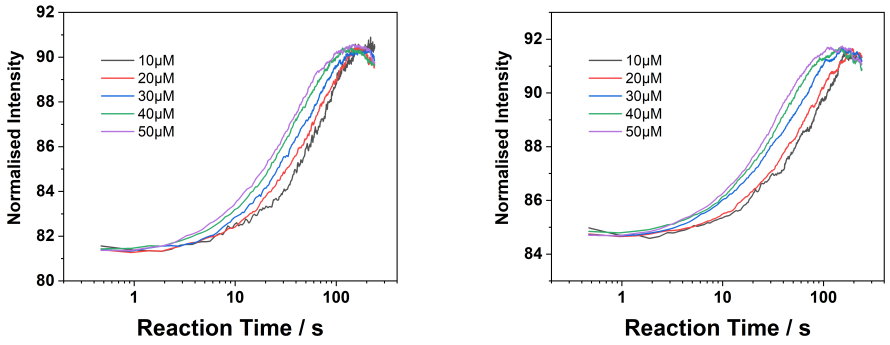
(B) HEPES Dependence of $k_{on(App)}$

Figure 8.1 Kinetics of Cu^{2+} binding to αSyn-SUV (both WT and NAc forms) conjugates. (A) Raw traces of αSyn-SUV binding with Cu^{2+} under various concentrations of HEPES. The experiments were performed in HEPES and 100 mM NaCl buffer solution at 298 K (pH 7.5). **(B)** HEPES dependence of $k_{on(App)}$. The HEPES independent k_{on} values are 6.4(7) × 10^6 M^{-1} s^{-1} for Cu^{2+} binding to WT-αSyn-SUV and 6.6(5) × 10^6 M^{-1} s^{-1} for Cu^{2+} binding to NAc-αSyn-SUV. Such values are similar to k_{on} of Cu^{2+} binding to SUV.

8.1(B)), which are virtually identical, and could not be statistically differentiated from the value of 6.3(3) × 10^6 M^{-1} s^{-1} for k_{on} of Cu^{2+} binding to SUV.

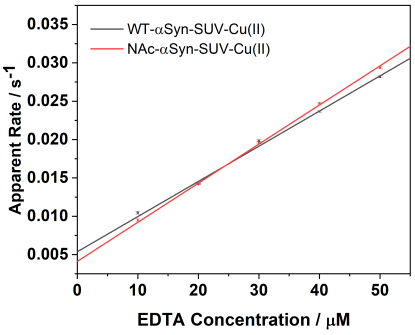
Such similar reaction traces and close k_{on} values between Cu^{2+} binding to αSyn-SUV conjugates and SUV may suggest that the SUV-bound αSyn is not the actual species binding to Cu^{2+}. Instead, the labelled αSyn may just act as a fluorescent probe, indicating how Cu^{2+} binds to SUV. To validate this assumption, I determined the Cu^{2+} dissociation rate constants (k_{off}) of αSyn-SUV-Cu(II) conjugates. In the measurements, 25 nM labelled αSyn was pre-mixed with 100 μM lipid (~4 nM SUV). After 10 min incubation, 1 μM $CuCl_2$ was added in the mixture, and the mixture was then treated with various concentrations of EDTA. The reaction traces are shown in Fig. 8.2(A). Plotting the derived apparent rate against EDTA concentration, k_{off} values can be determined from the intercepts of fitted data, which are 5.3(5) × 10^{-3} s^{-1} and 4.2(1) × 10^{-3} s^{-1} for WT-αSyn-SUV-Cu(II) and NAc-αSyn-SUV-Cu(II), respectively (Fig. 8.2(B)). Such values are similar to the value of 4.6(5) × 10^{-3} s^{-1} for k_{off} of SUV-Cu(II) conjugate, but significantly different from the k_{off} of αSyn-Cu(II) complexes (0.017(4) s^{-1} for WT-αSyn-Cu(II) and 0.10(1) s^{-1} for NAc-αSyn-Cu(II)). Therefore, it is very

likely that the SUV-bound αSyn does not participate in the Cu^{2+} binding to αSyn-SUV conjugates, while the actual role of Cu^{2+} binding is SUV.



WT-αSyn-SUV-Cu(II) NAc-αSyn-SUV-Cu(II)

(A) Normalised Traces

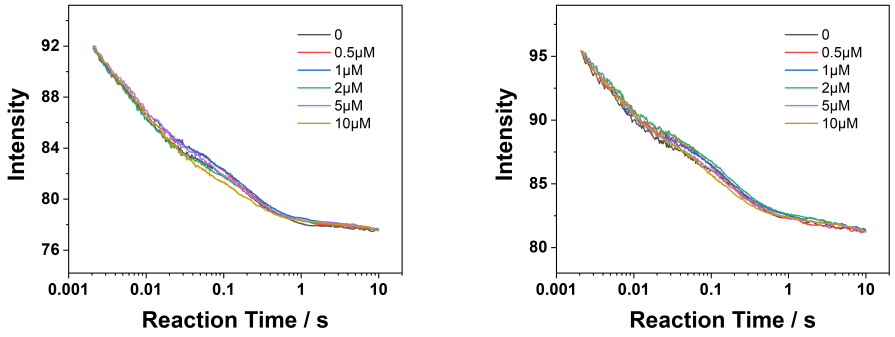


(B) Apparent Dissociation Rates

Figure 8.2 Kinetics of Cu^{2+} dissociation from αSyn-SUV-Cu(II) (both WT and NAc forms). **(A)** Normalised traces of Cu^{2+} dissociation from αSyn-SUV-Cu(II) under various concentrations of EDTA. The experiments were performed in 50 mM HEPES and 100 mM NaCl buffer solution at 298 K (pH 7.5). **(B)** Apparent dissociation rates of Cu^{2+} by EDTA from αSyn-SUV-Cu(II). The EDTA independent k_{off} values are $5.3(5) \times 10^{-3}$ s^{-1} for Cu^{2+} dissociation from WT-αSyn-SUV-Cu(II) and $4.2(1) \times 10^{-3}$ s^{-1} for Cu^{2+} dissociation from NAc-αSyn-SUV-Cu(II). Such values are very similar to k_{off} of Cu^{2+} dissociation from SUV-Cu(II).

Under the above experimental conditions, the ratio of αSyn to SUV in terms of the number is around 6:1. Such low ratio may not be able to ensure that each individual SUV is saturated with the binding of αSyn, as it has been reported that the number of αSyn per vesicle is around 70[317], and I estimated that this number is around 45 (see Section 6.2.2). I then asked the question whether, in the presence of a great excess of

αSyn, αSyn can affect the Cu^{2+} binding to SUV or not. To study this, the labelled SUV (100 μM total lipid, ~4 nM SUV) was pre-mixed with various micromolar concentrations of αSyn (both WT and NAc forms). At such concentrations of αSyn, all vesicles should be fully bound with αSyn, and could even leave excess free αSyn in solution. After 10 min incubation, the mixture was mixed with 1 μM $CuCl_2$. Fig. 8.3 shows the comparison of the raw traces in this experiment. It can be seen that no matter how much αSyn was added, the traces for Cu^{2+} binding to SUV remain identical, suggesting that αSyn cannot prevent or compete Cu^{2+} binding to SUV. This could be because the N-terminal Cu^{2+} binding site of SUV-bound αSyn is buried in the membrane and thus no longer available for Cu^{2+} binding. In fact, this is a proposed membrane binding configuration for the first 14 N-terminal residues of αSyn and it has been discussed in Chapter 6 (see Section 6.2.3). Furthermore, as SUV possesses a faster Cu^{2+} binding rate and stronger Cu^{2+} binding affinity than αSyn, free αSyn will have no chance to compete the binding of Cu^{2+} against SUV. In addition, it seems that the SUV-bound αSyn would not fully occupy the surface of SUV, even though a SUV has been saturated with αSyn, and thus the exposed DOPS of SUV is still able to bind Cu^{2+}.



Excess WT-αSyn　　Excess NAc-αSyn

Figure 8.3　Cu^{2+} binding to αSyn-SUV (both WT and NAc forms) under high concentrations of αSyn. Compared with Cu^{2+} binding to αSyn-free SUV, Cu^{2+} binding to SUV occurred under various excess concentrations of αSyn show the same traces, suggesting that αSyn does not participate in or affect Cu^{2+} binding to SUV. The experiments were performed in 50 mM HEPES and 100 mM NaCl buffer solution at 298 K (pH 7.5).

So far it seems clear that αSyn does not participate in the Cu^{2+} binding when it co-exists with synaptic-like SUV. To further strengthen the conclusion, an X-band EPR

measurement was conducted. SUV sample (15 mM total lipid, ~0.6 μM SUV) was pre-mixed with 50 μM αSyn (both WT and NAc forms). After 10 min incubation, 50 μM $CuCl_2$ was blended in the solution. The solution was subsequently flash-frozen with liquid helium for measurement. Fig. 8.4 shows the comparison of the EPR spectra for SUV-Cu(II), WT-αSyn-SUV-Cu(II) and NAc-αSyn-SUV-Cu(II) conjugates. All spectra are exactly the same, suggesting that the chemical environments of Cu^{2+} in these three conjugates are the same, which confirms that, Cu^{2+} will only bind to DOPS lipid in the presence of αSyn on SUV.

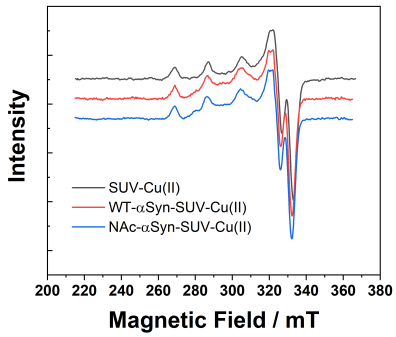
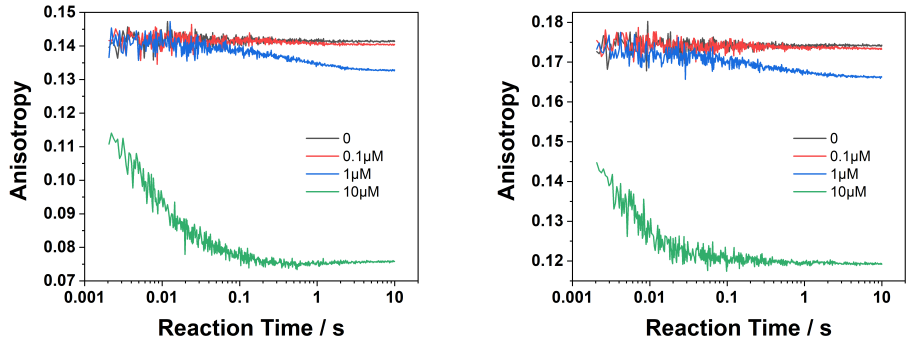


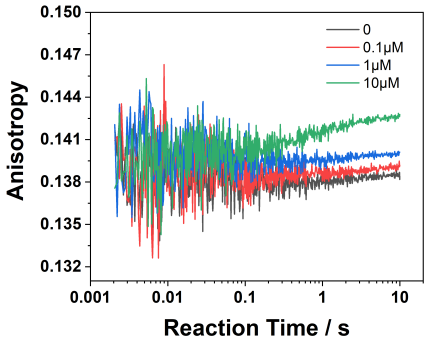
Figure 8.4 X-band EPR spectra of Cu^{2+} bound on αSyn-SUV (both WT and NAc forms). The spectrum of Cu^{2+} bound on αSyn-free SUV is shown for comparison. Three spectra are identical, suggesting that αSyn does not participate in Cu^{2+} binding to αSyn-SUV. The spectra were measured at 20 K, 9.4 GHz.

As the binding of Cu^{2+} could change the charge state of SUV, a question arises: could Cu^{2+} binding displace αSyn from the αSyn-SUV conjugate? Such question can be resolved by fluorescence anisotropy kinetics measurement. 25 nM labelled αSyn (both WT and NAc forms) was pre-mixed with 100 μM lipid (~4 nM SUV). After 10 min incubation, the mixture was treated with various concentrations of $CuCl_2$. The kinetic traces for fluorescence anisotropy of αSyn were recorded as shown in Fig. 8.5. Notably, both WT- and NAc-αSyn show decreased anisotropy when Cu^{2+} concentration is high, indicating that αSyn was dissociated from the αSyn-SUV conjugate during Cu^{2+} binding to SUV. The decrease under 1 μM Cu^{2+} is small, indicating that only few αSyn is detached from SUV under this condition, which may not have significant effect on the results of experiments described above. It can be inferred from the result of this

measurement that Cu^{2+}-bound and unbound SUV differ in αSyn binding property. Such difference will be investigated in the next section.



WT-αSyn NAc-αSyn



SUV (Control)

Figure 8.5 Fluorescence anisotropy kinetics of SUV-bound αSyn (both WT and NAc forms) after mixing with Cu^{2+}. Raw kinetic anisotropy traces under various concentrations of Cu^{2+} show that αSyn can be dissociated from αSyn-SUV after the addition of high concentration of Cu^{2+}. The kinetic anisotropy traces of αSyn-free labelled SUV after mixing with Cu^{2+} are shown as the control. The experiments were performed in 50 mM HEPES and 100 mM NaCl buffer solution at 298 K (pH 7.5).

8.2 Interactions of SUV-Cu(II) Conjugate with αSyn

Having investigated the interactions between αSyn-SUV conjugate and Cu^{2+}, I next shifted focus to how SUV-Cu(II) conjugate interacts with αSyn. We know that αSyn can easily bind to SUV. However, if there is Cu^{2+} bound on SUV, whether αSyn can still bind to SUV? To determine this, fluorescence anisotropy measurements were performed. I first conducted the titration experiments to evaluate the binding affinity of

αSyn to SUV-Cu(II) conjugate. In the experiments, $CuCl_2$ was blended in SUV solution to a ratio of 1:100 (Cu^{2+}: SUV lipid) to form SUV-Cu(II) conjugate. Then 100 nM labelled αSyn was titrated against various concentrations of the Cu^{2+}-mixed lipid, and the anisotropy values were measured by a fluorometer. Fig. 8.6 shows such titration results for WT-αSyn and NAc-αSyn, and the results of the titration without Cu^{2+} participation are shown as well for comparison. An obvious change of the anisotropy can be observed for the binding of NAc-αSyn. The dissociation constants (K_d) for NAc-αSyn binding to SUV-Cu(II) conjugate was obtained by the Hill-Langmuir equation fitting, which is 40(8) μM, five times larger than the K_d for the binding to SUV, suggesting that the Cu^{2+} bound on SUV weakens NAc-αSyn binding to SUV. This could be attributed to the loss of negative charges of SUV, or because the membrane binding conformational change of NAc-αSyn is affected by the bound Cu^{2+} on SUV, causing the less binding of NAc-αSyn. By contrast, the binding of WT-αSyn to SUV seems not to be affected by Cu^{2+}. The K_d for WT-αSyn binding to SUV-Cu(II) conjugate was determined to be 26(6) μM, the same with the K_d for the binding to SUV. This may suggest that the bound Cu^{2+} on SUV does not affect the membrane binding conformation of WT-αSyn. Further work is needed to explain why such difference is observed.

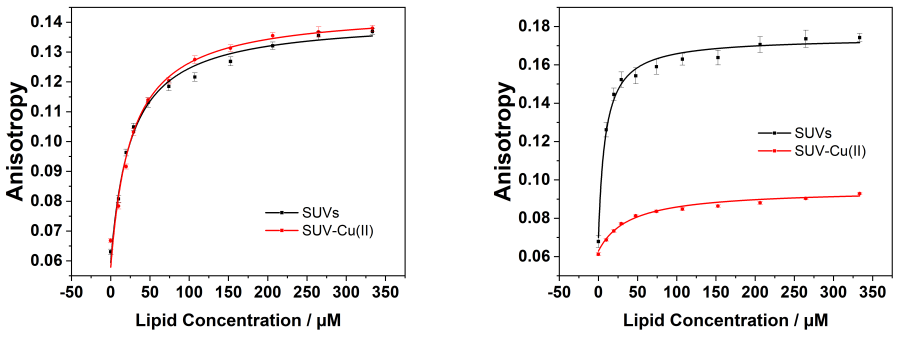
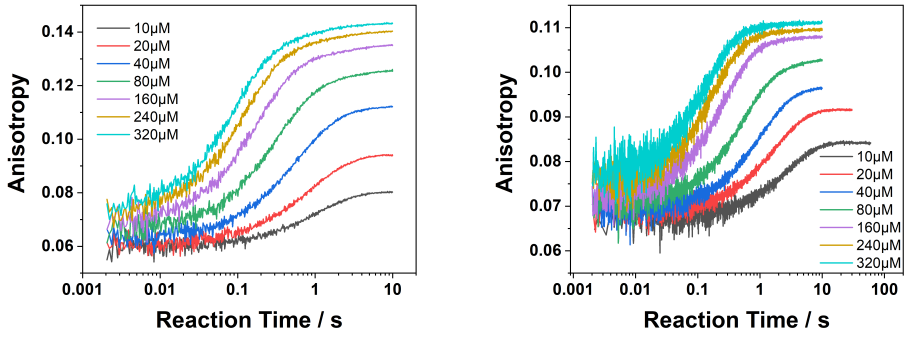


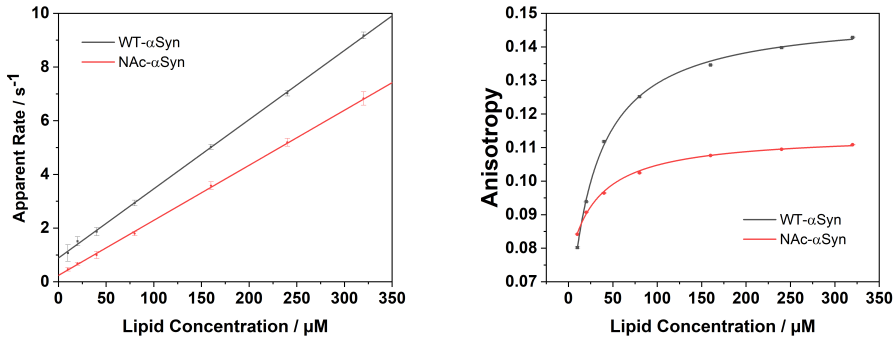
Figure 8.6 Fluorescence anisotropy titrations of αSyn (both WT and NAc forms) binding to SUV-Cu(II). Compared with the binding to SUV, WT-αSyn binding to SUV-Cu(II) shows a similar result, while NAc-αSyn binding to SUV-Cu(II) shows smaller anisotropy values and binding affinity. The measurements were performed in 50 mM HEPES and 100 mM NaCl buffer solution at 298 K (pH 7.5).

Afterwards, I studied the fluorescence anisotropy kinetics upon αSyn binding to SUV-Cu(II) conjugate. The Cu^{2+}-mixed lipid sample was prepared as described above, and 50 nM labelled αSyn (both WT and NAc forms) was treated with various concentrations of this sample. The kinetic anisotropy traces were recorded as shown in



WT-αSyn NAc-αSyn

(A) Raw Kinetic Anisotropy Traces



(B) Apparent Binding Rates (C) Final Anisotropy at Plateau

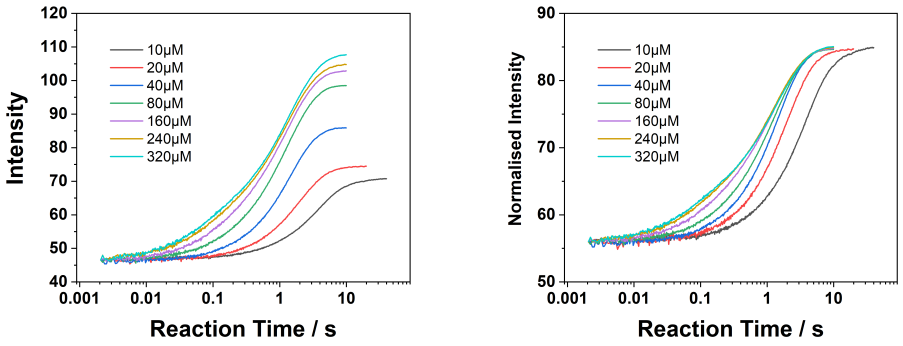
Figure 8.7 Fluorescence anisotropy kinetics of αSyn (both WT and NAc forms) binding to SUV-Cu(II). (A) Raw kinetic anisotropy traces of αSyn binding to various concentrations of SUV-Cu(II) (shown in the concentrations of lipid). The experiments were performed in 50 mM HEPES and 100 mM NaCl buffer solution at 298 K (pH 7.5). **(B)** Apparent binding rates of αSyn to SUV-Cu(II). **(C)** Final anisotropy from the fits as a function of SUV concentration (shown in the concentrations of lipid). The plots were fitted to derive the binding affinity values of αSyn to SUV-Cu(II), giving similar results to the values determined by anisotropy titration experiments.

Fig. 8.7(A). By fitting these traces with multi-exponentials, the apparent binding rates of αSyn binding to SUV-Cu(II) conjugate can be obtained, and they were plotted in Fig. 8.7(B) against the concentration of Cu^{2+}-mixed lipid. The binding rate constants (k_{on})

can be determined from the slopes of fits, which are 2.73(1) × 10^4 M^{-1} s^{-1} and 2.03(5) × 10^4 M^{-1} s^{-1} for WT-αSyn and NAc-αSyn, respectively. Compared with the k_{on} for αSyn binding to SUV (2.91(6) × 10^4 M^{-1} s^{-1} for WT-αSyn and 1.98(4) × 10^4 M^{-1} s^{-1} for NAc-αSyn), the values for the binding to SUV-Cu(II) seem quite similar, suggesting that the SUV-bound Cu^{2+} may not have impact on the binding rate of αSyn to SUV. In addition, by fitting the plateau values of the traces (Fig. 8.7(C)), I determined the K_d for αSyn binding to SUV-Cu(II) once more from such kinetic experiments, which are 27(4) μM and 34(6) μM for WT-αSyn and NAc-αSyn, respectively. These values are in agreement with the values determined by the titration experiments above.

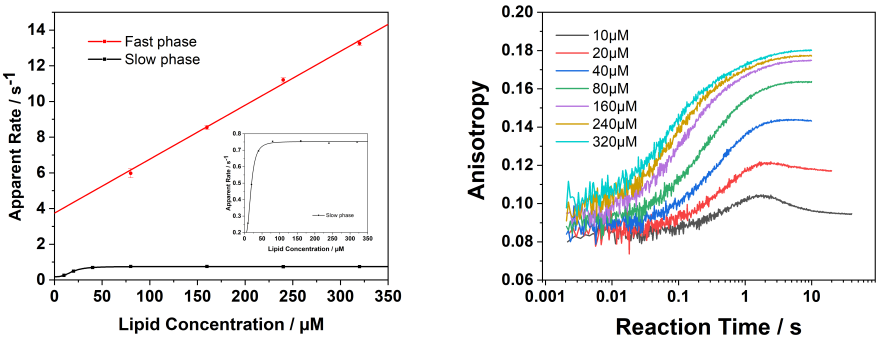
8.3 Interactions of αSyn-Cu(II) Complex with SUV

The study for the interactions between αSyn-Cu(II) complex and SUV was performed using WT-αSyn, as NAc-αSyn can hardly bind with Cu^{2+} to form the stable αSyn-Cu(II) complex under typical experimental condition. Stopped flow was employed to monitor the interaction process. In the measurement, αSyn-Cu(II) complex was pre-formed by mixing 50 nM labelled WT-αSyn with 50 nM $CuCl_2$. The solution was subsequently treated with various concentrations of SUV (shown in the concentrations of lipid). Fig. 8.8(A) shows the raw traces, and obvious fluorescence recovery can be observed, which may indicate that Cu^{2+} in αSyn-Cu(II) is dissociated by SUV or an αSyn-Cu(II)-SUV conjugate is formed. Considering that such concentrations of lipid are much higher than that of Cu^{2+}, if the recovery is due to Cu^{2+} dissociation, Cu^{2+} should be always fully dissociated and the recovery amplitude should be consequently maintained the same. However, as can be seen, the recovery amplitude rises upon increasing concentrations of lipid, thus suggesting that the interaction process between αSyn-Cu(II) complex and SUV could not be described as Cu^{2+} dissociation by SUV. By contrast, if the recovery is due to the formation of αSyn-Cu(II)-SUV conjugate, the interaction will not only depend on Cu^{2+}, but also correlate with WT-αSyn. In this experiment, WT-αSyn is always in excess compared with the



Raw Traces Normalised Traces

(A) Fluorescence Traces



(B) Apparent Rates (C) Raw Kinetic Anisotropy Traces

Figure 8.8 Kinetic interactions between WT-αSyn-Cu(II) and SUV. (A) Kinetic fluorescence traces of the interactions between WT-αSyn-Cu(II) and various concentrations of SUV (shown in the concentrations of lipid). The experiments were performed in 50 mM HEPES and 100 mM NaCl buffer solution at 298 K (pH 7.5). **(B)** Apparent interaction rates derived from the kinetic fluorescence traces. The rates of the slow phase are re-plotted in the inset for clarity. **(C)** Raw kinetic anisotropy traces recorded in the same experiments.

number of SUV. Due to this, at low concentrations of lipid (or SUV), SUV cannot associate with all of αSyn-Cu(II) complex, which could be the reason why small recovery is initially observed. When the concentration of SUV is increasing, more and more αSyn-Cu(II) will be bound on SUV, resulting in the growth of recovery. Therefore, the formation of αSyn-Cu(II)-SUV conjugate could be the more proper way to describe such interaction.

The interaction rate was derived by exponential fitting of the reaction traces. As can be seen from the normalised raw traces in Fig. 8.8(A), the traces under different

concentrations of lipid exhibit different shapes. The traces under low lipid concentrations (10 μM, 20 μM and 40 μM) can be fitted perfectly using single exponential fits, which may indicate the process of αSyn-Cu(II)-SUV conjugate formation. Whereas the traces obtained under higher lipid concentrations reveal two phases and a double exponential can better fit the data, which may indicate that a new interaction process is present at high lipid concentrations. In regard to these two phases, the fast one could correspond to the newly developed process, as the interaction rates are much different from and faster than the rates derived from former traces (Fig. 8.8(B)). In fact, such rates are similar to the SUV lipid binding rates of αSyn (see the binding rate graph in Section 6.2.4), thereby the process arisen could be the SUV binding of αSyn-Cu(II) via the portion of αSyn. When the concentration of lipid is low, the effect of such binding is minor, which could explain why such process is absent on the traces under low lipid concentrations. By contrast, the slow phase displays comparable rates with former traces, thus being considered to correspond to the same interaction process with former traces, i.e., the formation of αSyn-Cu(II)-SUV conjugate. The rates of this slow interaction process are even faster than the Cu^{2+} dissociation rates of αSyn-Cu(II) by EDTA (see the dissociation rate graph in Section 5.3.1), which may provide further evidence that such process is not simply due to Cu^{2+} dissociation by SUV, as Cu^{2+} dissociation by SUV cannot be faster than Cu^{2+} dissociation by EDTA. In addition, it can be noticed that the αSyn-Cu(II)-SUV conjugate formation rate is first increased and then becomes unchanged. This could be because at low concentrations of lipid (in this experiment, ≤ 40 μM), αSyn-Cu(II) is in excess compared with the number of SUV. The number of αSyn-Cu(II) molecules bound on SUV is dependent on SUV (or lipid) concentration. Thus, the conjugate formation rate shows dependence on lipid concentration. Whereas at high concentrations of lipid (> 40 μM), all αSyn-Cu(II) molecules have already quickly bound on SUV via αSyn portion, and then the Cu^{2+} in αSyn-Cu(II) transfers to DOPS lipid on SUV to form the final conjugate. In this case, the final formation can be seen as an intramolecular process, thus showing independence on lipid concentration.

The data of fluorescence anisotropy kinetics for such interaction process was also obtained from the same experiment (Fig. 8.8(C)). Since the fluorescence recovery traces mainly show the behaviour of Cu^{2+}, anisotropy kinetic traces can give more details on the binding of αSyn portion to SUV. As can be seen, at low concentrations of lipid, the anisotropy traces show increase and then decrease. This could be because αSyn-Cu(II) complex is initially bound to SUV via αSyn portion, causing increase in anisotropy. However, due to the limitation in the number of SUV, such binding cannot be further proceeded when all vesicles have been saturated with αSyn-Cu(II). Meanwhile, the Cu^{2+} of αSyn-Cu(II) is transferred to SUV, which may reduce lipid binding of αSyn-Cu(II), thereby dissociating some previously bound αSyn-Cu(II), resulting in the decrease in anisotropy. Whereas at high concentrations of lipid, the number of SUV is enough for binding all αSyn-Cu(II) molecules, and SUV is thus far from saturation with αSyn-Cu(II). Hence, the SUV binding attenuating of αSyn-Cu(II) induced by transferred Cu^{2+} is negligible and the SUV binding of αSyn-Cu(II) will not be disturbed. The anisotropy traces thus only show increase until reach the plateau. An illustration for the general process is shown in Fig. 8.9.

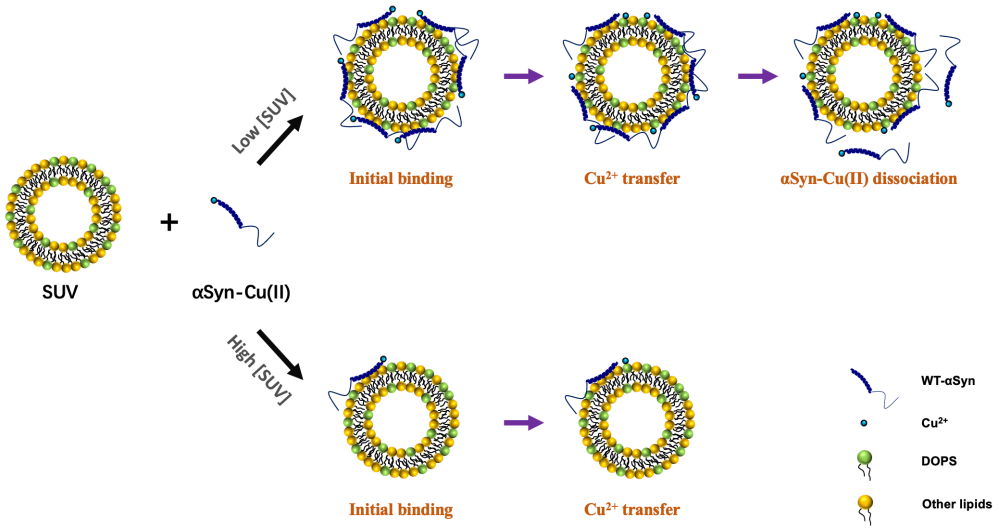
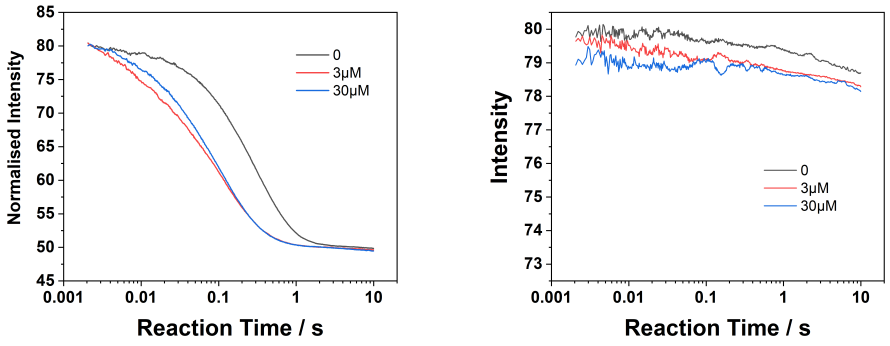


Figure 8.9 Proposed process of αSyn-Cu(II) complex binding to synaptic-like SUV. αSyn-Cu(II) initially binds to SUV via αSyn portion, and then the Cu^{2+} of αSyn-Cu(II) is transferred to DOPS lipid on SUV. At low concentration of SUV, some pre-bound αSyn-Cu(II) could be dissociated from SUV due to Cu^{2+} induced binding attenuation.

It can be seen that the whole interaction process of αSyn-Cu(II) complex with SUV is quite complicated. What I propose above is the most reasonable explanation based on current data. There is also another possibility that excess αSyn-Cu(II) complex may be able to disrupt the structure of SUV, causing the decrease in anisotropy. Further investigation is required to uncover the full mechanism.

8.4 Interactions of Micelle-Bound αSyn with Cu^{2+}

In addition to the above studies involving vesicles, some micelle engaged experiments were carried out as well. In Chapter 6, I have shown that αSyn is able to bind with GM1 micelle. To investigate whether GM1 binding of αSyn can affect Cu^{2+} binding to αSyn, I conducted an experiment using 50 nM labelled αSyn which was pre-mixed with different concentrations of GM1 lipid, and then mixed with 3 μM $CuCl_2$. Fig. 8.10 shows such Cu^{2+} binding traces of αSyn (both WT and NAc forms). It can be noticed that the Cu^{2+} binding rate of NAc-αSyn does not exhibit obvious change upon the adding of GM1, while the Cu^{2+} binding rate of WT-αSyn is increased significantly.



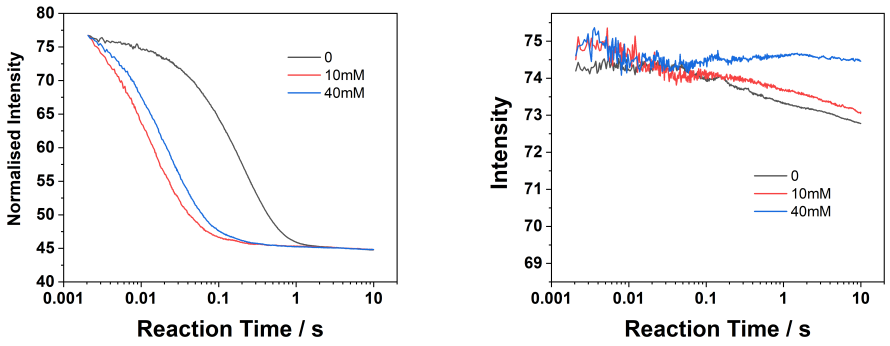
WT-αSyn-GM1 NAc-αSyn-GM1

Figure 8.10 Cu^{2+} binding to αSyn-GM1 (both WT and NAc forms) conjugates. The traces of Cu^{2+} binding to αSyn that is pre-mixed with various concentrations of GM1 lipid show that GM1 can boost Cu^{2+} binding to WT-αSyn but has no impact on Cu^{2+} binding to NAc-αSyn. The experiments were performed in 50 mM HEPES and 100 mM NaCl buffer solution at 298 K (pH 7.5).

This indicates that αSyn binding to GM1 micelle may be able to improve the Cu^{2+} binding ability of N-terminal binding site of αSyn. In addition, the unchanging Cu^{2+}

binding rate of NAc-αSyn may suggest that GM1 does not bind to Cu^{2+}, as if GM1 could bind, the attached labelled NAc-αSyn must be quenched by the bound Cu^{2+}. However, in fact this has not been observed, providing evidence that GM1 has no interaction with Cu^{2+}.

The same results recur when GM1 is substituted by SDS. Fig. 8.11 shows the Cu^{2+} binding traces of αSyn (both WT and NAc forms) in the presence of different concentrations of SDS. The experiment was performed in analogue to those above. The employed concentrations of SDS were selected over the CMC (8.2 mM). Combined the results, I can infer that both GM1 and SDS micelle can boost the N-terminal Cu^{2+} binding of WT-αSyn. However, it seems that the lower concentration of micelle can boost more compared to the higher concentration of micelle.



WT-αSyn-SDS NAc-αSyn-SDS

Figure 8.11 Cu^{2+} binding to αSyn-SDS (both WT and NAc forms) conjugates. The traces of Cu^{2+} binding to αSyn that is pre-mixed with various concentrations of SDS show that SDS can boost Cu^{2+} binding to WT-αSyn but has little impact on Cu^{2+} binding to NAc-αSyn. The experiments were performed in 50 mM HEPES and 100 mM NaCl buffer solution at 298 K (pH 7.5).

8.5 Summary

This Chapter has mainly investigated how αSyn, synaptic-like SUV and Cu^{2+} interact with each other, from the view of one element interacting with the conjugate formed by the other two elements. It has been shown that Cu^{2+} binds to αSyn-SUV conjugate via DOPS on SUV, whereas the αSyn on membrane (both WT and NAc forms) does not seem to participate in binding Cu^{2+}. In addition, it has been shown that

WT-αSyn binds to SUV-Cu(II) conjugate with the similar affinity to SUV, whereas NAc-αSyn presents weaker binding affinity to SUV-Cu(II) conjugate than that to SUV. Nevertheless, the k_{on} of both forms of αSyn binding to SUV-Cu(II) conjugate are maintained the same with those to SUV. In terms of SUV binding to αSyn-Cu(II) complex, the interaction could be quite complicated, but in the end, an αSyn-Cu(II)-SUV conjugate is likely to form. Finally, it has also been shown that the binding of GM1 or SDS micelle to WT-αSyn can accelerate the binding between WT-αSyn and Cu^{2+}.

Synaptic vesicle is the linchpin of neurotransmission, while the binding of αSyn is known to restrict its mobility. To ensure that neurotransmission can be proceeded properly, there must be a regulator to control this binding, and I hypothesised that Cu^{2+} could play this important role. Based on the results shown in this Chapter, we know that αSyn cannot affect synaptic-like SUV to bind Cu^{2+}, whereas the bound Cu^{2+} on SUV can affect and weaken SUV binding with αSyn, especially the binding with the physiologically predominant form, NAc-αSyn, leading to αSyn dissociation from the membrane. Therefore, it can be postulated that in presynaptic terminals, synaptic vesicles are restricted by abundant NAc-αSyn and moving slowly. Once the neurotransmission is triggered by an action potential, synaptic vesicles will start to bind Cu^{2+}, and the bound Cu^{2+} will reduce the binding of αSyn and dissociate them from synaptic vesicles, releasing synaptic vesicles and promoting the vesicular transport. The Cu^{2+}-bound synaptic vesicles only possess weak affinity with NAc-αSyn, which ensures that they can smoothly pass through the αSyn-abundant environment. Synaptic vesicles, αSyn and Cu^{2+} are all crucial in neurotransmission. Such hypothesis links them together to narrate the story of presynaptic vesicular trafficking and highlights the regulatory role of Cu^{2+}, which could give further insight into the process of synaptic transmission.

Chapter 9

Conclusion & Further Work

Amyloid-β and α-synuclein are well-accepted to be responsible for the cause of Alzheimer's disease and Parkinson's disease, respectively. However, the physiological and pathological roles of Aβ and αSyn are still mysterious to understand. The main aim of this thesis is to investigate the molecular interactions of Aβ and αSyn with Cu^{2+} and lipid membranes, trying to grasp the interaction mechanisms from kinetic and structural views, providing information about the potential biological functions of Aβ and αSyn as well as the Aβ and αSyn related pathogenesis of neurodegeneration.

Interactions of Post-Translational Modified Aβ with Cu^{2+}

This thesis starts with the investigation of post-translational modified Aβ-Cu^{2+} interactions, which is an extended study following the previous research elucidating the interactions between WT-Aβ and Cu^{2+}[206]. Based on the stopped flow kinetic results, it was found that serine 8 phosphorylated Aβ (pS8-Aβ) has the same Cu^{2+} binding mechanism with WT-Aβ, forming two co-existing Cu^{2+} coordination complexes after initial binding. However, pS8-Aβ was shown to possess a faster Cu^{2+}-bridged dimerisation rate than WT-Aβ, which correlates with a previous report demonstrating the acceleration of toxic Aβ aggregation by phosphorylation[256], indicating that phosphorylated Aβ could play a role in the development of AD.

N-truncated $A\beta_{4-42}$ is the most abundant Aβ isoform in brain. Using a model peptide $A\beta_{4-16}$, the mechanism of the kinetic interactions between Cu^{2+} and $A\beta_{4-16}$ was described. It was shown that the Cu^{2+} binding process of $A\beta_{4-16}$ is longer and more complicated than that of WT-Aβ. Generally, Cu^{2+} bound to $A\beta_{4-16}$ to form the first intermediate Species I in millisecond scale. Species I subsequently interconverted into Species II at ~2 s after the initial binding, and Species II finally transformed into a very tight complex (K_d = ~250 fM). Such high Cu^{2+} binding affinity of $A\beta_{4-16}$ may suggest that $A\beta_{4-x}$ possesses physiological function, e.g., Cu^{2+} transporter or scavenger in synapses. In addition, histidine was found to be able to prolong Cu^{2+} binding to $A\beta_{4-16}$, which may indicate that histidine is a modulator in $A\beta_{4-x}$ involved in Cu^{2+} transport. The kinetic reaction traces suggest that this modulation could occur via forming $A\beta_{4-16}$-Cu(II)-His ternary complex. Further work is needed to uncover the full interaction mechanism.

αSyn Sample Production

All αSyn samples used in this thesis were produced by the author. The fluorescent labelling efficiency of labelled αSyn samples was ~95%. In the step of labelling, it was surprisingly found that TCEP, which was used to break disulfide bonds, can disturb the thiol-maleimide labelling reaction, which is opposite to most of scientists' opinion. This discovery may raise concerns for other thiol-maleimide conjugation-based experiments.

Interactions among αSyn, Cu^{2+} and Lipid Membranes

WT-αSyn is able to bind with Cu^{2+}. However, the involvement of His50 in high-affinity Cu^{2+} binding is currently under dispute. Using stopped flow kinetic method, it was found that WT-αSyn and H50Q αSyn possess similar Cu^{2+} binding rate constants, and the corresponding Cu^{2+} coordinated αSyn complexes possess similar Cu^{2+} dissociation rate constants. Both results indicate that His50 is essentially irrelevant to Cu^{2+} binding to WT-αSyn when only the high affinity binding site is involved in the binding reaction. By contrast, NAc-αSyn was shown to bind Cu^{2+} around four orders of magnitude weaker than WT-αSyn, with K_d = 23(3) μM, and His50 was found to be

responsible for this weak binding as the N-terminal high-affinity Cu^{2+} binding site is abolished by acetylation. Considering that NAc-αSyn is the predominant αSyn form in brain, the result may indicate a potential physiological role of N-terminal acetylation of αSyn, which is preventing the binding with labile Cu^{2+}, thus safeguarding the labile Cu^{2+} in neurotransmission and also mitigating the risk of Cu^{2+} induced αSyn aggregation. In addition, it was found that WT-αSyn-Cu(II) complex is not as redox-active as WT-Aβ-Cu(II) complex. Hence, ROS may not be easily generated via αSyn-Cu(II) complex even when a considerable amount of WT-αSyn-Cu(II) has been formed.

αSyn is abundant in presynaptic cells and able to bind to synaptic vesicles. The binding conformation and affinity of αSyn for synaptic vesicle are essential to further understanding the molecular mechanism and physiological function of αSyn-synaptic vesicle interactions. Using smFRET technique, it was found that single αSyn molecule binding to synaptic-like SUV displays mixed extended, curved and antiparallel helical structures, while multiple αSyn molecules binding to one SUV is mainly via a curved helical structure. In addition, the binding affinity was determined by fluorescence anisotropy titration, from where the binding of NAc-αSyn to synaptic-like SUV (K_d = 8(2) μM) was found to be stronger than H50Q αSyn (K_d = 19(4) μM) and WT-αSyn (K_d = 26(5) μM) binding to SUV. This indicates that N-terminal acetylation of αSyn can increase membrane binding ability of αSyn. αSyn binding is believed to restrict the mobility of synaptic vesicles and decrease synaptic vesicle recycling[273]. Thus, the increased membrane binding induced by N-terminal acetylation of αSyn could be an important physiological function in vesicle trafficking and recycling regulation.

It was also found that synaptic-like SUV can strongly bind Cu^{2+}, with K_d = 0.7(1) nM, and the constituent, DOPS, was shown to be responsible for this high-affinity binding. Interestingly, the formed SUV-Cu(II) conjugate can be efficiently reduced by GSH, but cannot be reduced by ascorbate, which may indicate that synaptic vesicle can protect Cu^{2+} in an ascorbate-rich reducing environment and lead Cu^{2+} to the GSH metabolism pathway. These observations combined with the fact that synaptic vesicles are enriched in synapses, a hypothesis that synaptic vesicle is a crucial Cu^{2+} carrier in synaptic Cu^{2+} transportation, can be raised. Moreover, the presence of physiological

concentration of αSyn was shown negligible impact on Cu^{2+} binding to synaptic-like SUV. Whereas NAc-αSyn binding to synaptic-like SUV was significantly reduced by SUV-bound Cu^{2+}. These observations may reveal the cooperative regulation mechanism of these three elements in synaptic Cu^{2+} transportation.

Taken together, the potential role of $A\beta_{4-16}$, αSyn and synaptic vesicle in synaptic Cu^{2+} transportation can be proposed. The fast binding of Cu^{2+} to physiologically predominant $A\beta_{4-16}$ indicates that $A\beta_{4-16}$ is an efficient Cu^{2+} captor. However, considering that the physiological concentration of $A\beta_{4-16}$ is in picomolar to nanomolar level, $A\beta_{4-16}$ is unlikely to be a crucial Cu^{2+} transporter, but could be a residual Cu^{2+} scavenger during neurotransmission. By contrast, αSyn is more abundant in synapses. However, the normal αSyn is predominantly N-terminally acetylated, which only displays limited interaction with Cu^{2+}. Thus, physiological NAc-αSyn may not be a Cu^{2+} transporter, either. Instead, because it can strongly bind to synaptic vesicle and attenuate the mobility of synaptic vesicle, NAc-αSyn could mainly act as a regulator of synaptic vesicle movement. Whereas synaptic vesicle, by possessing fast Cu^{2+} binding rate, high Cu^{2+} binding affinity and enrichment in synapses, could be an important Cu^{2+} transporter. The ascorbate-inactive and GSH-active property of synaptic vesicle-Cu(II) conjugate ensures that Cu^{2+} can be transferred and metabolised through GSH reductive pathway. Meanwhile, Cu^{2+} binding to synaptic vesicle may help release synaptic vesicle from the restriction by NAc-αSyn, thus promoting vesicle trafficking and Cu^{2+} metabolism. The hypothesis that synaptic vesicle is a major Cu^{2+} transporter in synapse is novel, more work is required in future to validate and elucidate the comprehensive story.

Bibliography

[1] Alzheimer's Disease International. Dementia Statistics. (2020). at <https://www.alzint.org/about/dementia-facts-figures/dementia-statistics/>.

[2] Alzheimer, A. Uber eine eigenartige Erkrankung der Hirnrinde. *Zentralbl. Nervenh. Psych.* **18**, 177-179 (1907).

[3] Hardy, J. A. & Higgins, G. A. Alzheimer's disease: the amyloid cascade hypothesis. *Science* **256**, 184-186 (1992).

[4] Hardy, J. & Selkoe, D. J. The amyloid hypothesis of Alzheimer's disease: progress and problems on the road to therapeutics. *Science* **297**, 353-356 (2002).

[5] Karran, E., Mercken, M. & De Strooper, B. The amyloid cascade hypothesis for Alzheimer's disease: an appraisal for the development of therapeutics. *Nature reviews Drug discovery* **10**, 698-712 (2011).

[6] KoSIK, K. S., Joachim, C. L. & Selkoe, D. J. Microtubule-associated protein tau (tau) is a major antigenic component of paired helical filaments in Alzheimer disease. *Proceedings of the National Academy of Sciences* **83**, 4044-4048 (1986).

[7] Noble, W., Hanger, D. P., Miller, C. C. & Lovestone, S. The importance of tau phosphorylation for neurodegenerative diseases. *Frontiers in neurology* **4**, 83 (2013).

[8] Shafiei, S. S., Guerrero-Muñoz, M. J. & Castillo-Carranza, D. L. Tau oligomers: cytotoxicity, propagation, and mitochondrial damage. *Frontiers in aging neuroscience* **9**, 83 (2017).

[9] Nisbet, R. M., Polanco, J.-C., Ittner, L. M. & Götz, J. Tau aggregation and its interplay with amyloid-β. *Acta neuropathologica* **129**, 207-220 (2015).

[10] Pickett, E. K. *et al.* Amyloid beta and tau cooperate to cause reversible behavioral and transcriptional deficits in a model of Alzheimer's disease. *Cell reports* **29**, 3592-3604. e3595 (2019).

[11] Bush, A. I. & Tanzi, R. E. Therapeutics for Alzheimer's disease based on the metal hypothesis. *Neurotherapeutics* **5**, 421-432 (2008).

[12] Parkinson's Foundation. Statistics. (2020). at <https://www. parkinson.org/Understanding-Parkinsons/Statistics>.

[13] Parkinson, J. An essay on the shaking palsy (Printed by Whittingham and Rowland for Sherwood, Neely, and Jones), ed: London. (1817).

[14] Iwatsubo, T. Aggregation of α-synuclein in the pathogenesis of Parkinson's disease. *Journal of neurology* **250**, iii11-iii14 (2003).

[15] Bose, A. & Beal, M. F. Mitochondrial dysfunction in Parkinson's disease. *Journal of neurochemistry* **139**, 216-231 (2016).

[16] Gao, H.-M. *et al.* Neuroinflammation and oxidation/nitration of α-synuclein linked to dopaminergic neurodegeneration. *Journal of Neuroscience* **28**, 7687-7698 (2008).

[17] Gorell, J. M. *et al.* The risk of Parkinson's disease with exposure to pesticides, farming, well water, and rural living. *Neurology* **50**, 1346-1350 (1998).

[18] Masliah, E. *et al.* Dopaminergic loss and inclusion body formation in α-synuclein mice: implications for neurodegenerative disorders. *Science* **287**, 1265-1269 (2000).

[19] Kirik, D. *et al.* Nigrostriatal α-synucleinopathy induced by viral vector-mediated overexpression of human α-synuclein: a new primate model of Parkinson's disease. *Proceedings of the National Academy of Sciences* **100**, 2884-2889 (2003).

[20] De Lau, L. M. & Breteler, M. M. Epidemiology of Parkinson's disease. *The Lancet Neurology* **5**, 525-535 (2006).

[21] Klein, C. & Westenberger, A. Genetics of Parkinson's disease. *Cold Spring Harbor perspectives in medicine* **2**, a008888 (2012).

[22] Uversky, V. N. Intrinsically disordered proteins and their "mysterious"(meta) physics. *Frontiers in Physics* **7**, 10 (2019).

[23] Oldfield, C. J. & Dunker, A. K. Intrinsically disordered proteins and intrinsically disordered protein regions. *Annual review of biochemistry* **83**, 553-584 (2014).

[24] Garner, E. *et al.* Predicting disordered regions from amino acid sequence common themes despite differing structural characterization. *Genome Informatics* **9**, 201-213 (1998).

[25] Romero, P. *et al.* Thousands of proteins likely to have long disordered regions. *Pac Symp Biocomput.* **3**, 437-448 (1998).

[26] Logan, T. M., Thériault, Y. & Fesik, S. W. Structural characterization of the FK506 binding protein unfolded in urea and guanidine hydrochloride. *Journal of molecular biology* **236**, 637-648 (1994).

[27] Eliezer, D., Yao, J., Dyson, H. J. & Wright, P. E. Structural and dynamic characterization of partially folded states of apomyoglobin and implications for protein folding. *Nature structural biology* **5**, 148-155 (1998).

[28] Penkett, C. J. *et al.* NMR analysis of main-chain conformational preferences in an unfolded fibronectin-binding protein. *Journal of molecular biology* **274**, 152-159 (1997).

[29] Wright, P. E. & Dyson, H. J. Intrinsically unstructured proteins: re-assessing the protein structure-function paradigm. *Journal of molecular biology* **293**, 321-331 (1999).

[30] Dunker, A. K. *et al.* Intrinsic disorder and protein function. *Biochemistry* **41**, 6573-6582 (2002).

[31] Dunker, A. K. *et al.* Flexible nets: the roles of intrinsic disorder in protein interaction networks. *The FEBS journal* **272**, 5129-5148 (2005).

[32] Liu, J. *et al.* Intrinsic disorder in transcription factors. *Biochemistry* **45**, 6873-6888 (2006).

[33] Tantos, A., Han, K.-H. & Tompa, P. Intrinsic disorder in cell signaling and gene transcription. *Molecular and cellular endocrinology* **348**, 457-465 (2012).

[34] Wright, P. E. & Dyson, H. J. Intrinsically disordered proteins in cellular signalling and regulation. *Nature reviews Molecular cell biology* **16**, 18-29 (2015).

[35] Zhou, J., Zhao, S. & Dunker, A. K. Intrinsically disordered proteins link alternative splicing and post-translational modifications to complex cell signaling and regulation. *Journal of molecular biology* **430**, 2342-2359 (2018).

[36] Chakrabortee, S. *et al.* Catalytic and chaperone-like functions in an intrinsically disordered protein associated with desiccation tolerance. *Proceedings of the National Academy of Sciences* **107**, 16084-16089 (2010).

[37] Chu, X. *et al.* Importance of electrostatic interactions in the association of intrinsically disordered histone chaperone Chz1 and histone H2A. Z-H2B. *PLoS computational biology*

8, e1002608 (2012).

[38] Denning, D. P. *et al.* Disorder in the nuclear pore complex: the FG repeat regions of nucleoporins are natively unfolded. *Proceedings of the National Academy of Sciences* **100**, 2450-2455 (2003).

[39] Guharoy, M. *et al.* Intrinsic structural disorder in cytoskeletal proteins. *Cytoskeleton* **70**, 550-571 (2013).

[40] Gruszka, D. T. *et al.* Cooperative folding of intrinsically disordered domains drives assembly of a strong elongated protein. *Nature communications* **6**, 1-9 (2015).

[41] Busch, D. J. *et al.* Intrinsically disordered proteins drive membrane curvature. *Nature communications* **6**, 1-11 (2015).

[42] Malinovska, L., Kroschwald, S. & Alberti, S. Protein disorder, prion propensities, and self-organizing macromolecular collectives. *Biochimica et Biophysica Acta (BBA)-Proteins and Proteomics* **1834**, 918-931 (2013).

[43] Kirkitadze, M. D., Condron, M. M. & Teplow, D. B. Identification and characterization of key kinetic intermediates in amyloid β-protein fibrillogenesis. *Journal of molecular biology* **312**, 1103-1119 (2001).

[44] Glenner, G. G. & Wong, C. W. Alzheimer's disease and Down's syndrome: sharing of a unique cerebrovascular amyloid fibril protein. *Biochemical and biophysical research communications* **122**, 1131-1135 (1984).

[45] Masters, C. L. *et al.* Amyloid plaque core protein in Alzheimer disease and Down syndrome. *Proceedings of the National Academy of Sciences* **82**, 4245-4249 (1985).

[46] Haass, C. *et al.* Amyloid β-peptide is produced by cultured cells during normal metabolism. *Nature* **359**, 322-325 (1992).

[47] Priller, C. *et al.* Synapse formation and function is modulated by the amyloid precursor protein. *Journal of Neuroscience* **26**, 7212-7221 (2006).

[48] Phinney, A. *et al.* No hippocampal neuron or synaptic bouton loss in learning-impaired aged β-amyloid precursor protein-null mice. *Neuroscience* **90**, 1207-1216 (1999).

[49] Satpute-Krishnan, P. *et al.* A peptide zipcode sufficient for anterograde transport within amyloid precursor protein. *Proceedings of the National Academy of Sciences* **103**, 16532-16537 (2006).

[50] Nalivaeva, N. N. & Turner, A. J. The amyloid precursor protein: a biochemical enigma in brain development, function and disease. *FEBS letters* **587**, 2046-2054 (2013).

[51] Lee, M.-H. *et al.* Somatic APP gene recombination in Alzheimer's disease and normal neurons. *Nature* **563**, 639-645 (2018).

[52] Murphy, M. P. & LeVine, H., 3rd. Alzheimer's disease and the amyloid-beta peptide. *Journal of Alzheimer's disease : JAD* **19**, 311-323 (2010).

[53] Fonseca, M. B. *et al.* Amyloid β peptides promote autophagy-dependent differentiation of mouse neural stem cells. *Molecular neurobiology* **48**, 829-840 (2013).

[54] Puzzo, D. *et al.* Picomolar amyloid-β positively modulates synaptic plasticity and memory in hippocampus. *Journal of Neuroscience* **28**, 14537-14545 (2008).

[55] Morley, J. E. *et al.* A physiological role for amyloid-β protein: enhancement of learning and memory. *Journal of Alzheimer's disease* **19**, 441-449 (2010).

[56] Puzzo, D. *et al.* Endogenous amyloid-β is necessary for hippocampal synaptic plasticity and memory. *Annals of neurology* **69**, 819-830 (2011).

[57] Brothers, H. M., Gosztyla, M. L. & Robinson, S. R. The physiological roles of amyloid-β peptide hint at new ways to treat Alzheimer's disease. *Frontiers in aging neuroscience* **10**, 118 (2018).

[58] Zou, K., Gong, J.-S., Yanagisawa, K. & Michikawa, M. A novel function of monomeric amyloid β-protein serving as an antioxidant molecule against metal-induced oxidative damage. *Journal of Neuroscience* **22**, 4833-4841 (2002).

[59] Sinha, M., Bhowmick, P., Banerjee, A. & Chakrabarti, S. Antioxidant role of amyloid β protein in cell-free and biological systems: implication for the pathogenesis of Alzheimerdisease. *Free Radical Biology and Medicine* **56**, 184-192 (2013).

[60] Hu, X. *et al.* Amyloid seeds formed by cellular uptake, concentration, and aggregation of the amyloid-beta peptide. *Proceedings of the National Academy of Sciences* **106**, 20324-20329 (2009).

[61] Novo, M., Freire, S. & Al-Soufi, W. Critical aggregation concentration for the formation of early Amyloid-β (1–42) oligomers. *Scientific reports* **8**, 1-8 (2018).

[62] J Baranello, R. *et al.* Amyloid-beta protein clearance and degradation (ABCD) pathways and their role in Alzheimer's disease. *Current Alzheimer Research* **12**, 32-46 (2015).

[63] Iwata, N. *et al.* Metabolic regulation of brain Abeta by neprilysin. *Science* **292**, 1550-1552 (2001).

[64] Marr, R. A. & Hafez, D. M. Amyloid-beta and Alzheimer's disease: the role of neprilysin-2 in amyloid-beta clearance. *Frontiers in aging neuroscience* **6**, 187 (2014).

[65] Vekrellis, K. *et al.* Neurons regulate extracellular levels of amyloid β-protein via proteolysis by insulin-degrading enzyme. *Journal of Neuroscience* **20**, 1657-1665 (2000).

[66] Qiu, W. Q. & Folstein, M. F. Insulin, insulin-degrading enzyme and amyloid-β peptide in Alzheimer's disease: review and hypothesis. *Neurobiology of aging* **27**, 190-198 (2006).

[67] Pappolla, M. *et al.* Evidence for lymphatic Aβ clearance in Alzheimer's transgenic mice. *Neurobiology of disease* **71**, 215-219 (2014).

[68] Barbero-Camps, E. *et al.* Cholesterol impairs autophagy-mediated clearance of amyloid beta while promoting its secretion. *Autophagy* **14**, 1129-1154 (2018).

[69] Deane, R. *et al.* LRP/amyloid β-peptide interaction mediates differential brain efflux of Aβ isoforms. *Neuron* **43**, 333-344 (2004).

[70] Castellano, J. M. *et al.* Low-density lipoprotein receptor overexpression enhances the rate of brain-to-blood Aβ clearance in a mouse model of β-amyloidosis. *Proceedings of the National Academy of Sciences* **109**, 15502-15507 (2012).

[71] Bateman, R. J. *et al.* Human amyloid-β synthesis and clearance rates as measured in cerebrospinal fluid in vivo. *Nature medicine* **12**, 856-861 (2006).

[72] Selkoe, D. J. Alzheimer's disease: genes, proteins, and therapy. *Physiological reviews* (2001).

[73] Roychaudhuri, R., Yang, M., Hoshi, M. M. & Teplow, D. B. Amyloid β-protein assembly and Alzheimer disease. *Journal of Biological Chemistry* **284**, 4749-4753 (2009).

[74] Cohen, S. I. *et al.* Proliferation of amyloid-β42 aggregates occurs through a secondary nucleation mechanism. *Proceedings of the National Academy of Sciences* **110**, 9758-9763 (2013).

[75] Snyder, E. M. *et al.* Regulation of NMDA receptor trafficking by amyloid-β. *Nature neuroscience* **8**, 1051-1058 (2005).

[76] Yamamoto, N. *et al.* A Ganglioside-induced Toxic Soluble Aβ Assembly: Its Enhanced Formation from Aβbearing the Arctic Mutation. *Journal of Biological Chemistry* **282**, 2646-2655 (2007).

[77] Magdesian, M. H. *et al.* Amyloid-β binds to the extracellular cysteine-rich domain of Frizzled and inhibits Wnt/β-catenin signaling. *Journal of Biological Chemistry* **283**, 9359-9368 (2008).

[78] Laurén, J. *et al.* Cellular prion protein mediates impairment of synaptic plasticity by amyloid-β oligomers. *Nature* **457**, 1128-1132 (2009).

[79] Arispe, N., Pollard, H. B. & Rojas, E. Giant multilevel cation channels formed by Alzheimer disease amyloid beta-protein [A beta P-(1-40)] in bilayer membranes. *Proceedings of the National Academy of Sciences* **90**, 10573-10577 (1993).

[80] Arispe, N., Rojas, E. & Pollard, H. B. Alzheimer disease amyloid beta protein forms calcium channels in bilayer membranes: blockade by tromethamine and aluminum. *Proceedings of the National Academy of Sciences* **90**, 567-571 (1993).

[81] Wärmländer, S. K. *et al.* Metal binding to the amyloid-β peptides in the presence of biomembranes: potential mechanisms of cell toxicity. *JBIC Journal of Biological Inorganic Chemistry* **24**, 1189-1196 (2019).

[82] Tseng, B. P. *et al.* Aβ inhibits the proteasome and enhances amyloid and tau accumulation. *Neurobiology of aging* **29**, 1607-1618 (2008).

[83] Cheignon, C. *et al.* Oxidative stress and the amyloid beta peptide in Alzheimer's disease. *Redox biology* **14**, 450-464 (2018).

[84] Selfridge, J. E., Lezi, E., Lu, J. & Swerdlow, R. H. Role of mitochondrial homeostasis and dynamics in Alzheimer's disease. *Neurobiology of disease* **51**, 3-12 (2013).

[85] Sayre, L. M. *et al.* 4-Hydroxynonenal-derived advanced lipid peroxidation end products are increased in Alzheimer's disease. *Journal of neurochemistry* **68**, 2092-2097 (1997).

[86] Gu, Z., Nakamura, T. & Lipton, S. A. Redox reactions induced by nitrosative stress mediate protein misfolding and mitochondrial dysfunction in neurodegenerative diseases. *Molecular neurobiology* **41**, 55-72 (2010).

[87] Halliwell, B. Oxidative stress and neurodegeneration: where are we now? *Journal of neurochemistry* **97**, 1634-1658 (2006).

[88] Huang, X. *et al.* The Aβ peptide of Alzheimer's disease directly produces hydrogen peroxide through metal ion reduction. *Biochemistry* **38**, 7609-7616 (1999).

[89] Atwood, C. S. *et al.* Characterization of copper interactions with Alzheimer amyloid β peptides: identification of an attomolar-affinity copper binding site on amyloid β1-42. *Journal of neurochemistry* **75**, 1219-1233 (2000).

[90] Huang, X. *et al.* Cu (II) potentiation of Alzheimer Aβ neurotoxicity: correlation with cell-free hydrogen peroxide production and metal reduction. *Journal of Biological Chemistry* **274**, 37111-37116 (1999).

[91] Milton, N. G. Phosphorylation of amyloid-β at the serine 26 residue by human cdc2 kinase. *Neuroreport* **12**, 3839-3844 (2001).

[92] Kumar, S. *et al.* Extracellular phosphorylation of the amyloid β-peptide promotes formation of toxic aggregates during the pathogenesis of Alzheimer's disease. *The EMBO journal* **30**, 2255-2265 (2011).

[93] Wiltfang, J. *et al.* Elevation of β-amyloid peptide 2–42 in sporadic and familial Alzheimer's

disease and its generation in PS1 knockout cells. *Journal of Biological Chemistry* **276**, 42645-42657 (2001).

[94] Miravalle, L. *et al.* Amino-terminally truncated Aβ peptide species are the main component of cotton wool plaques. *Biochemistry* **44**, 10810-10821 (2005).

[95] Harigaya, Y. *et al.* Amyloid β protein starting pyroglutamate at position 3 is a major component of the amyloid deposits in the Alzheimer's disease brain. *Biochemical and biophysical research communications* **276**, 422-427 (2000).

[96] Dong, J. *et al.* Metal binding and oxidation of amyloid-β within isolated senile plaque cores: Raman microscopic evidence. *Biochemistry* **42**, 2768-2773 (2003).

[97] Kubo, T., Kumagae, Y., Miller, C. A. & Kaneko, I. β-Amyloid racemized at the Ser26 residue in the brains of patients with Alzheimer disease: implications in the pathogenesis of Alzheimer disease. *Journal of Neuropathology & Experimental Neurology* **62**, 248-259 (2003).

[98] Shimizu, T. *et al.* Isoaspartate formation at position 23 of amyloid beta peptide enhanced fibril formation and deposited onto senile plaques and vascular amyloids in Alzheimer's disease. *Journal of neuroscience research* **70**, 451-461 (2002).

[99] Kummer, M. P. *et al.* Nitration of tyrosine 10 critically enhances amyloid β aggregation and plaque formation. *Neuron* **71**, 833-844 (2011).

[100] Halim, A. *et al.* Site-specific characterization of threonine, serine, and tyrosine glycosylations of amyloid precursor protein/amyloid β-peptides in human cerebrospinal fluid. *Proceedings of the National Academy of Sciences* **108**, 11848-11853 (2011).

[101] Kuo, Y.-M. *et al.* Irreversible dimerization/tetramerization and post-translational modifications inhibit proteolytic degradation of Aβ peptides of Alzheimer's disease. *Biochimica et Biophysica Acta (BBA)-Molecular Basis of Disease* **1406**, 291-298 (1998).

[102] Whitmarsh, A. & Davis, R. Regulation of transcription factor function by phosphorylation. *Cellular and Molecular Life Sciences CMLS* **57**, 1172-1183 (2000).

[103] Johnson, L. & Barford, D. The effects of phosphorylation on the structure and function of proteins. *Annual review of biophysics and biomolecular structure* **22**, 199-232 (1993).

[104] Alonso, A. d. C., Zaidi, T., Grundke-Iqbal, I. & Iqbal, K. Role of abnormally phosphorylated tau in the breakdown of microtubules in Alzheimer disease. *Proceedings of the National Academy of Sciences* **91**, 5562-5566 (1994).

[105] Hampel, H. *et al.* Total and phosphorylated tau protein as biological markers of Alzheimer's disease. *Experimental gerontology* **45**, 30-40 (2010).

[106] Kumar, S. *et al.* Early intraneuronal accumulation and increased aggregation of phosphorylated Abeta in a mouse model of Alzheimer's disease. *Acta neuropathologica* **125**, 699-709 (2013).

[107] Kummer, M. P. & Heneka, M. T. Truncated and modified amyloid-beta species. *Alzheimer's research & therapy* **6**, 1-9 (2014).

[108] Sergeant, N. *et al.* Truncated beta-amyloid peptide species in pre-clinical Alzheimer's disease as new targets for the vaccination approach. *Journal of neurochemistry* **85**, 1581-1591 (2003).

[109] Lewis, H. *et al.* Quantification of Alzheimer pathology in ageing and dementia: age-related accumulation of amyloid-β (42) peptide in vascular dementia. *Neuropathology and applied neurobiology* **32**, 103-118 (2006).

[110] Portelius, E. *et al.* Mass spectrometric characterization of brain amyloid beta isoform signatures in familial and sporadic Alzheimer's disease. *Acta neuropathologica* **120**, 185-193 (2010).

[111] Antonios, G. *et al.* N-truncated Abeta starting with position four: early intraneuronal accumulation and rescue of toxicity using NT4X-167, a novel monoclonal antibody. *Acta neuropathologica communications* **1**, 1-15 (2013).

[112] Bayer, T. A. & Wirths, O. Focusing the amyloid cascade hypothesis on N-truncated Abeta peptides as drug targets against Alzheimer's disease. *Acta neuropathologica* **127**, 787-801 (2014).

[113] Mital, M. *et al.* A functional role for Aβ in metal homeostasis? N-truncation and high-affinity copper binding. *Angewandte Chemie* **127**, 10606-10610 (2015).

[114] Barykin, E. P., Mitkevich, V. A., Kozin, S. A. & Makarov, A. A. Amyloid β modification: a key to the sporadic Alzheimer's disease? *Frontiers in genetics* **8**, 58 (2017).

[115] Maroteaux, L., Campanelli, J. T. & Scheller, R. H. Synuclein: a neuron-specific protein localized to the nucleus and presynaptic nerve terminal. *Journal of Neuroscience* **8**, 2804-2815 (1988).

[116] Perni, M. *et al.* A natural product inhibits the initiation of α-synuclein aggregation and suppresses its toxicity. *Proceedings of the National Academy of Sciences* **114**, E1009-E1017 (2017).

[117] Mor, D. E., Ugras, S. E., Daniels, M. J. & Ischiropoulos, H. Dynamic structural flexibility of α-synuclein. *Neurobiology of disease* **88**, 66-74 (2016).

[118] Segrest, J. *et al.* The amphipathic helix in the exchangeable apolipoproteins: a review of secondary structure and function. *Journal of lipid research* **33**, 141-166 (1992).

[119] Segrest, J. P., Jackson, R. L., Morrisett, J. D. & Gotto Jr, A. M. A molecular theory of lipid—protein interactions in the plasma lipoproteins. *FEBS letters* **38**, 247-253 (1974).

[120] Pirc, K. & Ulrih, N. P. α-Synuclein interactions with phospholipid model membranes: Key roles for electrostatic interactions and lipid-bilayer structure. *Biochimica et Biophysica Acta (BBA)-Biomembranes* **1848**, 2002-2012 (2015).

[121] Rovere, M., Sanderson, J. B., Fonseca-Ornelas, L. & Bartels, T. Reconstitution of helical soluble α-synuclein through transient interaction with lipid interfaces. *bioRxiv*, 202994 (2017).

[122] Dong, C. *et al.* Structural characteristics and membrane interactions of tandem α-synuclein oligomers. *Scientific reports* **8**, 1-11 (2018).

[123] Ulmer, T. S., Bax, A., Cole, N. B. & Nussbaum, R. L. Structure and dynamics of micelle-bound human α-synuclein. *Journal of Biological Chemistry* **280**, 9595-9603 (2005).

[124] Ferreon, A. C. M., Gambin, Y., Lemke, E. A. & Deniz, A. A. Interplay of α-synuclein binding and conformational switching probed by single-molecule fluorescence. *Proceedings of the National Academy of Sciences* **106**, 5645-5650 (2009).

[125] Trexler, A. J. & Rhoades, E. α-Synuclein binds large unilamellar vesicles as an extended helix. *Biochemistry* **48**, 2304-2306 (2009).

[126] Cholak, E. *et al.* Avidity within the N-terminal anchor drives α-synuclein membrane interaction and insertion. *The FASEB Journal* **34**, 7462-7482 (2020).

[127] Uéda, K. *et al.* Molecular cloning of cDNA encoding an unrecognized component of amyloid in Alzheimer disease. *Proceedings of the National Academy of Sciences* **90**, 11282-

11286 (1993).
[128] Tuttle, M. D. *et al.* Solid-state NMR structure of a pathogenic fibril of full-length human α-synuclein. *Nature structural & molecular biology* **23**, 409-415 (2016).
[129] Fields, C. R., Bengoa-Vergniory, N. & Wade-Martins, R. Targeting alpha-synuclein as a therapy for Parkinson's disease. *Frontiers in molecular neuroscience* **12**, 299 (2019).
[130] Du, H.-N. *et al.* A peptide motif consisting of glycine, alanine, and valine is required for the fibrillization and cytotoxicity of human α-synuclein. *Biochemistry* **42**, 8870-8878 (2003).
[131] Giasson, B. I., Murray, I. V., Trojanowski, J. Q. & Lee, V. M.-Y. A hydrophobic stretch of 12 amino acid residues in the middle of α-synuclein is essential for filament assembly. *Journal of Biological Chemistry* **276**, 2380-2386 (2001).
[132] Koo, H.-J., Choi, M. Y. & Im, H. Aggregation-defective α-synuclein mutants inhibit the fibrillation of Parkinson's disease-linked α-synuclein variants. *Biochemical and biophysical research communications* **386**, 165-169 (2009).
[133] George, J. M., Jin, H., Woods, W. S. & Clayton, D. F. Characterization of a novel protein regulated during the critical period for song learning in the zebra finch. *Neuron* **15**, 361-372 (1995).
[134] Uversky, V. N., Gillespie, J. R. & Fink, A. L. Why are "natively unfolded" proteins unstructured under physiologic conditions? *Proteins: structure, function, and bioinformatics* **41**, 415-427 (2000).
[135] Dedmon, M. M. *et al.* Mapping long-range interactions in α-synuclein using spin-label NMR and ensemble molecular dynamics simulations. *Journal of the American Chemical Society* **127**, 476-477 (2005).
[136] Li, W. *et al.* Aggregation promoting C-terminal truncation of α-synuclein is a normal cellular process and is enhanced by the familial Parkinson's disease-linked mutations. *Proceedings of the National Academy of Sciences* **102**, 2162-2167 (2005).
[137] Bartels, T., Choi, J. G. & Selkoe, D. J. α-Synuclein occurs physiologically as a helically folded tetramer that resists aggregation. *Nature* **477**, 107-110 (2011).
[138] Wang, W. *et al.* A soluble α-synuclein construct forms a dynamic tetramer. *Proceedings of the National Academy of Sciences* **108**, 17797-17802 (2011).
[139] Fauvet, B. *et al.* α-Synuclein in central nervous system and from erythrocytes, mammalian cells, and Escherichia coli exists predominantly as disordered monomer. *Journal of Biological Chemistry* **287**, 15345-15364 (2012).
[140] Burré, J. *et al.* Properties of native brain α-synuclein. *Nature* **498**, E4-E6 (2013).
[141] Theillet, F.-X. *et al.* Structural disorder of monomeric α-synuclein persists in mammalian cells. *Nature* **530**, 45-50 (2016).
[142] Luth, E. S. *et al.* Purification of α-synuclein from human brain reveals an instability of endogenous multimers as the protein approaches purity. *Biochemistry* **54**, 279-292 (2015).
[143] Dettmer, U. *et al.* Parkinson-causing α-synuclein missense mutations shift native tetramers to monomers as a mechanism for disease initiation. *Nature communications* **6**, 1-16 (2015).
[144] Cabin, D. E. *et al.* Synaptic vesicle depletion correlates with attenuated synaptic responses to prolonged repetitive stimulation in mice lacking α-synuclein. *Journal of Neuroscience* **22**, 8797-8807 (2002).
[145] Nemani, V. M. *et al.* Increased expression of α-synuclein reduces neurotransmitter release

by inhibiting synaptic vesicle reclustering after endocytosis. *Neuron* **65**, 66-79 (2010).

[146] Wang, L. *et al.* α-synuclein multimers cluster synaptic vesicles and attenuate recycling. *Current Biology* **24**, 2319-2326 (2014).

[147] Fusco, G. *et al.* Structural basis of synaptic vesicle assembly promoted by α-synuclein. *Nature communications* **7**, 1-12 (2016).

[148] Dalfo, E. & Ferrer, I. α-Synuclein binding to rab3a in multiple system atrophy. *Neuroscience letters* **380**, 170-175 (2005).

[149] Burré, J. *et al.* α-Synuclein promotes SNARE-complex assembly in vivo and in vitro. *Science* **329**, 1663-1667 (2010).

[150] Abeliovich, A. *et al.* Mice lacking α-synuclein display functional deficits in the nigrostriatal dopamine system. *Neuron* **25**, 239-252 (2000).

[151] Tehranian, R. *et al.* Alpha-synuclein inhibits aromatic amino acid decarboxylase activity in dopaminergic cells. *Journal of neurochemistry* **99**, 1188-1196 (2006).

[152] Chandra, S. *et al.* α-Synuclein cooperates with CSPα in preventing neurodegeneration. *Cell* **123**, 383-396 (2005).

[153] Liu, G. *et al.* α-Synuclein is differentially expressed in mitochondria from different rat brain regions and dose-dependently down-regulates complex I activity. *Neuroscience letters* **454**, 187-192 (2009).

[154] Schaser, A. J. *et al.* Alpha-synuclein is a DNA binding protein that modulates DNA repair with implications for Lewy body disorders. *Scientific reports* **9**, 1-19 (2019).

[155] Öhrfelt, A. *et al.* Identification of novel α-synuclein isoforms in human brain tissue by using an online nanoLC-ESI-FTICR-MS method. *Neurochemical research* **36**, 2029-2042 (2011).

[156] Bartels, T., Kim, N. C., Luth, E. S. & Selkoe, D. J. N-alpha-acetylation of α-synuclein increases its helical folding propensity, GM1 binding specificity and resistance to aggregation. *PloS one* **9**, e103727 (2014).

[157] Setty, S. R. *et al.* Golgi targeting of ARF-like GTPase Arl3p requires its Nalpha-acetylation and the integral membrane protein Sys1p. *Nat Cell Biol* **6**, 414-419 (2004).

[158] Scott, D. C. *et al.* N-terminal acetylation acts as an avidity enhancer within an interconnected multiprotein complex. *Science* **334**, 674-678 (2011).

[159] Iyer, A. *et al.* The impact of N-terminal acetylation of α-synuclein on phospholipid membrane binding and fibril structure. *Journal of Biological Chemistry* **291**, 21110-21122 (2016).

[160] Watson, M. D. & Lee, J. C. N-terminal acetylation affects α-synuclein fibril polymorphism. *Biochemistry* **58**, 3630-3633 (2019).

[161] Runfola, M. *et al.* The N-terminal acetylation of α-synuclein changes the affinity for lipid membranes but not the structural properties of the bound state. *Scientific reports* **10**, 1-10 (2020).

[162] Gruschus, J. M. *et al.* NMR structure of calmodulin complexed to an N-terminally acetylated α-synuclein peptide. *Biochemistry* **52**, 3436-3445 (2013).

[163] Birol, M., Wojcik, S. P., Miranker, A. D. & Rhoades, E. Identification of N-linked glycans as specific mediators of neuronal uptake of acetylated α-Synuclein. *PLoS biology* **17**, e3000318 (2019).

[164] Mason, R. J., Paskins, A. R., Dalton, C. F. & Smith, D. P. Copper binding and subsequent aggregation of α-synuclein are modulated by N-terminal acetylation and ablated by the

H50Q missense mutation. *Biochemistry* **55**, 4737-4741 (2016).
[165] Vinueza-Gavilanes, R. *et al.* N-terminal acetylation mutants affect alpha-synuclein stability, protein levels and neuronal toxicity. *Neurobiology of disease* **137**, 104781 (2020).
[166] Iwata, A. *et al.* Alpha-synuclein degradation by serine protease neurosin: implication for pathogenesis of synucleinopathies. *Human molecular genetics* **12**, 2625-2635 (2003).
[167] Klucken, J. *et al.* Hsp70 reduces α-synuclein aggregation and toxicity. *Journal of Biological Chemistry* **279**, 25497-25502 (2004).
[168] Webb, J. L. *et al.* α-Synuclein is degraded by both autophagy and the proteasome. *Journal of Biological Chemistry* **278**, 25009-25013 (2003).
[169] McNaught, K. S. P. *et al.* Proteasome inhibition causes nigral degeneration with inclusion bodies in rats. *Neuroreport* **13**, 1437-1441 (2002).
[170] Cuervo, A. M. *et al.* Impaired degradation of mutant α-synuclein by chaperone-mediated autophagy. *Science* **305**, 1292-1295 (2004).
[171] Wood, S. J. *et al.* α-synuclein fibrillogenesis is nucleation-dependent: implications for the pathogenesis of Parkinson's disease. *Journal of Biological Chemistry* **274**, 19509-19512 (1999).
[172] Greenbaum, E. A. *et al.* The E46K mutation in α-synuclein increases amyloid fibril formation. *Journal of Biological Chemistry* **280**, 7800-7807 (2005).
[173] Ghosh, D. *et al.* The Parkinson's disease-associated H50Q mutation accelerates α-Synuclein aggregation in vitro. *Biochemistry* **52**, 6925-6927 (2013).
[174] Zhang, J., Li, X. & Li, J.-D. The roles of post-translational modifications on α-synuclein in the pathogenesis of Parkinson's diseases. *Frontiers in neuroscience* **13**, 381 (2019).
[175] Paik, S. R. *et al.* Copper (II)-induced self-oligomerization of α-synuclein. *Biochemical Journal* **340**, 821-828 (1999).
[176] Nath, S., Goodwin, J., Engelborghs, Y. & Pountney, D. Raised calcium promotes α-synuclein aggregate formation. *Molecular and Cellular Neuroscience* **46**, 516-526 (2011).
[177] Xiao, Y. *et al.* Iron promotes α-synuclein aggregation and transmission by inhibiting TFEB-mediated autophagosome-lysosome fusion. *Journal of neurochemistry* **145**, 34-50 (2018).
[178] Guerrero-Ferreira, R. *et al.* Cryo-EM structure of alpha-synuclein fibrils. *Elife* **7**, e36402 (2018).
[179] Luk, K. C. *et al.* Exogenous α-synuclein fibrils seed the formation of Lewy body-like intracellular inclusions in cultured cells. *Proceedings of the National Academy of Sciences* **106**, 20051-20056 (2009).
[180] Luk, K. C. *et al.* Pathological α-synuclein transmission initiates Parkinson-like neurodegeneration in nontransgenic mice. *Science* **338**, 949-953 (2012).
[181] Winner, B. *et al.* In vivo demonstration that α-synuclein oligomers are toxic. *Proceedings of the National Academy of Sciences* **108**, 4194-4199 (2011).
[182] Choi, B.-K. *et al.* Large α-synuclein oligomers inhibit neuronal SNARE-mediated vesicle docking. *Proceedings of the National Academy of Sciences* **110**, 4087-4092 (2013).
[183] Hsu, L. J. *et al.* α-Synuclein promotes mitochondrial deficit and oxidative stress. *The American journal of pathology* **157**, 401-410 (2000).
[184] Cooper, A. A. *et al.* α-Synuclein blocks ER-Golgi traffic and Rab1 rescues neuron loss in Parkinson's models. *Science* **313**, 324-328 (2006).
[185] Mazzulli, J. R. *et al.* α-Synuclein–induced lysosomal dysfunction occurs through

disruptions in protein trafficking in human midbrain synucleinopathy models. *Proceedings of the National Academy of Sciences* **113**, 1931-1936 (2016).

[186] Deas, E. *et al.* Alpha-synuclein oligomers interact with metal ions to induce oxidative stress and neuronal death in Parkinson's disease. *Antioxidants & redox signaling* **24**, 376-391 (2016).

[187] González, N. *et al.* Effects of alpha-synuclein post-translational modifications on metal binding. *Journal of neurochemistry* **150**, 507-521 (2019).

[188] Wang, C. *et al.* Redox reactions of the α-synuclein− Cu2+ complex and their effects on neuronal cell viability. *Biochemistry* **49**, 8134-8142 (2010).

[189] Meloni, G. & Vašák, M. Redox activity of α-synuclein–Cu is silenced by Zn7-metallothionein-3. *Free Radical Biology and Medicine* **50**, 1471-1479 (2011).

[190] Miotto, M. C. *et al.* Site-specific copper-catalyzed oxidation of α-synuclein: Tightening the link between metal binding and protein oxidative damage in Parkinson's disease. *Inorganic chemistry* **53**, 4350-4358 (2014).

[191] Rodríguez, E. E. *et al.* Role of N-terminal methionine residues in the redox activity of copper bound to alpha-synuclein. *JBIC Journal of Biological Inorganic Chemistry* **21**, 691-702 (2016).

[192] Meade, R. M., Fairlie, D. P. & Mason, J. M. Alpha-synuclein structure and Parkinson's disease–lessons and emerging principles. *Molecular neurodegeneration* **14**, 1-14 (2019).

[193] Xu, L., Ma, B., Nussinov, R. & Thompson, D. Familial mutations may switch conformational preferences in α-synuclein fibrils. *ACS chemical neuroscience* **8**, 837-849 (2017).

[194] Mohite, G. M. *et al.* Parkinson's disease associated α-synuclein familial mutants promote dopaminergic neuronal death in Drosophila melanogaster. *ACS chemical neuroscience* **9**, 2628-2638 (2018).

[195] Ruf, V. C. *et al.* Different effects of α-synuclein mutants on lipid binding and aggregation detected by single molecule fluorescence spectroscopy and ThT fluorescence-based measurements. *ACS chemical neuroscience* **10**, 1649-1659 (2019).

[196] Rovere, M. *et al.* E46K-like α-synuclein mutants increase lipid interactions and disrupt membrane selectivity. *Journal of Biological Chemistry* **294**, 9799-9812 (2019).

[197] Lautenschläger, J. *et al.* C-terminal calcium binding of α-synuclein modulates synaptic vesicle interaction. *Nature communications* **9**, 1-13 (2018).

[198] Breydo, L. & Uversky, V. N. Role of metal ions in aggregation of intrinsically disordered proteins in neurodegenerative diseases. *Metallomics* **3**, 1163-1180 (2011).

[199] Faller, P., Hureau, C. & La Penna, G. Metal ions and intrinsically disordered proteins and peptides: from Cu/Zn amyloid-β to general principles. *Accounts of chemical research* **47**, 2252-2259 (2014).

[200] D'Ambrosi, N. & Rossi, L. Copper at synapse: Release, binding and modulation of neurotransmission. *Neurochemistry international* **90**, 36-45 (2015).

[201] Smith, D. G., Cappai, R. & Barnham, K. J. The redox chemistry of the Alzheimer's disease amyloid β peptide. *Biochimica et Biophysica Acta (BBA)-Biomembranes* **1768**, 1976-1990 (2007).

[202] Lovell, M. *et al.* Copper, iron and zinc in Alzheimer's disease senile plaques. *Journal of the neurological sciences* **158**, 47-52 (1998).

[203] Miller, L. M. *et al.* Synchrotron-based infrared and X-ray imaging shows focalized accumulation of Cu and Zn co-localized with β-amyloid deposits in Alzheimer's disease. *Journal of structural biology* **155**, 30-37 (2006).

[204] Pall, H. *et al.* Raised cerebrospinal-fluid copper concentration in Parkinson's disease. *The Lancet* **330**, 238-241 (1987).

[205] Mezzaroba, L., Alfieri, D. F., Simão, A. N. C. & Reiche, E. M. V. The role of zinc, copper, manganese and iron in neurodegenerative diseases. *Neurotoxicology* **74**, 230-241 (2019).

[206] Branch, T., Girvan, P., Barahona, M. & Ying, L. Introduction of a fluorescent probe to amyloid-β to reveal kinetic insights into its interactions with copper (II). *Angewandte Chemie* **127**, 1243-1246 (2015).

[207] Weibull, M. G. *et al.* Effects of Cu (II) on the aggregation of amyloid-β. *JBIC Journal of Biological Inorganic Chemistry* **24**, 1197-1215 (2019).

[208] Drew, S. C. *et al.* Cu2+ binding modes of recombinant α-synuclein− insights from EPR spectroscopy. *Journal of the American Chemical Society* **130**, 7766-7773 (2008).

[209] De Ricco, R. *et al.* Remote His50 acts as a coordination switch in the high-affinity N-terminal centered copper (II) site of α-synuclein. *Inorganic chemistry* **54**, 4744-4751 (2015).

[210] Tian, Y. *et al.* Copper2+ binding to α-synuclein. Histidine50 can form a ternary complex with Cu2+ at the N-terminus but not a macrochelate. *Inorganic chemistry* **58**, 15580-15589 (2019).

[211] Dudzik, C. G., Walter, E. D. & Millhauser, G. L. Coordination features and affinity of the Cu2+ site in the α-synuclein protein of Parkinson's disease. *Biochemistry* **50**, 1771-1777 (2011).

[212] Moriarty, G. M., Minetti, C. a. o. A., Remeta, D. P. & Baum, J. A revised picture of the Cu (II)− α-synuclein complex: the role of N-terminal acetylation. *Biochemistry* **53**, 2815-2817 (2014).

[213] Miotto, M. C. *et al.* Copper binding to the N-terminally acetylated, naturally occurring form of alpha-synuclein induces local helical folding. *Journal of the American Chemical Society* **137**, 6444-6447 (2015).

[214] Monson, C. F. *et al.* Phosphatidylserine reversibly binds Cu2+ with extremely high affinity. *Journal of the American Chemical Society* **134**, 7773-7779 (2012).

[215] Cong, X. *et al.* Unquenchable surface potential dramatically enhances Cu2+ binding to phosphatidylserine lipids. *Journal of the American Chemical Society* **137**, 7785-7792 (2015).

[216] Poyton, M. F., Sendecki, A. M., Cong, X. & Cremer, P. S. Cu2+ binds to phosphatidylethanolamine and increases oxidation in lipid membranes. *Journal of the American Chemical Society* **138**, 1584-1590 (2016).

[217] Qu, L., Akbergenova, Y., Hu, Y. & Schikorski, T. Synapse-to-synapse variation in mean synaptic vesicle size and its relationship with synaptic morphology and function. *Journal of Comparative Neurology* **514**, 343-352 (2009).

[218] Lim, L. & Wenk, M. Neuronal membrane lipids – their role in the synaptic vesicle cycle. (ed. Lajtha, A., Tettamanti, G. & Goracci, G.) 223-238 (New York: Springer Publications, 2010).

[219] Ambroggio, E. E. *et al.* Surface behavior and lipid interaction of Alzheimer β-amyloid peptide 1–42: a membrane-disrupting peptide. *Biophysical journal* **88**, 2706-2713 (2005).

[220] Hicks, D. A., Nalivaeva, N. N. & Turner, A. J. Lipid rafts and Alzheimer's disease: protein-lipid interactions and perturbation of signaling. *Frontiers in physiology* **3**, 189 (2012).

[221] Seghezza, S., Diaspro, A., Canale, C. & Dante, S. Cholesterol drives Aβ (1–42) interaction with lipid rafts in model membranes. *Langmuir* **30**, 13934-13941 (2014).

[222] Yu, X. & Zheng, J. Cholesterol promotes the interaction of Alzheimer β-amyloid monomer with lipid bilayer. *Journal of molecular biology* **421**, 561-571 (2012).

[223] Habchi, J. *et al.* Cholesterol catalyses Aβ42 aggregation through a heterogeneous nucleation pathway in the presence of lipid membranes. *Nature chemistry* **10**, 673-683 (2018).

[224] Okada, T., Wakabayashi, M., Ikeda, K. & Matsuzaki, K. Formation of toxic fibrils of Alzheimer's amyloid β-protein-(1–40) by monosialoganglioside GM1, a neuronal membrane component. *Journal of molecular biology* **371**, 481-489 (2007).

[225] Matsuzaki, K., Kato, K. & Yanagisawa, K. Aβ polymerization through interaction with membrane gangliosides. *Biochimica et Biophysica Acta (BBA)-Molecular and Cell Biology of Lipids* **1801**, 868-877 (2010).

[226] Wakabayashi, M., Okada, T., Kozutsumi, Y. & Matsuzaki, K. GM1 ganglioside-mediated accumulation of amyloid β-protein on cell membranes. *Biochemical and biophysical research communications* **328**, 1019-1023 (2005).

[227] Ikeda, K. *et al.* Mechanism of amyloid β-protein aggregation mediated by GM1 ganglioside clusters. *Biochemistry* **50**, 6433-6440 (2011).

[228] Lindberg, D. J. *et al.* Lipid membranes catalyse the fibril formation of the amyloid-β (1–42) peptide through lipid-fibril interactions that reinforce secondary pathways. *Biochimica et Biophysica Acta (BBA)-Biomembranes* **1859**, 1921-1929 (2017).

[229] Georgieva, E. R. *et al.* The lipid-binding domain of wild type and mutant α-synuclein: compactness and interconversion between the broken and extended helix forms. *Journal of Biological Chemistry* **285**, 28261-28274 (2010).

[230] Lokappa, S. B. & Ulmer, T. S. α-Synuclein populates both elongated and broken helix states on small unilamellar vesicles. *Journal of Biological Chemistry* **286**, 21450-21457 (2011).

[231] Drescher, M. *et al.* Antiparallel arrangement of the helices of vesicle-bound α-synuclein. *Journal of the American Chemical Society* **130**, 7796-7797 (2008).

[232] Drescher, M. *et al.* Spin-label EPR on α-synuclein reveals differences in the membrane binding affinity of the two antiparallel helices. *ChemBioChem* **9**, 2411-2416 (2008).

[233] Ysselstein, D. *et al.* Effects of impaired membrane interactions on α-synuclein aggregation and neurotoxicity. *Neurobiology of disease* **79**, 150-163 (2015).

[234] Bartels, T. *et al.* The N-terminus of the intrinsically disordered protein α-synuclein triggers membrane binding and helix folding. *Biophysical journal* **99**, 2116-2124 (2010).

[235] Jao, C. C., Der-Sarkissian, A., Chen, J. & Langen, R. Structure of membrane-bound α-synuclein studied by site-directed spin labeling. *Proceedings of the National Academy of Sciences* **101**, 8331-8336 (2004).

[236] Ouberai, M. M. *et al.* α-Synuclein senses lipid packing defects and induces lateral expansion of lipids leading to membrane remodeling. *Journal of Biological Chemistry* **288**, 20883-20895 (2013).

[237] Fusco, G. *et al.* Structural ensembles of membrane-bound α-synuclein reveal the molecular determinants of synaptic vesicle affinity. *Scientific reports* **6**, 1-9 (2016).

[238] Middleton, E. R. & Rhoades, E. Effects of curvature and composition on α-synuclein binding to lipid vesicles. *Biophysical journal* **99**, 2279-2288 (2010).

[239] Braun, A. R. *et al.* α-Synuclein induces both positive mean curvature and negative Gaussian curvature in membranes. *Journal of the American Chemical Society* **134**, 2613-2620 (2012).

[240] Stöckl, M., Fischer, P., Wanker, E. & Herrmann, A. α-Synuclein selectively binds to anionic phospholipids embedded in liquid-disordered domains. *Journal of molecular biology* **375**, 1394-1404 (2008).

[241] Zarbiv, Y. *et al.* Lysine residues at the first and second KTKEGV repeats mediate α-Synuclein binding to membrane phospholipids. *Neurobiology of disease* **70**, 90-98 (2014).

[242] Hannestad, J. K. *et al.* Single-vesicle imaging reveals lipid-selective and stepwise membrane disruption by monomeric α-synuclein. *Proceedings of the National Academy of Sciences* **117**, 14178-14186 (2020).

[243] Zhu, M. & Fink, A. L. Lipid binding inhibits α-synuclein fibril formation. *Journal of Biological Chemistry* **278**, 16873-16877 (2003).

[244] Galvagnion, C. *et al.* Lipid vesicles trigger α-synuclein aggregation by stimulating primary nucleation. *Nature chemical biology* **11**, 229-234 (2015).

[245] Killinger, B. A., Melki, R., Brundin, P. & Kordower, J. H. Endogenous alpha-synuclein monomers, oligomers and resulting pathology: Let's talk about the lipids in the room. *npj Parkinson's Disease* **5**, 1-8 (2019).

[246] Man, W. K. *et al.* A role of cholesterol in modulating the binding of α-synuclein to synaptic-like vesicles. *Frontiers in neuroscience* **14**, 18 (2020).

[247] Gaspar, R. *et al.* Ganglioside lipids accelerate α-synuclein amyloid formation. *Biochimica et Biophysica Acta (BBA)-Proteins and Proteomics* **1866**, 1062-1072 (2018).

[248] Martinez, Z., Zhu, M., Han, S. & Fink, A. L. GM1 specifically interacts with α-synuclein and inhibits fibrillation. *Biochemistry* **46**, 1868-1877 (2007).

[249] Lakowicz, J. R. *Principles of fluorescence spectroscopy*. (Springer science & business media, 2013).

[250] Aitken, C. E., Marshall, R. A. & Puglisi, J. D. An oxygen scavenging system for improvement of dye stability in single-molecule fluorescence experiments. *Biophysical journal* **94**, 1826-1835 (2008).

[251] Förster, T. Zwischenmolekulare energiewanderung und fluoreszenz. *Annalen der physik* **437**, 55-75 (1948).

[252] Hess, S. T. & Webb, W. W. Focal volume optics and experimental artifacts in confocal fluorescence correlation spectroscopy. *Biophysical journal* **83**, 2300-2317 (2002).

[253] Haustein, E. & Schwille, P. Fluorescence correlation spectroscopy: an introduction to its concepts and applications. *Biophysics Textbook Online* (2004).

[254] Kuo, Y.-M. *et al.* Isolation, chemical characterization, and quantitation of Aβ 3-pyroglutamyl peptide from neuritic plaques and vascular amyloid deposits. *Biochemical and biophysical research communications* **237**, 188-191 (1997).

[255] Milton, N. G. Phosphorylated amyloid-β: the toxic intermediate in Alzheimer's disease neurodegeneration. *Alzheimer's Disease*, 381-402 (2005).

[256] Kumar, S. & Walter, J. Phosphorylation of amyloid beta (Aβ) peptides–A trigger for formation of toxic aggregates in Alzheimer's disease. *Aging (Albany NY)* **3**, 803 (2011).

[257] Alies, B. *et al.* pH-Dependent Cu (II) coordination to amyloid-β peptide: impact of

sequence alterations, including the H6R and D7N familial mutations. *Inorganic chemistry* **50**, 11192-11201 (2011).

[258] Girvan, P. *et al.* Kinetics of the interactions between copper and amyloid-β with FAD mutations and phosphorylation at the N terminus. *ChemBioChem* **17**, 1732-1737 (2016).

[259] Garai, K. & Frieden, C. Quantitative analysis of the time course of Aβ oligomerization and subsequent growth steps using tetramethylrhodamine-labeled Aβ. *Proceedings of the National Academy of Sciences* **110**, 3321-3326 (2013).

[260] Hane, F., Tran, G., Attwood, S. J. & Leonenko, Z. Cu2+ affects amyloid-β (1–42) aggregation by increasing peptide-peptide binding forces. *PloS one* **8**, e59005 (2013).

[261] Pushie, M. J. *et al.* Using N-terminal coordination of Cu (II) and Ni (II) to isolate the coordination environment of Cu (I) and Cu (II) bound to His13 and His14 in Amyloid-β (4–16). *Inorganic chemistry* **58**, 15138-15154 (2019).

[262] Goch, W. & Bal, W. Numerical simulations reveal randomness of Cu (II) induced Aβ peptide dimerization under conditions present in glutamatergic synapses. *PloS one* **12**, e0170749 (2017).

[263] Lau, S.-J. & Sarkar, B. Ternary coordination complex between human serum albumin, copper (II), and L-histidine. *Journal of Biological Chemistry* **246**, 5938-5943 (1971).

[264] Girvan, P. *et al.* Redox kinetics of the amyloid-β-Cu complex and its biological implications. *Biochemistry* **57**, 6228-6233 (2018).

[265] Yako, N. *et al.* Copper binding and redox chemistry of the Aβ16 peptide and its variants: insights into determinants of copper-dependent reactivity. *Metallomics* **9**, 278-291 (2017).

[266] Zhang, W. *et al.* N4-tetradentate chelators efficiently regulate copper homeostasis and prevent ROS production induced by copper-amyloid-β1–16. *Chemistry–A European Journal* **24**, 7825-7829 (2018).

[267] Huang, J. *et al.* The TDMQ regulators of copper homeostasis do not disturb the activities of Cu, Zn-SOD, tyrosinase, or the CoIII cofactor vitamin B12. *European Journal of Inorganic Chemistry* **2019**, 1384-1388 (2019).

[268] Dringen, R. & Hirrlinger, J. Glutathione pathways in the brain. *Biological chemistry* **384**, 505-516 (2003).

[269] Musci, G., Di Marco, S., Bellenchi, G. C. & Calabrese, L. Reconstitution of ceruloplasmin by the Cu (I)-glutathione complex: evidence for a role of Mg2+ and ATP. *Journal of Biological Chemistry* **271**, 1972-1978 (1996).

[270] Ciriolo, M. R., Desideri, A., Paci, M. & Rotilio, G. Reconstitution of Cu, Zn-superoxide dismutase by the Cu (I). glutathione complex. *Journal of Biological Chemistry* **265**, 11030-11034 (1990).

[271] Freedman, J. H., Ciriolo, M. R. & Peisach, J. The role of glutathione in copper metabolism and toxicity. *Journal of Biological Chemistry* **264**, 5598-5605 (1989).

[272] Nguyen, M. *et al.* Transfer of copper from an amyloid to a natural copper-carrier peptide with a specific mediating ligand. *Chemistry–A European Journal* **21**, 17085-17090 (2015).

[273] Scott, D. & Roy, S. α-Synuclein inhibits intersynaptic vesicle mobility and maintains recycling-pool homeostasis. *Journal of Neuroscience* **32**, 10129-10135 (2012).

[274] Vargas, K. J. *et al.* Synucleins regulate the kinetics of synaptic vesicle endocytosis. *Journal of Neuroscience* **34**, 9364-9376 (2014).

[275] Galvagnion, C. The role of lipids interacting with α-synuclein in the pathogenesis of

Parkinson's disease. *Journal of Parkinson's disease* **7**, 433-450 (2017).
[276] Breydo, L., Wu, J. W. & Uversky, V. N. α-Synuclein misfolding and Parkinson's disease. *Biochimica et Biophysica Acta (BBA)-Molecular Basis of Disease* **1822**, 261-285 (2012).
[277] Lashuel, H. A., Overk, C. R., Oueslati, A. & Masliah, E. The many faces of α-synuclein: from structure and toxicity to therapeutic target. *Nature Reviews Neuroscience* **14**, 38-48 (2013).
[278] Dettmer, U., Selkoe, D. & Bartels, T. New insights into cellular α-synuclein homeostasis in health and disease. *Current opinion in neurobiology* **36**, 15-22 (2016).
[279] Spillantini, M. G. *et al.* α-Synuclein in Lewy bodies. *Nature* **388**, 839-840 (1997).
[280] Baba, M. *et al.* Aggregation of alpha-synuclein in Lewy bodies of sporadic Parkinson's disease and dementia with Lewy bodies. *The American journal of pathology* **152**, 879 (1998).
[281] Goedert, M., Spillantini, M. G., Del Tredici, K. & Braak, H. 100 years of Lewy pathology. *Nature Reviews Neurology* **9**, 13 (2013).
[282] Zhang, H., Griggs, A., Rochet, J.-C. & Stanciu, L. A. In vitro study of α-synuclein protofibrils by cryo-EM suggests a Cu2+-dependent aggregation pathway. *Biophysical journal* **104**, 2706-2713 (2013).
[283] Abeyawardhane, D. L. *et al.* C-Terminal CuII coordination to α-synuclein enhances aggregation. *ACS chemical neuroscience* **10**, 1402-1410 (2018).
[284] Paik, S. R., Shin, H.-J. & Lee, J.-H. Metal-catalyzed oxidation of α-synuclein in the presence of copper (II) and hydrogen peroxide. *Archives of biochemistry and biophysics* **378**, 269-277 (2000).
[285] Kanda, S. *et al.* Enhanced vulnerability to oxidative stress by α-synuclein mutations and C-terminal truncation. *Neuroscience* **97**, 279-284 (2000).
[286] Jakes, R., Spillantini, M. G. & Goedert, M. Identification of two distinct synucleins from human brain. *FEBS letters* **345**, 27-32 (1994).
[287] Trexler, A. J. & Rhoades, E. N-terminal acetylation is critical for forming α-helical oligomer of α-synuclein. *Protein Science* **21**, 601-605 (2012).
[288] Huang, C., Ren, G., Zhou, H. & Wang, C.-c. A new method for purification of recombinant human α-synuclein in Escherichia coli. *Protein expression and purification* **42**, 173-177 (2005).
[289] Wislet-Gendebien, S. *et al.* Differential regulation of wild-type and mutant alpha-synuclein binding to synaptic membranes by cytosolic factors. *BMC neuroscience* **9**, 1-16 (2008).
[290] Ren, G. *et al.* Translocation of α-synuclein expressed in Escherichia coli. *Journal of bacteriology* **189**, 2777-2786 (2007).
[291] Golts, N. *et al.* Magnesium inhibits spontaneous and iron-induced aggregation of α-synuclein. *Journal of Biological Chemistry* **277**, 16116-16123 (2002).
[292] Coelho-Cerqueira, E. *et al.* α-Synuclein as an intrinsically disordered monomer–fact or artefact? *The FEBS journal* **280**, 4915-4927 (2013).
[293] Hoyer, W. *et al.* Dependence of α-synuclein aggregate morphology on solution conditions. *Journal of molecular biology* **322**, 383-393 (2002).
[294] Araki, K. *et al.* A small-angle X-ray scattering study of alpha-synuclein from human red blood cells. *Scientific reports* **6**, 1-8 (2016).
[295] Narhi, L. *et al.* Both familial Parkinson's disease mutations accelerate α-synuclein

aggregation. *Journal of Biological Chemistry* **274**, 9843-9846 (1999).

[296] Choi, J. Y. *et al.* Rapid purification and analysis of α-synuclein proteins: C-terminal truncation promotes the conversion of α-synuclein into a protease-sensitive form in Escherichia coli. *Biotechnology and applied biochemistry* **36**, 33-40 (2002).

[297] Uversky, V. N., Li, J. & Fink, A. L. Evidence for a partially folded intermediate in α-synuclein fibril formation. *Journal of Biological Chemistry* **276**, 10737-10744 (2001).

[298] Uversky, V. N. *et al.* Methionine oxidation inhibits fibrillation of human α-synuclein in vitro. *FEBS letters* **517**, 239-244 (2002).

[299] Zhou, W. *et al.* Methionine oxidation stabilizes non-toxic oligomers of α-synuclein through strengthening the auto-inhibitory intra-molecular long-range interactions. *Biochimica et Biophysica Acta (BBA)-Molecular Basis of Disease* **1802**, 322-330 (2010).

[300] Davidson, W. S., Jonas, A., Clayton, D. F. & George, J. M. Stabilization of α-synuclein secondary structure upon binding to synthetic membranes. *Journal of Biological Chemistry* **273**, 9443-9449 (1998).

[301] Jo, E. *et al.* α-Synuclein membrane interactions and lipid specificity. *Journal of Biological Chemistry* **275**, 34328-34334 (2000).

[302] Appel-Cresswell, S. *et al.* Alpha-synuclein p. H50Q, a novel pathogenic mutation for Parkinson's disease. *Movement disorders* **28**, 811-813 (2013).

[303] Proukakis, C. *et al.* A novel α-synuclein missense mutation in Parkinson disease. *Neurology* **80**, 1062-1064 (2013).

[304] Khalaf, O. *et al.* The H50Q mutation enhances α-synuclein aggregation, secretion, and toxicity. *Journal of Biological Chemistry* **289**, 21856-21876 (2014).

[305] Panchuk-Voloshina, N. *et al.* Alexa dyes, a series of new fluorescent dyes that yield exceptionally bright, photostable conjugates. *Journal of Histochemistry & Cytochemistry* **47**, 1179-1188 (1999).

[306] Tyagarajan, K., Pretzer, E. & Wiktorowicz, J. E. Thiol-reactive dyes for fluorescence labeling of proteomic samples. *Electrophoresis* **24**, 2348-2358 (2003).

[307] Peisach, J. & Blumberg, W. Structural implications derived from the analysis of electron paramagnetic resonance spectra of natural and artificial copper proteins. *Archives of biochemistry and biophysics* **165**, 691-708 (1974).

[308] Spector, R. Vitamin homeostasis in the central nervous system. *New England Journal of Medicine* **296**, 1393-1398 (1977).

[309] Covarrubias-Pinto, A. *et al.* Old things new view: ascorbic acid protects the brain in neurodegenerative disorders. *International journal of molecular sciences* **16**, 28194-28217 (2015).

[310] Forman, H. J., Zhang, H. & Rinna, A. Glutathione: overview of its protective roles, measurement, and biosynthesis. *Molecular aspects of medicine* **30**, 1-12 (2009).

[311] Deponte, M. Glutathione catalysis and the reaction mechanisms of glutathione-dependent enzymes. *Biochimica et Biophysica Acta (BBA)-General Subjects* **1830**, 3217-3266 (2013).

[312] Licastro, F. *et al.* Studies of blood brain barrier permeability and of intrathecal IgG synthesis in patients with Alzheimer's disease and multi-infarct dementia. *ADVANCES IN THE BIOSCIENCES-OXFORD-* **87**, 283-283 (1993).

[313] Kirsipuu, T. *et al.* Copper (II)-binding equilibria in human blood. *Scientific reports* **10**, 1-11 (2020).

[314] Sonnino, S. *et al.* Aggregative properties of gangliosides in solution. *Chemistry and physics of lipids* **71**, 21-45 (1994).

[315] Šachl, R., Mikhalyov, I., Hof, M. & Johansson, L. B. A comparative study on ganglioside micelles using electronic energy transfer, fluorescence correlation spectroscopy and light scattering techniques. *Physical Chemistry Chemical Physics* **11**, 4335-4343 (2009).

[316] Dudzik, C. G. *et al.* Copper coordination to the membrane bound form of α-synuclein. *Biochemistry* **52**, 53-60 (2013).

[317] Fakhree, M. A. *et al.* The number of α-synuclein proteins per vesicle gives insights into its physiological function. *Scientific reports* **6**, 1-9 (2016).